Aerosol Synthesis and Characterization of Silicon Nanocrystals

Thesis by

Renato Penha Camata

In Partial Fulfillment of the Requirements

for the Degree of

Doctor of Philosophy

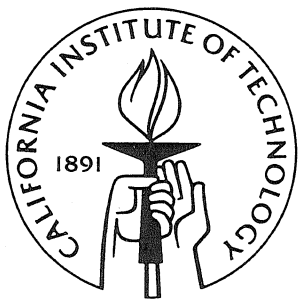

California Institute of Technology

Pasadena, California

1998

(Submitted July 29, 1997)

To my wife, Silvia

"I lift my eyes to the hills – where does my help come from?

My help comes from the Lord, the Maker of heaven and earth."

The Bible, Psalm 121.1

Acknowledgments

First and foremost I wish to thank God for giving me life, health, and the skills necessary for my five years of graduate studies at Caltech. His love, faithfulness, and care for me and my family have been wonderful during this season of our lives.

I am also deeply grateful to my advisors, Professors Harry A. Atwater, Richard C. Flagan, and Kerry J. Vahala for their guidance and support. I have benefited greatly from their scientific knowledge, insight, and enthusiasm as well as from their patience and availability. Their different areas of expertise provided me with a unique graduate experience. I thank Professor Atwater for his emphasis on materials properties. I am grateful to Professor Flagan for introducing me to the field of Aerosol Science. I thank Professor Vahala for sharing with me some of his knowledge in semiconductor nanostructures. I have greatly appreciated not only their scientific advice, but also their friendship. I am sure their example will continue to inspire me throughout my future career.

During my years of graduate school I have also benefited from the help of many other people. I thank Dr. Winston Saunders, Dr. M. V. Ramana Murty, Dr. Charles S. Tsai, and Susan Melnik, for their help in my initial experiments. I will always be thankful to Dr. Channing Ahn and Dr. Carol M. Garland for teaching me transmission electron microscopy. I also thank Maggie E. Taylor for her help and patience during the times I used the pulsed laser ablation system. Likewise, I wish to thank Dr. Toyokazu Tambo for his assistance in the maintenance and improvement of the surface analysis system, as well as Claudine Chen and Dr. Chih-Ming Yang for taking

care of our computers.

For their role in the aerosol investigations, I thank Patrick Chuang, Dr. Paul J. Drayton and Sulekha Chattopadhyay. I appreciated their suggestions and assistance with the experiments. I also wish to give special thanks to Dr. Shou-Hua Zhang for his invaluable help with aerosol instrumentation.

Thanks to Michael P. Easterbrook who has provided we with general technical advice in countless opportunities.

I also wish to thank many friends who, although not directly involved in my work, helped make my time at Caltech an enjoyable one: Roberto Paiella, Guido Hunziker, Regina Ragan, Jim Smith, Per Olof Hedekvist, Denis Phares, Ashish Bhardwaj, Masashi Fukazawa, Richard Dandliker, Weihua Xu, Hunsuk Kim, Heather Frase, Hiroshi Yoshino, Lada Adamic, Geraldine Nogaki, Joseph Christopherson, Michele Ostraat, Mark L. Brongersma, Kay Saipetch, Paula Samazan, Mehrdad Mahmoudi Zarandi, Matt J. Carlson, Dr. Imram Hashim, Dr. Hyun Sung Joo, Dr. Eric Bakke, Dr. Volnei Pedroni, Dr. Jung Shin, Dr. Ruth Brain, Dr. Selmer Wong, Dr. Robert B. Lee, Dr. David F. Geraghty, Dr. Kirill Shcheglov, Dr. Seongil Im, Dr. Jianhui Zhou, Dr. Namkyoo Park, Dr. Minyu Yao, Dr. David Dougherty, and Dr. John Hartman.

I am particularly grateful to Dr. Zhe Wu for his friendship during my first weeks at Caltech. I also thank Kyu Sung Min and Dr. Gang He for their close friendship and for some of the most stimulating scientific discussions I have ever had.

I owe special thanks to Elizabeth A. Boer for all her help in the final stages of this

thesis work. Cooperating with her in the aerosol nanocrystal synthesis has been an enjoyable and encouraging experience.

I am also grateful to Joe Fontana, Rodney Rojas, and John Van Deusen for invaluable assistance in the building of aerosol equipment. Ms. Rosalie Rowe, our secretary, and Ms. Linda Dozsa were a constant help by taking care of so many administrative details. Thanks also to Mrs. Fidelina Gann for keeping our office and lab environment always clean.

I thank the Brazilian *Conselho Nacional de Desenvolvimento Científico e Tecnológico* (CNPq, Brasília, Brazil) and the Charles Lee Powell foundation for the financial support. I also thank Professors Atwater, Flagan, and Vahala for often facilitating the implementation of my financial support.

I would like to express my gratitude also to Professors José R. Leite, Marco A. P. Lima and Vincent B. McKoy for their support when I first came to Caltech. Their trust and encouragement are greatly appreciated and will forever be remembered with gratefulness in my heart.

Last, but not least, I must thank our families. I am grateful to my parents, Gevilson Camata and Luzia P. Camata, and to my parents-in-law, Frédy A. Gisiger and Odette E. Gisiger, for their consistent support during our absence. I also wish to express my gratitude to Alva and Carol Larsen who have embraced us as part of their own family.

Most of all, I want to thank my wife, Silvia, for her love, sacrifices, and patience. Without her I would not have reached this point. She is my great source of encour-

agement and the most precious person I know on earth. I also want to thank my children, Enrico and Graziella, for sharing, in their own way, our joy and challenges during this time.

Abstract

Synthesis and processing of optically active silicon nanocrystals are explored from an aerosol science perspective.

Spark ablation, laser ablation and thermal evaporation in inert atmospheres are employed alternatively as vapor phase sources of nanocrystals. Nanocrystals generated employing these techniques comprise a highly polydisperse and morphologically diverse aerosol. After collection on a solid substrate, samples of these nanocrystals exhibit wide-band visible photoluminescence. A system for size classification of the initial polydisperse nanocrystal aerosol is demonstrated employing differential mobility analysis. Working at low nanocrystal concentrations (around 10^5 cm^{-3}) size control within 15% to 20% is achieved in the 2 to 10 nm size regime with a radial differential mobility analyzer at the expense, however, of low throughputs which make optical studies challenging.

Seeking higher throughputs, the physics of aerosol size classification by this technique is investigated in detail by self-consistent numerical simulations of the particle transport inside the differential mobility analyzer. Our results lead to the identification of critical design characteristics required to maximize the analyzer performance from the viewpoint of semiconductor nanocrystal synthesis. With the guidance of these theoretical predictions, an optimized differential mobility analyzer design is suggested. This instrument has its parameters chosen to perform high resolution, high throughput size classification of nanocrystals in the 0.5 to 10 nm range.

Optical characterization studies on polydisperse and size-classified silicon nanocrys-

tal samples are performed. Results suggest that at least two mechanisms for light emission are at work in aerosol synthesized silicon nanocrystals.

X-ray photoelectron measurements on size-classified silicon nanocrystals reveal that an oxide layer with thickness in excess of several nanometers forms on the silicon nanocrystals within a few minutes of air exposure. In order to preserve and control the surface chemistry of the nanocrystals, a system for anaerobic transfer of the size-classified silicon nanocrystals is designed and built. The system couples the nanocrystal synthesis experiment with the ultra high vacuum chamber of a surface analysis system via a load lock high vacuum chamber. Optical characterization capabilities are also installed. Preliminary results on nanocrystal synthesis and characterization using this *in situ* setup are presented and discussed.

Contents

List of Figures

Chapter 1

Introduction

Nanostructured semiconductor materials comprise an interesting class of advanced materials for scientific investigation. Both, from fundamental and technological points of view, these materials hold the potential for significant breakthroughs in technological applications and in the study of new physics.

Nanostructured materials in general refer to materials whose building blocks are small structures in the nano-scale regime. In the case of semiconductors, these nano-scale structures are tiny crystals comprised of tens of thousands, thousands, or even only hundreds of atoms. These minute structures are expected to have unique properties characteristic of mesoscopic systems, i.e., they behave neither as molecular systems nor as bulk objects. In fact, their electronic and optical properties are expected to be strongly dependent on size. These characteristics open new avenues for engineering the properties of these materials once one can manipulate their size, shape and structure.

The recent interest in materials containing nanocrystals of the elements of Column

IV of the periodic table arises from the fact that the semiconductor industry has its foundation on silicon technology, which has become a mature endeavor. However, as the limits of silicon technology begin to become an issue, alternatives are being sought to meet current and future growth demands. Silicon nanocrystals have emerged as one of these alternatives, with the potential of breaking through the optoelectronic barrier (due to the indirect gap of bulk silicon) while still preserving compatibility with the established technologies.

One of the difficulties that has hampered conclusive understanding of the mechanisms to explain the electronic and optical properties of semiconductor nanocrystals is the fact that samples containing nanocrystals are usually polydisperse. They comprise a morphologically diverse collection of nano-particles with a broad range of sizes and shapes.

In this thesis the synthesis and characterization of silicon nanocrystals are explored from an aerosol science perspective, addressing size control of nanocrystals as a primary goal.

Chapter 2 is an introduction to Group IV semiconductor nanocrystals in general. It presents the basic semiconductor nanocrystal physics necessary to understand the size effects that are expected to become important in the nano-scale. The issue of surface and interface localized states in nanocrystals is also discussed and some potential applications of materials containing these nanocrystals are described.

Chapter 3 is a systematic overview of the aerosol strategies and techniques employed in this thesis work. It includes discussions on vapor phase synthesis of silicon

nanocrystals and aerosol techniques such as differential mobility analysis. It also describes instrumentation that was designed and built during the course of this work such as the electrostatic precipitator and the hypersonic impactor.

Chapter 4 presents experimental results on the synthesis of size-classified silicon nanocrystals from three different vapor phase techniques, namely, spark ablation, laser ablation, and thermal evaporation.

In chapter 5 a systematic study of the limits to differential mobility analysis is presented. This is done through numerical simulations of the physical phenomena that limit the effectiveness of differential mobility analysis as a size classification technique in the nanometer regime. From this analysis, an optimized differential mobility analyzer is introduced.

Chapter 6 presents a summary of the measured optical properties of aerosol synthesized silicon nanocrystals. A system for process control and *in situ* characterization of size-classified nanocrystals is also described and preliminary results are presented and discussed.

Chapter 7 summarizes the conclusions of this thesis and also presents some prospects for expanding the use of aerosol techniques in semiconductor nanocrystals synthesis. The possibility of a high-throughput, high-resolution size classification system is discussed from the perspective of the nanocrystal source, the aerosol charge state, and the differential mobility analyzer. Questions regarding improvement in shape control and high quality passivation are briefly addressed.

Chapter 2

Group IV semiconductor nanocrystals

2.1 Introduction

Semiconductor nanocrystals made of elements from the Column IV of the periodic table, i.e., Si and Ge, comprise a particular class of materials within the broader research field of semiconductor nanocrystals.

The interest in semiconductor nanocrystals in general springs from several motivating factors. First of all, the achievement of semiconductor structures with low dimensionality has been a major scientific and technological endeavor of the last two decades. The advent of crystal-growth techniques with atomic monolayer control, such as Molecular Beam Epitaxy and Organometallic Physical Vapor Epitaxy has brought about the ability to engineer semiconductor heterostructures with abrupt interfaces. This fostered the development of a vast array of semiconductor devices

utilizing heterostructures and quantum wells. The high electron mobility transistor [1] and the quantum well semiconductor laser [2, 3] are just two examples of devices based on semiconductor heterostructures exhibiting one-dimensional quantum confinement that have had great technological impact. The possibility of extending quantum confinement effects into further dimensions in nanocrystals has motivated a great deal of research geared towards efficient fabrication routes and fundamental physical understanding of these nanostructures. These materials hold the potential for enhanced linear and nonlinear optical properties as one of the consequences of quantum confinement is the discretization of the energy levels, enabling the concentration of bulk oscillator strength into single spectral lines and small volumes [4].

Originally, most of the interest in semiconductor nanocrystals was focused on materials that exhibit direct-gap in the bulk form. Nanocrystals made of direct-gap III-V semiconductors (e.g., GaAs, InSb, etc.) and direct-gap II-VI semiconductors (e.g., CdS, CdSe, ZnO, etc.) were the first to be studied theoretically and experimentally. The reason for that was the great success of these materials in the fabrication of heterostructures with quantum confinement in one dimension. Their choice as the preferred materials in the initial attempts to synthesize and describe nanocrystals with three-dimensional confinement was, thus, a natural one.

The discovery of visible room-temperature photoluminescence from porous silicon [5, 6], synthesized by anodic etching of Si initiated a whole new interest in Group IV semiconductor nanocrystals. Although its morphological characterization was difficult from the start, porous silicon has since been interpreted as a network of highly

irregular nanostructures [17]. Models involving nanocrystalline wires and islands rapidly emerged in the attempt to describe its morphology. At the same time, a number of techniques were demonstrated to synthesize visible-luminescent Group IV nanocrystals, both in free-standing configurations [7, 8, 9, 10, 11] and embedded in solid [12, 13, 14] or liquid matrices [15, 16]. Although quantum efficiencies for demonstrated devices are still low, these findings opened new possibilities for silicon-based light emitters as a viable alternative to other more complex optoelectronic materials [17, 18]. Due to the advantages of the mature silicon technology, the prospect of silicon-based or silicon-compatible optoelectronics became an additional motivating factor in the study of Group IV semiconductor nanocrystals.

More recently some authors have demonstrated an information storage device utilizing the potential well of silicon nanocrystals [21, 22, 23]. This memory device uses the silicon nanocrystal as a charge storage compartment. A number of recent reports also point towards single electron electronics demonstrating single-nanocrystal transistors and logic devices [24, 25]. Therefore, potential applications for Group IV semiconductor nanocrystals are being envisioned not only in the realm of optoelectronics, but also as an information storage medium and electronic transport material.

In the following sections we discuss the basic physics of Group IV semiconductor nanocrystals in order to understand why their optical properties differ from their bulk counterparts. We also briefly address some of the complicating issues in understanding the behavior of these nanocrystals, namely, surface and interface localized states.

2.2 Quantum confinement effects

In a bulk semiconductor crystal, the physical dimensions of the system are much larger than the de Broglie wavelength of the electrons. As a result, a given electron in the solid is solely under the influence of the lattice potential and the potential of the other electrons. In the independent electron approximation [26], these interactions are represented by an effective one-electron potential $U(\mathbf{r})$, reducing the quantum mechanical description of the system to the time-independent Schröedinger equation for a single electron written as

$$H\Psi(\mathbf{r}) = \left[-\frac{\hbar^2}{2m}\nabla^2 + U(\mathbf{r})\right]\Psi(\mathbf{r}) = E\Psi(\mathbf{r}) \tag{2.1}$$

where the one-electron potential $U(\mathbf{r})$ has the periodicity of the crystal lattice.

The solution of Eq. 2.1 provides, in principle, the eigenstates and energy eigenvalues for electrons in the semiconductor. However, a number of general properties of these electronic states can be inferred from other fundamental results of the quantum theory of solids without attempting to solve the above equation.

The one-electron wave functions that satisfy Eq. 2.1 can be written, according to Bloch's theorem [27], as a plane wave times a function with the periodicity of the crystalline lattice.

$$\Psi_{n\mathbf{k}}(\mathbf{r}) = e^{i\mathbf{k}\cdot\mathbf{r}}u_{n\mathbf{k}}(\mathbf{r}) \tag{2.2}$$

where $u_{n\mathbf{k}}(\mathbf{r})$ has the periodicity of the lattice. The index n is introduced in Bloch's theorem because for a given value of the propagation constant $\mathbf{k}$, there are many solutions to the Schröedinger equation. For each n, there exists a set of energy

eigenvalues $E_n(\mathbf{k})$ that define an energy band of the crystal. Under the influence of an external force $\mathbf{F}_e$, an electron in band $E_n(\mathbf{k})$ experiences an acceleration

$$\frac{d\mathbf{v}_n(\mathbf{k})}{dt} = \frac{\mathbf{F}_e}{m_n^*} \tag{2.3}$$

where m_n^* is given by

$$m_n^* = \frac{\hbar^2}{\frac{d^2E_n(\mathbf{k})}{dk^2}} \tag{2.4}$$

The quantity m_n^* is the effective mass of the electron. It determines the electron dynamics in the crystalline periodic potential.

As a result of the finiteness of the system, boundary conditions will force the quantization of the wave vector $\mathbf{k}$, which leads to

$$k_j = \frac{2\pi s_j}{L_j} \tag{2.5}$$

where $j = x, y, z$, s_j are integers, and L_j are the physical dimensions of the crystal. The k-space volume per eigenstate is thus $8\pi^3/V$ where $V = L_xL_yL_z$ is the physical volume of the crystal. Since L_j is much larger than the lattice constant, a continuum representation may be used for k-space, and the density of available states can be found by dividing the volume of a spherical shell of radius k and thickness dk ($4\pi k^2 dk$) by the volume per eigenstate ($8\pi^3/V$). This gives

$$\rho(k)dk = \frac{k^2V}{\pi^2}dk \tag{2.6}$$

where a factor of two has been added to account for the two spin states of an electron.

Virtually all the electronic properties of a semiconductor are determined by the relatively few electrons excited into the conduction band and holes left behind in the

valence band. The excited electrons are found close to the bottom of the conduction band while most of the holes lie near the top of the valence band. Therefore, the parabolic band approximation can be used and the relationship between E and k is simply given by

$$E_{c,v}(k) = \frac{\hbar^2 k^2}{2m^*_{c,v}} \tag{2.7}$$

where the subscripts c and v denote the conduction and valence bands. Similarly, m^*_c and m^*_v are the effective masses for electrons in the conduction band and holes in the valence band, respectively, and E is measured from the band edge extremum. Combining Eqs. 2.6 and 2.7, the density of states per unit energy interval in the conduction band and valence bands can be expressed as

$$\rho_{c,v}(E) = \frac{1}{V}\rho_{c,v}(k)\frac{dk}{dE} = \frac{1}{2\pi^2}\left(\frac{2m^*_{c,v}}{\hbar^2}\right)^{3/2} E^{1/2} \tag{2.8}$$

The above expression gives the density of states for electrons in the conduction band and holes in the valence band in a bulk semiconductor. Its continuous character and dependence with the square-root of the energy are immediately obvious.

In a semiconductor nanocrystal the situation is significantly different. The physical dimensions of the system are now comparable to or smaller than the de Broglie wavelength of the electrons. Therefore, electrons are subjected to an envelope potential $V(\mathbf{r})$, which induces further quantization effects. This envelope potential varies in the length scale of the nanocrystal size and its presence is responsible for what has been called quantum confinement effects in semiconductor nanocrystals.

Although Bloch's theorem of Eq. 2.2 is no longer valid, if one assumes that the nanocrystal size is large enough to preserve the crystalline structure of the bulk

material, it is possible to retain the cell periodic parts of the bulk Bloch functions and write the wave functions for the confined carriers as

$$\Psi_{c,v}(\mathbf{r}) = \psi_{c,v}(\mathbf{r})u_{c,v}(\mathbf{r}) \tag{2.9}$$

where $\psi_{c,v}(\mathbf{r})$ is an envelope wave function that obeys the following time-independent effective mass Schröedinger equation

$$H\psi_{c,v}(\mathbf{r}) = \left[-\frac{\hbar^2}{2m^*_{c,v}}\nabla^2 + V(\mathbf{r})\right]\psi_{c,v}(\mathbf{r}) = E\psi_{c,v}(\mathbf{r}) \tag{2.10}$$

In what follows we review two simple solutions for this problem that model the main consequences of quantum confinement in semiconductor nanocrystals. In these solutions two high-symmetry three-dimensional confining potentials are chosen which allow the straightforward analytic solution of Eq. 2.10, namely, a spherical potential well and a cubic potential well, both with infinite depths. A diagram of these potentials can be seen in Fig. 2.1. For these cases, the electron and hole eigenstates are simply the particle-in-a-sphere and particle-in-a-box states.

Using, once again, the subscripts c and v to denote the conduction and valence bands respectively, and introducing the following conventions,

$$\begin{aligned} \nu &= c, v \\ m_c = m_e, &\qquad m_v = -m_h, \end{aligned} \tag{2.11}$$

the wave functions and the discrete energy spectrum for a sphere with radius R are found to be

$$\Psi_{\nu nlm}(\mathbf{r}) = Y_{lm}(\theta,\phi)\frac{1}{R}\left(\frac{2}{r}\right)^{1/2}\frac{J_{l+1/2}(k_{nl}r)}{J_{l+3/2}(k_{nl}R)}u_\nu(\mathbf{r}), \tag{2.12}$$

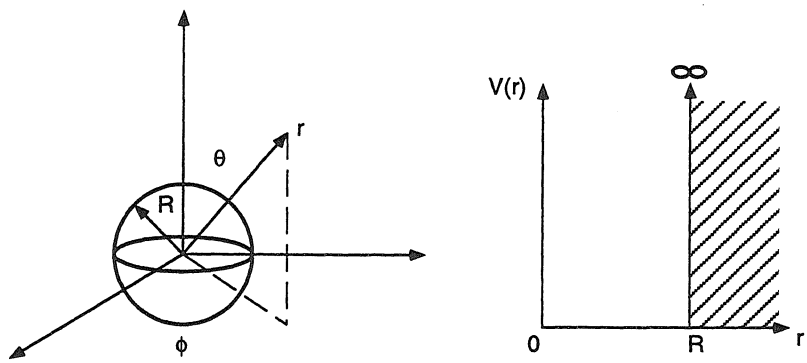

(a) Spherical semiconductor nanocrystal

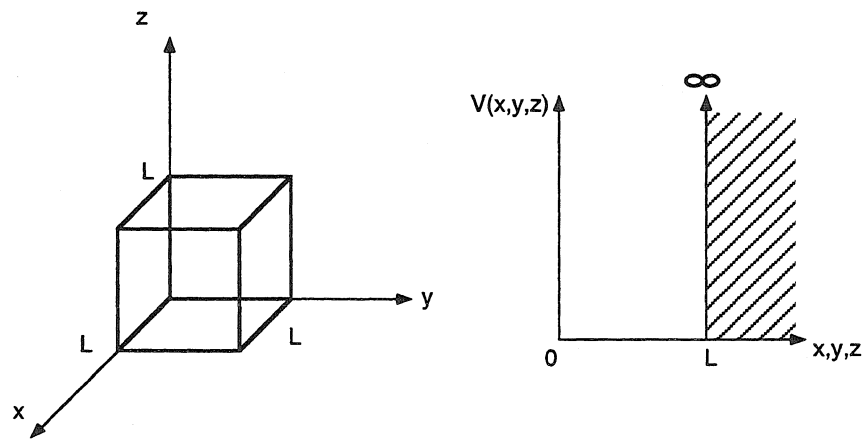

(b) Cubic semiconductor nanocrystal

Figure 2.1: Simple high-symmetry confining potentials for electrons: (a) Particle in a sphere and (b) particle in a box.

$$E_{\nu nl} = \pm\frac{E_g}{2} + \frac{\hbar^2 k_{nl}^2}{2m_\nu}, \tag{2.13}$$

where $-l \leq m \leq l$; $l = 0, 1, 2, ...$; $n = 1, 2, 3, ...$; and

$$J_{l+1/2}(k_{nl}R) = 0; \tag{2.14}$$

Similarly, for a cube with length L, one obtains

$$\Psi_{\nu nlm}(\mathbf{r}) = \left(\frac{2}{L}\right)^{3/2} \sin\left(\frac{n\pi}{L}x\right) \sin\left(\frac{l\pi}{L}y\right) \sin\left(\frac{m\pi}{L}z\right) u_\nu(\mathbf{r}), \tag{2.15}$$

$$E_{\nu nlm} = \pm\frac{E_g}{2} + \frac{\hbar^2\pi^2}{2m_\nu l^2}(n^2 + l^2 + m^2), \tag{2.16}$$

where $n, l, m = 1, 2, 3, ...$;

In Eqs. 2.13 and 2.16 the energy is measured from the middle of the energy gap. These equations reveal that quantum confinement raises the energy of electron states and lowers the energy of hole states. The overall effect is a blue shift in the optical transitions. In addition, the energy levels become discrete, i.e., quantum confinement splits the bulk conduction and valence bands into a series of discrete energy levels. As a result, the density of states (DOS) changes from its bulk $\sqrt{E}$ dependence to a δ-function like dependence with energy. One of the most attractive features of this discretization of the energy levels is that it enables the concentration of bulk oscillator strength into single spectral lines and small volumes, so that an enhanced linear and nonlinear optical response is to be expected. As the optoelectronic properties of a semiconductor are determined by both the Fermi-Dirac distribution and the DOS, the ability to engineer and tune the DOS in nanocrystals opens new avenues for optoelectronic applications using these materials.

Another feature that is relevant in semiconductor nanocrystals with quantum confinement effects is related to the binding energy of excitons. In fact, quantum confinement is expected to raise the exciton binding energy, and significant excitonic effects may be important even at room temperature [29].

Figure 2.2 summarizes the ideas we have discussed so far, presenting a comparison between a bulk semiconductor and a semiconductor nanocrystal from the point of view of the electronic band structure in real space.

Although the simple expressions 2.13 and 2.16 for the energy levels help us to understand the origin of quantum confinement effects, they have little predictive power in Group IV materials like silicon. The size dependence of the band gap of a silicon nanocrystal, for example, will not be predicted correctly due to the oversimplification of the model.

A great deal of research has been done in an attempt to describe quantum confinement in ever more realistic terms. Many different calculations of the band structure of semiconductor nanocrystals have been performed using different models and approximations with various degrees of sophistication.

In what follows, we review the results of several electronic structure calculations which are intended to have predictive power for the properties of silicon nanocrystals. We also discuss briefly the methods and assumptions employed in each one of these calculations.

Takagahara and Takeda [29] worked within the effective mass approximation to study the effect of quantum confinement on excitons in Si and Ge nanocrystals. In

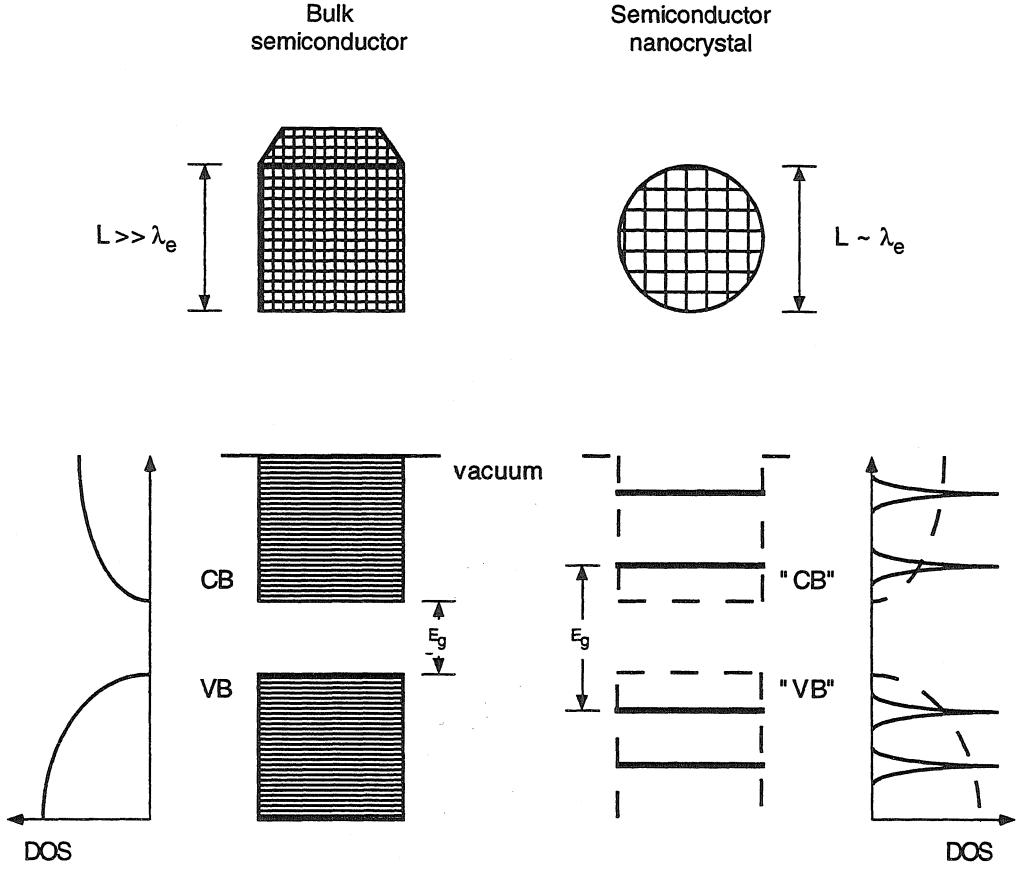

Figure 2.2: Comparison between a bulk semiconductor and a semiconductor nanocrystal showing the splitting of the bulk conduction and valence bands into discrete energy levels in the nanocrystal, accompanied by the concentration of the density of states into sharp features.

this approximation, the one-electron periodic potential $U(\mathbf{r})$ is replaced by a constant potential and the kinetic energy operator is replaced by an effective mass operator, derived from the parabolic expansion of the bulk band structure [30]. For nanocrystals with radius smaller than the bulk exciton Bohr radius a_0 (about 1 nm for Si), electrons and holes are individually confined with little electron-hole correlation. For nanocrystals with radius 2-4 times a_0, of a hydrogenic exciton forms and the optical properties are likely to be of excitonic origin rather than arising from the recombination of free electron-hole pairs [4]. Therefore, an attempt to describe the system over these two size regimes must take into account the Coulomb interaction between confined electrons and holes. In order to do that, Takagahara and Takeda evaluated quantum-confinement induced changes in the energy spectrum a hydrogenic Hamiltonian, which, in the effective mass approximation, can be written as

$$\left[-\frac{\hbar^2}{2m_e^*}\nabla_e^2 - \frac{\hbar^2}{2m_h^*}\nabla_h^2 + \frac{e^2}{\epsilon|\mathbf{r}_e - \mathbf{r}_h|}\right]\psi(\mathbf{r}) = E\psi(\mathbf{r}) \tag{2.17}$$

Their calculations predict a dramatic increase in the band gap for silicon nanocrystal diameters below 4 nm with sizable shifts even at a nanocrystal diameter as large as 8 nm (see Fig. 2.3). The oscillator strength calculated with the effective mass wave functions seems to be consistent with a change in the character of the optical transitions from indirect to direct for confinement size below a few times the lattice constant. The effective mass approximation, however, may become seriously inaccurate when describing these very small nanocrystals ($\leq$ 4 nm) because the parabolic band approximation might no longer be valid. It is also likely that an overestimation of the energy gap occurs due to the assumptions of infinite potential barrier and

parabolic dispersion of the bands.

Trying to move away from the limitations of effective mass calculations, Delley and Steigmeier have used the density-functional approach for finite structures to calculate the electronic structure of silicon nanocrystals up to 3-nm diameter (706 atoms) [35]. The local density approximation is used and the wave functions are expanded on a small basis of linear combination of atomic orbitals. They face the opposite problem of the effective mass calculations, as their approach can only be justified for rather small nanocrystals. In this calculation the nanocrystals were assumed to be spherical with no relaxation of the bulk lattice and the dangling bonds were saturated with hydrogen atoms. Based on their results a claim is made that silicon becomes essentially a direct-band-gap material when in nanocrystalline form, as optical transitions across the gap are symmetry allowed. Their results for the size dependence of the energy gap are also presented in Fig. 2.3 and the obtained values are among the highest estimates. Fig. 2.4(a) also presents their calculation of the oscillator strength for nanocrystal diameter up to 3 nm. It is amazing that, according to Delley and Steigmeier's prediction, the oscillator strength changes by as much as six orders of magnitude for nanocrystals between 3 nm and molecular structures.

Tight binding calculations have also been developed. Delerue *et al.* used the linear combination of atomic orbitals (LCAO) technique with empirical parameters including interactions up to third nearest neighbors [33]. A different technique was proposed by Hill and Whaley who developed a time-dependent tight binding calculation [32]. Both of these tight binding approaches assume hydrogen terminated silicon

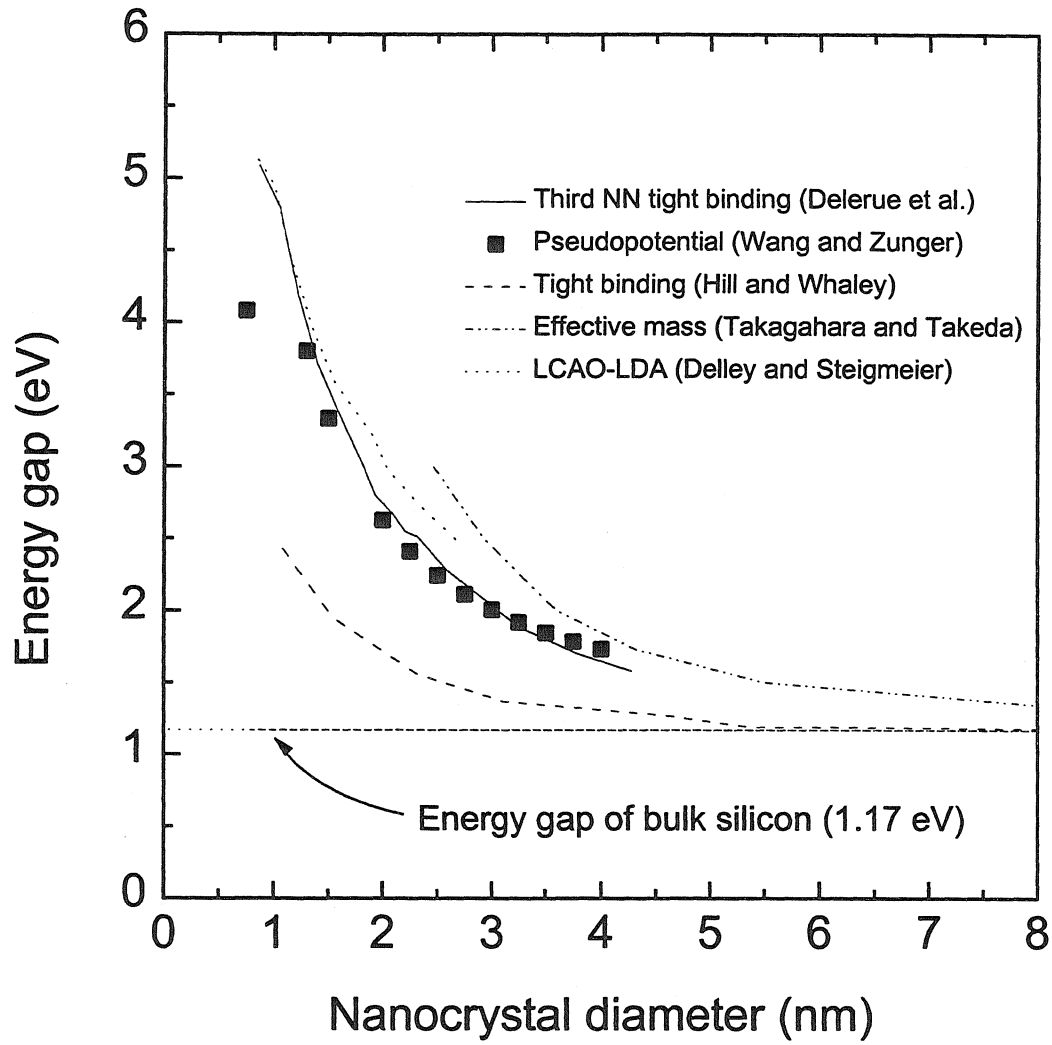

Figure 2.3: Calculated size dependence of the energy gap of silicon nanocrystals by different authors and methods.

nanocrystals, and their predictions for the size dependence of the band gap are also plotted in Fig. 2.3. The method of Hill and Whaley presents the most conservative estimates for the changes in the energy band gap with significant blue shifts predicted only below 2 nm.

Still a different strategy was adopted by Wang and Zunger [34]. They developed an empirical pseudopotential calculation. In this case, the total potential in the Hamiltonian of the problem is approximated by a superposition of atomic pseudopotentials adjusted to fit the bulk Si band structure, the effective masses, and the surface work function. Their prediction of the energy gap approximately matches the third-nearest-neighbor tight-binding approach of Delerue *et al.* [33].

Radiative recombination times have also been predicted and can provide an additional tool to recognize processes resulting from quantum confinement. Figure 2.4 (b) presents the results of one such calculation predicting the size dependence of cubic Si nanocrystals for both zero-phonon transitions and phonon assisted transitions.

A feature that becomes obvious by inspecting Fig. 2.3 is the significant variation between the predictions of different calculations. For 2-nm nanocrystals, for example, predictions vary by as much as 2 eV corresponding to differences of almost 500 nm in the emission wavelength.

One of the facts that has made it difficult to validate and use these calculations in comparison with experiment is the lack of direct experimental data demonstrating the changes in the described quantities as a function of nanocrystal size. All the available measurements in porous silicon are difficult to interpret due to the complex

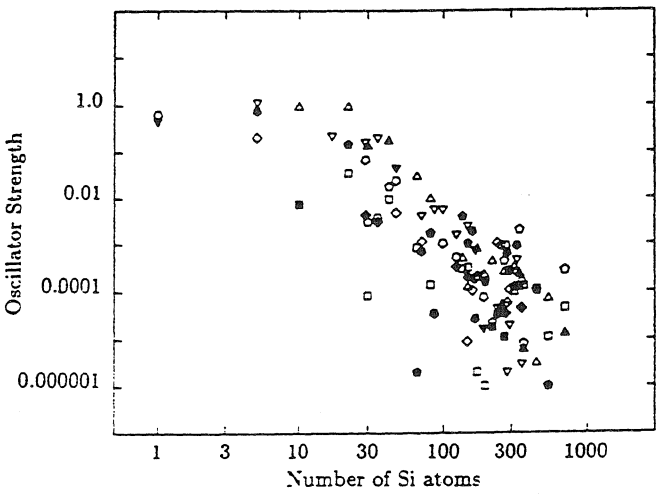

(a)

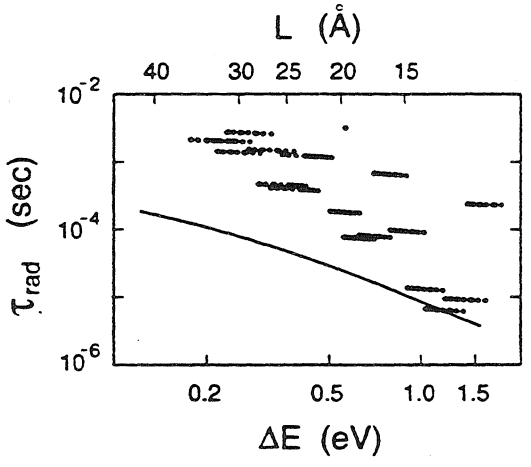

(b)

Figure 2.4: Calculated size dependence of (a) the oscillator strength (Ref. [35]) and (b) the radiative recombination time of optical transitions in silicon nanocrystals (Ref. [31]). In (b) dots correspond to zero-phonon transitions while the line indicates TO phonon-assisted transitions.

and varied morphology of that material. Experimental measurements in free-standing nanocrystals are also difficult to interpret as these materials are usually comprised of large chains of agglomerated nanostructures polydisperse in size and shape.

In view of this reality, one of the goals of this thesis was to generate samples of size-classified semiconductor nanocrystals whose optical properties could be directly checked against the calculations described above.

2.3 Surface and defect states

In a bulk semiconductor the effect of the shape and size of the surface is essentially negligible. As one looks at a semiconductor nanocrystal, however, the shape and size of the surface can no longer be neglected in the study of the electronic properties. In fact, as the nanocrystal size decreases, the surface-to-volume ratio increases and surface effects become ever more important. The very stability of the semiconductor nanocrystal as such depends on the fraction of atoms at the surface. As a free-standing nanocrystal in vacuum becomes smaller and the fraction of atoms at the surface increases, the high energetic cost of dangling bonds at the surface causes the system to collapse into more closed packed molecular clusters that minimize the number of broken bonds [36]. For nanocrystals embedded in matrices, much smaller stable sizes are achievable due to the saturation of the surface bonds by the matrix atoms.

Most of the electronic structure calculations for semiconductor nanocrystals assume that the carrier wave functions vanish at the surface. Although this assumption

simplifies the problem of determining confinement effects and some electronic structure calculations have made use of it, it is obviously not true in reality. In real nanocrystals the confining barriers have finite height, and penetration of the wave functions into the barriers are a fact particularly for states that lie high in the potential well. In addition, localized states at the surface trap carriers and may induce changes in the shape of the confining potential.

Surface effects not only complicate simple descriptions of quantum confinement effects, but also introduce totally new aspects in the optical properties of nanocrystals. From the chemical point of view, the surface of silicon nanocrystals, for example, is very reactive. Therefore, morphologically identical nanocrystals prepared by different routes or techniques may contain chemically different surface layers. Free-standing nanocrystals generated by vapor phase methods are particularly complicated in this matter because much of their characterization is done after air exposure. Due to the absence of an encapsulating layer, oxygen and hydroxyl groups will modify the surface chemistry leading to the formation of chemical compounds containing silicon, oxygen and hydrogen. This complicates the optical properties, as these compounds have been found to possess luminescence spectral lines in the visible range.

Hydrides and polysilanes, for example, are certain to form on the surface of non-stabilized silicon nanocrystals upon air exposure. Many of these Si-based structures have been found to be optically active in the visible range. SiH_x complexes, for instance, are known to exhibit room temperature photoluminescence around 1.7 eV [39]. An interesting feature of these complexes is that their emission wavelength and

quantum efficiency depend strongly on the hydrogen content. Tight-binding calculations of the Si-H bonding predict that the presence of hydrides with 30% hydrogen content causes the band gap of Si to increase to 1.7 eV [41]. This phenomenon is also believed to be the explanation for the band gap reduction of a-Si:H upon 500°C anneal [42]. Polysilane chains $(SiH_2)_n$ have also been reported to possess a band gap somewhere in the visible with energy gap variations due to changes in chain length [40].

It has also been proposed that siloxene compounds (i.e., $Si_6O_3H_6$ and its derivatives) form on the surface of nanoscale Si structures [43]. These compounds display visible luminescence in the 500-750 nm range depending upon the number of OH ligands replacing hydrogen in the siloxene molecule [44].

Although these complexes are not stable at high temperatures, their presence on nanocrystals that have not undergone heat treatments is almost assured. The evolution of hydrogen begins to occur at 230°C, and around 500°C hydrogen desorption becomes complete in nanoscale Si after a few minutes. The possibility of out-annealing hydrogen-related structures is therefore encouraging, as it occurs at temperatures where structural changes to the nanocrystal core may be considered limited.

In Group IV nanocrystals, hydrogen-related optically active structures may be classified as extrinsic defects as they are related to an impurity introduced in the material unintentionally, i.e., due to air exposure or contamination.

Another issue that has to be considered when synthesizing Group IV semicon-

ductor nanocrystals is the possible presence of intrinsic (i.e., not impurity related) optically active defects. In the case of Si nanocrystals these may be even more important than the hydrogen-related compounds, because they may be stable up to 800-900°C. These defects may be present in the crystallite core, in the passivation layer (usually SiO_2), or in the interfacial region.

Several intrinsic defects have been identified in the Si/SiO_2 system in general, and should therefore be expected to a certain extent in surface-oxidized silicon nanocrystals. These intrinsic defects may be classified into *natural* defects, generated during the thermal SiO_2 growth process, and *damage* defects, introduced in a postoxidation stage by irradiation with some kind of energetic species (e.g., γ and x photons, electrons, ions).

In the class of *natural* intrinsic defects, the most common and well understood defect is the so-called P_b which is essentially a trivalent Si atom at the Si/SiO_2 interface (i.e., Si dangling bond). Although not optically active, the P_b center has profound implications in the behavior of any Si structure. Energetically, it generates a deep level close to the middle of the gap, trapping carriers and providing non-radiative recombination paths.

Another center that should be expected to be relevant in surface-oxidized silicon nanocrystals is the non-bridging oxygen hole center (NBOHC). This center is an undercoordinated O atom bonded to a single Si atom with a hole in its nonbonding $2p$ orbital ($\equiv$Si-O$\cdot$) [45]. First identified in silica glasses, NBOHCs are found in isolated form in that material, and exhibit absorption bands in the 4.8- and 2-eV regions, and

a photoluminescence band in the 1.8-1.9-eV range [46]. Their luminescence characteristics may change significantly with the hydride/hydroxide content [47], which makes them all the more important in the study of free-standing nanocrystals exposed to air. In silica glasses NBOHC centers have been recognized in three different forms: (i) its most simple manifestation (≡Si-O·) which is related to low energy photoluminescence (towards the near IR), low quantum efficiency, and no PL shifts with heat treatments [48], (ii) a hydrogen-stabilized form (≡Si-O···H-Si≡) (only stable below 350°C) present in silica with high H and OH concentration and displays blueshifts and higher quantum efficiencies with increased H concentration [47, 48], and (iii) a not well understood NBOHC likely caused by the strain of bonding at an interface between two materials of different bond lengths, density, or structure [48].

In addition to the NBOHC, at least two other intrinsic *natural* defect centers in the Si/SiO_2 system are considered to be of importance in the interpretation of the optical properties of Si nanocrystals, namely, the $NL8$ center in crystalline Si and the EX center in SiO_2.

The $NL8$ center is a shallow thermal donor with a small cluster of atoms at the core. Thermal donors are commonly formed in oxygen-rich crystalline Si by annealing at 400-500°C for long periods of time (several hours). The formation mechanism is probably the diffusion of interstitial oxygen to form small clusters [49]. A center with similar properties, designated SD (for shallow donor) has been identified in porous Si [52]. The formation mechanism for the SD, however, has distinguishing features as it is found in samples that have not undergone heat treatments. One possible

explanation is that in silicon nanocrystals the diffusion length for oxygen may be smaller, allowing diffusion of O from the Si/SiO_x interface at lower temperatures. It is interesting to note that a current interpretation of these SD centers is that they are clusters of NBOHCs and should be expected to be optically active in the visible. In fact, electron spin resonance experiments in porous Si have determined that visible red luminescence in that material scales with the SD concentration [52].

The EX center is thought to have a similar core to the thermal donor SD, but which is located in the oxide [51]. In thin SiO_2 layers on Si the EX center has been described as a hole delocalized on three or four Si-O- linkages [50] which establishes the EX center also as an NBOHC cluster. EX centers have also been identified in porous Si, and once again, its concentration has been found to track with visible luminescence intensity [52].

Figure 2.5 illustrates the hydrogen-based compounds and oxygen-related defects discussed here, while Fig. 2.6 shows a schematic diagram of the levels expected to exist in the band gap of Si and SiO_2 due to the presence of the described defects and compounds.

For synthesis techniques that involve energetic irradiation of SiO_2, one has to consider the potential generation of optically active *damage* defects as well. The most studied *damage* defect in SiO_2 is the E' defect. It actually comprises a whole class of defects with several species recognized by electron spin resonance. The most common is viewed as a defect Si hybrid orbital at the site of an O vacancy, usually denoted as $O_3{\equiv}Si\cdot$ [53]. Although many other irradiation-induced defects may exist in

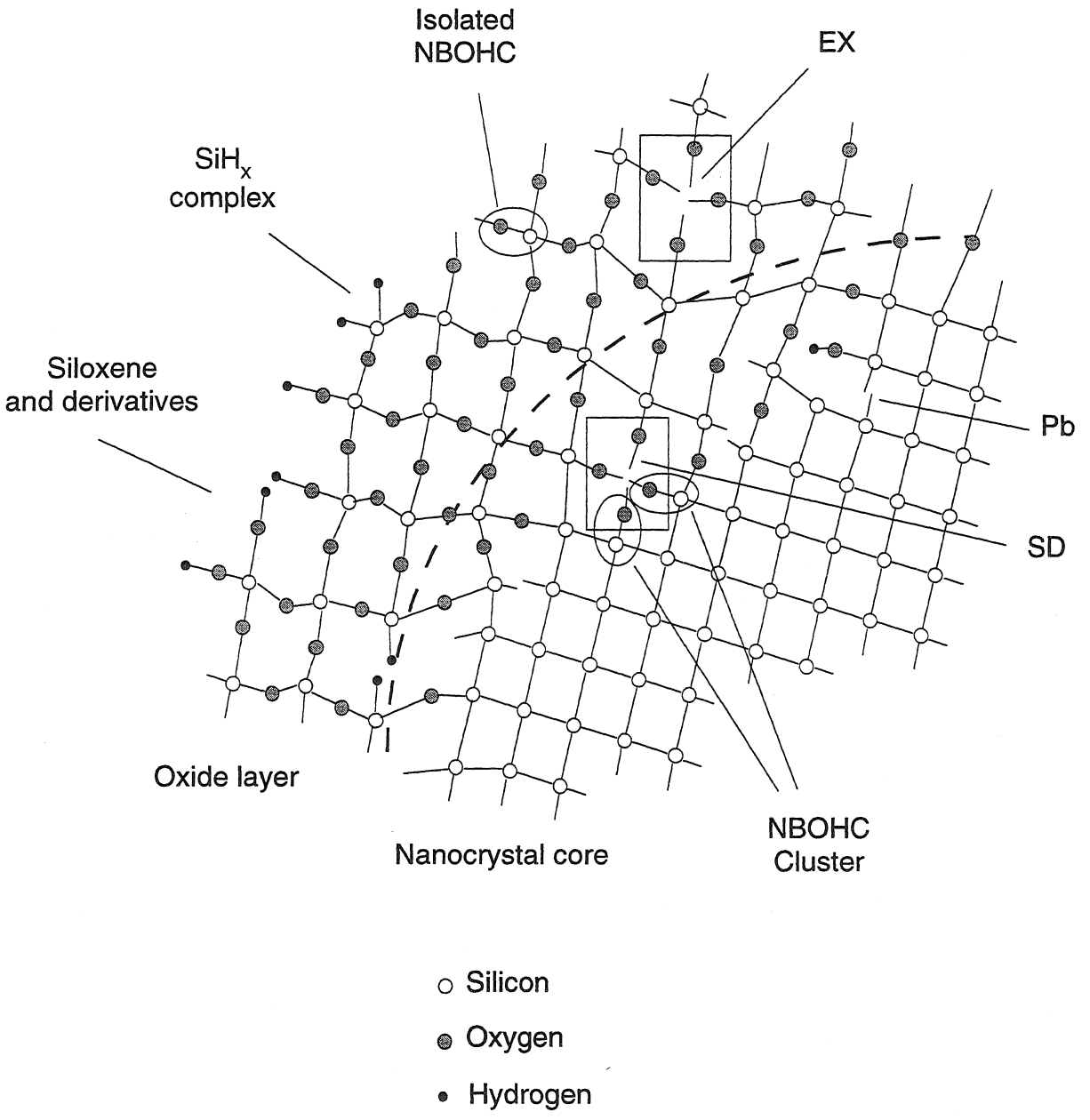

Figure 2.5: Illustration of the interfacial region of a silicon nanocrystal, depicting hydrogen-related complexes, dangling bonds, non-bridging oxygen hole centers, and their relationship to shallow donor and EX centers.

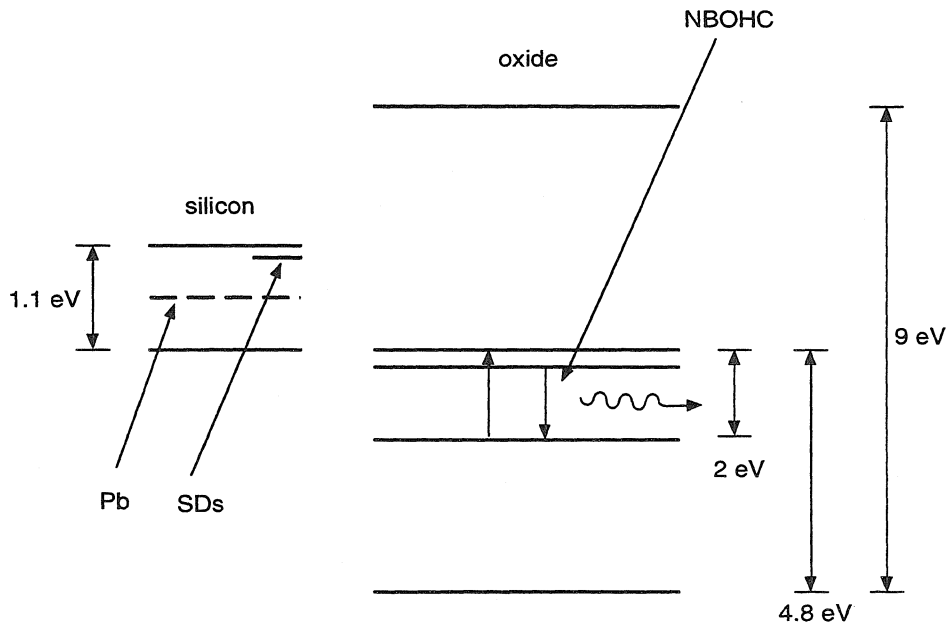

Figure 2.6: Schematic diagram showing the defect levels for hydrogen-related complexes, dangling bonds and shallow donors in Si, and non-bridging oxygen hole centers in silica glass.

SiO_2, E' defects provide a good example of an optically active (observed to luminesce in the blue) localized state.

The role of defects in SiO_2 in the observed optical properties of Group IV nanocrystals has been clarified recently for ion-beam synthesized nanocrystals in glass matrices but not yet studied in free-standing nanocrystals. Min *et al.* have performed extensive hydrogen-passivation experiments on glass samples containing Si and Ge nanocrystals and have been able to distinguish between a defect-related photoluminescence band and a nanocrystal-related band [37, 38]. An important observation of these authors was that even after high temperature annealing ($T \leq 1100°C$), the oxide matrix still contained various Si^{x+} oxidation states characteristic of a suboxide, which imply a pervasive presence of defects even after high temperature treatments [38].

The brief discussion presented here indicates how complex the study of optical properties of silicon nanocrystals may become due to the presence of surface and defect states that manifest themselves by atomic-type optical transitions inhomogeneously broadened by the effects of the chemical environment. Often, quantum confinement effects are far from being the dominant mechanism in the optical properties.

In order to discriminate between quantum-confined-state- and surface/defect-state-transitions, one strategy is to devise passivation schemes (e.g., the one proposed by Min *et al.* [37, 38]) that may allow the switching on and off of one or several mechanisms, simplifying the optical properties.

2.4 Potential device applications

Several potential device applications have been suggested employing Group IV semiconductor nanocrystals. These devices can be divided into three different classes, namely, optoelectronic devices, information-storage devices, and logic and control devices.

Due to its room-temperature visible photoluminescence, the first suggested potential application for Group IV semiconductor nanocrystals was as a light emitter. Although several devices have been demonstrated, their quantum efficiencies are low if compared to typical materials used as light emitters in current technologies (e.g., GaAs, InGaP, etc.). Devices based on both free-standing [20] and glass-embedded nanocrystals [19] have been reported. In the case of nanocrystals embedded in SiO_2, the electroluminescence efficiency was estimated to be of the order of 10^{-4}-10^{-5}.

More recently some authors have demonstrated an information storage device utilizing the potential well of silicon nanocrystals [21, 22, 23]. This memory device apparently uses the nanocrystal as a charge storage compartment. Although the device has good performance, being free of degradation effects (up to 10^9 write/erase cycles) and possessing a long-retention time ($> 10^5$ seconds), the mechanism by which charge is stored and retrieved is not well established.

A number of recent reports also point toward single electron electronics by demonstrating single-nanocrystal transistors and logic devices [24, 25]. Therefore, potential applications for Group IV semiconductor nanocrystals are being envisioned not only in the realm of optoelectronics, but also as an information storage medium and elec-

tronic transport material.

2.5 Discussion

Emerging devices based on Group IV semiconductor nanocrystals are a promising alternative for several limiting factors on current technologies. However, optimization of device performance and processing is required before judgments can be made on their long-term viability. Basic understanding of the properties of nanocrystals is vital if they are ever to achieve their full potential as a substrate for a new technology.

In this chapter we have reviewed several issues involved in the understanding of the properties of Group IV semiconductor nanocrystals. Reports of unambiguously identified quantum confinement effects in Group IV semiconductor nanocrystals have been few. This is due to complications such as broad size distributions of nanocrystals, morphological diversity of nano- and microcrystals, and abundant presence of optically active defect- and surface-related states. One cannot possibly treat all of these problems at once. Many studies have been reported involving heat treatments in different atmospheres that indicate that both quantum confinement and surface/defect-related effects are important in the characterization of Group IV semiconductor nanocrystals [7, 8, 9, 10, 11]. Few studies present convincing arguments to rule out one or the other mechanism [16, 38].

In this thesis we have chosen as our primary focus the size control of nanocrystals, a problem that has been given very limited attention due to the complexities involved. Most of the cases, in which a relative amount of size control has been reported,

deal with a fortuitous feature of the synthesis technique rather than an intentionally chosen process parameter. In our case, we have designed and implemented a system to deliberately size-classify semiconductor nanocrystals with the long-term goals of looking at their optical response as a function of size, and of synthesizing dense arrays of nearly equal-sized nanocrystals.

Bibliography

[1] See, for example, K. Nishiuchi, T. Mimura, S. Kuroda, S. Hiyamizu, H. Nishi, and M. Abe, "Device characteristics of short channel high electron-mobility transistor (HEMT)," *IEEE Trans. Electron Dev.*, vol. 30, pp. 1569–1570, 1983.

[2] H. Okamoto, "Semiconductor quantum well lasers for optoelectronic applications," *Jpn. J. Appl. Phys.*, vol. 26, p. 315, 1987.

[3] H. Okamoto, Special Issue on "Semiconductor quantum wells and superlattices: physics and applications," *IEEE J. Quant. Elect.*, vol. QE-22, Sept. 1986.

[4] L. E. Brus, "Quantum cristallites and nonlinear optics," *Appl. Phys. A*, vol. 53, pp. 465–474, 1991.

[5] L. T. Canham, "Silicon quantum wire array fabrication by electrochemical and chemical dissolution of wafers," *Appl. Phys. Lett.*, vol. 57, pp. 1046–1048, 1990.

[6] V. Lehmann and U. Gösele, "Porous silicon formation: A quantum wire effect," *Appl. Phys. Lett.*, vol. 58, pp. 856–858, 1991.

[7] W. A. Saunders, P. C. Sercel, R. B. Lee, H. A. Atwater, K. J. Vahala, R. C. Flagan, and E. J. Escorcia-Aparcio, "Synthesis of luminescent silicon clusters by spark ablation," *Appl. Phys. Lett.*, vol. 63, pp. 1549–1551, 1993.

[8] Y. Kanemitsu, K. Suzuki, H. Uto, Y. Masumoto, T. Matsumoto, S. Kyushin, K. Higuchi, and H. Matsumoto, "Visible photoluminescence of silicon-based nanostructures: porous silicon and small silicon-based clusters," *Appl. Phys. Lett.*, vol. 61, pp. 2446–2448, 1992.

[9] L. A. Chiu, A. A. Seraphin, and K. D. Kolenbrander, "Gas phase synthesis and processing of silicon nanocrystallites: characterization by photoluminescence emission spectroscopy," *J. Electron. Mat.* , vol. 23, pp. 347–354, 1994.

[10] L. N. Dinh, L. L. Chase, M. Balooch, W. J. Siekhaus, and F. Wooten, "Optical properties of passivated Si nanocrystals and SiO_x nanostructures," *Phys. Rev. B*, vol. 54, pp. 5029–5037, 1996.

[11] S. Li, S. J. Silvers, and M. S. El-Shall, "Surface oxidation and luminescence properties of weblike agglomeration of silicon nanocrystals produced by a laser vaporization-controlled condensation technique," *J. Phys. Chem. B*, vol. 101, pp. 1794–1802, 1997.

[12] H. A. Atwater, K. V. Shcheglov, S. S. Wong, K. J. Vahala, R. C. Flagan, M. L. Brongersma, and A. Polman, "Ion beam synthesis of luminescent Si and Ge nanocrystals in a silicon dioxide matrix," *Mat. Res. Soc. Symp. Proc.*, vol. 316, pp. 409–420, 1994.

[13] S. Hayashi, T. Nagareda, Y. Kanzawa, and K. Yamamoto, "Photoluminescence of Si-rich SiO_2 films: Si clusters as luminescent centers," *Jpn. J. Appl. Phys.*, vol. 32, pp. 3840–3845, 1993.

[14] X. Liu, X. Wu, X. Bao, and Y. He, "Photoluminescence from nanocrystallites embedded in hydrogenated amorphous silicon films prepared by plasma enhanced chemical vapor deposition," *Appl. Phys. Lett.*, vol. 64, pp. 220–222, 1993.

[15] K. A. Littau, P. J. Szajowski, A. J. Muller, A. R. Kortan, L. E. Brus, "A luminescent silicon nanocrystal colloid via a high-temperature aerosol reaction," *J. Phys. Chem.*, vol. 97, pp. 1224–1230, 1992.

[16] W. L. Wilson, P. F. Szajowski, and L. E. Brus, "Quantum confinement in size-selected, surface-oxidized silicon nanocrystals," *Science*, vol. 262, pp. 1242–1244, 1993.

[17] L. T. Canham, "Progress toward crystalline-silicon-based light-emmitting diodes," *Mat. Res. Soc. Bulletim*, pp. 22–28, July 1993.

[18] R. A. Soref, "Silicon-based optoelectronics," *Proc. IEEE*, vol. 81, pp. 1687–1706, 1993.

[19] K. V. Shcheglov, C. M. Yang, K. J. Vahala, and H. A. Atwater, "Electroluminescence and photoluminescence of Ge-implanted $Si/SiO_2/Si$ structures," *Appl. Phys. Lett.*, vol. 66, pp. 745–747, 1994.

[20] T. A. Burr and K. D. Kolenbrander, "Carrier transport in silicon nanocrystallite-based multilayer electroluminescent devices," *Mat. Res. Soc. Symp. Proc.*, vol. 405, pp. 271–276, 1996.

[21] H. I. Hanafi, S. Tiwari, and I. Khan, "Fast and long retention-time nanocrystal memory," *IEEE Trans. Electron Devices*, vol. ED-43, pp. 1553–1558, 1996.

[22] S. Tiwari, F. Rana, H. Hanafi, A. Hartstein, E. F. Crabbé, and K. Chan, "A silicon nanocrystals based memory," *Appl. Phys. Lett.*, vol. 68, pp. 1377–1379, 1996.

[23] S. Tiwari, F. Rana, K. Chan, L. Shi, and H. Hanafi, "Single charge and confinement effects in nanocrystal memories," *Appl. Phys. Lett.*, vol. 69, pp. 1233–1234, 1996.

[24] D. C. Ralphs, C. T. Black, and M. Tinkham, "Gate-voltage studies of discrete electronic states in aluminum nanoparticles," *Phys. Rev. Lett.*, vol. 78, pp. 4087–4090, 1997.

[25] H. Fahmy and K. Ismail, "Analysis of a single-electron decimal adder," *Appl. Phys. Lett.*, vol. 70, pp. 2613–2615, 1997.

[26] See, for example, N. W. Ashcroft and N. D. Mermin *Solid State Physics*, W. B. Saunders Company, 1976, pp. 132–133.

[27] See, for example, N. W. Ashcroft and N. D. Mermin *Solid State Physics*, W. B. Saunders Company, 1976, pp. 133–141.

[28] L. E. Brus, "Electron-electron and electron-hole interactions in small semiconductor crystallites: The size dependence of the lowest excited electronic state," *J. Chem. Phys.*, vol. 80, pp. 4403–4409, 1984.

[29] T. Takagahara and K. Takeda, "Theory of the quantum confinement effect on excitons in quantum dots of indirect-gap materials," *Phys. Rev. B*, vol. 46, pp. 15578–15581, 1992.

[30] G. Bastard, "Wave mechanics applied to semiconductor heterostructure," Paris, 1990.

[31] M. S. Hybertsen, "Absorption and emission of light in nanoscale silicon structures," *Phys. Rev. Lett.*, vol. 72, pp. 1514–1517, 1994.

[32] N. A. Hill and K. B. Whaley, "Size dependence of excitons in silicon nanocrystals," *Phys. Rev. Lett.*, vol. 75, pp. 1130–1133, 1995.

[33] C. Delerue, G. Allan, and M. Lannoo, "Theoretical aspects of the luminescence of porous silicon," *Phys. Rev. B*, vol. 48, pp. 11024–11036, 1993.

[34] L. -W. Wang and A. Zunger, "Electronic structure pseudopotential calculations of large ($\sim$ 1000 atoms) Si quantum dots," *J. Phys. Chem.*, vol. 98, pp. 2158–2165, 1994.

[35] B. Delley and E. F. Steigmeier, "Quantum confinement in Si nanocrystals," *Phys. Rev. B*, vol. 47, pp. 1397–1400, 1993.

[36] D. Tománek and M. A. Schlüter, "Calculation of magic numbers and the stability of small Si clusters," *Phys. Rev. Lett.*, vol. 56, pp. 1055–1058, 1986.

[37] K. S. Min, K. V. Shcheglov, C. M. Yang, H. A. Atwater, M. L. Brongersma, and A. Polman, "The role of quantum-confined excitons vs defects in the visible luminescence of SiO_2 films containing Ge nanocrystals," *Appl. Phys. Lett.*, vol. 68, pp. 2511–2513, 1996.

[38] K. S. Min, K. V. Shcheglov, C. M. Yang, H. A. Atwater, M. L. Brongersma, and A. Polman, "Defected-related versus excitonic light emission from ion beam synthesized Si nanocrystals in SiO_2," *Appl. Phys. Lett.*, vol. 69, pp. 2033–2035, 1996.

[39] D. J. Wolford, B. A. Scott, J. A. Reimer, and J. A. Bradley, "Efficient visible luminescence from hydrogenated amorphous-silicon," *Phys. B&C* vol. 117, pp. 920–922, 1983.

[40] C. G. Pitt, M. M. Bursey, and P. F. Rogerson, "Catenates of the Group IV elements. Correlation of σ electron energies," *J. Am. Chem. Soc.*, vol. 92, pp. 519–522, 1970.

[41] D. A. Papaconstantopoulos and E. N. Economu, "Calculations of the electronic properties of hydrogenated silicon," *Phys. Rev. B* vol. 24, pp. 7233–7246, 1981.

[42] S. Yamasaki, N. Hata, T. Yoshida, H. Oheda, A. Matsuda, H. Okushi, and K. Tanaka, *J. Phys. Colloq.* vol. 42, p. C4, 1981.

[43] M. S. Brandt, H. D. Fuchs, M. Stutzmann, J. Weber, and M. Cardona, "The origin of visible luminescence from porous silicon - a new interpretation," *Solid State Commun.* vol. 81, pp. 307–312, 1992.

[44] M. S. Brandt, A. Breitschwerdt, H. D. Fuchs, A. Höpner, M. Rosenbauer, M. Stutzmann, and J. Weber, "New growth technique of luminescent layers on silicon," *Appl. Phys. A* vol. 54, pp. 567–569, 1992.

[45] L. Skuja and A. R. Silin, "Optical properties and energetic structure of nonbridging oxygen centers in vitreous SiO_2," *Phys. Stat. Sol. A* vol. 56, pp. K11–K13, 1979.

[46] L. Skuja, "Time resolved low-temperature luminescence of nonbridging oxygen hole-centers in silica glasses," *Solid State Commun.* vol. 84, pp. 613–616, 1992.

[47] K. Nagasawa, Y. Hoshi, Y. Ohki, and K. Yahaagi, "Radiation effects on pure silica core optical fibers by gamma-rays - relation between 2 eV band and nonbridging oxygen hole-centers," *Jpn. J. Appl. Phys.* vol. 25, pp. 464–468, 1986.

[48] S. Munekuni, T. Yamanaka, Y. Shimogaichi, R. Tohmon, Y. Ohki, K. Nagasawa, and Y. Hama, "Various types of nonbridging oxygen hole centers in high-purity silica glass," *J. Appl. Phys.* vol. 68, pp. 1212–1217, 1990.

[49] Daniel J. Lépine, "Spin resonance of localized and delocalized electrons in phosphorus-doped silicon between 20 and 30 K," *Phys. Rev. B* vol. 2, pp. 2429–2439, 1970.

[50] A. Stesmans and F. Scheerlinck, "Natural intrinsic EX center in thermal SiO_2 on Si: ^{17}O hyperfine interaction," *Phys. Rev. B* vol. 50, pp. 5204–5212, 1994.

[51] W. E. Carlos and S. M. Prokes, "The EX defect center in porous silicon" *J. Appl. Phys.* vol. 78, pp. 2129–2131, 1995.

[52] S. M. Prokes and W. E. Carlos, "Oxygen defect center red room temperature photoluminescence from freshly etched and oxidized porous silicon," *J. Appl. Phys.* vol. 78, pp. 2671–2674, 1995.

[53] K. S. Song and R. T. Williams, "Self-trapped excitons," Springer Verlag, New York, 1996, pp. 270–299.

Chapter 3

Aerosol synthesis and manipulation of semiconductor nanocrystals

3.1 Introduction

The use of aerosol processes in the synthesis and manipulation of semiconductor nanocrystals is a promising pathway to control the electronic properties of these structures. In principle, any vapor phase technique capable of generating a stable aerosol of semiconductor nanocrystals may be employed as a source to be coupled with aerosol instrumentation to achieve size, shape and chemical control.

Although vapor phase methods have been used to produce semiconductor nanocrystals in several studies [1, 2, 3], few attempts have been made to manipulate the resulting aerosol. One of these attempts is a hybrid aerosol/colloid approach. It involves

the aerosol synthesis of Si nanocrystals by pyrolisis of disilane with subsequent formation of a Si nanocrystal colloid. In this case virtually all nanocrystal processing is done in the colloid phase [4, 5]. Another recent attempt is geared towards the generation of GaAs nanocrystals by reacting a well characterized gallium aerosol with arsine [6]. An alternative idea is the use of aerosol particles not as the active semiconductor material, but as nanometer-scale masks for selective etching of quantum well semiconductor structures. In this way, lateral confinement may potentially be induced in what was originally a one-dimensional quantum well [7].

We have employed several aerosol techniques to directly generate and process an aerosol of silicon nanocrystals [8]. In this chapter we describe the basic physical principles necessary to understand each of these techniques in light of the requirements for nanocrystal synthesis.

3.2 Aerosol formation and evolution

The principles that govern aerosol formation from a vapor phase precursor are independent of the specific material and production technique (Fig. 3.1). The initial stage is the generation of a supersaturated vapor of the material of interest. At a high supersaturation, the vapor will nucleate into a large number of small particles. These nuclei act as seeds for particle growth by condensation or other vapor deposition process as they simultaneously undergo rapid coagulation. Initially, when the particles are still quite small, coagulation is followed by rapid coalescence, so dense particles are formed. As the aerosol cools, however, the particles grow large enough

that they can no longer coalesce completely between coagulation events. As a result, the aerosol evolves into a population of aggregates with a complex fractal-like structure. Precise control of the crystallite size is possible only in the early stage of dense particle growth. Figure 3.1 depicts the various stages in the formation and growth of aerosol particles.

The mathematical description of the evolution of an aerosol population has been worked out by several authors [10]. In its most common form it is written in terms of a *general dynamic equation*. Defining $n(v,t)dv$ as the concentration of particles with volume between v and $v+dv$ at time t, the continuum representation of the *general dynamic equation* may be written as [10]

$$\begin{aligned}\frac{\partial n(v,t)}{\partial t} &= \frac{1}{2}\int_0^v K(v-u,u)\, n(v-u,t)\, n(u,t)\, du \\ &- n(v,t)\int_0^\infty K(v,u)\, n(u,t)\, du \\ &- \frac{\partial}{\partial v}\left[I(v,t)\, n(v,t)\right] + J(v^*,t) \qquad (3.1)\end{aligned}$$

The term on the left-hand side gives the evolution of the aerosol number distribution with time. The first term on the right-hand side represents the coagulation of particles of volume smaller than v (i.e., $v-u$) forming a particle of volume v, with $K(v,\tilde{v})$ representing the coagulation rate coefficient for particles of volume v with those of volume $\tilde{v}$; the second term represents the coagulation of particles of volume v with all other particles, to form particles whose volumes are larger than v; the third term represents the change in the aerosol size distribution due to physical or chemical vapor deposition, evaporation or etching; and the fourth term represents the nucleation of particles from the vapor phase. This nucleation takes place at a critical particle size at

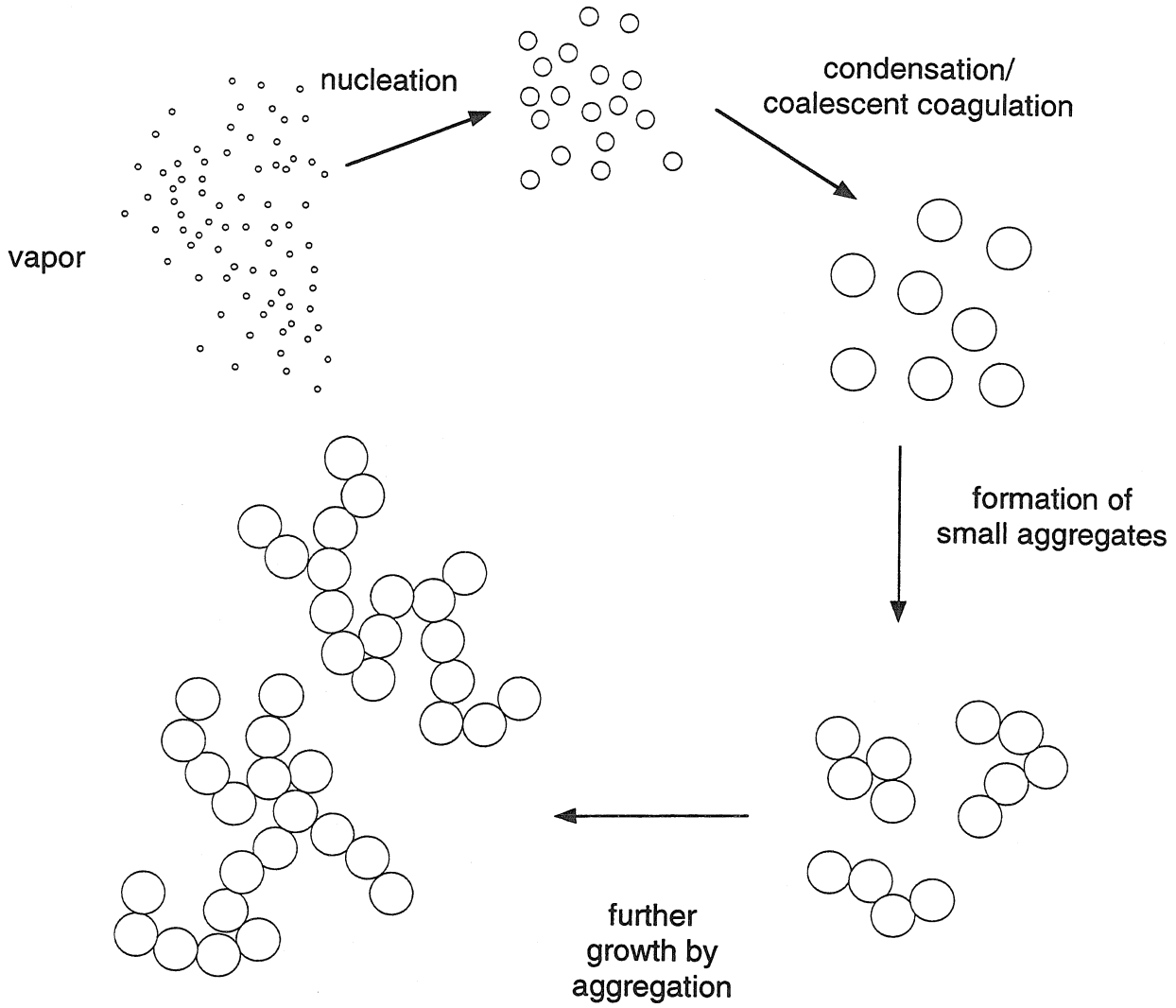

Figure 3.1: Illustration of the formation and growth processes of a population of aerosol particles.

volume v^*. The term $J(v^*, t)$, then, represents the rate of formation of new particles of volume v^* by nucleation.

When the particle diameter D_p is the variable of interest, Eq. 3.1 becomes

$$\begin{aligned}\frac{\partial n(D_p,t)}{\partial t} &= D_p^2 \int_0^{D_p/2^{1/3}} \frac{K[(D_p^3-\tilde{D}_p^3)^{1/3}, \tilde{D}_p]\; n[(D_p^3-\tilde{D}_p^3)^{1/3}, t]\; n(\tilde{D}_p,t)\; d\tilde{D}_p}{(D_p^3-\tilde{D}_p^3)^{2/3})} \\ &- n(D_p,t) \int_0^{\infty} K(D_p,\tilde{D}_p)\; n(\tilde{D}_p,t)\; d\tilde{D}_p \\ &- \frac{\partial}{\partial D_p}[I_D(D_p,t)\; n(D_p,t)] + J(D_p^*,t) \end{aligned} \tag{3.2}$$

In this thesis work three different means of generating a supersaturated silicon vapor are considered, namely, spark ablation, laser ablation, and thermal evaporation (Chapter 4). In each case the aerosol is continuously generated in a flow reactor and then transported away from the vapor source by a carrier gas. Consequently, the stages depicted in Fig. 3.1 occur at different time scales and even at different locations in the reactor. In the hot region very close to the vapor source, nucleation followed by rapid coalescent coagulation dominates. As the aerosol is carried away from this hot area, temperatures drop rapidly and aggregation becomes the dominant mechanism of particle growth.

From our perspective, aggregates should be avoided because they contribute to significant broadening of the optical properties. It is desirable, therefore, to limit growth by coagulation when the gas temperatures prevent coalescence from occurring. This can be achieved by vigorous dilution of the aerosol in the early stages of coagulation. When done successfully, this can generate dense spherical particles which may approach their ideal behavior in terms of optical properties.

The physical quantity that provides basic information for the coagulation dynamics of aerosol particles is the coagulation coefficient $K(D_p, \tilde{D}_p)$. Assuming that the only coagulation mechanism is Brownian diffusion, Fuchs has derived the following expression for the coagulation coefficient of spherical particles ranging from the free molecular regime limit to particles much larger than the mean free path of particle motion, l_i [9]:

$$K(D_{pi}, D_{pj}) = 2\pi(D_i + D_j)(D_{pi} + D_{pj}) \left[\frac{D_{pi} + D_{pj}}{D_{pi} + D_{pj} + 2g_{ij}} + \frac{8(D_i - D_j)}{\bar{c}_{ij}(D_{pi} + D_{pj})} \right]^{-1} \quad (3.3)$$

where $g_{ij} = (g_i^2 + g_j^2)^{1/2}$,

$$g_i = \frac{1}{3D_{pi}l_i} \left[(D_{pi} + l_i)^3 - (D_{pi}^2 + l_i^2)^{3/2} \right] - D_{pi} \quad (3.4)$$

$$l_i = \frac{8D_i}{\pi \bar{c}_i} \quad (3.5)$$

with $D_i = kTC_c/3\pi\mu D_{pi}$ and $\bar{c}_i = (8kT/\pi m_i)^{1/2}$

Figure 3.2 presents the behavior of $K(D_p, \tilde{D}_p)$ for spherical particles in the 1-10,000 nm range. It is apparent that for the whole diameter spectrum, a minimum in the coagulation occurs for equal-sized particles. The presence of particles of unequal sizes may increase the coagulation probability by orders of magnitude. This suggests that even small numbers of large particles should be avoided if aggregation is to be limited. Scavenging of small particles by large ones may rapidly lead to the depletion of nanocrystals in the size range of interest (i.e., 1-10 nm).

A particularly simple and useful solution of Eq. 3.2 can be found when only coagulation governs the aerosol evolution. This is the case when the aerosol has been formed by a rapid burst of homogeneous nucleation and condensation and is then

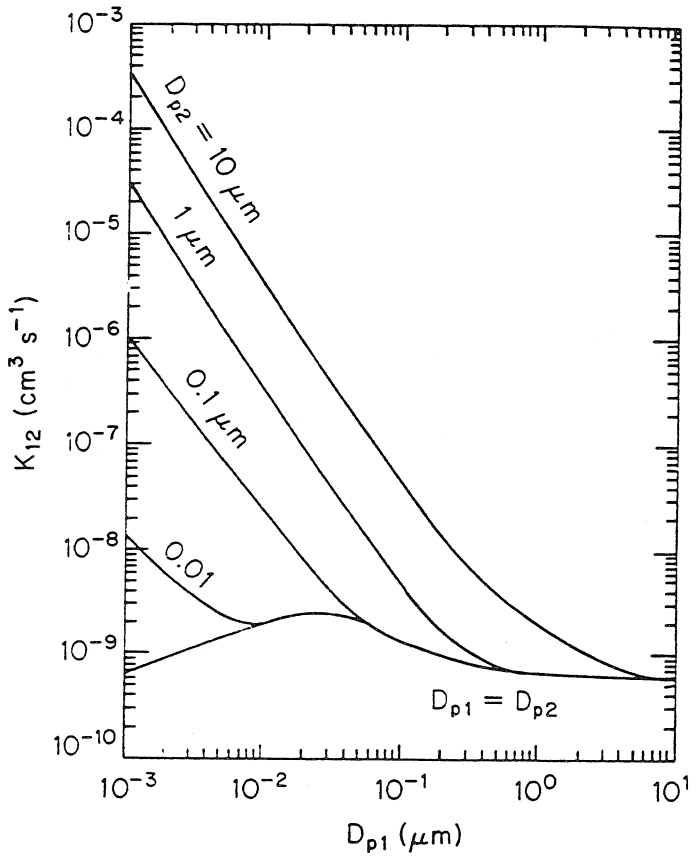

Figure 3.2: Dependence of the Brownian coagulation coefficient with particle diameter for spherical particles with density $\rho = 1$ g cm^{-3} in air at 298 K, 1 atm (reproduced from Ref. [9]).

carried away from the source. No additional evaporation and condensation occur and the particles grow only by coagulation. With the further assumptions that we have an initially monodisperse aerosol and that the coagulation coefficient does not change appreciably as the coagulation proceeds (i.e., $K(D_p, \tilde{D}_p) \equiv K$), Eq. 3.2 reduces to:

$$\frac{dn}{dt} = -\frac{1}{2}Kn^2 \tag{3.6}$$

If the total initial particle concentration is n_0, the solution of Eq. 3.6 is given by

$$n(t) = \frac{n_0}{1 + t/\tau_c} \tag{3.7}$$

where the quantity

$$\tau_c = \frac{2}{Kn_0} \tag{3.8}$$

is defined as the characteristic time for coagulation, i.e., the time required for the concentration of an initially monodisperse aerosol to be reduced by a factor of two due to coagulation.

A plot of the characteristic coagulation time is presented in Fig. 3.3 for different aerosol number concentrations. One obvious feature is the dependence on the number concentration. An aerosol with number concentration in the 10^3 cm^{-3} range would take, in principle, 10 days to coagulate to one half of its initial concentration, whereas, if in the 10^{12} cm^{-3} concentration range, one half of the initial concentration would be reached in less than 1 ms. Therefore, given the residence time of an aerosol reactor, the characteristic time for coagulation sets an upper limit on the maximum number concentration that can be achieved in that system. A 10-second residence time, for example, will lead to a maximum concentration in the 10^8 cm^{-3} range. Recollecting

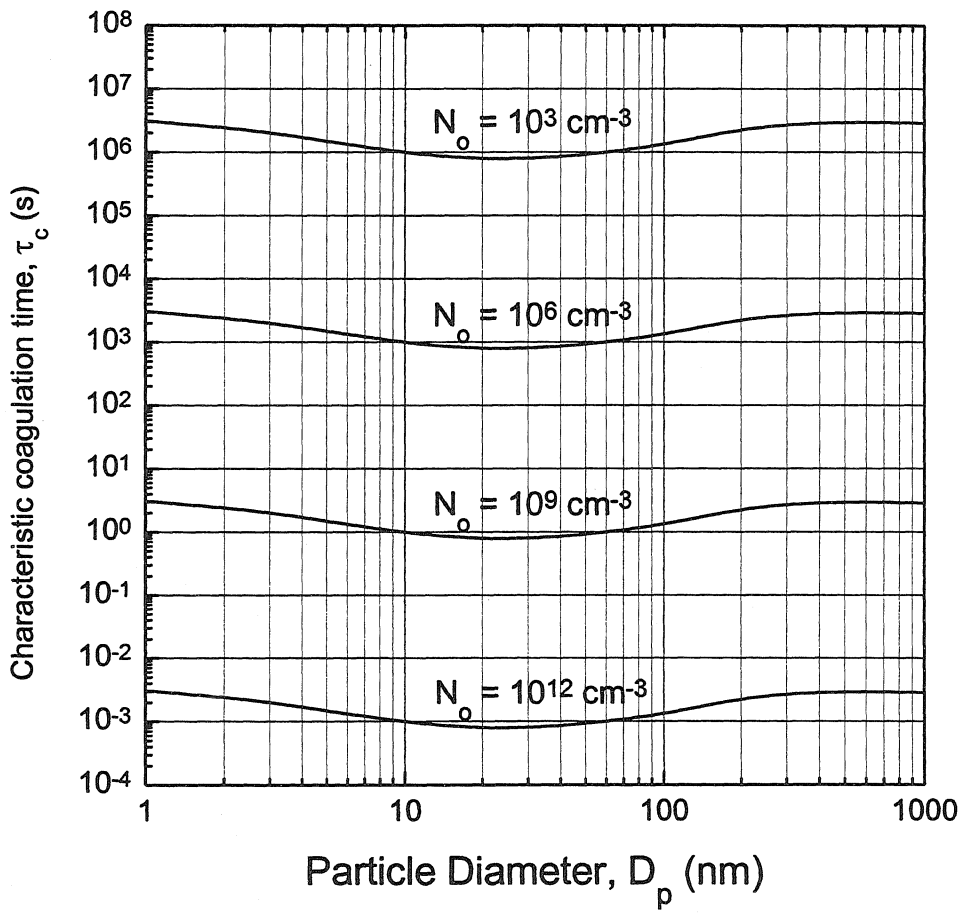

Figure 3.3: Characteristic coagulation time for an initially monodisperse aerosol.

that this simplistic analysis is for a monodisperse aerosol, and that typical geometric standard deviations for coagulation aerosols are around 1.4, one should even expect a somewhat lower maximum concentration, probably in the 10^7 cm^{-3} range.

3.3 Aerosol charging

In this work, the technique chosen to manipulate the nanocrystal size is differential mobility analysis (described in the next section). The successful implementation of this technique requires knowledge of the charge state of the nanocrystal aerosol. In general, the charge state of an aerosol is a complex combination of the charge states of its individual particles which, in turn, depend on the details of the generation process. The individual particles are often charged with multiple electric charges which is undesirable if differential mobility analysis is to be used for analytical or processing purposes. A common procedure to avoid this problem is to impart on the aerosol a known charge distribution. This can be done either by *field charging* or by *diffusion charging*.

Two classical charging devices to achieve this purpose are the corona discharge unipolar charger and the radioactive bipolar charger. A schematic of the operation principles of these two devices is presented in Fig. 3.4.

In the case of the corona discharge charger, the aerosol particles are usually exposed to a stream of unipolar ions generated by a corona discharge (Fig. 3.4 (a)). A feedback controlled DC grid voltage is added to allow the variation of the charging current. In this device, charging may occur either by *field charging*, or by *diffusion*

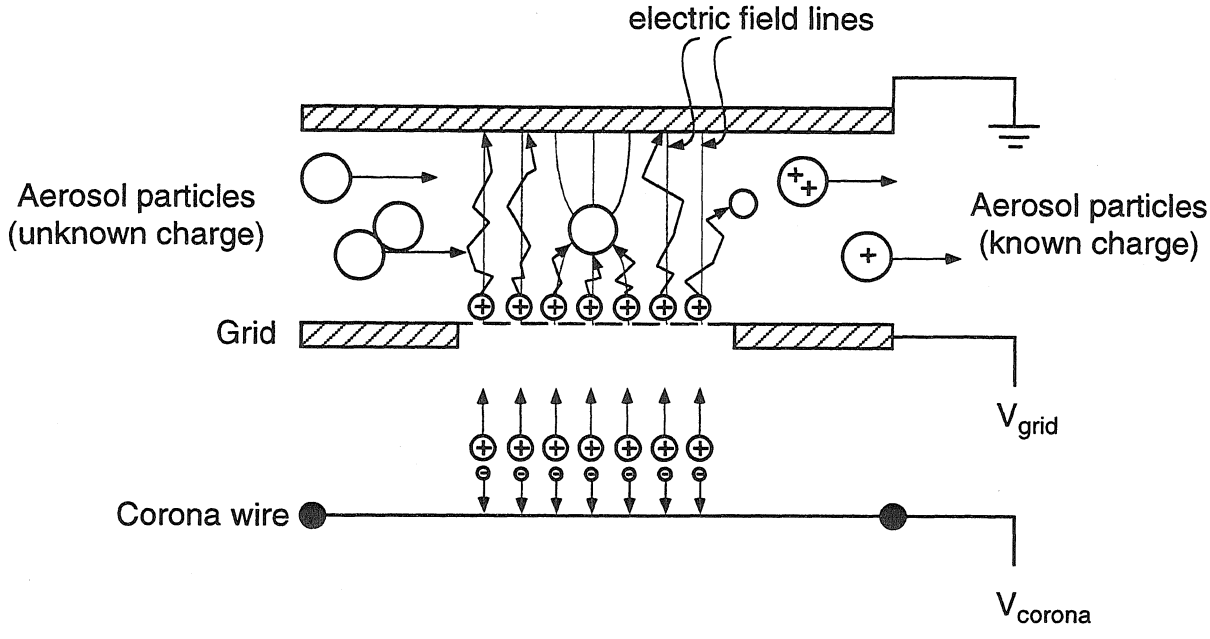

(a) Corona discharge unipolar charger

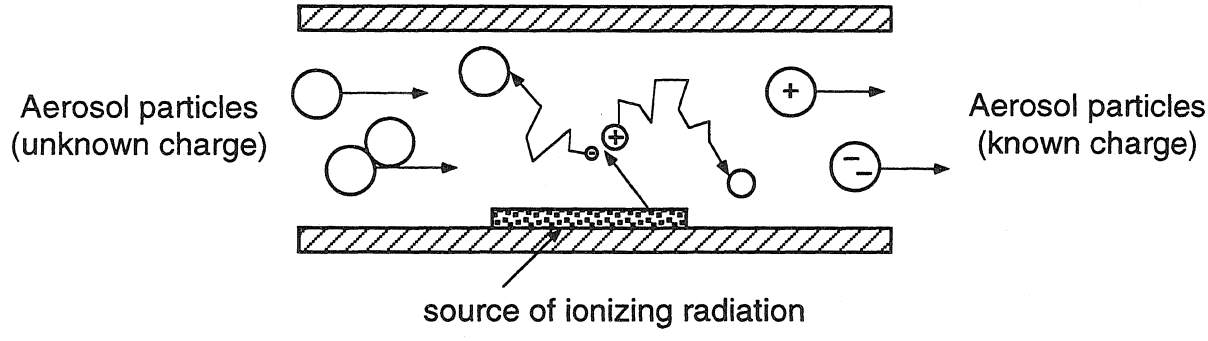

(b) Radioactive bipolar charger

Figure 3.4: Schematic of two aerosol charging devices: (a) the corona discharge unipolar charger and (b) the radioactive bipolar charger.

charging. *Field charging* occurs as the aerosol particles fall under the bombardment of unipolar ions migrating in the applied electric field. Distortions of the field lines due to the presence of the particles enhance ion motion towards them. Particle charging occurs by ion attachment upon collision. As the charging level of a particle increases due to the ion bombardment, a point is reached when electric repulsion between the particle and the ions causes charging to slow down and eventually an equilibrium charge state is reached. Ion motion in the corona charger is governed not only by electrical migration but also by Brownian diffusion. When charging occurs as a result of collisions due to the random thermal motion, the process is referred to as *diffusion charging*. For particle diameters above 1 μm, field charging is the dominant mechanism, whereas below 1 μm diffusion charging is the most efficient process. One serious limitation of the use of corona chargers with ultrafine particles is the field-induced particle loss. Below $\sim$ 20 nm a high ion concentration is required for particle charging which can only be achieved with high electric fields in the charging region. This field causes deflection and precipitation of the charged particles, virtually depleting all particles smaller than $\sim$ 10 nm from the exiting aerosol.

An alternative charging device that has proved to be more appropriate for ultrafine particles is the radioactive bipolar charger (Fig. 3.4(b)). In this case the carrier gas is exposed to ionizing radiation from a radioactive source (e.g., ^{85}Kr (β radiation) or ^{210}Po (α radiation)). Reactions of the aerosol particles with the ambipolar gas ions result in a steady-state charge distribution with respect to particle size that has been predicted theoretically and vindicated by experiment [11]. Because the particles

are exposed to ions of both signs with approximately the same concentration, the aerosol that exits this device is also approximately neutral, and consequently, the bipolar charger is commonly referred to as a "neutralizer." Due to the absence of an electric field, losses of ultrafine particles are greatly reduced in comparison with the traditional DC corona chargers. In this case, the only available mechanism for charging is diffusion charging. For particles in the nanometer range, in which our interest is focused, this is not a problem since field charging plays virtually no role in the charging of particles in this size scale. Thus, radioactive bipolar chargers are used throughout this thesis work. Figure 3.5 shows a plot of the calculated bipolar equilibrium charge distribution for aerosol particles in the 1-100 nm size range [11]. This charge distribution is expected to be imparted on an aerosol traversing the radioactive bipolar charger.

An inspection of Fig. 3.5 reveals that multiple-charge states are absent for particles below $\sim$ 20 nm. This is an important feature as a one-to-one correlation between electrical mobility and particle size can be established in differential mobility analysis (next section). The figure also indicates the charging probabilities, ranging from 0.4% to 4% in the 1-10 nm range. This low charging efficiency introduces a further limitation in the number concentration of size-classified particles that can be achieved in a typical aerosol system. In the system with a 10-second residence time, for which coagulation set an upper concentration limit of about 10^7 cm^{-3}, the use of a bipolar charger will restrict the number of charged particles in the 1-10 nm range to about 10^5 cm^{-3}. For processing techniques that utilize electric forces, only charged particles

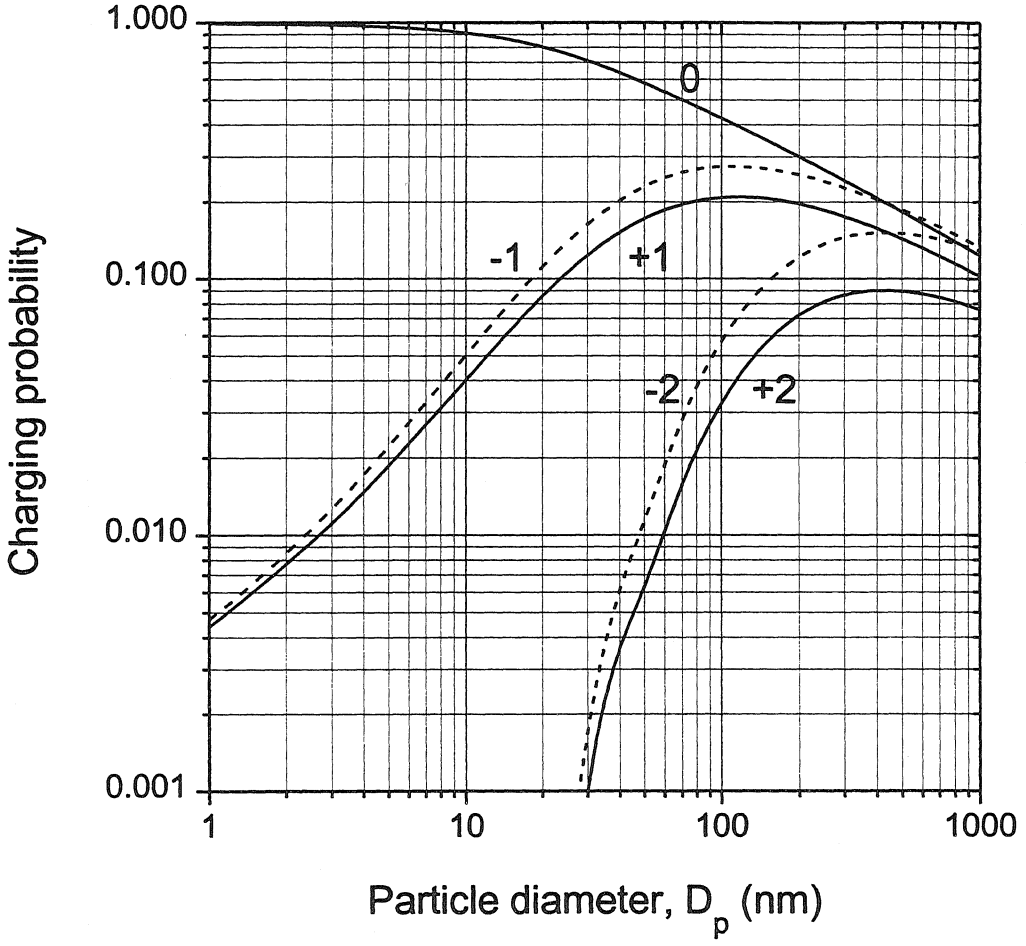

Figure 3.5: Bipolar equilibrium charge distribution for nanometer scale aerosols, as calculated by Fuchs theory.

are available, and therefore maximum concentrations of about 10^5 cm^{-3} are common.

3.4 Size classification by differential mobility analysis

3.4.1 The physics of differential mobility analysis

The differential mobility analyzer (DMA) is the key instrument in the measurement of ultrafine aerosol particles, being used directly in many of the measurements on such systems, and indirectly, as a calibration source for most of the other instruments that are used for measurements in this size regime. The DMA is the aerodynamic analog of a dispersive mass spectrometer. Physically, this instrument is a capacitor in which the charged aerosol particles migrate across a laminar flow of a particle-free sheath gas as a result of an electric field. Because the particle electrical mobility is a function of its projected area, particles with different mobilities have distinct trajectories inside the DMA. A sampling orifice suitably placed at the analyzer electrode opposite to the aerosol inlet extracts only particles in a narrow window of mobilities. By varying the voltage across the capacitor, the applied field is varied and the mobility of the classified particles can be continuously tuned.

The use of DMAs to generate monodisperse particle deposits of functional materials, and particularly of semiconductors, is a relatively new endeavor. The motivation behind this approach is the study of size dependent properties in large ensembles of nearly monodisperse particles, which are usually averaged out in samples with broad particle size distributions [6, 7, 8].

The basic physical principles that govern the DMA operation are relatively simple

and may be understood purely in terms of classical particle motion in a fluid suspension. Figure 3.6 illustrates in a planar geometry the physics of differential mobility analysis.

The sketch illustrates a parallel plate capacitor with a plate separation b, an applied voltage V, and a gas with viscosity μ and velocity $\mathbf{u}$ flowing in the laminar regime between the plates. In this initial description, we neglect Brownian diffusion and space charge fields, which will be considered in detail in chapter 5. With these simplifications, charged aerosol particles that are introduced in the capacitor with negligible momentum in the direction normal to the sheath gas flow will obey the following equation of motion

$$m\frac{d\mathbf{v}}{dt} = \frac{3\pi\mu D_p}{C_c}(\mathbf{u}-\mathbf{v}) + q\mathbf{E} \tag{3.9}$$

where m, D_p, and q are the mass, the diameter, and the electric charge of the particle, respectively, and $\mathbf{E}$ is the electric field. The quantity C_c is the slip correction factor which accounts for deviations from the Stokes drag for particles that are small compared to the mean free path of the gas molecules and is given by

$$C_c = 1 + K_n\left[\alpha + \beta\exp\left(-\frac{\gamma}{K_n}\right)\right] \tag{3.10}$$

where K_n is the *Knudsen number*, defined as the ratio of the gas mean free path to the particle radius (i.e., $K_n = 2\lambda/D_p$). The parameters α, β, and γ have been determined in numerous experiments [12]. The difference in the values of C_c for different sets of α, β, and γ is always below about 2% for K_n ranging from 0.001 to 100. Typically, accepted values are:

$$\alpha = 1.257 \qquad \beta = 0.40 \qquad \gamma = 1.10 \tag{3.11}$$

The first term on the right-hand side of Eq. 3.9 is the drag force on a particle moving with velocity $\mathbf{v}$ in a fluid with velocity $\mathbf{u}$, and the second term is the electrical force. In the case of our parallel plate capacitor the electric field is simply given by

$$\mathbf{E} = \frac{V}{b}\hat{z} \tag{3.12}$$

where $\hat{z}$ is the unit vector in the vertical direction.

The steady state solution for Eq. 3.9 gives a particle migration velocity $\mathbf{v}_e$ parallel to the applied electric field $\mathbf{E}$

$$\mathbf{v}_e = Z_p\mathbf{E} \tag{3.13}$$

where the proportionality constant, Z_p, is the particle electrical mobility which is defined as

$$Z_p = \frac{qC_c}{3\pi\mu D_p} \tag{3.14}$$

Thus, the electrical mobility of a particle and its migration velocity increase with decreasing particle size (see Fig. 3.6 (b)). This establishes the basis for size classification by mobility, provided that particles can be suitably extracted from the capacitor region without disturbing the flow and electric fields. As can be seen from Eq. 3.14, control over the charge state of the aerosol is also necessary for a one-to-one relationship between particle diameter D_p and electrical mobility Z_p. Multiply charged particles in the DMA will lead to multiple peaks in the size distribution of the classified aerosol.

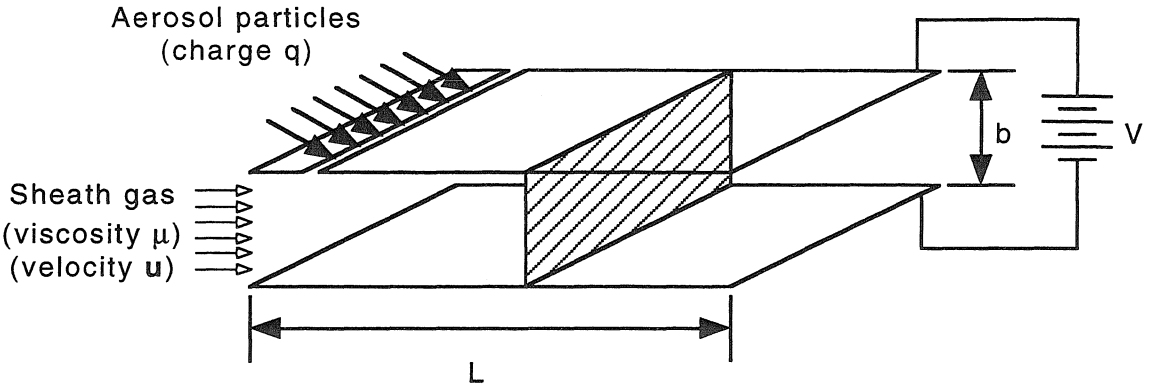

(a)

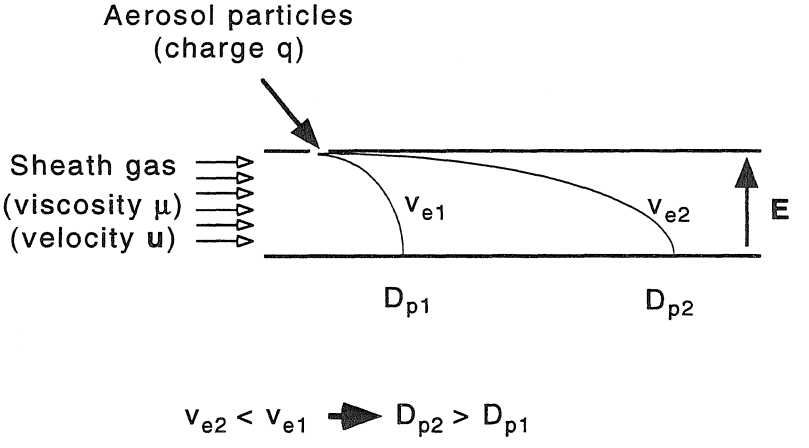

(b)

Figure 3.6: Schematic of a parallel plate capacitor that illustrates the physical principles involved in the size classification by differential mobility analysis.

3.4.2 The radial differential mobility analyzer

Differential mobility analyzers were originally developed to analyze aerosol particles in the near-submicron regime, operating with typical number concentrations below 10^5 particles/cm^3. The interest in nanometer-scale aerosols, however, has been driving investigators to apply these instruments to the analysis of ever smaller particles. Differential mobility analyzers are now routinely used for measurement and generation of calibration standards down to particle diameters as small as a few nanometers. In a few instances, these instruments have been used to classify 1 nm diameter or smaller particles and even ions [8, 17].

Differential mobility analyzers with different design characteristics have been proposed and implemented. The original instrument was a cylindrical DMA developed at the University of Minnesota by Knutson and Whitby in the 1970's [13]. Its good performance for particle diameters above 100 nm made it an excellent tool for the study of submicron aerosols. However, for ultrafine particles ($D_p < 100$ nm) this original instrument presented significant particle losses by deposition in the aerosol entrance and exit regions. In addition, for particles below 40 nm the resolution of the mobility classification degrades rapidly due to Brownian diffusion effects. Several changes of the original DMA design were made along the years [14, 15, 16] with significant reductions in particle losses and improved resolution at the ultrafine end of the particle spectrum.

Recently, new radial-flow designs for the DMA have been demonstrated [18, 19]. Figure 3.7 (a) presents a schematic cross-section view of one of these instruments,

the radial DMA (RDMA) developed at Caltech [19]. The RDMA is a parallel plate capacitor with radial symmetry. An inward radial laminar flow of sheath gas is established after a tangential inlet. The aerosol flow is also introduced tangentially through a sharp-edged ring carefully designed to allow turbulence-free mixing of the aerosol and sheath flows. The sampling orifice is placed at the center of the analyzer, opposite to the conical excess flow outlet. A short residence time in the classification region and a high transmission efficiency of the incoming aerosol (85-95% in the 3-10 nm size range (Fig. 3.7 (b)) enable the RDMA to classify semiconductor nanocrystals down to sizes relevant to quantum size effects. For this reason, the RDMA was chosen for the work pursued in this thesis.

A classical description of the DMA is usually given in terms of a transfer function $\Omega(Z_p)$. The transfer function is the probability that a particle with electrical mobility Z_p that enters the RDMA through the aerosol inlet will exit through the sampling outlet. To calculate $\Omega(Z_p)$ we start with the particle trajectories in the RDMA.

Neglecting diffusion and space charge effects, the particle trajectories inside the RDMA are governed by the following equations [13, 19]

$$\begin{aligned} \frac{dr}{dt} &= u_r + Z_p E_r \\ \frac{dz}{dt} &= u_z + Z_p E_z \end{aligned} \tag{3.15}$$

where r and z denote the radial and axial coordinates, u_r and u_z the radial and axial components of the gas flow velocity, E_r and E_z the radial and axial components of the applied electric field, and Z_p the particle electrical mobility.

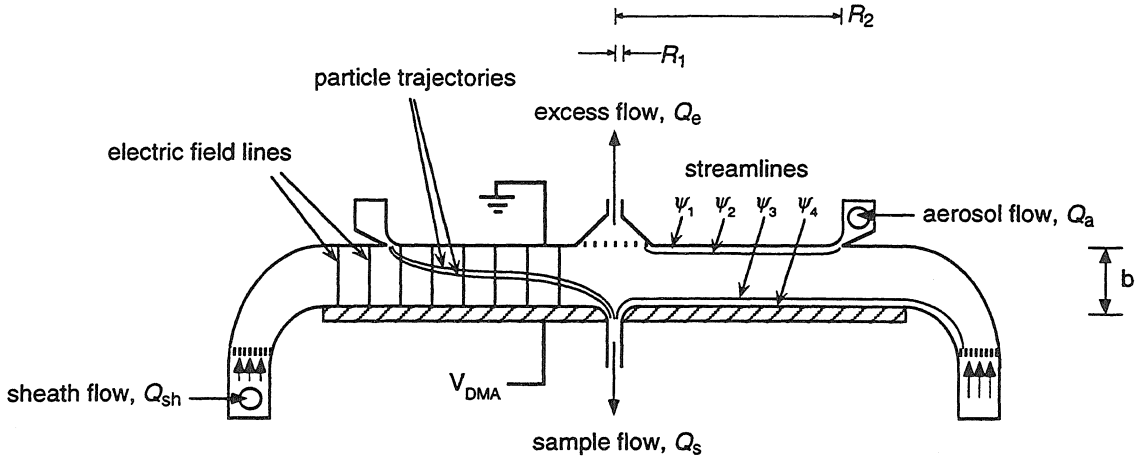

(a)

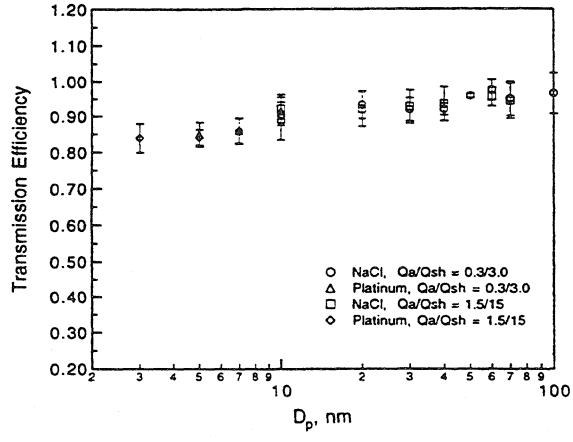

(b)

Figure 3.7: (a) Schematic cross-section view of the radial differential mobility analyzer and (b) its measured transmission efficiency in the 3-100 nm size range (reproduced from Ref. [19]).

Introducing the fluid stream function ψ, which is defined such that

$$\begin{aligned} u_r &= \frac{1}{r}\frac{\partial \psi}{\partial z} \\ u_z &= -\frac{1}{r}\frac{\partial \psi}{\partial r} \end{aligned} \tag{3.16}$$

and the electric field function ϕ defined such that

$$\begin{aligned} E_r &= \frac{1}{r}\frac{\partial \phi}{\partial z} \\ E_z &= -\frac{1}{r}\frac{\partial \phi}{\partial r}, \end{aligned} \tag{3.17}$$

it can be shown that Eq. 3.15 implies that particles will migrate through the DMA along trajectories of constant particle stream function,

$$\Gamma = \psi + Z_p \phi \tag{3.18}$$

We consider the streamlines ψ_1 and ψ_2, that bound the incoming aerosol flow, and the streamlines ψ_3 and ψ_4 that bound the sampling flow. As the flow bounded by any two streamlines ψ_i and ψ_j is $2\pi(\psi_j - \psi_i)$, we have

$$\begin{aligned} 2\pi(\psi_2 - \psi_1) &= -Q_a \\ 2\pi(\psi_4 - \psi_2) &= -Q_{sh} \\ 2\pi(\psi_4 - \psi_3) &= -Q_s \\ 2\pi(\psi_3 - \psi_1) &= -Q_e \end{aligned} \tag{3.19}$$

where Q_a, Q_{sh}, Q_s, and Q_e are the aerosol inlet, the sheath, the sample, and the excess flows respectively. Under normal operation conditions we assume $Q_a + Q_{sh} = Q_s + Q_e$. Due to the definition of stream function in Eq. 3.16, the sign convention is such that $\psi_1 > \psi_2 > \psi_3 > \psi_4$.

The electric field in the RDMA is simply

$$E_z = \frac{V}{b} \tag{3.20}$$

Integrating Eq. 3.18 one finds that the particle trajectory in the RDMA is

$$\psi = \psi_{in} - Z_p(\phi - \phi_{in}) \tag{3.21}$$

where ψ_{in} and ϕ_{in} are the stream function and potential values at which the particles enter the RDMA. For particles that are transmitted through the RDMA, the value of ψ at the exit is

$$\psi_{out} = \psi_{in} - Z_p \Delta\phi \tag{3.22}$$

where $\Delta\phi$ is found by integration of Eq. 3.17 from the aerosol inlet, R_2, to the sample outlet R_1,

$$\Delta\phi = \frac{R_2^2 - R_1^2}{2} E_z = \frac{R_2^2 - R_1^2}{2b} V \tag{3.23}$$

The particles that will be transmitted through the RDMA will have mobilities in the window $Z_{p_{min}} < Z_p < Z_{p_{max}}$. Using Eq. 3.22 one finds

$$Z_{p_{min}} = -\frac{\psi_3 - \psi_2}{\Delta\phi} = \frac{Q_{sh} - Q_s}{\pi(R_2^2 - R_1^2)} \frac{b}{V} \tag{3.24}$$

and

$$Z_{p_{max}} = -\frac{\psi_4 - \psi_1}{\Delta\phi} = \frac{Q_{sh} + Q_a}{\pi(R_2^2 - R_1^2)} \frac{b}{V} \tag{3.25}$$

Particles with $Z_p \geq Z_{p_{min}}$ that will exit on ψ_3 will have $\psi_{in} \leq (1-f_1)(\psi_2-\psi_1)+\psi_1$, which by Eq. 3.22 implies that the fraction f_1 of transmitted particles in this range

of mobilities is

$$f_1 = -\frac{\psi_3 - \psi_2 + Z_p\Delta\phi}{\psi_2 - \psi_1} = \frac{Q_s - Q_{sh} + 2\pi\Delta\phi Z_p}{Q_a} \tag{3.26}$$

By analogy, particles with $Z_p \leq Z_{p_{max}}$ that will exit on ψ_4 will have $\psi_{in} \leq (1 - f_2)(\psi_2 - \psi_1) + \psi_1$, which by Eq. 3.22 implies that the fraction f_2 of transmitted particles in this range of mobilities is

$$f_2 = -\frac{\psi_4 - \psi_1 + Z_p\Delta\phi}{\psi_2 - \psi_1} = \frac{Q_a - Q_{sh} + 2\pi\Delta\phi Z_p}{Q_a} \tag{3.27}$$

The transfer function, $\Omega(Z_p)$, may be written in algebraic form by realizing that in the whole range of mobilities it cannot exceed unity, the ratio of the sample flow rate to the aerosol flow rate, f_1, or f_2. Thus

$$\Omega = \max\left[0, \min\left(1, \frac{Q_s}{Q_a}, \frac{Q_a - Q_{sh} + 2\pi\Delta\phi Z_p}{Q_a}, \frac{Q_a - Q_{sh} + 2\pi\Delta\phi Z_p}{Q_a}\right)\right] \tag{3.28}$$

The resulting transfer function for the RDMA has the shape of a truncated isosceles triangle whose centroid and exact angles depend on the flow rates and the applied field. It is depicted in Fig. 3.8.

The peak of the transfer function occurs at

$$Z_p^* = \frac{2Q_{sh} + Q_a - Q_s}{4\pi\Delta\phi} = \frac{2Q_{sh} + Q_a - Q_s}{2\pi(R_2^2 - R_1^2)}\frac{b}{V} \tag{3.29}$$

and has a half width

$$\Delta Z_p = \frac{Q_a + Q_s}{2\pi(R_2^2 - R_1^2)}\frac{b}{V} \tag{3.30}$$

When the aerosol and sample flows are equal, one has

$$Z_p^* = \frac{Q_{sh}b}{\pi(R_2^2 - R_1^2)V} \tag{3.31}$$

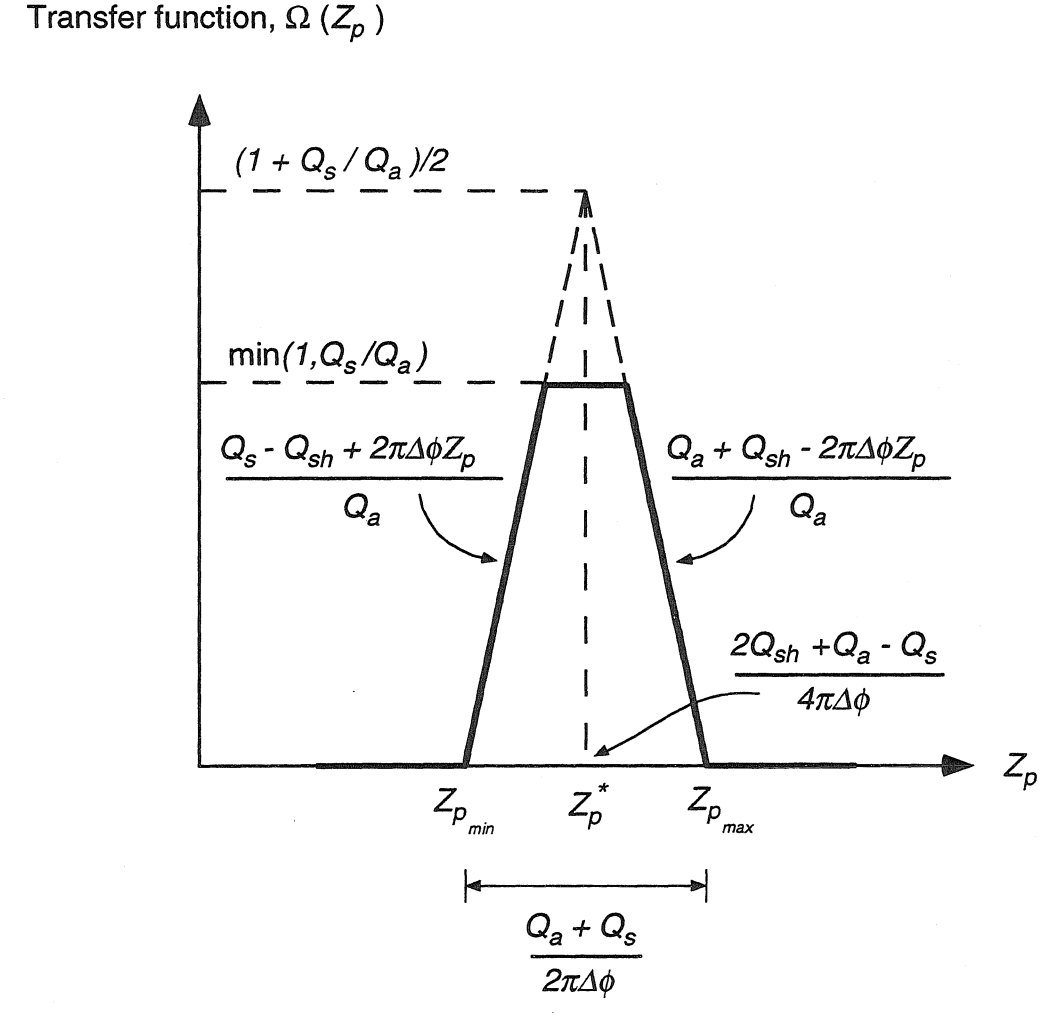

Figure 3.8: Graphical depiction of the ideal transfer function of the radial differential mobility analyzer.

and

$$\Delta Z_p = \frac{Q_a b}{\pi(R_2^2 - R_1^2)V} \tag{3.32}$$

Equations 3.29 and 3.30 give the parameters for the RDMA ideal transfer function. In reality, significant distortions may occur in the shape and peak location of $\Omega(Z_p)$ due to diffusion and space charge effects. A detailed treatment of these effects is presented in chapter 5. For the moment, it suffices to mention that Zhang and Flagan [20] have described a semi-analytical model to account for the diffusion broadening of the RDMA transfer function. According to this model the diffusion broadened RDMA transfer function is given by

$$\Omega_d = \frac{\tilde{\sigma}}{\sqrt{2}\beta(1-\delta)}\left\{\mathcal{E}\left[\frac{\tilde{Z}-(1-\beta)}{\sqrt{2}\tilde{\sigma}}\right] + \mathcal{E}\left[\frac{\tilde{Z}-(1+\beta)}{\sqrt{2}\tilde{\sigma}}\right]\right.$$

$$\left. -\mathcal{E}\left[\frac{\tilde{Z}-(1-\delta\beta)}{\sqrt{2}\tilde{\sigma}}\right] - \mathcal{E}\left[\frac{\tilde{Z}-(1+\delta\beta)}{\sqrt{2}\tilde{\sigma}}\right]\right\} \tag{3.33}$$

where $\mathcal{E}(x)$ is defined in terms of the error function $\mathrm{erf}(x)$ as

$$\mathcal{E}(x) \equiv \int_0^x \mathrm{erf}(u)du = x\mathrm{erf}(x) + \frac{1}{\sqrt{\pi}}\exp(-x^2) \tag{3.34}$$

and $\tilde{Z}$ is the normalized mobility, i.e., $\tilde{Z} \equiv Z/Z^*$. In addition,

$$\beta = \frac{Q_s + Q_a}{Q_e + Q_{sh}} \tag{3.35}$$

$$\delta = \frac{Q_s - Q_a}{Q_s + Q_a} \tag{3.36}$$

The parameter $\tilde{\sigma}$ is given by

$$\tilde{\sigma}^2 = \frac{\tilde{G}}{\mathrm{Pe}_{mig}} \tag{3.37}$$

where Pe_{mig} is the migration Peclet number (i.e., $\mathrm{Pe}_{mig} = qV/kT$ for the RDMA, see chapter 5) and $\tilde{G}$ is a dimensionless geometry factor that for creeping flow in the RDMA takes the value $\tilde{G} = 2.92$ [20].

In Figure 3.9 a comparison is made between the ideal and the diffusion broadened RDMA transfer functions plotted as a function of the normalized mobility $\tilde{Z}$. It is apparent that, in the size range of interest for synthesis of semiconductor nanocrystals, diffusion broadening of the transfer function does play an important role in the resolution of the RDMA. The effect of diffusion becomes more severe as lower voltages are used. As a result, the smaller the particle, the lower the resolution of the system. A broadening of as much as 50% in mobility is expected for 1 nm particles.

Assuming singly charged particles, Eq. 3.14 establishes a one-to-one relationship between electrical mobility and particle diameter. By doing so the transfer functions of Fig. 3.9 may be plotted as a function of particle diameter as shown in Fig. 3.10. This figure reveals that for the RDMA diffusion broadening in the 1-10 nm range is a problem of limited magnitude. Reasonable size classification should be possible in this size regime as 1 nm particles can be resolved if the RDMA is operated close to its resolution limit.

3.5 Collection techniques

3.5.1 Introduction

It is often desirable that the end product of a material that has been synthesized by aerosol routes be laden on a solid substrate or liquid matrix. If useful samples

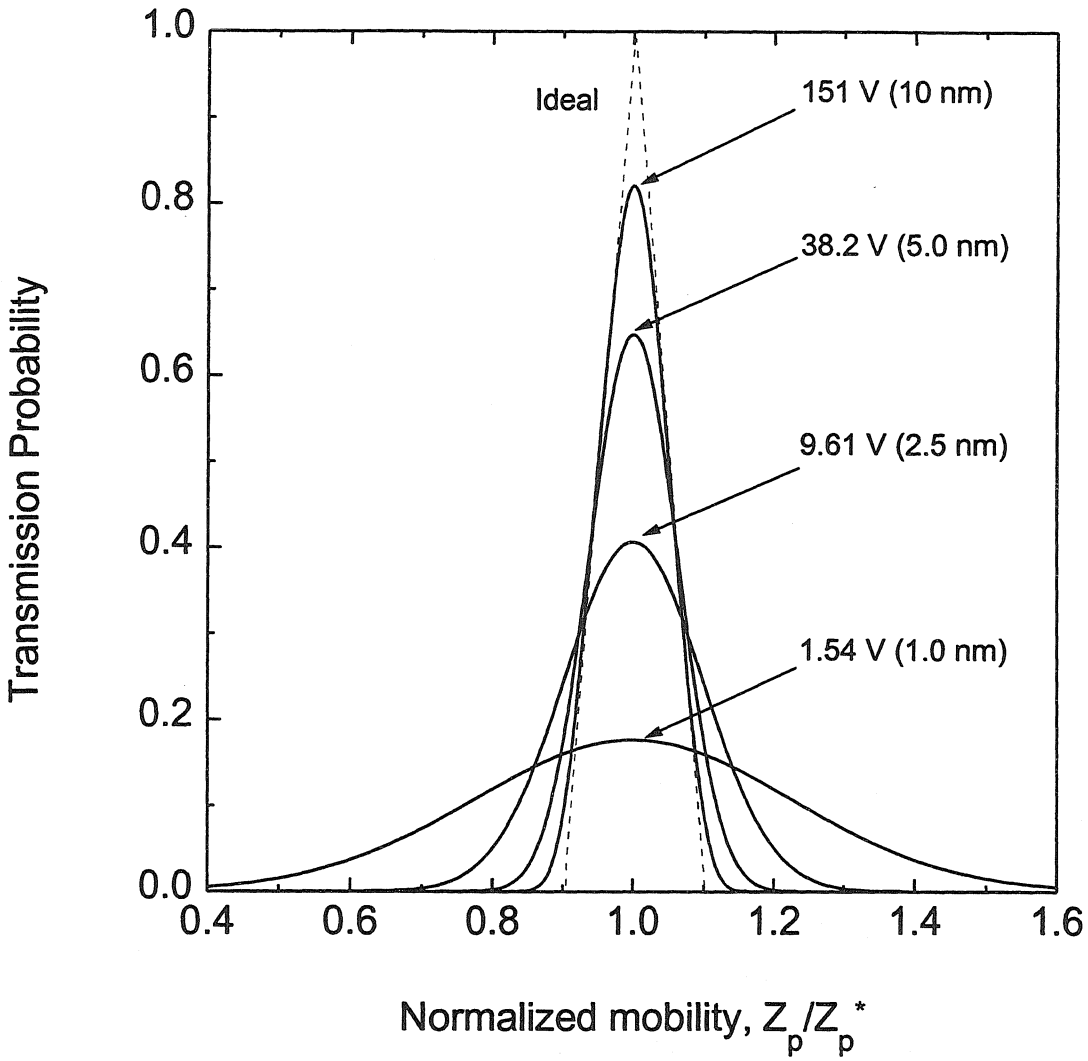

Figure 3.9: Comparison between the ideal and diffusion broadened transfer functions of the radial differential mobility analyzer as a function of normalized mobility. Diffusion broadened transfer functions were calculated using Zhang and Flagan's model with $\beta = 0.1$ ($Q_a = Q_s = 1.5$ lpm, $Q_{sh} = 15$ lpm).

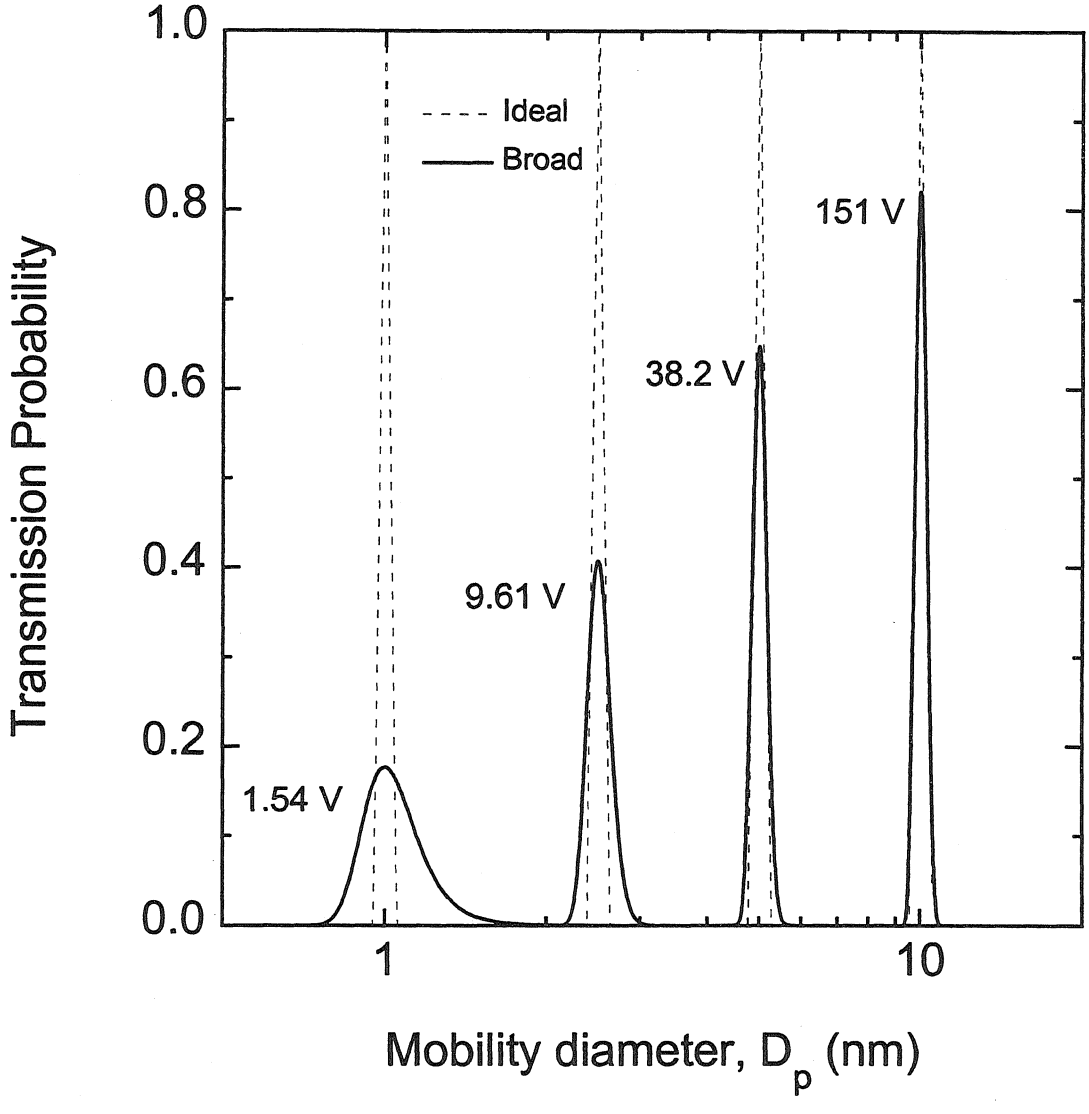

Figure 3.10: Comparison between the ideal and diffusion broadened transfer functions of the radial differential mobility analyzer as a function of particle diameter. Diffusion broadened transfer functions were calculated using Zhang and Flagan's model with $\beta = 0.1$ ($Q_a = Q_s = 1.5$ lpm, $Q_{sh} = 15$ lpm).

are to be obtained in this way, an intentional collection step may be required. It is, therefore, necessary to employ efficient techniques for extracting the particles from the carrier gas flow. In this section we describe briefly three techniques to deposit aerosol particles on solid substrates, namely, thermophoretic collection, electrostatic precipitation, and hypersonic impaction.

3.5.2 Thermophoretic collection

Temperature gradients cause particles to migrate in a gas medium. This phenomenon provides a means for particle collection. In order to know how strong this effect is for nanoparticles and in which conditions it may provide an efficient collection technique, it is useful to estimate the thermophoretic velocity of a particle. This velocity may be expressed in the following way [21]:

$$v_T = -\frac{\mu}{\rho}\frac{1}{T}\frac{dT}{dx}\mathrm{Th} \tag{3.38}$$

where μ and ρ are the viscosity of the gas and the particle density respectively, T is the gas temperature, dT/dx is the temperature gradient (< 0) in the direction of motion, and Th is a thermal dimensionless group. For particles in the nanometer size regime (Kn $\gg 1$), Th is found to be essentially size independent. Experimental measurements give values for Th of about 0.5 [21].

Several simple ways of generating a steep temperature gradient exist. One that has often been used for collection of semiconductor nanocrystals is the cooling of a substrate holder down to liquid nitrogen temperatures while the carrier gas is kept at room temperature or higher [2, 22]. In this case temperature gradients are roughly in

the 200-2000°C range, depending on the flow conditions and exact temperature in the reactor. Using Eq. 3.38, with Th = 0.5 and $T = 300$°C, one finds $v_T \sim 0.1$ - 1.0 cm/s. For aerosol reactors with flow velocities comparable or lower than v_T, thermophoretic collection is an option for efficient particle extraction from the gas stream. Often, however, short residence times are required to minimize particle losses, which, coupled to reasonable reactor dimensions, imply gas flow velocities in excess of 100 cm/s. In this case, thermophoretic collection is very inefficient and other collection techniques must be used.

3.5.3 Electrostatic precipitation

One of the most suitable collection techniques for the generation of deposits of semiconductor nanocrystals is the electrostatic precipitation. In this technique charged nanocrystals are extracted from the gas flow and deposited on a solid substrate by the action of an electric field. The deposition velocities are significantly higher than in the case of thermophoretic collection. A typical electric field of 20 kV/cm will cause migration velocities of $\sim$ 400 cm/s for singly charged 10 nm particles. These velocities are high enough to allow compatibility with short-residence-time systems but still low enough to permit soft particle deposition with no observable deformation. Several geometries have been proposed for the implementation of this technique. Two of the most common are the point-to-plane geometry [23] for sampling of small amounts of material typically for microscopy analysis and the cylindrical geometry for gas cleaning [24].

Targeting a more efficient geometry with minimization of particle losses, we have

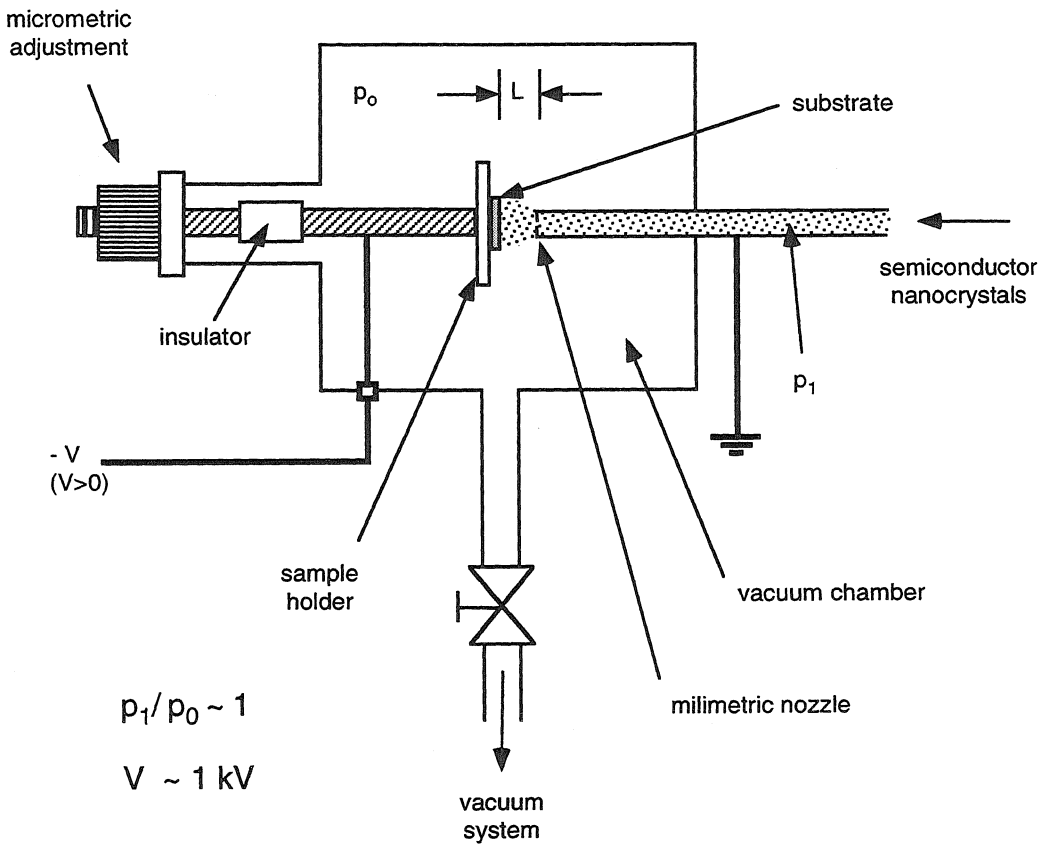

Figure 3.11: Diagram of the nozzle-to-plane electrostatic precipitator.

designed and implemented an electrostatic precipitator in the nozzle-to-plane configuration. Figure 3.11 presents a schematic diagram of this device. A nozzle with a 1 mm diameter was prepared simply by drilling a hole in a plug at the end of a 1/4 inch tube. The device is connected to a vacuum pump that provides the pressure difference required for the gas flow. A vacuum feedthrough with micrometric adjustment is connected to a substrate holder where a conductive substrate may be placed for the collection of the nanocrystal deposit. The micrometer adjustment allows the positioning of the substrate within 0.4 to 0.6 mm from the nozzle, which has been found to be an appropriate distance for the collection of nanocrystals in the 3.0 to 15 nm size range.

Assuming a simple outward radial flow field, the voltage required to generate a deposit of radius R is trivially deduced to be

$$V_{EP} = \frac{Q_{EP} L}{2\pi Z_p R(R - R_0)} \tag{3.39}$$

where Q_{EP} is the volumetric flow through the precipitator, L is the nozzle-to-plane distance, and R_0 is the nozzle radius. Due to the fact that the electrical mobility scales with the inverse of the particle diameter (Eq. 3.14), the larger the particle, the higher the electric field required for its collection. As a result of the voltage breakdown limit of typical carrier gases (approximately 30 kV/cm for N_2), an upper bound exists in the diameter of the particle that can be collected by electrostatic precipitation. For flow rates around 1 lpm, the electrostatic precipitator is a powerful collection device for nanoparticles with diameter below approximately 20 nm.

Figure 3.12 shows the required voltage to obtain a certain deposit radius of singly

charged 10 nm particles for different nozzle-to-plane distances L. Similarly, Fig. 3.13 indicates the applied voltage required to obtain a certain deposit radius for different particle diameters using $L = 0.5$ mm.

In the nozzle-to-plane geometry, for a given applied field, the radius of the resulting deposit scales with the particle diameter. Based on this behavior, a limited experiment to verify the predicted performance of the electrostatic precipitator was carried out. In Fig. 3.14 experimentally measured radii of deposits of silicon nanocrystals of known size are compared with the simple theoretical prediction for the device based on Eq. 3.39. As these deposits typically constitute less than a monolayer of nanometer-scale particles, their visualization for measurement is rather challenging. This difficulty leads to the large error bars shown in the figure. Although few experimental points are available, the measured deposit radii present the same trend predicted by the simple deposition model. However, their values seem larger than the calculated ones. This is probably due to the assumption of a radial flow field and to the uncertainties involved in Q_{EP}, L, and R_0 that were not taken into account when using Eq. 3.39 to calculate the deposit radius. In any case, Fig. 3.14 indicates that the nozzle-to-plane electrostatic precipitator performs adequately in the collection of nanocrystals with diameters below 15 nm.

3.5.4 Hypersonic impaction

Another alternative technique that has been demonstrated to generate fairly uniform deposits of nanocrystals is hypersonic impaction. In this case particles are removed from the gas stream as a result of inertial forces. The aerosol is forced to undergo

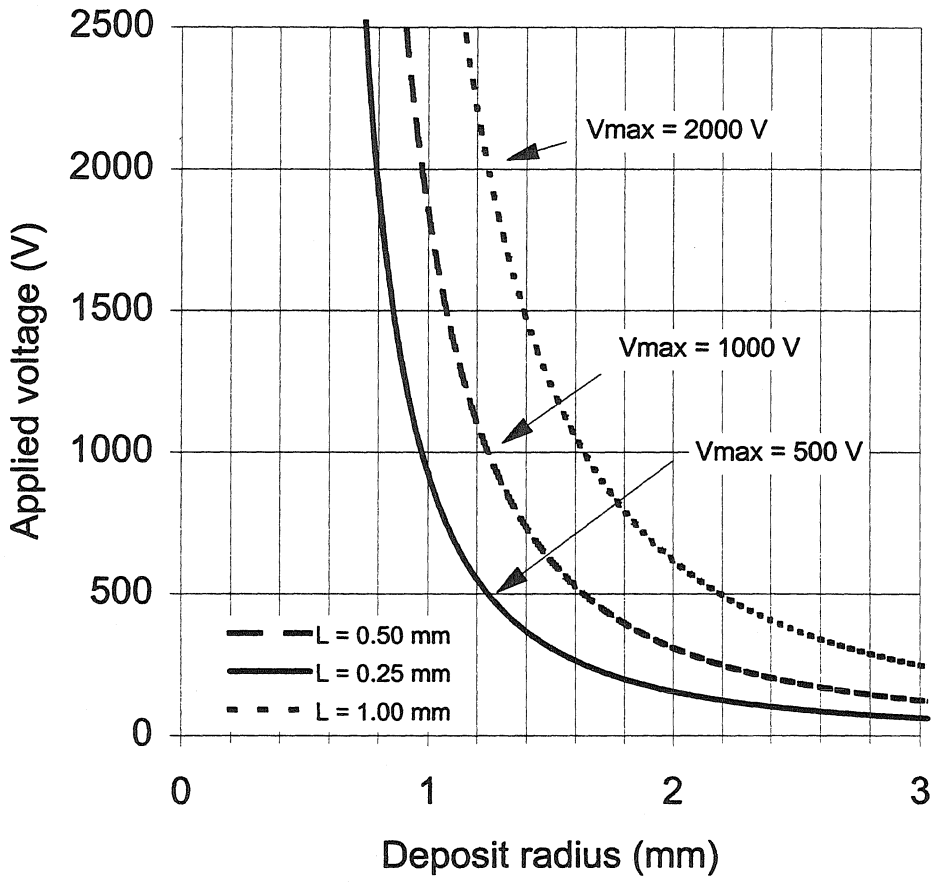

Figure 3.12: Required voltage to obtain a certain radius of the deposit for different nozzle-to-plane distances L. ($Q_{EP} = 1.4$ lpm, $D_p = 10$ nm, $R_0 = 0.5$ mm).

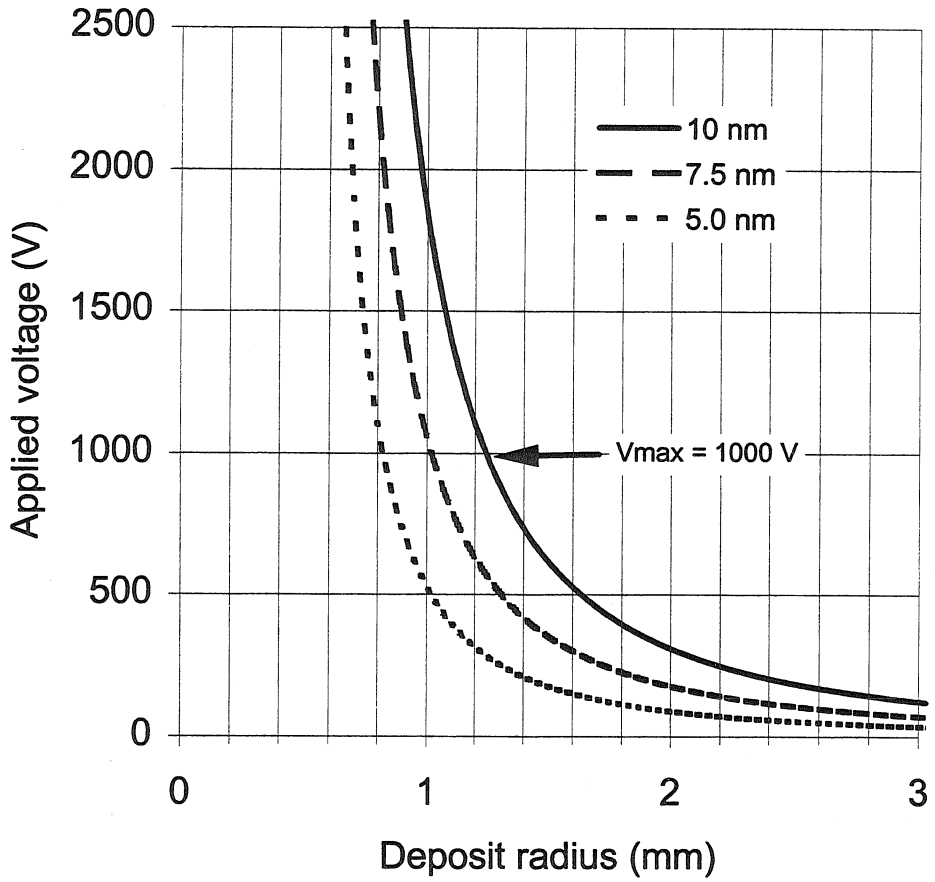

Figure 3.13: Required voltage to obtain a certain radius of the deposit for different diameters of singly charged particles ($Q_{EP} = 1.4$ lpm, $L = 0.5$ mm, $R_0 = 0.5$ mm).

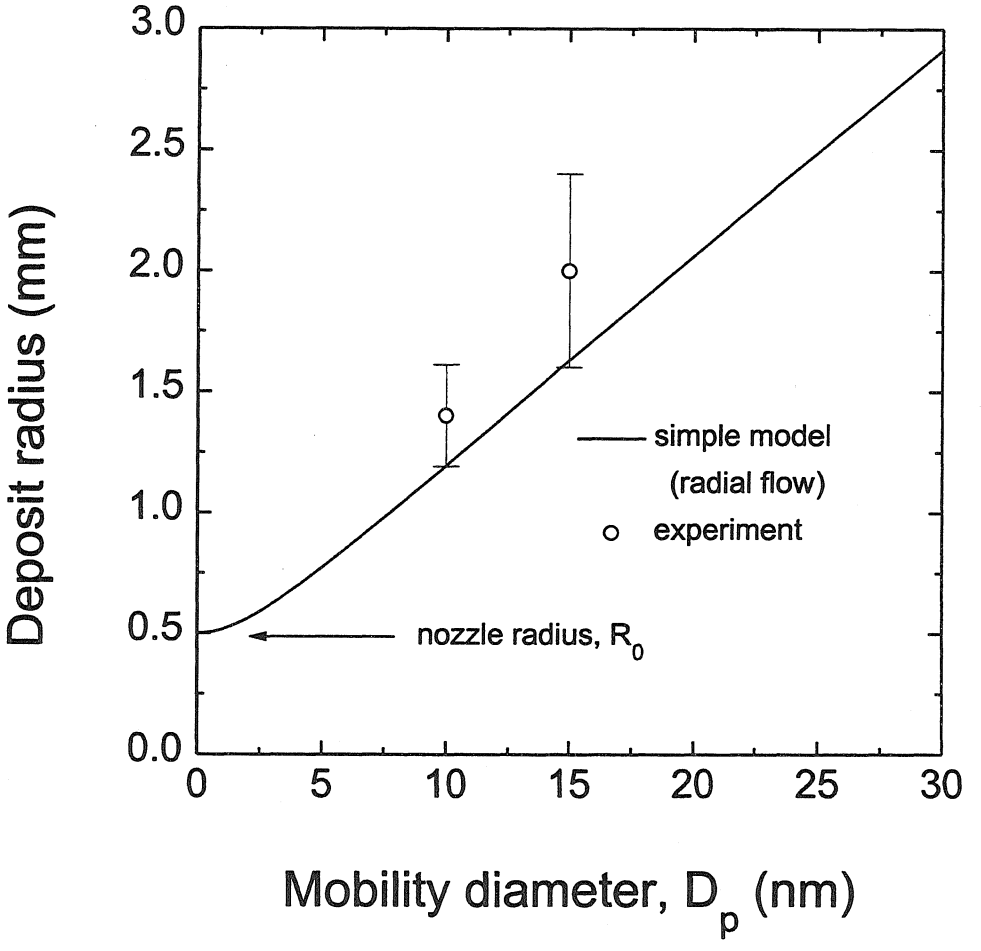

Figure 3.14: Comparison between predicted and observed sizes of deposits on the electrostatic precipitator as a function of particle size.

a free expansion as it passes through a sub-millimetric nozzle connecting a region at pressure p_0 to a region at lower pressure p_1. In this process the nanoparticles acquire velocities in excess of the speed of sound (34000 cm/s), allowing them to be collected by inertial impaction on a substrate placed normal to the gas jet. Deposition velocities are significantly higher than in the collection techniques described in the previous sections and particle deformation upon impaction may become an issue for soft clusters.

Although the fluid dynamics of a supersonic free jet impinging on a surface is not fully understood, some work has been done recently in the attempt to characterize the hypersonic impactor as a tool for size-resolved measurements on nanometer-scale aerosols [25, 26]. The parameter that is usually used to describe impaction processes is the Stokes number S defined as

$$\mathrm{S} = \frac{\tau U}{d} \tag{3.40}$$

where τ is the particle relaxation time, U is the gas characteristic velocity, and d is the characteristic system dimension.

For a hypersonic impactor with nozzle diameter d_n and nozzle-to-plane distance L, the Stokes number becomes [25]:

$$\mathrm{S} = 6.34 \frac{\rho_p D_p c^2}{d_n p_0} \left(\frac{L}{d_n} \right) \tag{3.41}$$

where ρ_p and D_p are the density and the diameter of the particle, respectively, c is the speed of sound, and p_0 is the pressure upstream the nozzle. Impaction is expected to occur for values of S larger than a critical threshold, $\mathrm{S}_{1/2}$, which is of order unity for

dense spherical particles. Below the critical diameter corresponding to $S_{1/2}$, particles cannot be collected efficiently.

As part of this thesis work we have designed and built a hypersonic impactor to be employed as a collection device. Figure 3.15 shows a schematic diagram of this instrument. Its geometry is essentially identical to the electrostatic precipitator described in the previous section. The significant modifications are the sub-millimeter nozzle whose diameter was chosen to be $d_n = 0.2$ mm allowing pressure ratios p_0/p_1 as high as 760 with the available pumping capacity ($\sim$ 7000 liters per minute).

Although we have not performed a thorough characterization of this instrument, enough information of its performance was gathered to ensure efficient collection in the size range of interest. This was done by introducing silicon particles that had been size classified with the DMA into the hypersonic impactor. By monitoring the number concentration of size classified particles with an electrometer, the total number of particles that entered the impactor was determined. The fraction of those particles that was captured on the solid substrate was then determined by transmission electron microscopy (TEM). In this way, the collection efficiency could be estimated. Operating the impactor with $p_0/p_1 \sim 760$ and $L/d_n = 9.30$, a collection efficiency of 0.79 ± 0.14 was found for 7.5 nm Si particles. In a different measurement under the same conditions, a polydisperse aerosol was introduced in the impactor and the size distribution of the collected particles was determined by TEM. A plot of this size distribution, normalized so its peak corresponds to the efficiency measured at 7.5 nm, is shown in Fig. 3.16. At a first glance, the absence of particles with diameter below 6

nm seems to indicate that the size cut of the impactor is around that value. However, as the size distribution of the particles entering the impactor was not measured, it is not known whether particles in that size regime were present in the aerosol. Based on values of $S_{1/2}$ determined by careful studies of hypersonic impaction of silver nanoparticles [26], Eq. 3.41 predicts a size cut of $\sim$ 3.5 nm for Si particles impacting on an effectively infinite surface.

Another measurement made with $L/d_n = 15.3$ yielded a collection efficiency of 0.39 $\pm$ 0.09 for 10 nm Si particles. In this case, the lower efficiency may be related to the termination of the expansion, which in the absence of an impaction plate is expected to happen at $L/d_n \sim 18.5$ for the used pressure ratio [25]. This lower efficiency for $L/d_n = 15.3$ may also be a consequence of the small substrate used (3 mm diameter). As L/d_n is increased, deviations from the behavior predicted for an effectively infinite surface become more severe.

For our purpose of using the hypersonic impactor as a collection device, the efficiency estimated in Fig. 3.16 was considered adequate. Operation conditions of p_0/p_1 $\sim$ 760 and $L/d_n = 9.30$ lead to collection efficiency above 80% for particles larger than 7.5 nm. Due to the unclear performance below 6 nm, deposition of particles in that size range was generally performed using electrostatic precipitation.

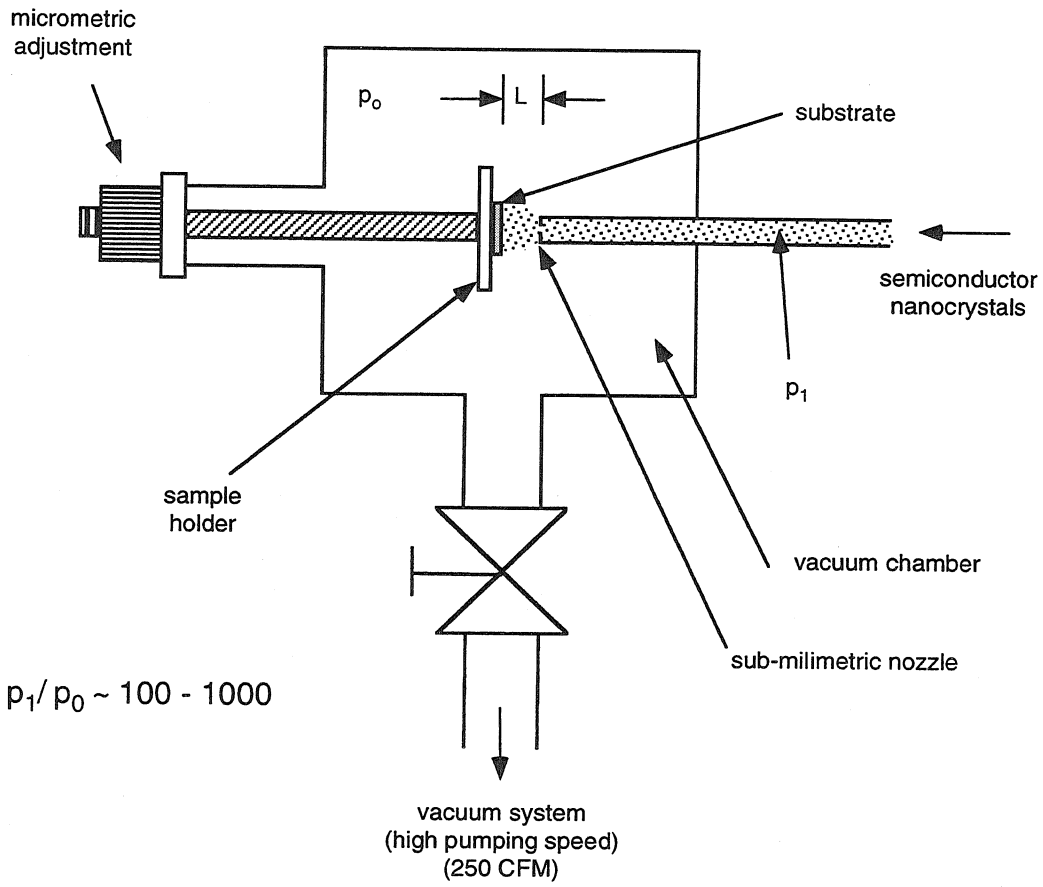

Figure 3.15: Diagram of the hypersonic impactor.

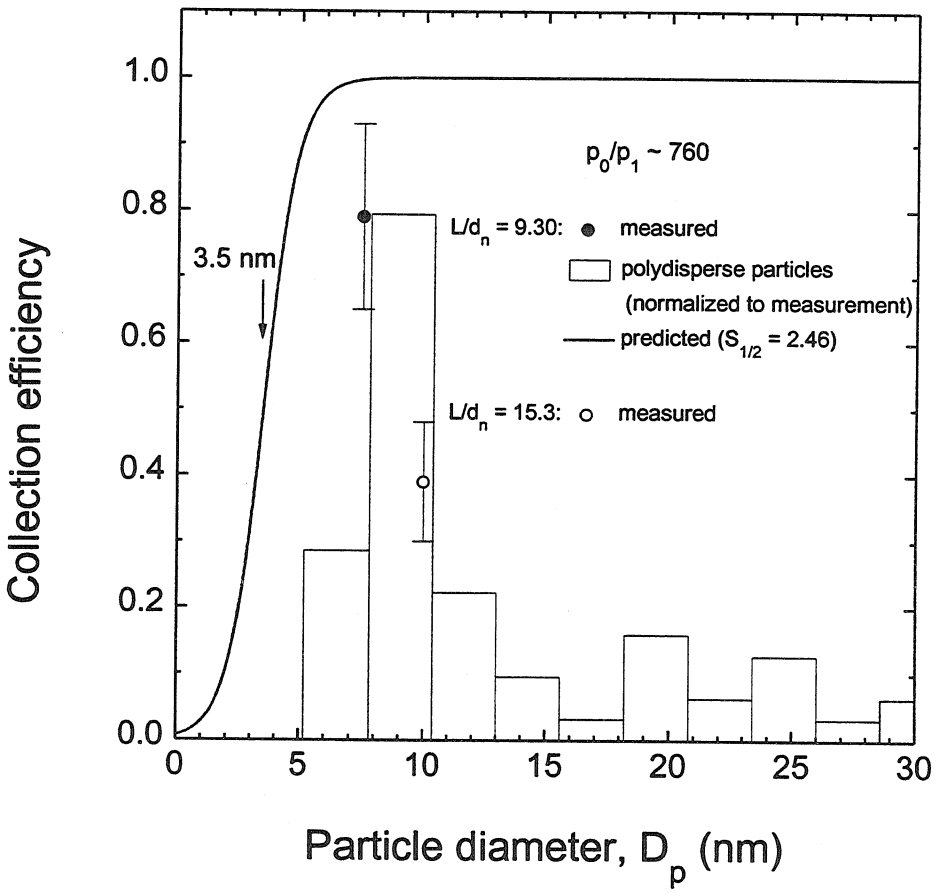

Figure 3.16: Estimate of the size cut-off of the hypersonic impactor as measured by transmission electron microscopy and differential mobility analysis experiments for the indicated operation parameters.

Bibliography

[1] S. Hayashi, S. Tanimoto, and K. Yamamoto, "Analysis of surface oxides of gas-evaporated Si small particles with infrared spectroscopy, high-resolution electron microscopy, and x-ray photoemission spectroscopy," *J. Appl. Phys.*, vol. 68, pp. 5300–5308, 1990.

[2] P. C. Sercel, W. A. Saunders, H. A. Atwater, K. J. Vahala, and R. C. Flagan, "Nanometer-scale GaAs clusters from organometallic precursors," *Appl. Phys. Lett.*, vol. 61, pp. 696–698, 1992.

[3] L. N. Dinh, L. L. Chase, M. Balooch, W. J. Siekhaus, and F. Wooten, "Optical properties of passivated Si nanocrystals and SiO_x nanostructures," *Phys. Rev. B*, vol. 54, pp. 5029–5037, 1996.

[4] K. A. Littau, P. J. Szajowski, A. J. Muller, A. R. Kortan, and L. E. Brus, "A luminescent silicon nanocrystal colloid via a high-temperature aerosol reaction," *J. Phys. Chem.*, vol. 97, pp. 1224–1230, 1992.

[5] W. L. Wilson, P. F. Szajowski, and L. E. Brus, "Quantum confinement in size-selected, surface-oxidized silicon nanocrystals," *Science*, vol. 262, pp. 1242–1244, 1993.

[6] K. Deppert and L. Samuelson, "GaAs nanocrystals from Ga aerosols," *Proc. of the European Aerosol Conference*, Helsinki, Finland.

[7] A. Wiedensohler, H. -C. Hansson, I. Maximov, A. Gustafsson, W. Seifert, and L. Samuelson, "Production of zero-dimensional quantum dot structures using ultrafine aerosol particles," *Synthesis and measurement of ultrafine particles*, Delft University Press, Delft, 1993, pp. 13–19.

[8] R. P. Camata, H. A. Atwater, K. J. Vahala, and R. C. Flagan, "Size classification of silicon nanocrystals," *Appl. Phys. Lett.*, vol. 68, pp. 3162–3164, 1996.

[9] R. C. Flagan and J. H. Seinfeld, *Fundamentals of air pollution engineering*, Prentice Hall, Englewood Cliffs, New Jersey, 1988, pp. 332–333.

[10] See, for example, R. C. Flagan and J. H. Seinfeld, *Fundamentals of air pollution engineering*, Prentice Hall, Englewood Cliffs, New Jersey, 1988, pp. 328–331.

[11] A. Wiendensohler, "An approximation of the bipolar charge distribution for particles in the submicron size range," *J. Aerosol Sci.*, vol. 19, pp. 387–389, 1988.

[12] M. D. Allen and O. G. Raabe, "Re-evaluation of Millikan's oil drop data for the motion of small particles in air," *J. Aerosol Sci.*, vol. 13, pp. 537–547, 1982.

[13] E. O. Knutson and K. T. Whitby, "Aerosol classification by electric mobility: apparatus, theory, and applications," *J. Aerosol Sci.*, vol. 6, pp. 453–460, 1975.

[14] A. Wiendensohler, "Effect of Brownian diffusion on electrical classification of ultrafine aerosol particles in differential mobility analyzer," *J. Chem. Eng. Japan*, vol. 19, pp. 401–407, 1986.

[15] G. P. Reischl, "The relationship of input and output aerosol characteristics for an ideal differential mobility analyzer particle standard," *J. Aerosol Sci.*, vol. 22, pp. 297–312, 1991.

[16] W. Winklmayr, G. P. Reischl, A. O. Lidner, and A. Berner, "A new electromobility spectrometer for the measurement of aerosol size distributions in the size range from 1 to 1000 nm," *J. Aerosol Sci.*, vol. 22, pp. 289–296, 1991.

[17] J. Rosell-Llompart, I. G. Loscertales, D. Bingham, and J. Fernández de la Mora, "Sizing nanoparticles and ions with a short differential mobility analyzer," *J. Aerosol Sci.*, vol. 27, pp. 695–719, 1996.

[18] B. Mesbah, "Le Spectrometre de Mobilite Electrique Circulaire: Theorie, Performances et Applications," Ph.D. Thesis, University of Paris, 1994.

[19] S. -H. Zhang, Y. Akutsu, L. M. Russell, R. C. Flagan, and J. H. Seinfeld "Radial Differential Mobility Analyzer," *Aerosol Sci. Technol.*, vol. 23, pp. 357–372, 1995.

[20] S. -H. Zhang and R. C. Flagan, "Resolution of the radial differential mobility analyzer," *J. Aerosol Sci.*, vol. 27, pp. 1179–1200, 1996.

[21] See, for example, R. C. Flagan and J. H. Seinfeld, *Fundamentals of air pollution engineering*, Prentice Hall, Englewood Cliffs, New Jersey, 1988, pp. 313–314.

[22] W. A. Saunders, P. C. Sercel, R. B. Lee, H. A. Atwater, K. J. Vahala, R. C. Flagan, and E. J. Escorcia-Aparcio, "Synthesis of luminescent silicon clusters by spark ablation," *Appl. Phys. Lett.*, vol. 63, pp. 1549–1551, 1993.

[23] See, for example, Y.-S. Cheng, H.-C. Yeh, and G. M. Nanapilly, "Collection efficiencies of a point-to-plane electrostatic precipitator," *Am. Ind. Hyg. Assoc. Journal*, vol. 42, pp. 605–610, 1981.

[24] See, for example, R. C. Flagan and J. H. Seinfeld, *Fundamentals of air pollution engineering*, Prentice Hall, Englewood Cliffs, New Jersey, 1988, pp. 411–415.

[25] J. Fernandez de la Mora, S. V. Hering, N. Rao, and P. H. McMurry, "Hypersonic impaction of ultrafine particles," *J. Aerosol Sci.*, vol. 21, pp. 169–187, 1990.

[26] J. Fernandez de la Mora and A. Schmidt-Ott, "Performance of a hypersonic impactor with silver particles in the 2 nm range," *J. Aerosol Sci.*, vol. 24, pp. 409–415, 1993.

Chapter 4

Synthesis of size-classified silicon nanocrystals

4.1 Introduction

Visible luminescent group IV nanostructured materials such as porous silicon [1] and silicon and germanium nanocrystals [2, 3] are potential candidates for silicon-compatible optoelectronic devices. Although a number of studies on these nanostructured materials have been carried out recently, the mechanism of visible luminescence has not yet been completely established. Models involving quantum confinement of excitons and interface electronic states have been proposed in attempts to explain this phenomenon [4, 5, 6]. As described in chapter 2, quantum confinement should in principle lead to size-dependent luminescence spectra, if this is the dominant mechanism for photocarrier recombination [7, 8]. Experimental confirmation of this mechanism requires that measurements be made either on single nanocrystals or carefully con-

trolled size ensembles. Although size classification of silicon nanocrystals has been achieved to a certain extent by size-selective chemical precipitation [4], as successfully demonstrated also for II-VI semiconductor crystallites [9], most of the studies to date have involved samples with broad size distributions containing large chains of nanostructures, complicating the interpretation of the luminescence behavior [5, 6]. In this chapter, we demonstrate the generation of nearly monodisperse, nonagglomerated silicon nanocrystals using the aerosol techniques described in the previous chapter. These nanocrystals can potentially be used in optical experiments and help clarify the luminescence mechanism.

4.2 Experimental setup

In the experiments presented in this chapter, we combine the aerosol techniques described in chapter 3 to synthesize and size classify silicon nanocrystals. The experimental apparatus used contains five principal elements: a nanocrystal aerosol source, an aerosol neutralizer, a radial differential mobility analyzer, an aerosol concentration monitor and a collection device. These elements are arranged as shown in Fig. 4.1. Their functions are summarized as follows.

The silicon nanocrystals are produced in the form of an aerosol alternatively by three different vapor phase methods, namely, spark ablation [11], laser ablation [13], and thermal evaporation [15]. A description of each one of these techniques will be presented in coming sections. For the moment we focus on the features of the experimental approach that were common throughout this work, regardless of the

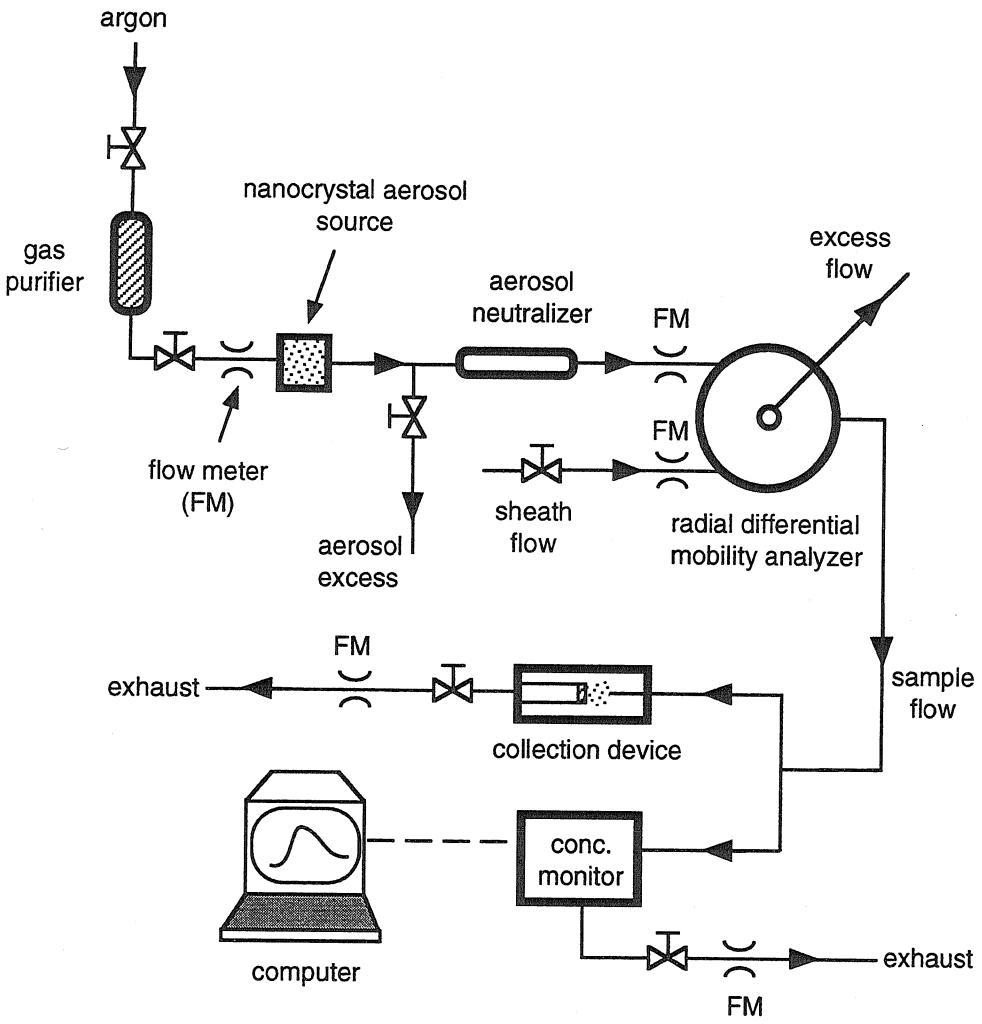

Figure 4.1: Schematic of the experimental apparatus for synthesis and size classification of silicon nanocrystals, showing the nanocrystal aerosol source, the aerosol neutralizer, radial differential mobility analyzer, the aerosol concentration monitor (electrometer or condensation nucleus counter), and the collection device (thermophoretic collector, hypersonic impactor, or electrostatic precipitator).

specific vapor phase source chosen.

The vaporization of silicon occurs in a continuous-flow inert gas atmosphere. For this purpose, research purity argon (99.9995% minimum purity) is run through a gas purifier (< 1 ppb impurities) flows through the chamber containing the nanocrystal source as a carrier medium for the nanocrystals that nucleate from the vapor phase. The source is adjusted to generate an ultrafine aerosol in the 1 to 10 nm size range. The charge state of this initial aerosol is not well known. A known charge distribution is imparted on the aerosol by exposing it to ionizing radiation from a sealed ^{85}Kr β source. Reactions with the ambipolar gas ions in this "neutralizer" result in a steady-state charge distribution with respect to nanocrystal size that has been predicted by Fuchs [16].

Downstream from the neutralizer, the nanocrystal aerosol is classified with respect to particle size using a radial differential mobility analyzer (RDMA) [17]. By varying the voltage across the RDMA, the applied field is varied and the size of the classified nanocrystals can be continuously tuned. A short residence time and a high transmission efficiency of the incoming aerosol in the 3.0 to 10 nm size range enable the RDMA to classify silicon nanocrystals according to mobility down to sizes relevant to quantum size effects. The concentration of classified nanocrystals is monitored by taking 6-20% (depending on operation conditions) of the classified aerosol into a femto-ampere sensitivity electrometer or, alternatively, into a condensation nucleus counter [18]. The combined operation of the RDMA and the concentration monitor allows determination of the nanocrystal size distribution, providing information to

maintain constant operation of the source. Most of the classified nanocrystals (80 - 94%) are removed from the gas flow and deposited on a substrate. For this purpose, a thermophoretic collector [11], a hypersonic impactor [19], and an electrostatic precipitator [20] have been used alternatively as collection devices.

The maintenance of stable and reproducible flow rates throughout the experiment is one of the most important conditions for good performance of the size classification. The flow rates were monitored by measuring the pressure drop through laminar flow elements using differential pressure transducers.

4.3 Silicon nanocrystals by spark ablation

4.3.1 The spark ablation nanocrystal source

The generation of aerosol particles by spark discharge provides a simple means to obtain nanoscale clusters of conducting and semiconducting materials [10]. We use this technique to produce silicon nanocrystals by direct ablation or evaporation of crystalline silicon substrates in a high-voltage electric spark discharge [11]. A schematic of the spark ablation source used is presented in Fig. 4.2. A flashlamp circuit (L, C, and R_1) is used to drive the spark discharge, while an additional resistor (R_2) limits the spark current to avoid excessive particle generation which leads to rapid depletion of nanometer-scale individual particles due to coagulation.

The source is operated at 1 atm pressure while voltage, current, frequency, and diluent flow rate in the spark discharge region are adjusted to generate an ultrafine aerosol in the 1 to 10 nm size range. The values used for the components of the

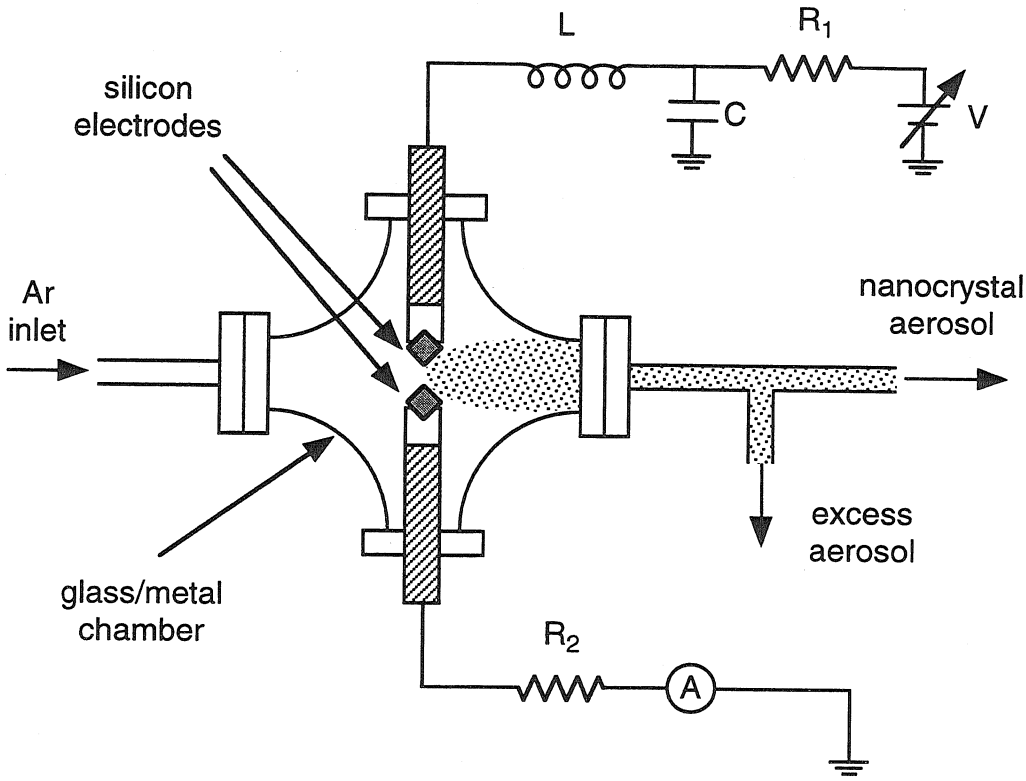

Figure 4.2: Schematic of the spark ablation source of silicon nanocrystals.

driving circuit are R_1 = 10 kΩ, C = 0.125 μF, L = 70 μH. The spark current is usually best controlled by varying the resistance R_2. Values between zero and 200 kΩ have been used to vary the spark current in the $\sim$ 1-500 mA range. Typical voltage and frequency values were 1 kV and 120 Hz respectively, and the volumetric flow rates in the nanocrystal chamber could be varied between 0.5 and 20 lpm.

4.3.2 Polydisperse silicon nanocrystals

Without any size classification, nanocrystal samples generated by spark ablation consist of large chain agglomerates. Figure 4.3(a) shows a transmission electron micrograph of nanocrystals generated with a simplified version of the experimental setup of Fig. 4.1. In this case the collection device was connected directly downstream from the nanocrystal source, bypassing all the other instrumentation. The source was operated at 1 kV and 120 Hz with $R_2 = 0$ (spark current $\sim$ 500 mA) and an aerosol flow rate of 1 lpm. The nanocrystals were collected by thermophoresis on an amorphous carbon substrate for a total time of 130 min. Although the size of the primary particles is found to be below 10 nm, micron-sized chain agglomerates dominate the aerosol. In this mode of operation, it is estimated that collection rates for the generated material is as high as 10^{15} - 10^{16} particles/cm^{2}h (or 1 mg/h). In Fig. 4.3(b) an electron diffraction pattern obtained from this polydisperse sample indicates that at least a significant number of the particles are crystalline with bulk-like diamond cubic crystal structure.

To evaluate their degree of oxidation, polydisperse samples like the one shown in Fig. 4.3 were collected on germanium substrates and subjected to x-ray photoelectron

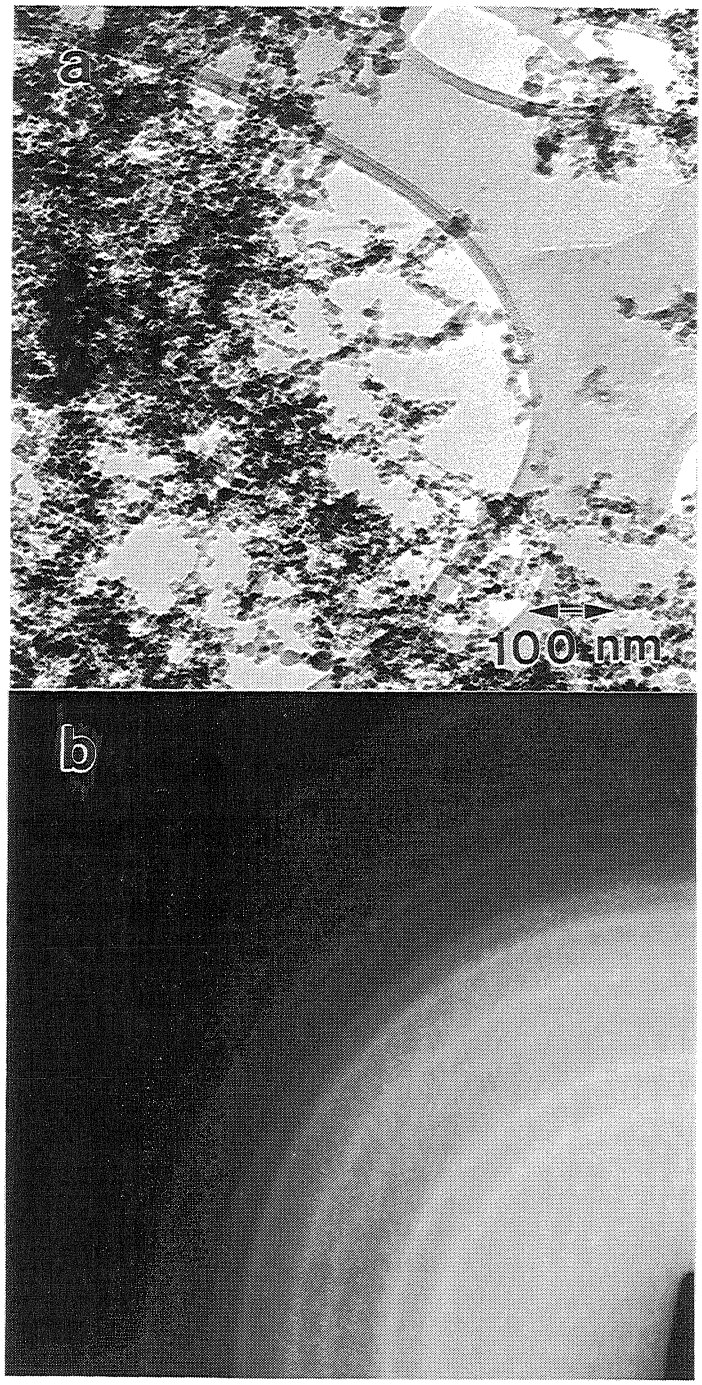

Figure 4.3: (a) Transmission electron micrograph and (b) electron diffraction pattern of silicon nanocrystals made by spark ablation. Collected by thermophoresis on an amorphous carbon substrate just downstream from the spark source.

analysis (XPS) using monochromated Al $K\alpha$ radiation at 1487 eV, with a resolution of ~ 0.7 eV. In Fig. 4.4 we show XPS spectra for a sample as it was collected and after annealing in air at 400°C for 6 and 14 minutes. The figure shows the spectral region corresponding to the binding energy of Si 2p core electrons. The spectra for the as-collected and annealed samples present the characteristic peak of the unoxidized Si 2p core level at about 99 eV. The photoelectron peak corresponding to the oxidized Si 2p core level shifts from 102.2 eV to 102.8 eV and 102.9 eV as the sample is annealed for 6 and 14 minutes, respectively. The position of this peak correlates to the oxidation state of the Si atoms at the surface region of the nanocrystals. The observed shift corresponds to a trend in the oxide stoichiometry moving from a suboxide toward stoichiometric SiO_2. The changes in the relative intensities of the XPS peaks as the sample is annealed indicates the thickening of the oxide layer.

Based on the above TEM and XPS data, the particles generated by spark ablation may be regarded as nanometer-scale silicon crystallites surrounded by a substoichiometric oxide that evolves toward a stoichiometric oxide upon annealing. Thus, the crystalline nature of the particles has been confirmed, and the presence of oxide shells on the nanocrystals detected. However, in this study no attempt has been made to distinguish between crystallite size and crystallite-plus-oxide-shell size. Therefore, the term nanocrystal size should be understood as the "nanocrystal" size as resolved from low resolution TEM micrographs or aggregate particle size as determined by the RDMA mobility distribution measurement.

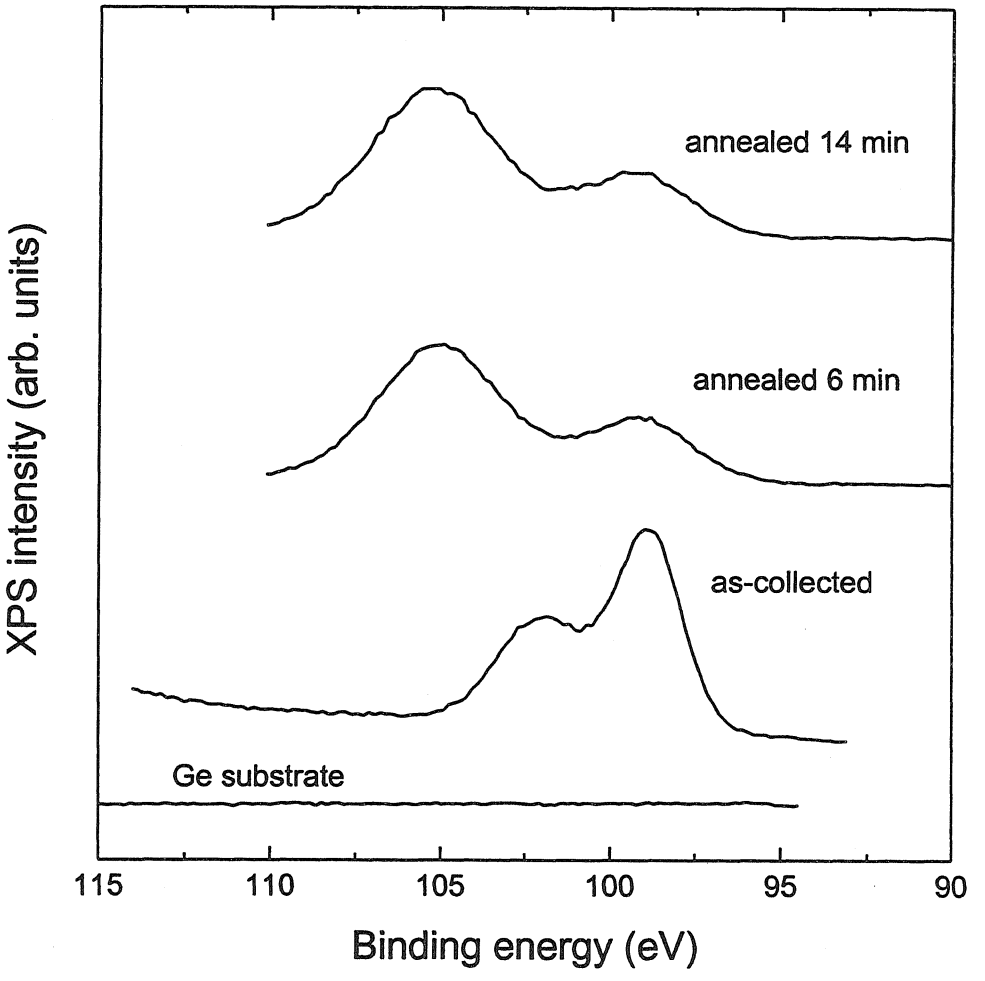

Figure 4.4: X-ray photoemission spectroscopy on silicon nanocrystals by spark ablation. Data obtained using monochromated Al $K\alpha$ radiation at 1487 eV with a resolution of $\sim$ 0.7 eV.

4.3.3 Mobility measurements on the spark ablation aerosol

In order to characterize the nanocrystal aerosol produced by the spark ablation source, we have performed differential mobility analysis measurements. For this purpose we turned off the collection device of Fig. 4.1 and deflected the whole aerosol flow into the concentration monitor. Operating in stepping mode, the RDMA voltage was varied between 1 V and 7,759 V, thereby probing sizes in the 1-100 nm range. The nanocrystal concentration was measured by a condensation nucleus counter and an electrometer at given sizes as determined from the voltage on the RDMA. In Fig. 4.5 we show plots of the size distribution with the spark source operated at 120 Hz and 1 kV, for two different values of spark current (4.1 mA and 40 mA). This data indicates broad, approximately log-normal size distributions with geometric standard deviation $\sigma_g \sim 1.6$. The mean diameter of the size distribution shifts from $\sim$ 6.5 nm to $\sim$ 20 nm as the spark current is increased from 4.1 to 40 mA. It is interesting to note that a change of only one order of magnitude in the spark current causes an increase of three orders of magnitude in the number concentration, lowering significantly the characteristic coagulation time. The change in the size distribution with spark current suggests the evolution of the aerosol is dominated by coagulation. The TEM micrograph of Fig. 4.3 shows this is indeed the case, indicating sizes of primary particles in the 1 - 10 nm range.

Figure 4.6 shows the influence of dilution on the nanocrystal size distribution. We notice that a dilution rate of 15:1 reduces coagulation. In this way, nanocrystal concentrations of $\sim 10^5$ cm^{-3} can be obtained down to $\sim$ 6 nm with a spark current

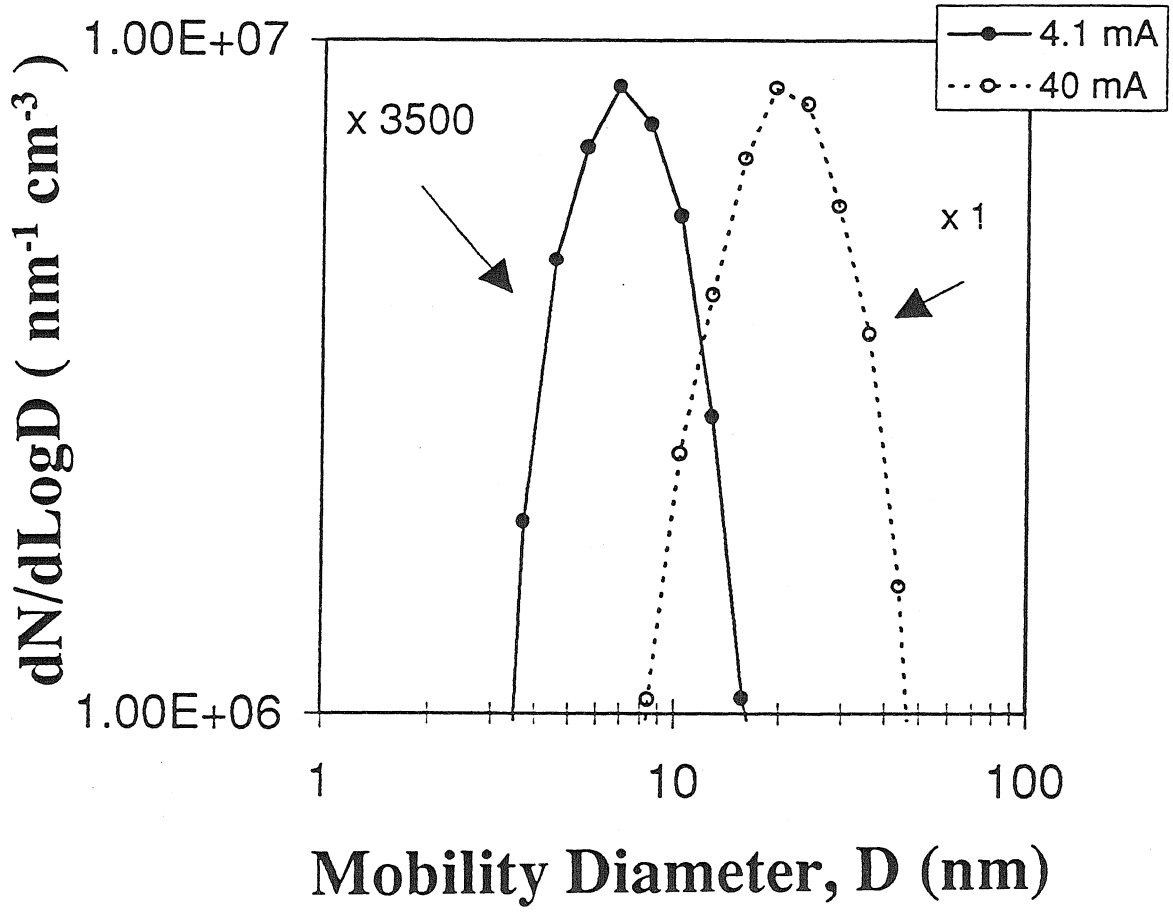

Figure 4.5: Effect of spark current on the size distribution of silicon nanocrystals by spark ablation. Source operated at 1 kV, 120 Hz, and 1 lpm flow rate. The radial differential mobility analyzer was operated with a sheath flow of 10 lpm and an aerosol flow of 1 lpm.

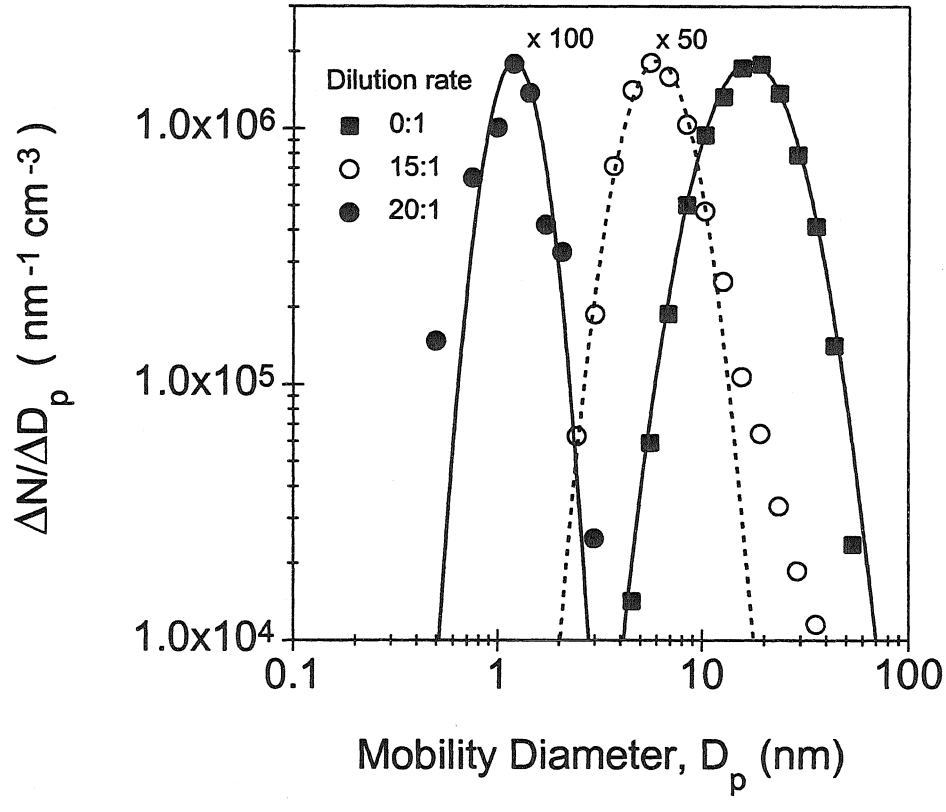

Figure 4.6: Effect of dilution rate on the size distribution of silicon nanocrystals by spark ablation. Source operated at 1 kV, 120 Hz, and 40 mA. The radial differential mobility analyzer was operated with a sheath flow of 10 lpm and an aerosol flow of 1 lpm.

of 40 mA. Although a 15:1 dilution rate significantly limits coagulation and the size distribution still looks approximately log-normal, but a non log-normal tail at the large size of the particle spectrum is observed. This may be due to non-uniform mixing at the dilution region. By increasing the dilution rate to 20:1 we have been able to take the mean diameter of the size distribution down to 1.3 nm with a 0.5 nm standard deviation. It must be said, however, that the exact nature of these 1 nm particles has not been determined. Nevertheless, this result establishes, at least qualitatively, the efficient transmission of the RDMA down to the 1 nm regime. Based on the resolution predicted for this instrument in this size regime (see Chapter 3), it can potentially be used to classify silicon nanocrystals smaller than 1 nm diameter, where changes in band structure are expected to be large.

The control of the nanocrystal size distribution presented in Fig. 4.6 indicates that dilution in the spark region significantly increases the number of unagglomerated nanocrystals below 10 nm. These more dilute samples were collected by hypersonic impaction and analyzed by TEM. Figure 4.7 presents a comparison between a sample generated with no dilution and one with relatively low dilution at the source ($\sim$ 5:1). Residence times of $\sim$ 10 s between synthesis and collection were used for these samples. Figures 4.7(a) and (b) show TEM micrographs for the samples without and with dilution respectively. Confirming the RDMA measurements, it is apparent that the availability of individual particle and small agglomerates is significantly increased due to dilution.

An alternative way to limit coagulation is by reducing the time between vapor

phase synthesis and collection. Some evaluations indicate that coagulation was virtually suppressed for residence times of $\sim$ 0.3 s, which is consistent with initial number concentrations below 10^{10} cm^{-3} (Fig. 3.3). In this case, TEM analysis shows the generation of a compact continuous deposit of nanometer-scale particles (Fig. 4.8). The disadvantage of this approach, from our perspective, is the limited time for processing. Differential mobility analysis using the present RDMA requires processing for several seconds, rendering dilution the only practical way of limiting coagulation. A DMA that is optimized for classification of high concentration aerosols might relax this constraint.

4.3.4 Generation of size-classified deposits of nanocrystals

To collect samples containing deposits of size-classified nanocrystals, the spark ablation source parameters were first adjusted to generate a high-concentration aerosol in the 1-10 nm size range. Typical source parameters that generate this condition are a 1 kV voltage, a 120 Hz frequency, a 40 mA spark current (R_2 = 10 kΩ), a 1 lpm aerosol flow rate, and a 5:1 dilution rate. After this initial tune-up of the aerosol, the RDMA voltage was then maintained at specific values. In Fig. 4.9 we present bright field and dark field TEM micrographs of a sample size classified for 10 nm and collected by electrostatic precipitation. The RDMA was operated with a sheath flow of 10 lpm and an aerosol flow of 1 lpm. Although a few larger particles are still present, size classification has been achieved, as the vast majority of the nanocrystals are of the expected size. A limited degree of agglomerate formation has occurred, though, which may be the result of precipitation due to field enhancement at edges

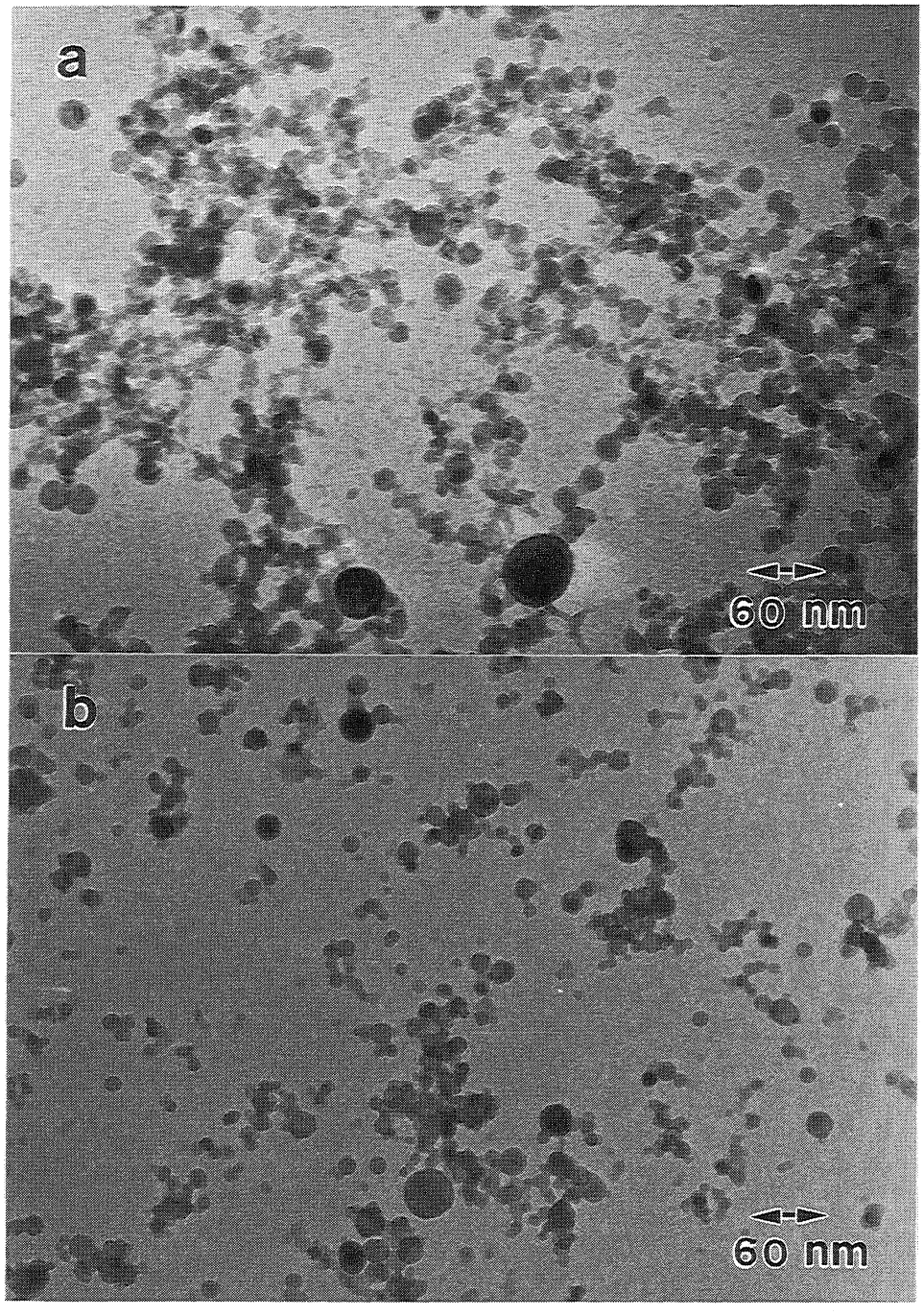

Figure 4.7: TEM micrograph of polydisperse samples generated with no dilution (a) and with a dilution rate of $\sim$ 5:1 (b).

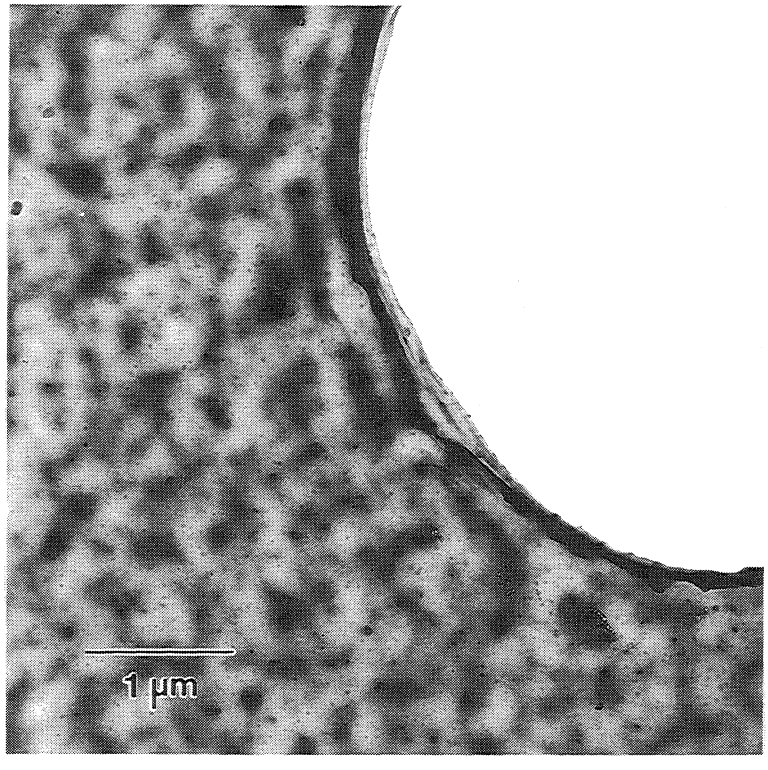

Figure 4.8: Transmission electron micrograph of a sample generated by hypersonic impaction with short residence time ($\sim$ 0.3 s) between synthesis and collection, showing the formation of a compact film of apparently uncoagulated particles.

rather than aerosol-phase coagulation. This mechanism for the formation of the agglomerates is suggested by the observed abundance of such particles at the edges of the substrate.

Classification for different sizes was achieved by changing the RDMA voltage. Figure 4.10 presents TEM micrographs from samples size classified for (a) 3.0 nm, (b) 5.0 nm, (c) 7.5 nm, and (d) 10 nm by RDMA voltages of 10.0 V, 24.5 V, 54.1 V and 111 V, respectively. To minimize particle loss, the sample size classified for 3.0 nm was collected by electrostatic precipitation on a substrate suitably inserted directly into the sampling port of the RDMA. The 5.0 nm sample was collected in a point-to-plane electrostatic precipitator [20] and the samples size classified for 7.5 nm and 10 nm were collected by hypersonic impaction. Nanocrystals are nonagglomerated and found in concentrations around 10^{11} nanocrystals/cm^2. Approximately spherical as well as irregularly shaped nanocrystals are observed. Size distributions obtained from the micrographs are shown in the insets. The horizontal axis in the insets corresponds to nanocrystal diameter. It begins at 0 and the distance between two adjacent ticks is 2.0 nm. The vertical axis indicates nanocrystal counts in arbitrary units. Gaussian fits to the size distribution data points yield mean diameters of 2.8 nm, 5.2 nm, 8.0 nm, and 11 nm in the samples classified for 3.0 nm, 5.0 nm, 7.5 nm and 10 nm, respectively. The nanocrystal diameters determined by TEM agree within the experimental error with the values predicted by the RDMA calibration.

Although the size distribution in Fig. 4.10(a) presents a well defined peak at 2.8 nm, a significant number of larger nanocrystals can be identified in the 5-9 nm

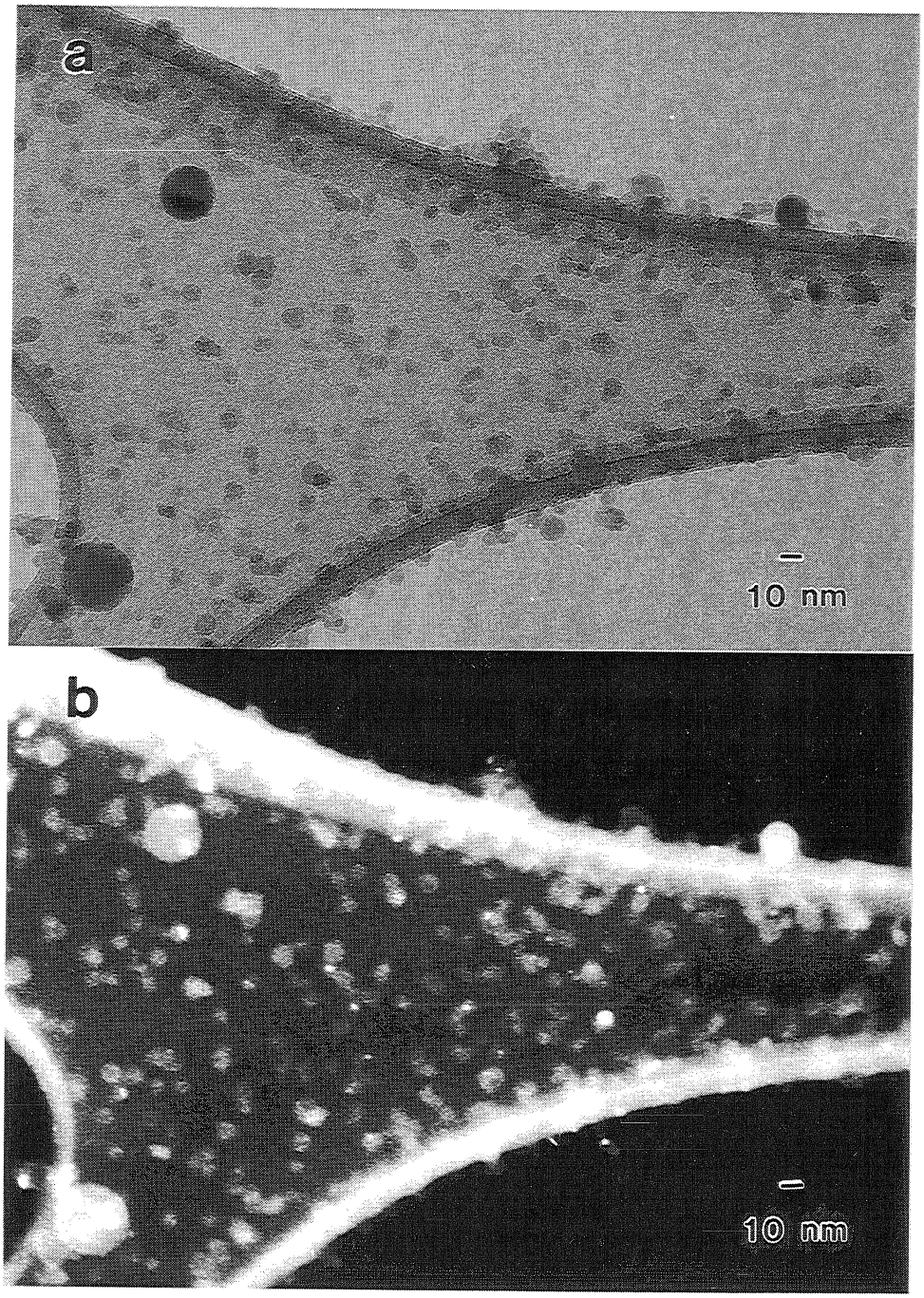

Figure 4.9: (a) Bright field and (b) dark field transmission electron micrographs of a sample size classified for 10 nm and collected by electrostatic precipitation. The RDMA was operated with a sheath flow of 10 lpm and an aerosol flow of 1 lpm.

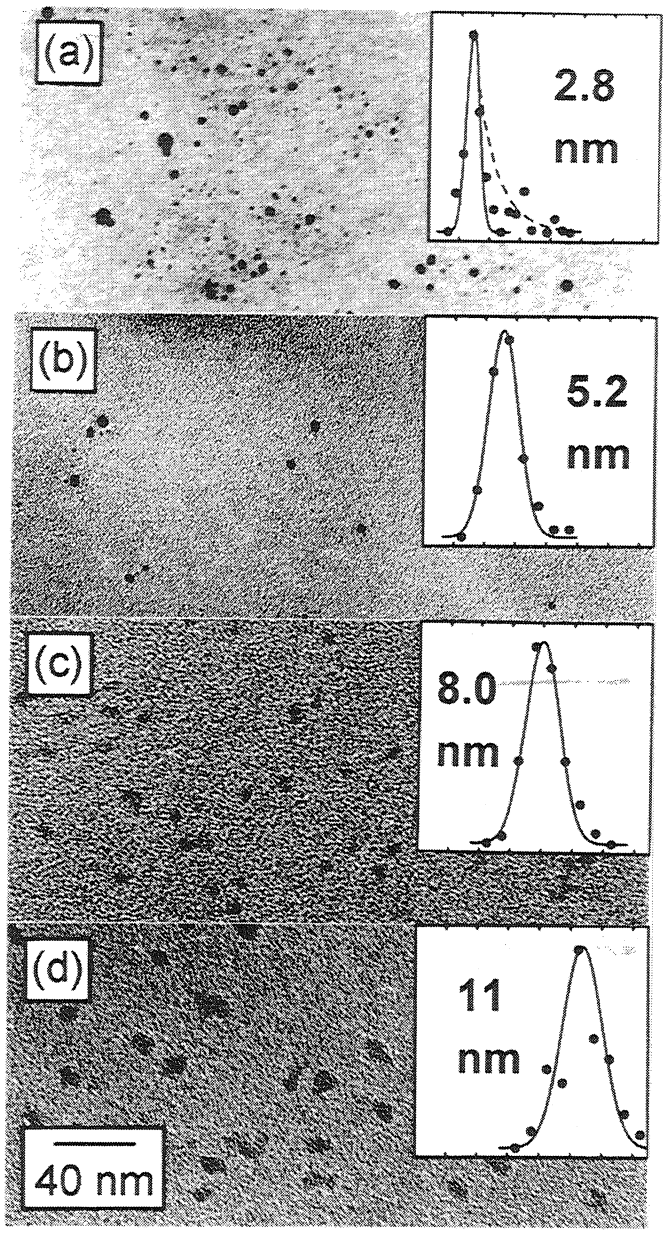

Figure 4.10: Bright-field transmission electron micrographs from four samples of silicon nanocrystals on amorphous carbon substrates. Size classification was aimed at (a) 3.0 nm (10.0 V at the size classifier), (b) 5.0 nm (24.5 V), (c) 7.5 nm (54.1 V), and (d) 10 nm (111 V).

range. This may have been caused by multiply charged crystallites that entered the RDMA as, for the particular experiment that led to this result, the aerosol neutralizer had been removed from the setup (Fig. 4.1) to reduce the nanocrystal loss at these small sizes. However, particles with more than one elementary charge are usually rare in this size regime. An additional problem with this interpretation is that the size of the larger particles is different than what would be expected from particles with double or triple charge (i.e., 4.6 and 5.9 nm respectively). As already mentioned, another unique characteristic of the sample size classified at 3.0 nm is the fact that electrostatic precipitation was done on a substrate inserted into the sampling port of the RDMA. Consequently, larger particles may have been collected due to flow field distortions resulting from the slightly unbalanced operation of the RDMA. In any case, this slight degradation of the size distribution is not observed to occur when the neutralizer and a collection device external to the RDMA are used.

Figure 4.11 compares size distributions before and after classification. The size distributions before classification shown in Fig. 4.11(a) are those that were presented in Fig. 4.6. In Fig. 4.11(b) Gaussian fits to size distribution data points obtained from the TEM results in Fig. 4.10 are presented. Classified nanocrystals show size distributions with $\sigma_g \sim$ 1.2-1.3. By size classification we have achieved control over mean nanocrystal size within 15-20% down to a median diameter of 2.8 nm. Figure 4.11(b) reveals that the size distribution broadens as larger nanocrystals are classified. All size distributions have, however, approximately the same σ_g, indicating consistent operation of the RDMA.

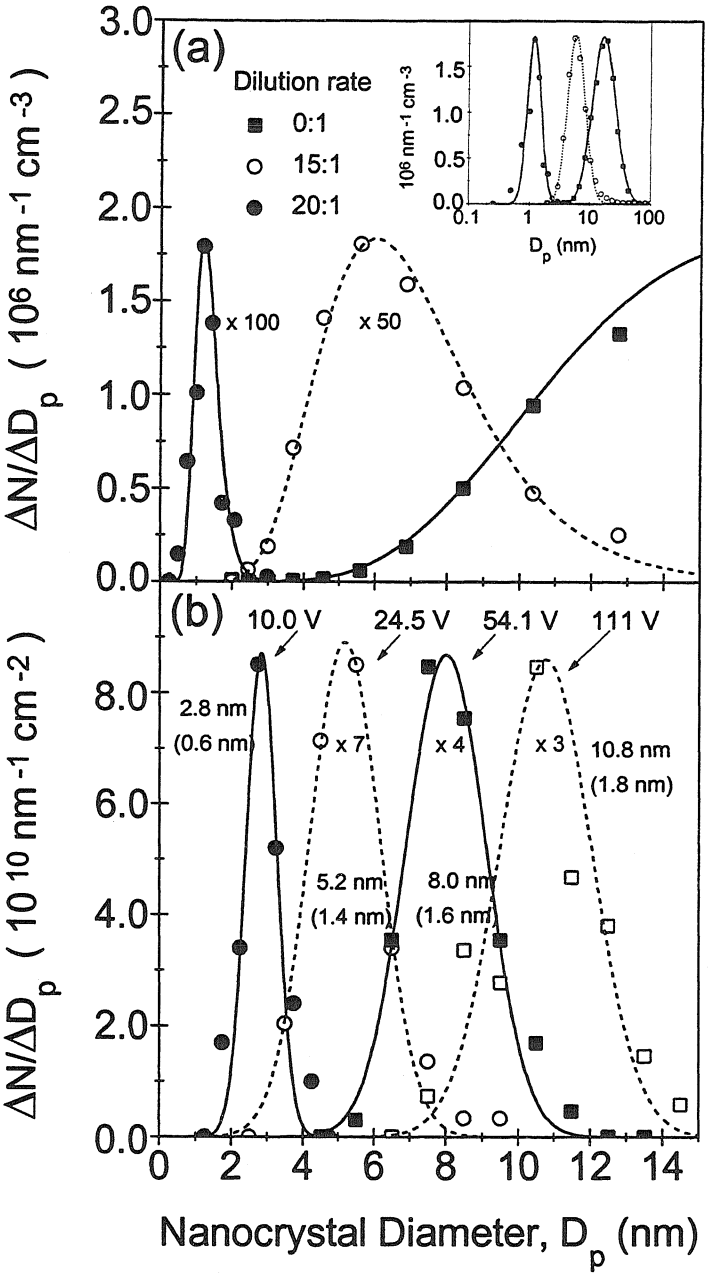

Figure 4.11: (a) Nanocrystal size distributions prior to size classification, generated using the size classifier as a spectrometer ($\sigma_g \sim$ 1.4-1.6), and (b) after size classification, by Gaussian fits to transmission electron microscopy results of Fig. 4.10 ($\sigma_g \sim$ 1.2-1.3). Mean diameter, standard deviation (in parentheses), and classifier voltage are shown. Only the well defined peak at 2.8 nm shown in the inset of Fig. 4.10(a) is reproduced here.

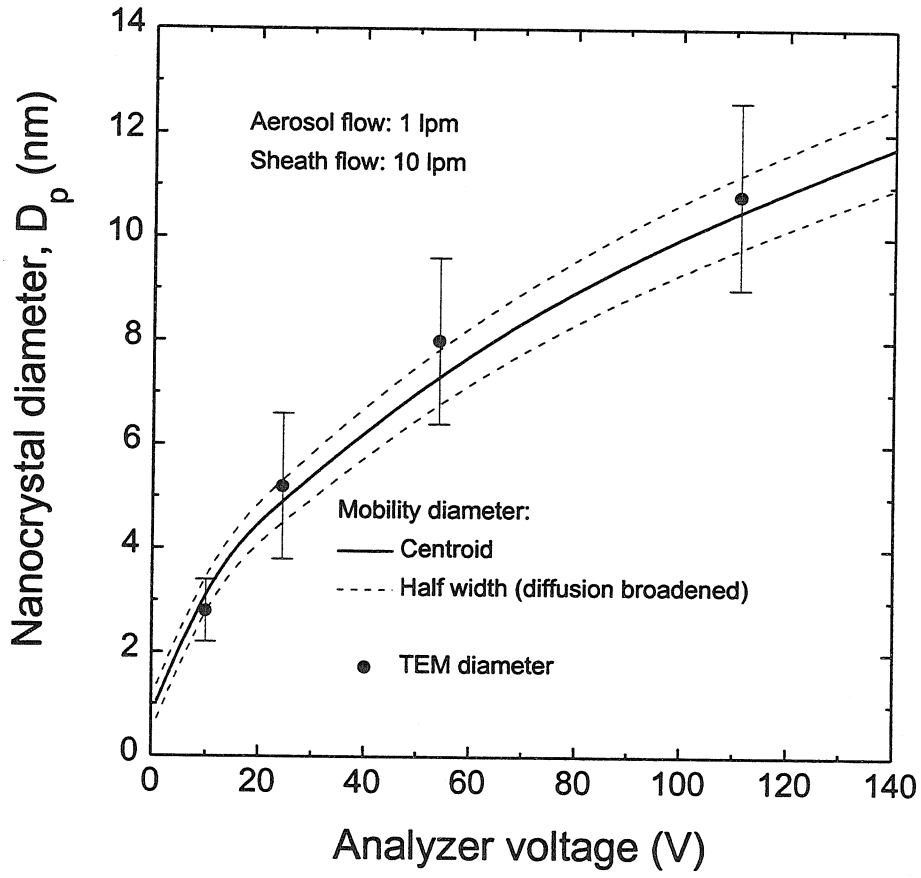

Figure 4.12: Comparison between nanocrystal diameters measured by transmission electron microscopy on collected samples and mobility diameter predicted by the radial differential mobility analyzer calibration.

Although Fig. 4.11 demonstrates that size classification has been achieved in the 3-10 nm size range, it is important to verify how close to the resolution limit of the radial differential mobility analyzer the experiment was carried out. Figure 4.12 compares the observed performance of the size classification with the width of the transfer function based on Zhang and Flagan's measurements of the RDMA resolution [21]. A linear interpolation of their data was used to estimate the width of the transfer function for our flow conditions. The comparison reveals that there is still room for improvement of size classification using the RDMA. The broadening observed with respect to the performance previously measured by Zhang and Flagan [21] is probably due to the RDMA operation over extended periods of time plus flow fluctuations. Although efforts were made to keep flow rates as constant as possible, the system was not automated for feedback control of the flow rates which, when uncorrected, were observed to drift by as much as 15% over extended periods of time. Supporting evidence for this explanation is in the fact that the sample size classified for 3.0 nm was collected for about half as long as the other samples and it shows broadening closer to the width of the transfer function. The full automation of the flow control system should improve size resolution of the nanocrystal deposits. In addition the operation at higher aerosol concentrations should allow sample generation over shorter periods of time, further reducing the broadening of the size distributions.

4.3.5 Structural characterization of size-classified nanocrystals

The synthesis of deposits of size-classified nanocrystals requires that the spark source be operated at conditions significantly different from those used to generate the poly-

disperse deposits of Fig. 4.3. Lower spark currents and higher dilution rates could in principle contribute to structural changes in the nanoparticles. Both of these changes lead to much less vaporized material than in the case of polydisperse samples. As a result, the ratio of silicon atoms to impurity molecules (e.g., O_2, H_2O, hydrocarbons) is expected to be lower. This could lead to particle formation in an oxidizing environment resulting in amorphous SiO_x particles. In order to ensure that even after size classification we are still dealing with silicon nanocrystals, a structural characterization of size selected samples was made by high resolution transmission electron microscopy (HRTEM) and electron diffraction.

Figure 4.13 shows a HRTEM micrograph with a close look at a few nanocrystals from a deposit size classified for 10 nm. The nanocrystals lie on an amorphous carbon substrate. The most prominent nanocrystals are $\sim$ 6 nm and $\sim$ 10 nm in diameter. A layer of 1-3 nm of amorphous material surrounds the nanocrystals. This observation is consistent with XPS measurements on other size-classified samples that indicate the presence of an SiO_x layer on the surface of the nanocrystals.

Although electron diffraction measurements on size-classified samples are challenging due to the small amount of material, the diffraction data obtained clearly establishes the crystallinity of the particles. In Fig. 4.14 a series of micrographs taken from a sample size classified for 10 nm and collected by electrostatic precipitation illustrates the point. Figure 4.14(a) and (b) present a bright field/dark field pair of images from nanocrystals that landed on a continuous region of the amorphous carbon substrate. In this case, high quality diffraction patterns are very difficult to

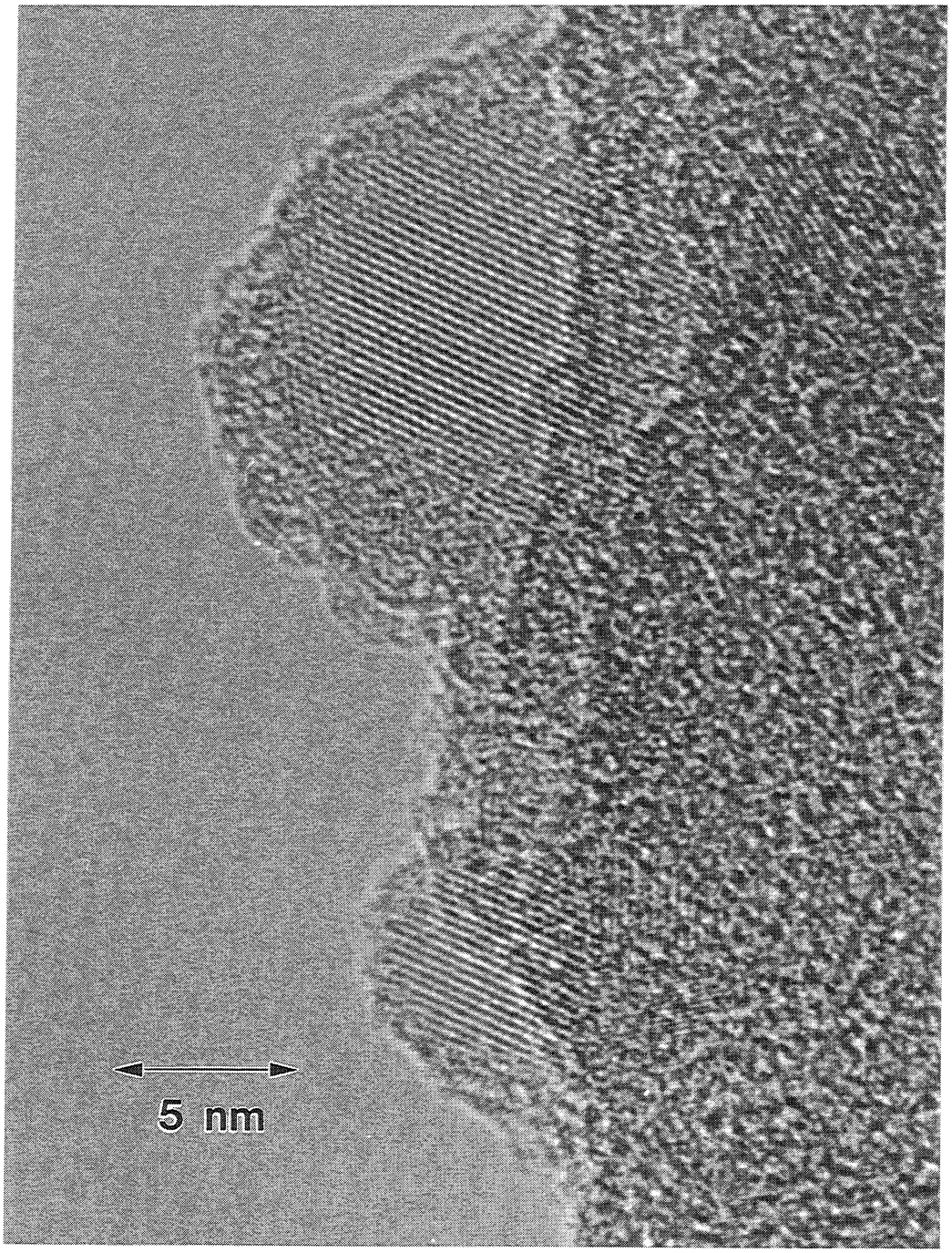

Figure 4.13: High resolution transmission electron microscopy on size-classified silicon nanocrystals.

obtain due to scattering by the substrate. In Fig. 4.14(c), however, particles are found to be more concentrated in a narrow region of the substrate between two holes. In addition, relatively less substrate material is found in this region reducing diffuse scattering in electron diffraction. This region selected in Fig. 4.14(c) yields a crystalline diffraction pattern (Fig. 4.14(d)).

As demonstrated in this and previous sections, spark ablation is a useful technique in the generation of Si nanocrystals. Limitations in the stability of the spark ablation source exist, however, due to the coupling of the electric discharge with the gas flow. As the flow rate is increased to control coagulation, the characteristics of the plasma in the spark discharge region change dramatically, leading to unexpected transitions into different modes of operation. As the spark itself is responsible for vaporization of the material, a delicate balance of conditions is required to maintain steady operation. As the electrodes age, the character of the spark discharge also changes, leading to further modifications in the efficiency of particle generation, resulting in large uncontrollable variations in size distribution. These problems led us to consider other vapor-phase techniques as alternative sources for the Si aerosol. In the next sections we present results in the nanocrystal synthesis using laser ablation and thermal evaporation.

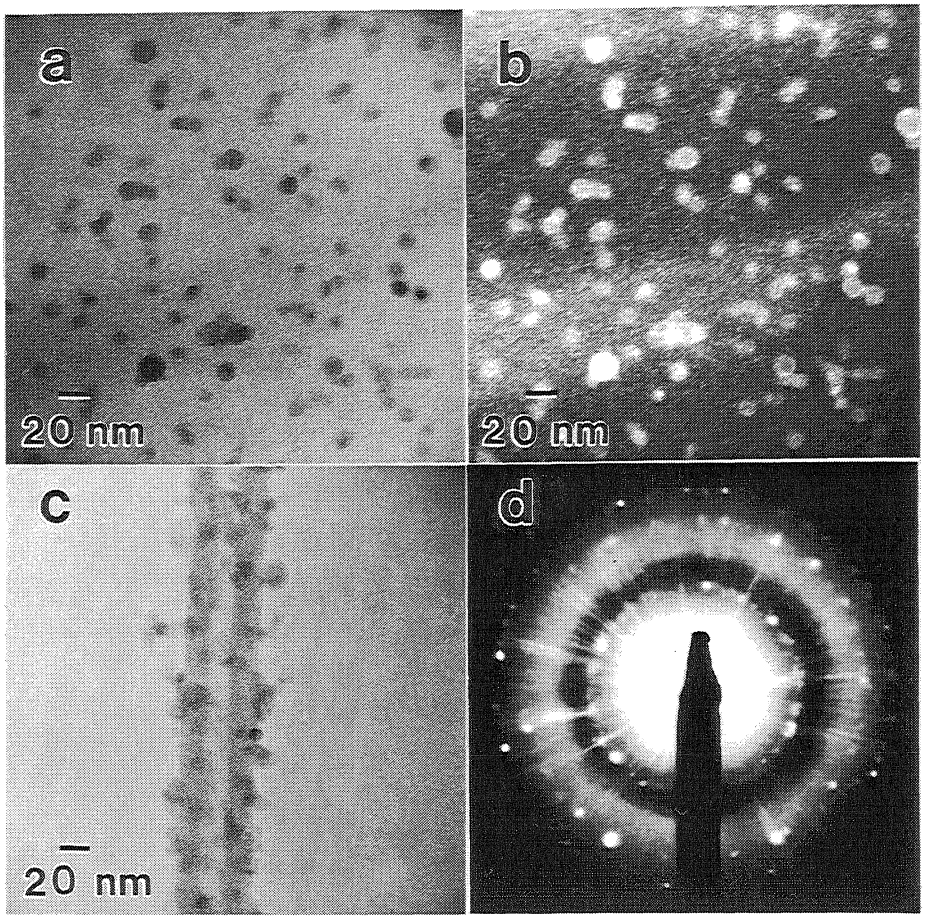

Figure 4.14: (a) Bright field and (b) dark field images of size-classified silicon nanocrystals that landed on a continuous region of the carbon substrate. (c) Bright field image of the same sample from a narrow area of the substrate between two holes that yield the selected area diffraction pattern (d).

4.4 Silicon nanocrystals by laser ablation

4.4.1 The laser ablation nanocrystal source

Synthesis of silicon nanocrystals by laser ablation in background inert gases has been widely reported [12, 13]. The combination of laser ablation with aerosol technology to further manipulate the morphology of the semiconductor nanocrystals is, however, an unexplored research area.

Laser ablation as a means to generate aerosols, in general, has received some attention recently [14], and it is interesting to point out some inherent advantages of this technique if compared with the spark ablation method. First, due the fact that the energy source is located outside the vaporization chamber, it is decoupled from the gas flow. The amount of vaporized material is less dependent on target erosion and flow variations, which makes laser ablation a more reproducible means for the synthesis of nanocrystals.

Another advantage of using laser ablation is the fact that the region from which material is evaporated can be precisely controlled, decreasing the risk of contamination. In contrast, in the spark ablation technique sparks may occasionally hit metal parts and cause undesired vaporization of other species.

A schematic of the laser ablation source designed for this work is presented in Fig. 4.15. A pulsed KrF excimer laser provides the energy for silicon vaporization. It is focused by an antireflective coated lens with 20 mm focal distance. The 248 nm laser beam is introduced into the ablation chamber through a saphire window. The target is a 1/4 inch diameter Si rod. It is supported by a manipulator with manual

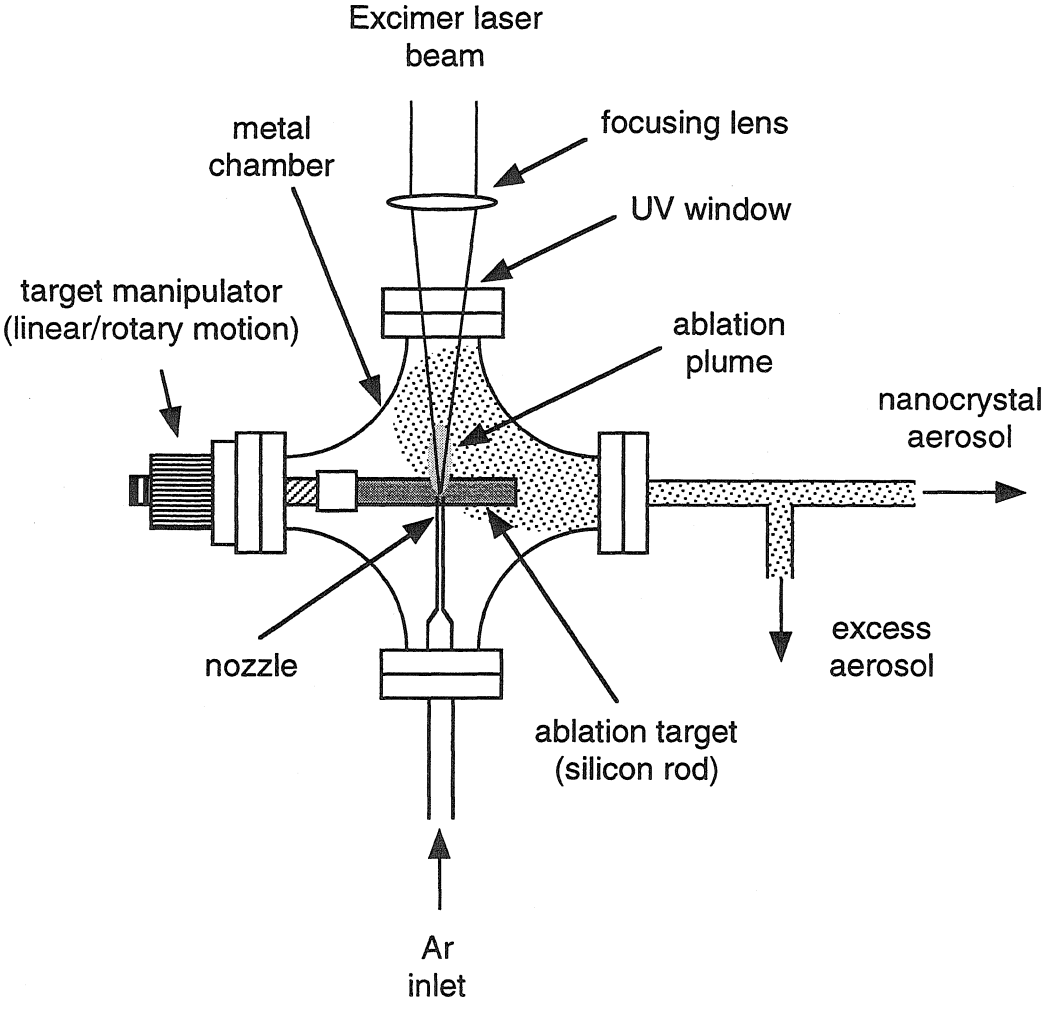

Figure 4.15: Schematic of the laser ablation source of silicon nanocrystals.

linear and rotary motion, allowing the ablation spot to be refreshed when necessary. Automatic rotation of the target was found to contribute to instabilities in the aerosol concentration and therefore static operation was chosen as the norm. A 1 mm nozzle takes the inert gas flow directly to the ablation spot so that dilution can be performed at the ablation plume.

4.4.2 Polydisperse silicon nanocrystals

In order to know the general morphology of the aerosol generated by the laser ablation source, polydisperse samples were collected once again using a simplified version of the experimental setup of Fig. 4.1. Bypassing the neutralizer and the RDMA, the laser ablation aerosol was deflected directly into the electrostatic precipitator. The source was operated at a repetition rate of 20 Hz and the sample collected for 30 minutes with an argon flow rate of 1.5 lpm. Transmission electron micrographs of the deposits generated are shown in Fig. 4.16. Figure 4.16(a) and (b) show low magnification TEM images that allow a large field of view. An inspection of this figure reveals a distinguishing feature of samples generated by laser ablation, i.e., the presence of compact, micron-sized, approximately spherical particles along with agglomerates of nanometer-scale ones. The size and shape of the micron-sized particles seen in Fig. 4.16(b) indicate that they are not formed by the same process from which the nanometer-scale particles originate. As discussed in chapter 3, the nanometer-scale primary particles are formed by nucleation from the vapor phase followed by coalescent coagulation. As the carrier gas cools, these particles no longer coalesce upon coagulation, but give rise to the large aggregates observed in Fig. 4.16(c).

These large aggregates could, in principle, sinter into the compact particles, but the temperatures and residence times required for that are not available in our synthesis process. The presence of micron-sized particulates has been a challenging problem in the synthesis of thin films by pulsed laser deposition [22]. Among the mechanisms that have been suggested for the generation of these large particles, we mention *exfoliational sputtering* and *hydrodynamic sputtering* as the possible formation routes for micron-sized particles in our experiment. *Exfoliational sputtering* refers to the detachment of flakes from the target due to repeated thermal shocks, and *hydrodynamic sputtering* are processes in which droplets of material are formed and expelled from the target as a result of transient melting [23]. A number of variables (e.g., laser wavelength, laser fluence, ambient gas pressure, target surface roughness) have been shown to impact the size and concentration of these particulates. Approaches to limit the number of these large particles involve working at lower laser fluences, introducing mechanical filters, using liquid targets, and employing impactors in the hydrodynamic region of the plume.

Away from the micron-sized particles, Fig. 4.16(c) reveals the abundance of nanometer-scale particles formed from the vapor phase. Selected area electron diffraction on the nanometer-scale particles of Fig. 4.16(c) yields a crystalline pattern indicating that the particles are crystalline with bulk-like diamond cubic crystal structure.

4.4.3 Mobility measurements on the laser ablation aerosol

Mobility measurements on the laser ablation aerosol were performed using the setup of Fig. 4.1 in the same way previously described for the spark ablation aerosol. As-

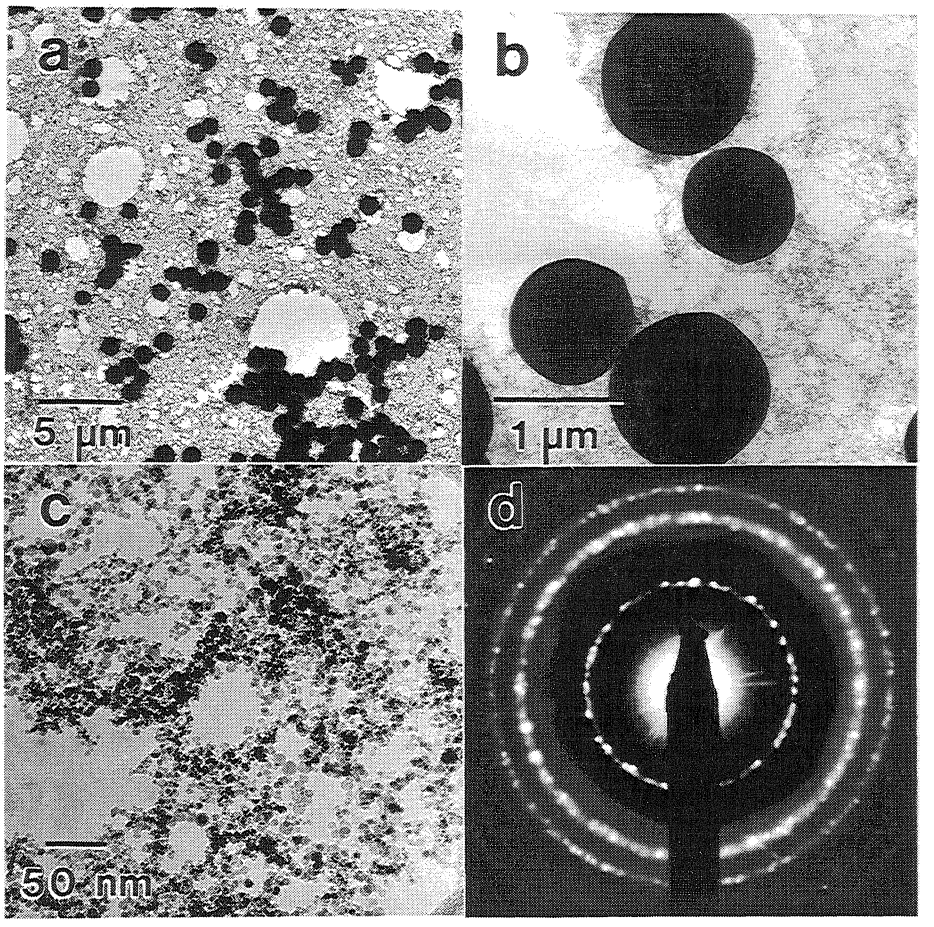

Figure 4.16: Bright-field transmission electron micrographs from a sample of silicon nanocrystals by laser ablation, showing micron-sized particles at low magnification ((a) and (b)) and only agglomerates of nanometer-scale particles at high magnification away from the large particles (c). In (d), a selected area diffraction pattern generated from nanometer-scale particles is shown. The substrate is an amorphous carbon film, and the collection was done by electrostatic precipitation.

measured size distributions are shown in Fig. 4.17. In this case, the purpose was not to measure the size distribution that characterizes the laser ablation aerosol, but to determine the actual concentration of nanocrystals available to generate size-classified deposits. Thus, the data presented in Fig. 4.17 is neither corrected for the charging efficiency of the neutralizer nor deconvoluted from the RDMA transfer function. The figure also shows the size distribution of the micron-sized particles as estimated from their concentration on the TEM images of Fig. 4.16. They present a remarkably sharp size distribution with geometric standard deviation much smaller than for the nanometer-scale particles, confirming their distinct formation mechanisms. The presence of the micron-sized particles is undoubtedly the cause for the low nanocrystal concentrations produced by the laser ablation technique (one order of magnitude lower than in the case of spark ablation). As discussed in section 3.2, the coagulation coefficient increases by orders of magnitude when particles of very different sizes are found in the same aerosol population. As a result, small particles are scavenged by the large ones, and the number concentration of nanocrystals in the nanometer size range drops significantly. Even in this situation, dilution helps to increase the number of particles below 10 nm. An increase in the dilution rate from 2:1 to 4:1 is found to shift the mean particle diameter from $\sim$ 25 nm down to $\sim$ 15 nm.

4.4.4 Generation of size-classified deposits of nanocrystals

The benefit of size classification using the RDMA is seen once again with the use of the laser ablation source. Total removal of micron-sized particles is achieved and deposits of nearly monodisperse silicon nanocrystals are obtained. An example of

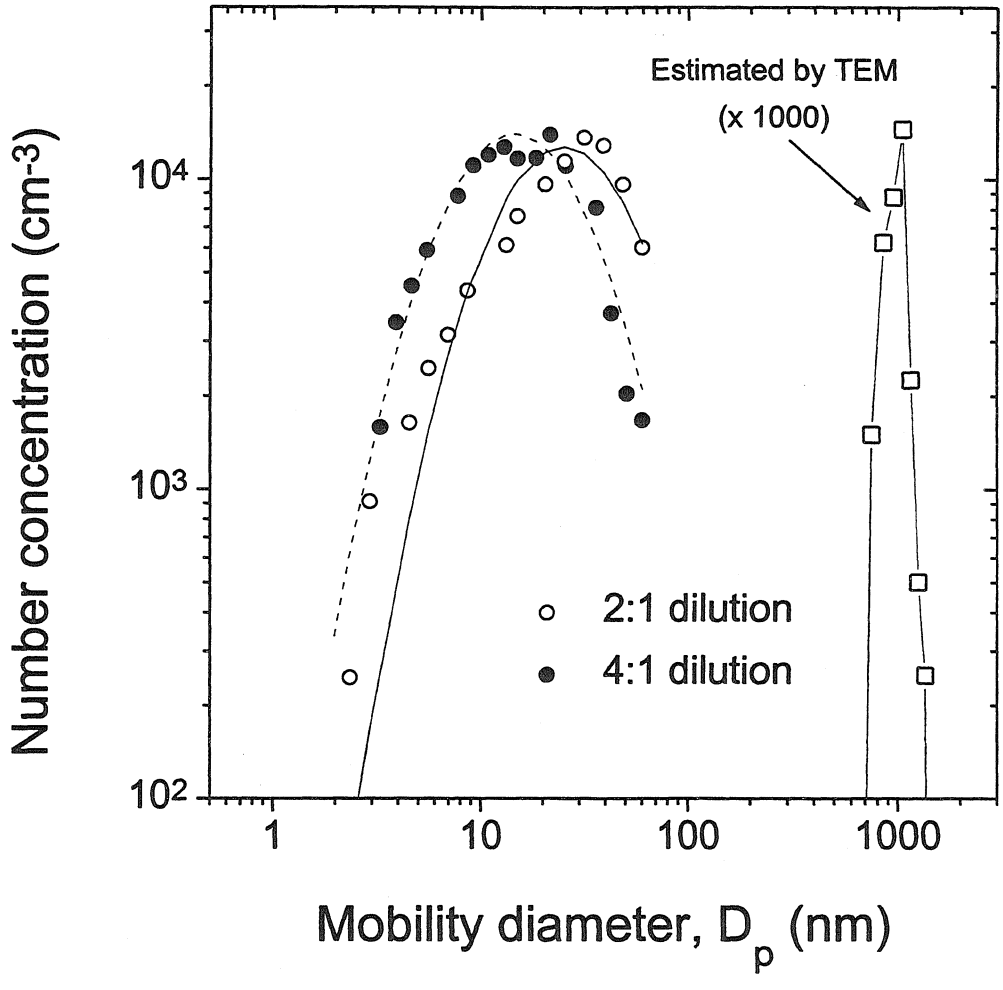

Figure 4.17: As-measured size distribution of silicon nanocrystals by laser ablation composed from data obtained by the radial differential mobility analyzer (1-100 nm range) and by transmission electron microscopy (0.8-1.2 μm).

a such deposit is shown in Fig. 4.18. A striking feature noticed in this figure is that the nanocrystals are much more irregular in shape than the ones that were size classified after spark ablation. This may result from the high cooling rates in the laser ablation source, which limit the time during which coalescent coagulation can occur. It appears that even 10 nm particles do not coalesce completely upon coagulation when this laser ablation source is used.

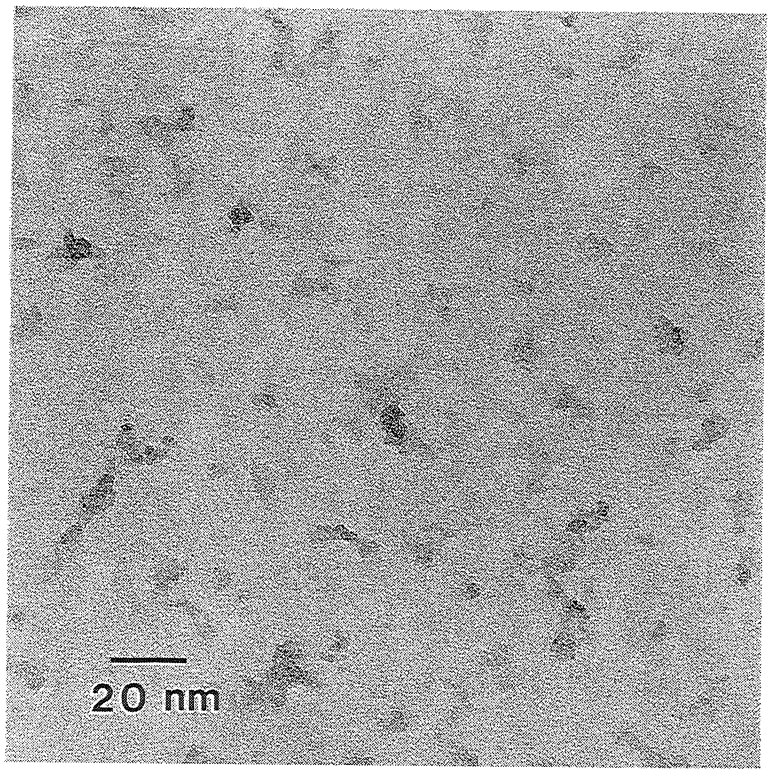

Figure 4.18: Bright-field transmission electron micrograph from a sample of silicon nanocrystals by laser ablation, showing nearly monodisperse particles from the viewpoint of mobility diameter, but largely polydisperse in shape probably owing to fast cooling rates in the laser ablation source. The substrate is an amorphous carbon film, and the collection was done by electrostatic precipitation.

4.5 Silicon nanocrystals by thermal evaporation

4.5.1 The thermal evaporation nanocrystal source

Thermal evaporation leading to gas-condensation has been used for decades to generate nanoscale aerosols. Recently, Si nanocrystals by thermal evaporation exhibiting visible photoluminescence have also been synthesized [15]. Reproducibility problems encountered with the spark ablation technique and particles with large deviations from sphericity in the laser ablation method have led us to consider thermal evaporation as a third alternative for silicon nanocrystal production. Its simplicity is apparent from the schematic presented in Fig. 4.19. A 30-70 ampere electric current is run through a thin, custom-made graphite crucible supported by water cooled copper electrodes. The crucible design is such that high temperatures are achieved only at the expected location of the melt. In this way the temperatures experienced by the copper electrodes are at low enough that copper vaporization is negligible. Only at the central region of the crucible enough resistive heating is provided to reach temperatures in excess of 1600°C. The crucible temperature was measured using a disappearing filament optical pyrometer. A Si wafer suspended from a linear motion manipulator brings material into the hot surface of the crucible allowing melting to occur. A 1/4 inch nozzle takes the inert gas flow directly to crucible region so that dilution can be performed close to where initial coagulation occurs. Temperatures at the chamber walls reach $\sim$ 300°C and therefore a bake-out procedure is required before synthesis of nanocrystals. For this purpose a turbomolecular pump was connected to the evaporation chamber through a valve. Before nanocrystal synthesis,

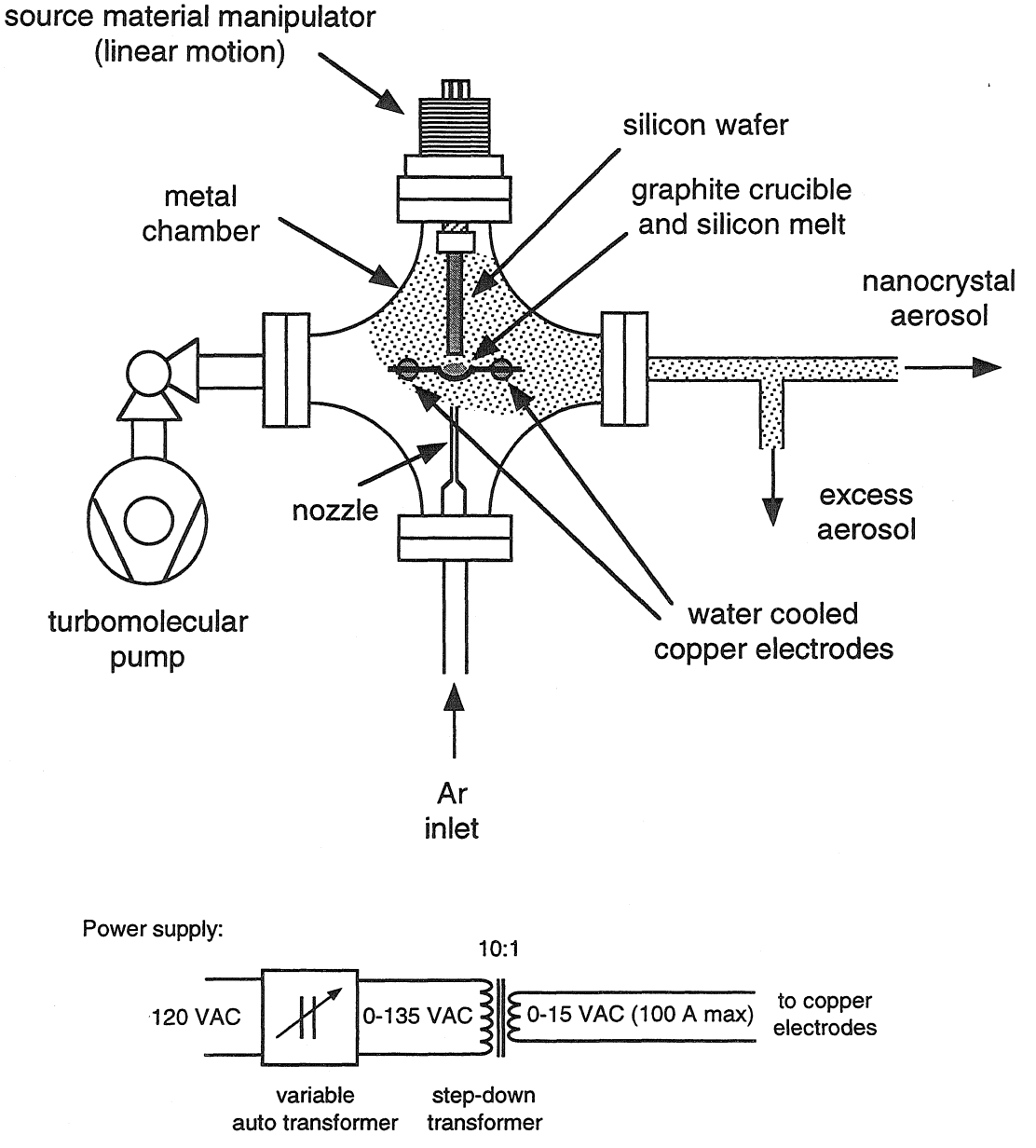

Figure 4.19: Schematic of the thermal evaporation source of silicon nanocrystals.

the system is routinely outgassed at normal operation conditions for about 12 hours.

4.5.2 Mobility measurements on the thermal evaporation aerosol

Mobility measurements on the thermal evaporation silicon aerosol were performed in the way previously described for the spark ablation and laser ablation aerosols (Fig. 4.1). As-measured size distributions are shown in Fig. 4.20 for a crucible temperature of $\sim 1500°C$. Number concentrations using the thermal evaporation source are higher by as much as a factor of 50 than those produced with the laser ablation source and by a factor of 5 than those generated with the spark ablation aerosol. An additional attractive feature of this source is its stability, which is desirable for consistent size classification. As long as enough Si exists in the crucible, dilution can tune the size distribution into the sub-10 nm size range up to the coagulation limits imposed by the system residence time and charging efficiency. A dilution rate of, for example, 7:1 is found to shift the mean of the size distribution from $\sim$ 45 nm down to $\sim$ 20 nm.

4.5.3 Generation of size-classified deposits of nanocrystals

Electron diffraction of size-classified deposits generated using thermal evaporation synthesis (Fig. 4.21(c)) shows crystalline particles. The particle shapes observed in Fig. 4.21(a) and (b) are much closer to spherical than resulted from laser ablation. In addition, XPS measurements on polydisperse and monodisperse samples show no above-normal carbon contamination (possibly from the graphite crucible) and no measurable copper that might have been introduced unintentionally due to electrode heating. Collection times are reduced with this source since higher concentrations

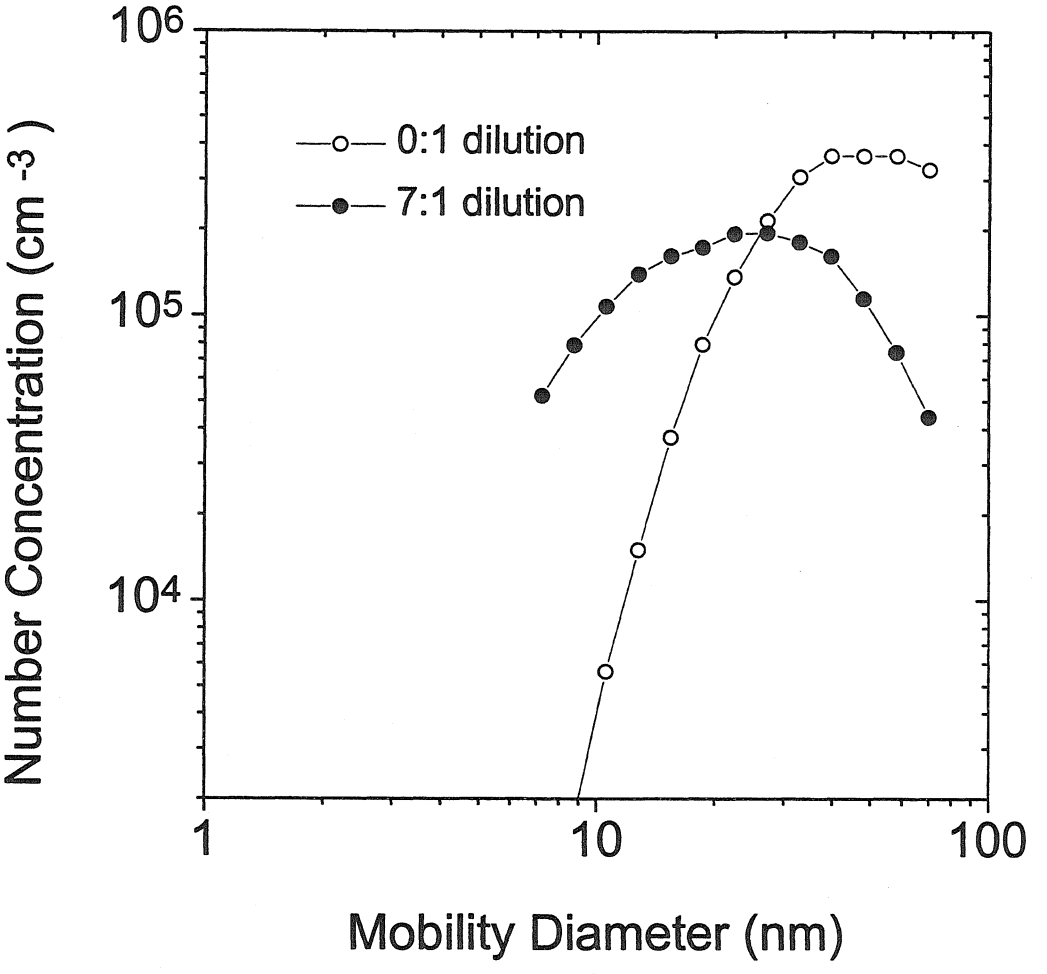

Figure 4.20: As-measured size distribution of silicon nanocrystals by thermal evaporation showing the above 10^5 cm^{-3} concentrations achievable and the control of coagulation by dilution. Radial differential mobility analyzer operated with a sheath flow of 15 lpm and an aerosol flow of 1.5 lpm.

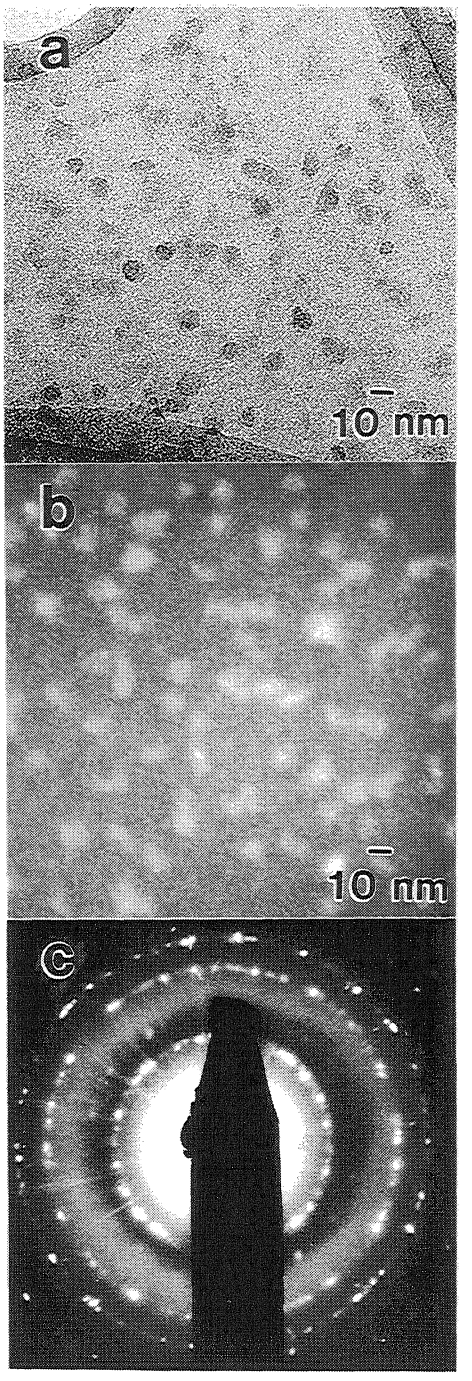

Figure 4.21: (a) Bright-field and (b) dark field transmission electron micrographs from a sample of silicon nanocrystals by thermal evaporation, showing nearly monodisperse particles. (c) Selected area diffraction pattern of the same area. The substrate is an amorphous carbon film, and the collection was done by electrostatic precipitation.

have been demonstrated.

4.6 Discussion and comparisons

In conclusion, we have demonstrated the synthesis of samples of nonagglomerated, size-classified silicon nanocrystals in the 2-10 nm size regime. Classified nanocrystal samples were produced by processing a polydisperse aerosol through a radial differential mobility analyzer. The resulting deposits of size-classified crystallites may be used in electronic structure characterization experiments and help clarify the luminescence behavior in silicon nanocrystals.

The procedure for size classification initially demonstrated for an aerosol generated by spark ablation is applicable to ultrafine particles generated by other vapor phase methods. Its application to nanocrystal aerosols by pulsed laser ablation and thermal evaporation is also demonstrated. These techniques are combined with differential mobility size classification to improve size control of nanocrystal samples.

From the point of view of size classification, the three sources showed comparable performances. In terms of stability of the resulting aerosol, however, thermal evaporation is superior. It does not present the unexpected variations observed with spark ablation, and the generated aerosol is free from the large particles characteristic of laser ablation. In the configuration used size-classified nanocrystals by laser ablation show large deviations from spherical shape, probably due to faster cooling rates if compared to the other techniques.

Bibliography

[1] L. T. Canham, "Silicon quantum wire array fabrication by electrochemical and chemical dissolution of wafers," *Appl. Phys. Lett.*, vol. 57, pp. 1046–1048, 1990.

[2] Y. Maeda, N. Tsukamoto, Y. Yazawa, Y. Kanemitsu, and Y. Matsumoto, "Visible photoluminescence of Ge microcrystals embedded in SiO_2 glassy matrices," *Appl. Phys. Lett.*, vol. 59, pp. 3168–3170, 1991.

[3] H. A. Atwater, K. V. Shcheglov, S. S. Wong, K. J. Vahala, R. C. Flagan, M. L. Brongersma, and A. Polman, "Ion beam synthesis of luminescent Si and Ge nanocrystals in a silicon dioxide matrix," *Mat. Res. Soc. Symp. Proc.*, vol. 316, pp. 409–420, 1994.

[4] W. L. Wilson, P. F. Szajowski, and L. E. Brus, "Quantum confinement in size-selected, surface-oxidized silicon nanocrystals," *Science*, vol. 262, pp. 1242–1244, 1993.

[5] S. Schuppler, S. L. Friedman, and M. A. Marcus, "Size, shape, and composition of luminescent species in oxidized Si nanocrystals and H-passivated porous Si," *Phys. Rev. B*, vol. 52, pp. 4910–4925, 1995.

[6] W. E. Carlos and S. M. Prokes, "Oxygen-associated defects near Si-SiO_2 interfaces in porous Si and their role in photoluminescence," *J. Vac. Sci. Technol.*, vol. 13, pp. 1653–1656, 1995.

[7] T. Takagahara and K. Takeda, "Theory of the quantum confinement effect on excitons in quantum dots of indirect-gap materials," *Phys. Rev. B*, vol. 46, pp. 15578–15581, 1992.

[8] B. Delley and E. F. Steigmeier, "Quantum confinement in Si nanocrystals," *Phys. Rev. B*, vol. 47, pp. 1397–1400, 1993.

[9] C. B. Murray, D. J. Norris, and M. G. Bawendi, "Synthesis and characterization of nearly monodisperse CdE (E = S, Se, Te) semiconductor nanocrystallites," *J. Am. Chem. Soc.*, vol. 115, pp. 8706–8715, 1993.

[10] S. Schwyn, E. Garwin, and A. Schmidt-Ott, "Aerosol generation by spark discharge," *J. Aerosol Sci.*, vol. 19, pp. 639–642, 1988.

[11] W. A. Saunders, P. C. Sercel, R. B. Lee, H. A. Atwater, K. J. Vahala, R. C. Flagan, and E. J. Escorcia-Aparcio, "Synthesis of luminescent silicon clusters by spark ablation," *Appl. Phys. Lett.*, vol. 63, pp. 1549–1551, 1993.

[12] E. Werwa, A. A. Seraphin, L. A. Chiu, C. X. Zhou, and K. D. Kolenbrander, "Synthesis and processing of silicon nanocrystallites using a pulsed-laser ablation supersonic expansion method," *Appl. Phys. Lett.*, vol. 64, pp. 1821–1823, 1994.

[13] T. Yoshida, S. Takeyama, Y. Yamada, and K. Mutoh, "Nanometer-sized silicon crystallites prepared by excimer laser ablation in constant pressure inert gas," *Appl. Phys. Lett.*, vol. 68, pp. 1772–1774, 1996.

[14] D. Boulaud, "Aerosol production by laser ablation," *Synthesis and measurement of ultrafine particles*, ed. J. C. M. Marijnissen and S. Pratsinis, Delft University Press, Delft, 1993, pp. 31–40.

[15] L. N. Dinh, L. L. Chase, M. Balooch, W. J. Siekhaus, and F. Wooten, "Optical properties of passivated Si nanocrystals and SiO_x nanostructures," *Phys. Rev. B*, vol. 54, pp. 5029–5037, 1996.

[16] A. Wiendensohler, "An approximation of the bipolar charge distribution for particles in the submicron size range," *J. Aerosol Sci.*, vol. 19, pp. 387–389, 1988.

[17] S. -H. Zhang, Y. Akutsu, L. M. Russell, R. C. Flagan, and J. H. Seinfeld "Radial Differential Mobility Analyzer," *Aerosol Sci. Technol.*, vol. 23, pp. 357–372, 1995.

[18] J. Kesten, A. Reineking, and J. Porstendorfer, "Calibration of a TSI-model-3025 ultrafine condensation particle counter," *Aerosol Sci. Technol.*, vol. 15, pp. 107–111, 1991.

[19] J. Fernandez de la Mora, S. V. Hering, N. Rao, and P. H. McMurry, "Hypersonic impaction of ultrafine particles," *J. Aerosol Sci.*, vol. 21, pp. 169–187, 1990.

[20] See, for example, Y.-S. Cheng, H.-C. Yeh, and G. M. Nanapilly, "Collection efficiencies of a point-to-plane electrostatic precipitator " *Am. Ind. Hyg. Assoc. Journal*, vol. 42, pp. 605–610, 1981.

[21] S. -H. Zhang and R. C. Flagan, "Resolution of the radial differential mobility analyzer," *J. Aerosol Sci.*, vol. 27, pp. 1179–1200, 1996.

[22] See, for example, L. -C. Chen, "Particulates generated by pulsed laser ablation," *Pulsed laser depositon of thin films*, ed. D. B. Chrisey and G. K. Hubler, John Wiley & Sons, New York, 1994, pp. 167–198.

[23] R. Kelly and A. Miotello, "Mechanisms of pulsed laser sputtering," *Pulsed laser depositon of thin films*, ed. D. B. Chrisey and G. K. Hubler, John Wiley & Sons, New York, 1994, pp. 55–87.

Chapter 5

Limits to differential mobility analysis

5.1 Introduction

In the work presented in the previous chapter, the differential mobility analyzer (DMA) is the principal device in the generation of size-classified silicon nanocrystals. With the described approach, size dependent properties can potentially be studied in large ensembles of nearly monodisperse semiconductor nanocrystals. The DMA is also the key instrument in the measurement of ultrafine aerosol particles in general, being used directly in a large fraction of the measurements on such systems and indirectly, as a calibration source for most of the other instruments that are used for measurements in the nanometer-size regime.

Differential mobility analyzers were originally developed to analyze aerosol particles in the near-submicron regime, operating with charged particle number con-

centrations that are tipically below 10^5 particles/cm^3. At these sizes and number concentrations, DMAs perform very near the ideal originally described by Knutson and Whitby [3]. In these limits, charged particles are transmitted with efficiency close to unity, and, for balanced polydisperse and monodisperse aerosol flows, the instrument response closely approximates the predicted performance. This nearly ideal performance has been achieved for a number of instruments including the cylindrical DMA (CDMA) that was originally developed at the University of Minnesota [3], the cylindrical DMA design developed at the University of Vienna (Vienna CDMA) [4, 5], and, recently, in radial flow designs (RDMA) [6, 7].

The interest in nanometer scale aerosols has, however, driven investigators to apply DMAs to the analysis of ever smaller particle diameters. Therefore, these instruments are now used for measurement, generation of calibration standards, and materials synthesis down to particle diameters as small as a few nanometers. In a few instances, DMAs have been used to classify 1 nm diameter or smaller particles and even ions [1, 2]. In the study of semiconductor nanocrystals we are particularly interested in these extreme sizes, because quantum confinement effects are expected to become dominant.

In our work, we have also been led to operate DMAs at charged particle number concentrations well beyond 10^5 particles/cm^3 due to our need to achieve the high throughput of size-classified nanocrystals that are required to produce dense nanocrystal deposits for optical characterization experiments. The need for high concentrations is made clear in Fig. 5.1. This figure shows the time required to collect one

monolayer of size-classified nanocrystals as a function of the number concentration. It is apparent that for typical aerosol concentrations of 10^4 particles/cm^3, several days are necessary to deposit one monolayer of 10 nm particles. Such extended time operation is usually impractical unless a fully automated system with large gas supplies is employed. High throughputs and reasonable collection times could, however, be achieved if elevated number concentrations could be processed in the DMA.

Thus, from the point of view of semiconductor nanocrystal synthesis, we would like to use the DMA outside its original operational boundaries. Ideally, we would like to size-classify 1-5 nm nanocrystals at concentrations above 10^6 cm^{-3}. Operation of the DMA at these conditions degrades the instrument performance by several mechanisms. This degradation must be understood and quantified if the DMA is to be used reliably in this regime.

At small particle sizes the performance of the DMA is degraded through increased diffusional losses of the fine particles in the entrance and exit regions of the instrument, and by diffusional broadening of the transfer function. The former problems were clearly elucidated with the University of Minnesota design, and modest improvements in the outlet region were demonstrated [8]. The University of Vienna CDMA incorporated a tangential aerosol inlet that dramatically reduced particle losses and allowed routine operation for measurement of nanometer particles. That inlet was also adopted in the Caltech RDMA. Combined with a particularly simple central outlet port, transmission efficiencies as high as 85% were achieved at 5 nm diameter in the RDMA. Diffusion broadening of the transfer function of the DMA was first modeled

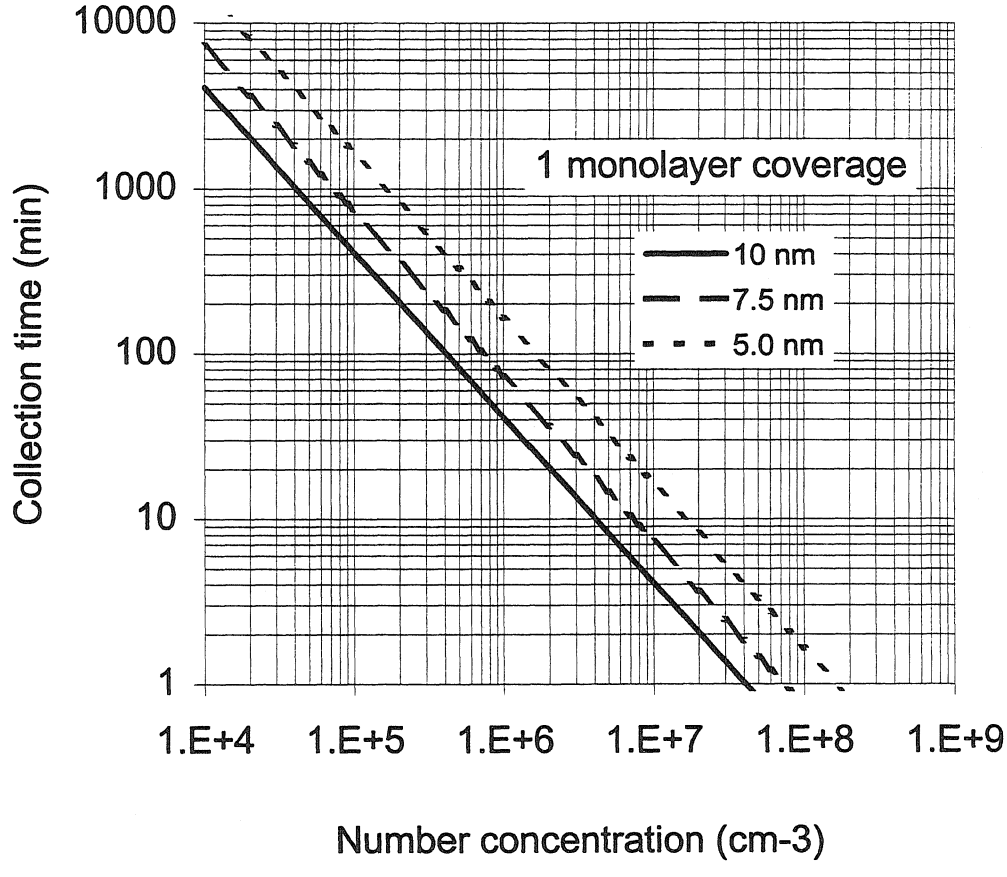

Figure 5.1: Time required to collect one monolayer of size-classified nanocrystals as a function of number concentration for different nanocrystal diameters. Calculation for the electrostatic precipitator with singly charged nanocrystals. Nozzle diameter of 1 mm, nozzle-to-plane distance of 0.5 mm, flow rate of 1.4 lpm, and deposit radius of 1.2 mm.

in detail by Kousaka et al. [8] who developed a numerical model of the migration and diffusion of fine particles in the University of Minnesota CDMA. Stolzenburg developed an approximate semianalytical model for diffusional broadening of the transfer function of the CDMA [9]. Mesbah [6] and Zhang and Flagan [10] applied that analysis to the radial DMA designs. Stolzenburg [9] and Zhang and Flagan [10] conducted extensive tandem differential mobility analyzer calibration studies for the CDMA and the RDMA, respectively, and demonstrated extremely close agreement between the predicted and observed broadening of the DMA response.

At high number concentrations the performance of the DMA is further degraded due to the electric field generated by the charged particles inside the instrument, the so-called space charge effect. When the space-charge field becomes comparable to the applied electric field, the transfer function of the instrument begins to deviate from its ideal shape. For given operation conditions, any DMA has an intrinsic upper bound in the number concentration it can handle before space charge effects begin to degrade its resolution and accuracy. However, little attention has been given to this problem in the literature because DMAs are usually operated well below the onset for these effects. A simplistic analysis of this phenomenon was first presented by Tammet [11], who derived the space charge field in a cylindrical capacitor completely filled with aerosol particles. That approach cannot be applied to a realistic situation because there are particle-free regions inside the DMA. Recently, Alonso and Kousaka have suggested a more realistic simplified analytical model to estimate the space charge field in the CDMA [12]. Their results show qualitatevely the ocurrence of shifts in

the transfer function as a function of total number concentration.

In this chapter, we attempt to predict quantitatively the DMA performance for small particles and large number concentrations. For that purpose, we have developed numerical calculations that account for the interplay of Brownian diffusion and space charge effects in the particle transport inside the instrument. Although this approach lacks the versatility of an analytical solution, distortions in the transfer function can be more realistically calculated as fewer approximations are necessary.

In the following sections we present, first of all, evidence of diffusion and space charge effects in our experiments, demonstrating the importance of taking these phenomena into account in the DMA operation. Secondly, we introduce a simple analysis based on dimensionless groups that allow quick evaluation of the importance of these effects. Thirdly, we describe the self-consistent calculation procedure and present predictions on how the DMA transfer function is distorted due to simultaneous diffusion and space charge effects. These results identify critical design parameters that should allow optimum DMA performance in the size and concentration regime of interest.

5.2 Experimental observation of limits to differential mobility analysis

5.2.1 Broadening of the transfer function

The usefulness of a DMA in a certain particle size range is determined by its resolution and accuracy. The resolution is related to the width of the instrument transfer function. The experiment of choice to probe this quantity is the tandem differen-

tial mobility analyzer (TDMA) arrangement. A typical TDMA setup used in our experiments to evaluate the width of the transfer function is shown in Fig. 5.2. An ultrafine aerosol is introduced into a first DMA after passing through a neutralizer. The aerosol classified by this first instrument is neutralized again and then allowed into a second DMA. By fixing the voltage on the first instrument, scanning the voltage on the second one, and measuring the number concentration after each DMA, the convolution of the instruments transfer functions is determined. If the DMAs are identical, a data deconvolution gives the transfer function. If the instruments are different but the transfer function is known for one of them, the transfer function for the other one may also, in principle, be found.

We have performed measurements with the setup of Fig. 5.2 using two identical RDMAs (RDMA-1, RDMA-2) and a laser ablation aerosol source as described in chapter 4. A typical result for these experiments may be seen in Fig. 5.3. In this case the aerosol and sheath flow rates were 1.5 lpm and 15 lpm, respectively, and the applied voltage was 150 V. The figure shows a comparison between the measured concentration after RDMA-2 and the convoluted ideal transfer function. It is apparent that the RDMA is performing far from the ideal behavior. The measured convolution of the transfer function is significantly broader than the ideal one. The removal of neutralizer-1 in the setup broadens even more the transfer function, probably as a result of the introduction of larger, doubly charged particles in the aerosol classified by RDMA-1. Broadening of the transfer function has usually been attributed to particle Brownian diffusion in the classification region of the DMA. Models developed to treat

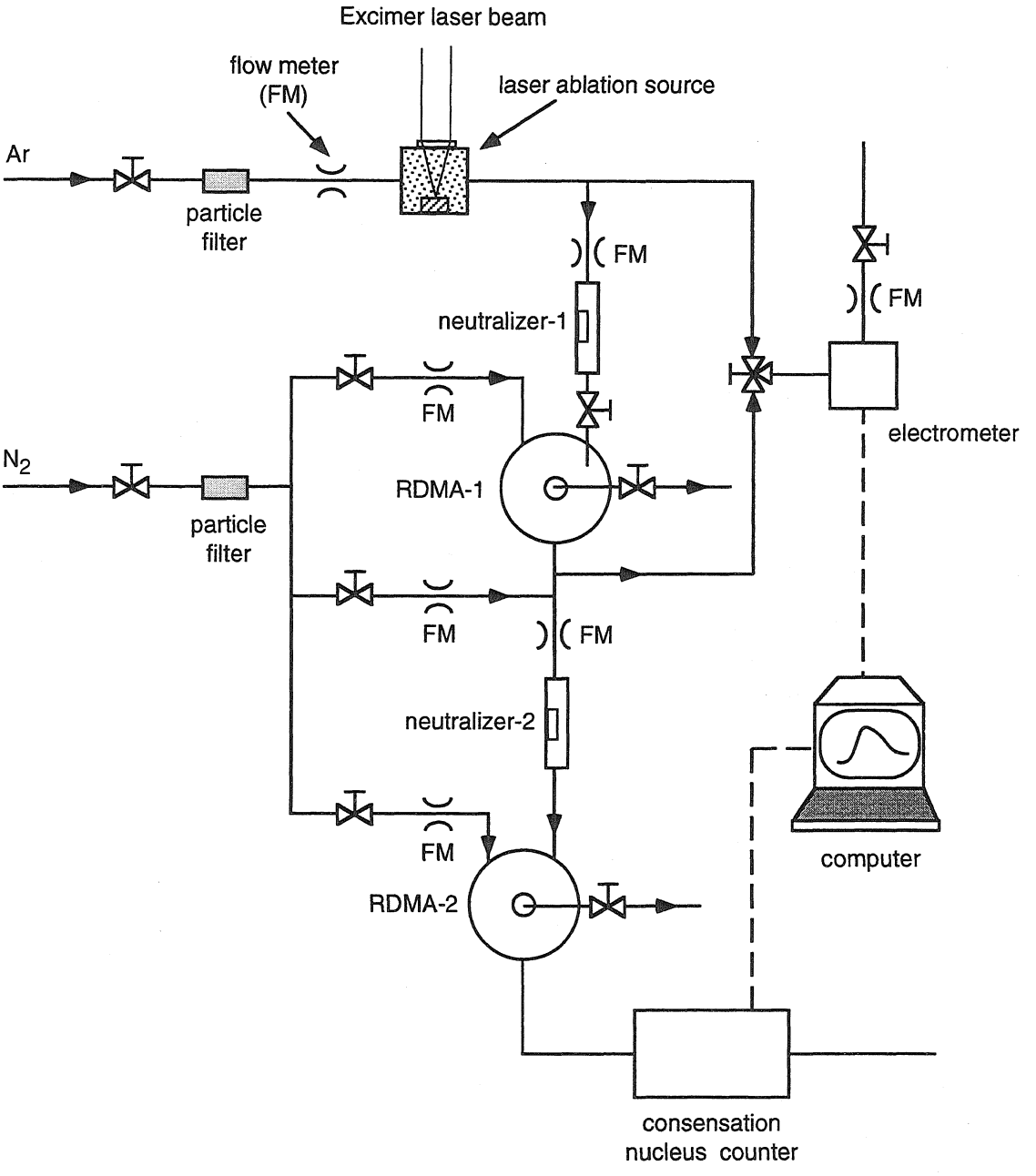

Figure 5.2: Schematic of a tandem differential mobility analyzer setup.

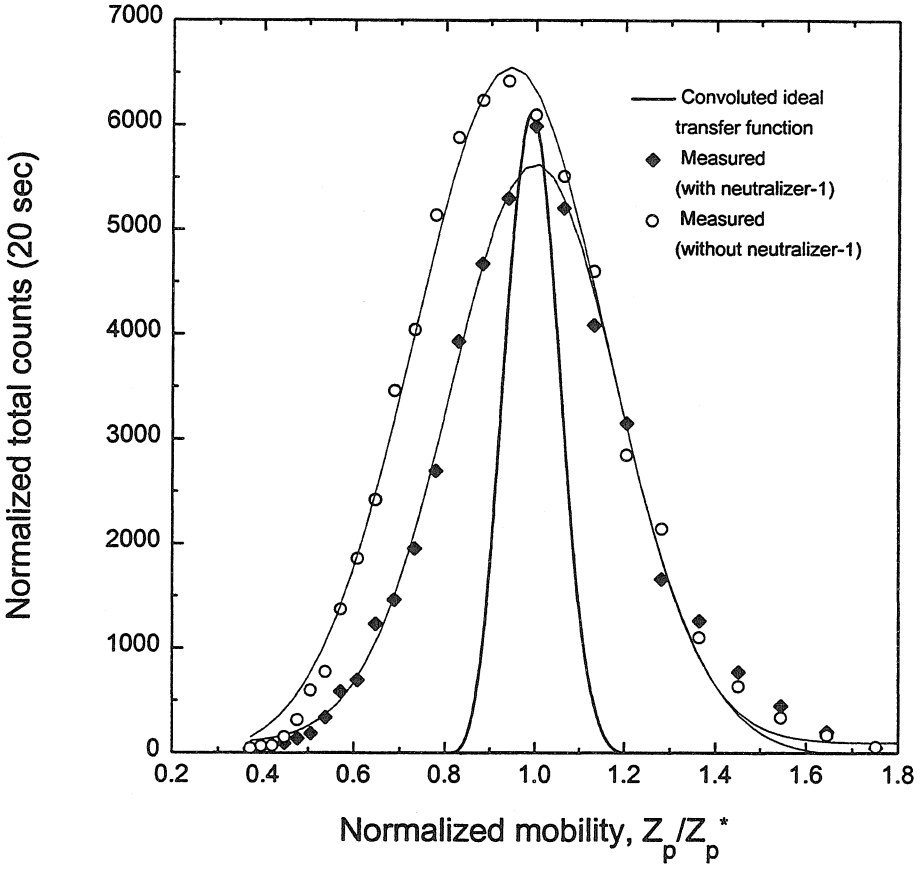

Figure 5.3: Comparison between the ideal and measured convoluted transfer function of the radial differential mobility analyzer for aerosol and sheath flow rates of 1.5 lpm and 15 lpm, respectively, and applied voltage of 150 V.

this problem [8, 9, 10] agree well with reported TDMA results.

5.2.2 Space charge effects

Another variable that determines the accuracy of aerosol classification is the electric field inside the DMA. If the field is distorted or changes in an uncontrolled fashion, mobility classification is compromised. Operation with high particle concentrations leads to increased charge in the analyzer and the effect of space charge fields may become important. In our experiments we have repeatedly experienced situations in which the aerosol charge inside the analyzer was so large as to cause the total breakdown of the size classification. Figure 5.4 shows one of these situations for an experiment run with the setup of Fig. 4.1 and the thermal evaporation silicon nanocrystal source. When a neutralizer is used upstream the DMA, a typical log-normal relationship between number concentration and analyzer voltage is obtained. Due to the neutralizer low charging probability for small particles (below 5%), one approach to try to increase the number concentration is to remove the neutralizer and attempt classification using the original aerosol charge state. This may increase the number of charged small particles, at the expense of introducing some larger particles due to double and triple charging. As shown in Fig. 5.4, however, for this particular aerosol the neutralizer removal did not lead to increased number concentrations. In fact, a small drop is observed. In addition, an apparent shift towards higher voltages (and therefore larger particles) is observed. Another important observation is that in this case particles were being sampled out of the analyzer even when the applied voltage was zero. If all the flows are laminar and stable, this is an indication that

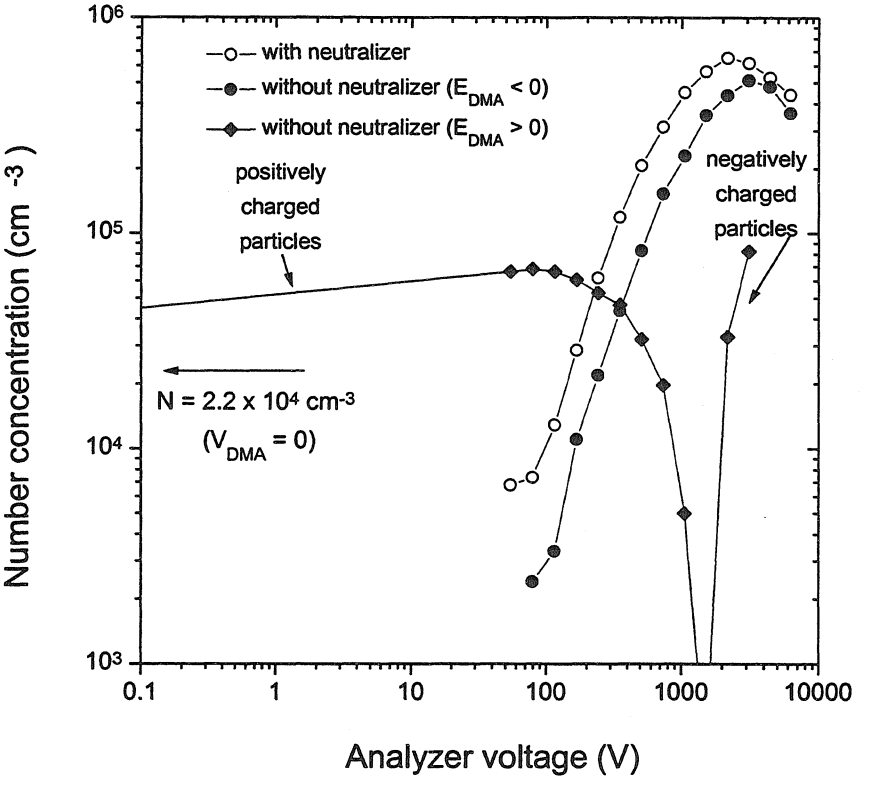

Figure 5.4: Number concentration (assuming singly charged particles) as a function of applied voltage on the radial DMA. The particles were silicon nanocrystals generated by thermal evaporation.

a large space charge field exists in the analyzer. When the field polarity is reversed in the DMA, a different behavior is observed. As we step through voltage, positively charged particles are sampled, and the number concentration remains approximately constant up to $\sim$ 100 V, dropping below noise level above $\sim$ 1000 V. As the voltage continues to be increased, particles with the opposite polarity begin to be sampled out of the instrument. This measurement indicates that, as a whole, the original aerosol has a net positive charge. By increasing the voltage, a point is reached when the space charge field is balanced and the positively charged particles are driven away from the sampling outlet. For higher voltages still, negatively charged particles start being sampled. Transmission electron microscopy results on samples collected with the DMA operating in these high charge conditions show broad size distributions with geometric standard deviations as large as 1.6, indicating that the size classification was severely compromised. When size classification was performed, this condition was carefully avoided by adjusting operation conditions to eliminate particle transmission at zero voltage.

5.3 Modeling of the particle transport in the differential mobility analyzer

5.3.1 General discussion

A more comprehensive understanding of the limits of differential mobility analysis should be achieved through careful modeling of the particle transport when Brownian diffusion and space charge effects are included.

Before we address the particle transport in detail, it is instructive to look at dimensionless groups that roughly estimate the importance of the physical phenomena involved in the process. For the diffusion effects, the migration Peclet number is the appropriate dimensionless group, while, for space charge effects, we introduce the space charge number.

Migration Peclet number

To characterize the diffusion effects in the DMA, we define the migration Peclet number as

$$\mathrm{Pe}_{mig} = \frac{v_E^* L_{gap}}{\mathcal{D}} \tag{5.1}$$

where v_E^* is the migration velocity, L_{gap} is the the distance between the DMA electrodes, and $\mathcal{D}$ is the diffusion coefficient. For the RDMA, with its parallel plate electrodes, we have $L_{gap} = b$, and

$$v_E^* = Z_p^* E_z = \frac{Q_e + Q_{sh}}{2\pi(R_2^2 - R_1^2)} \tag{5.2}$$

Therefore, the migration Peclet number for the RDMA is given by

$$\mathrm{Pe}_{mig} = \frac{(Q_e + Q_{sh})b}{2\pi(R_2^2 - R_1^2)\mathcal{D}} = \frac{qV}{kT} \tag{5.3}$$

The last expression indicates that the migration Peclet number in the RDMA reduces to the ratio of the electrostatic potential energy of the particle of mobility Z_p^* to its thermal energy. If the electrostatic potential energy is large, the particle will migrate without significant diffusion, whereas small potential energy will lead to substantial diffusion. This simple result points out the fact that the degree of diffusional broadening in the DMA is fundamentally related to the ratio of electrostatic to thermal

energy and not to the particle diameter. The result for the CDMA is slightly more complex. Letting $L_{gap} = r_2 - r_1$ and

$$v_E^* = \frac{Q_e + Q_{sh}}{4\pi L r} \tag{5.4}$$

the migration Peclet number becomes

$$\mathrm{Pe}_{mig} = \frac{qV}{kT} \frac{1 - (r_1/r_2)}{\ln(r_2/r_1)} \tag{5.5}$$

Figure 5.5 shows the dependence of the inverse of the Peclet number with applied voltage for both the RDMA and the CDMA at room temperature. Notice, therefore, that the resolution limit for differential mobility analysis is fundamentally related to the ratio of electrostatic to thermal energy and not to particle diameter. Therefore, a DMA able to classify small particle diameters using high voltages would achieve the best possible resolution. Evidently, in this case the instrument limitation is dictated by the flow rates it can handle without getting into the turbulent regime.

The space charge number

To characterize the space charge effect, we introduce the space charge number, which will provide a quick estimate of when this effect becomes important. In this simple analysis we assume that all of the particles entering the DMA stay confined to a region of width βb where

$$\beta = \frac{Q_a + Q_s}{Q_{sh} + Q_e} \tag{5.6}$$

and b is simply the distance between the DMA electrodes ($b = r_2 - r_1$ for the CDMA). Neglecting Brownian diffusion and space charge migration, this would be the situation

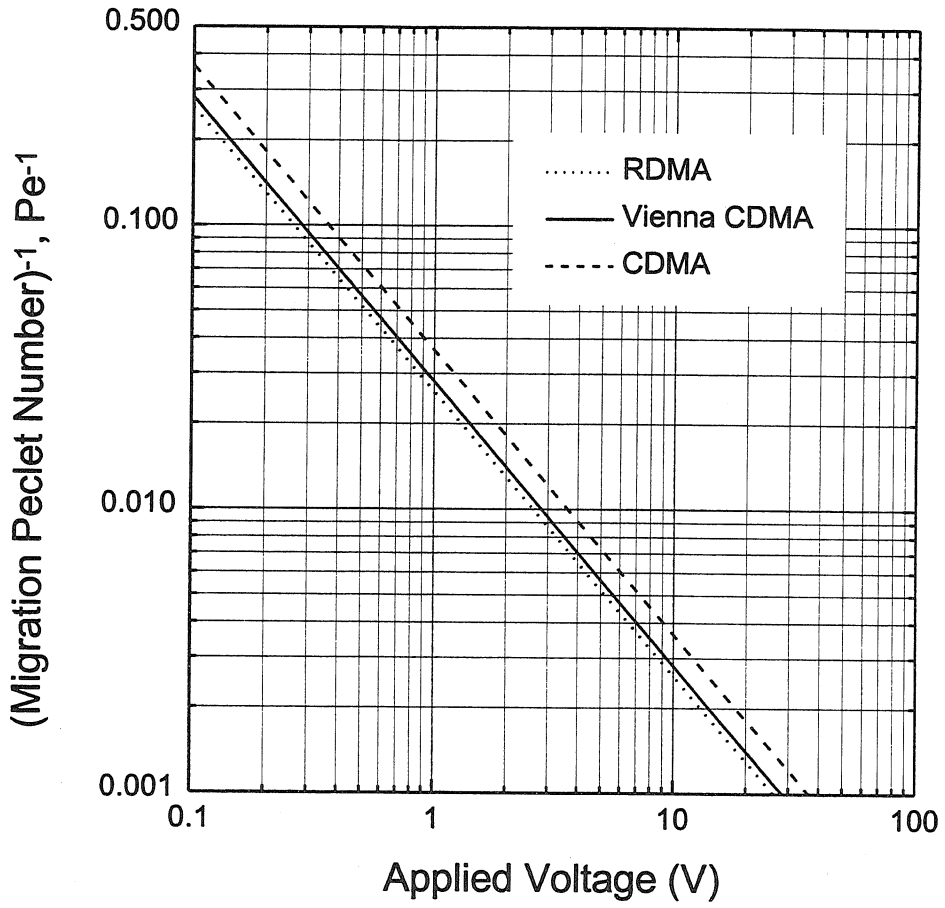

Figure 5.5: Inverse of the migration Peclet number as a function of applied voltage for different DMA geometries at room temperature.

when both DMA electrodes are at the same electrical potential (V_0=0). In this case the charge density in the classification region of the DMA varies only in the direction parallel to the applied field. For the RDMA this charge density may be written simply as

$$\rho(z) = \begin{cases} Ne, & z > (1-\beta)b \\ 0, & \text{otherwise} \end{cases} \tag{5.7}$$

The situation is totally analogous for the CDMA and the charge density may be written as a function of the variable r, which corresponds to the radial direction

$$\rho(r) = \begin{cases} Ne, & (1-\beta)b < r < r_2 \\ 0, & \text{otherwise} \end{cases} \tag{5.8}$$

In both geometries the solution of this problem can be immediatly found by solving Poisson's equation. For the RDMA this equation takes the form

$$\frac{\partial^2 \phi(z)}{\partial z^2} = -\frac{\rho(z)}{\epsilon} \tag{5.9}$$

with $\rho(z)$ given by Eq. 5.7. For the CDMA Poisson's equation is written as

$$\frac{1}{r}\frac{\partial}{\partial r}\left(r\frac{\partial \phi(r)}{\partial r}\right) = -\frac{\rho(r)}{\epsilon} \tag{5.10}$$

with $\rho(r)$ given by Eq. 5.8. Integrating twice and imposing boundary conditions, Eqs. 5.9 and 5.10 yield the electric potential inside the RDMA and CDMA respectively. Using the definition

$$\mathbf{E} = -\nabla\phi \tag{5.11}$$

the electric field is promptly calculated. Therefore, the electric field in the particle-free region of both instruments is found to be

$$E(z)^{RDMA} = \frac{V_0}{b}\left(1 + \frac{Ne}{\epsilon V_0} G_F\right) \tag{5.12}$$

and

$$E(r)^{CDMA} = \frac{V_0}{\ln\left(\frac{r_2}{r_1}\right)}\frac{1}{r}\left(1+\frac{Ne}{\epsilon V_0}G_F\right) \tag{5.13}$$

where G_F is a factor that depends on the flow rates and the specific geometry of the DMA.

Equations 5.12 and 5.13 were conveniently arranged to show that for both the RDMA and the CDMA, the applied electric field (quantity outside the parentheses) is modified by a dimensionless group that depends on the concentration of charged particles N, the applied voltage V_0, and the flow rates and the geometry of the DMA, G_F. We will call this dimensionless group the space charge number S_c, which we write as

$$S_c \equiv \frac{Ne}{\epsilon V_0}G_F \tag{5.14}$$

For the RDMA the factor G_F takes the form

$${G_F}^{RDMA} = \frac{1}{2}\beta^2 b^2 \tag{5.15}$$

while for the CDMA G_F is

$${G_F}^{CDMA} = \frac{1}{4}r_2^2 + \frac{1}{2}(r_2-\beta b)^2\left[\ln\left(1-\frac{\beta b}{r_2}\right)-\frac{1}{2}\right] \tag{5.16}$$

As expected, it can be shown that

$$\lim_{r_2\to\infty} G_F^{CDMA} = G_F^{RDMA} \tag{5.17}$$

In fact, for existing CDMAs, r_2 is large enough (2 to 3 cm) to allow the approximation

$$G_F^{CDMA} \approx G_F^{RDMA} = \frac{1}{2}\beta^2 b^2 \tag{5.18}$$

The space charge number defined by Eq. 5.14 can be used to estimate the importance of the space charge effect in a DMA under given operating conditions. The value of the space charge number can be interpreted simply as an estimate in percent of the distortion in the electric field inside the DMA with respect to the applied electric field. A typical dependence of the space charge number with number concentration is shown in Fig. 5.6 for different applied voltages and electrode distances.

Due to the validity of the approximation of Eq. 5.18, the results for the CDMA and the RDMA are identical as long as the electrode separation is the same. It can be seen that the most dramatic distortions are expected when low applied voltages are used. At 1 V, for example, a field alteration of as much as 60% is predicted for N $= 10^8$ cm^{-3}. Increased applied voltages and reduced electrode separations diminish the relative importance of space charge by simply strengthening the applied electric field. Figure 5.6 also indicates why space charge effects are usually ignored in DMA studies. It turns out that the field distortions are negligible for number concentrations below 10^5 cm^{-3} and particle size above 10 nm (applied voltages in excess of 100 V), which is the regime where most of the DMA studies are performed. However, as these traditional instruments begin to be applied to high concentrations of particles as small as 1 nm and even to ions, space charge distortions will have to either be taken into account or limited by the proper choice of applied voltage and geometry.

Resolving power and peak location error

From the qualitative discussion based on the groups Pe_{mig} and S_c, it becomes evident that when one operates the DMA at low voltages, limits in the resolution and inac-

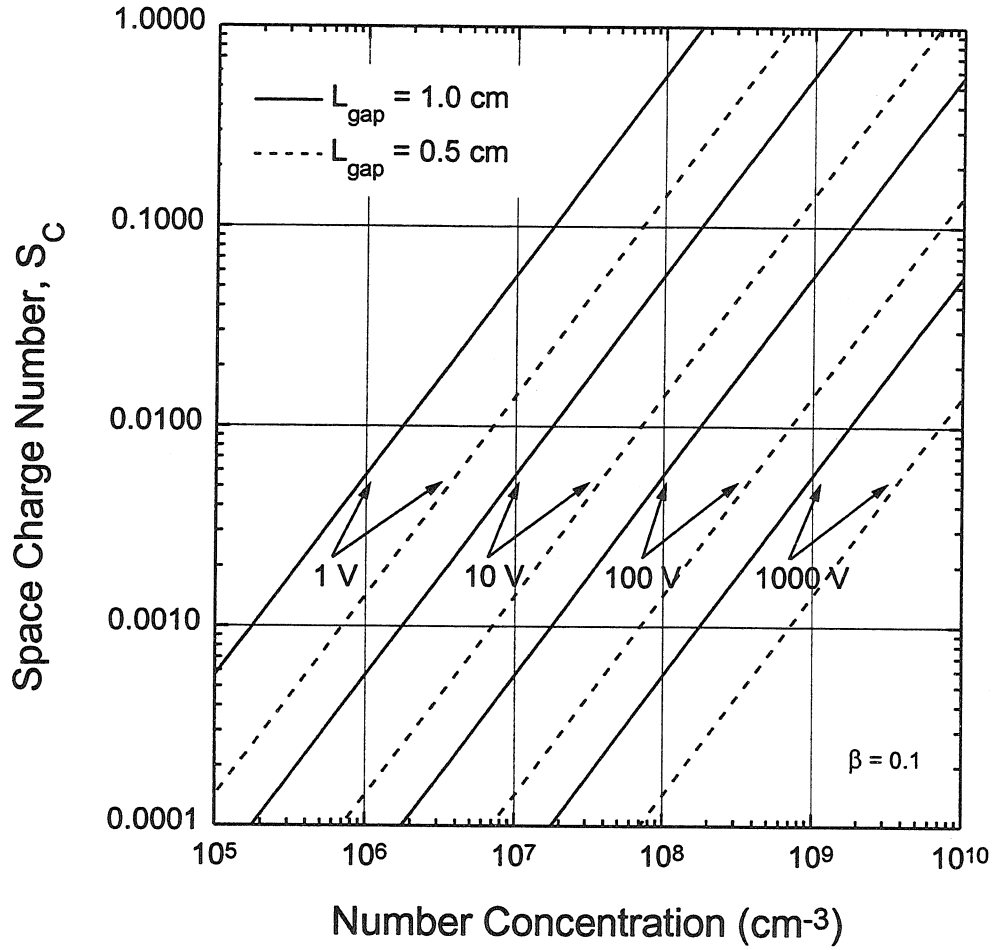

Figure 5.6: Space charge number as a function of number concentration of charged particles for different applied voltages and electrode separations ($\beta = 0.1$).

curacy in the peak location of the transfer function are introduced. To quantify these distortions me may define, by analogy to the terminology used in mass spectrometry, the *resolving power* of the DMA as

$$\mathcal{R} = \frac{Z_c}{\Delta Z_{1/2}} \tag{5.19}$$

where Z_c is the centroid mobility and $\Delta Z_{1/2}$ is the full width at half maximum of the transfer function. For the ideal, triangular transfer function, this quantity becomes

$$\mathcal{R} = \frac{Z^*}{\Delta Z} = \frac{Q_{sh} + Q_e}{Q_a + Q_s} \tag{5.20}$$

Secondly, we denote the error in peak location as

$$\mathcal{E} = \frac{Z_c}{Z^*} - 1 \tag{5.21}$$

We seek to define operating limits that prevent serious reductions in $\mathcal{R}$ or increases in $\mathcal{E}$.

5.3.2 Particle transport in the differential mobility analyzer

Having gained insight on the performance limits of the DMA through the behavior of the migration Peclet number and the space charge number, we move on to model the particle transport inside the instrument.

As we consider this modeling, we start with the deterministic trajectories in the absence of diffusion and space charge fields. We then introduce a numerical solution to account for the diffusion broadening and compare it with Stolzenburg's semianalytical model that has been vindicated by experiment. As a next step, we describe the calculation procedure to obtain a self-consistent solution for the space charge field

and then integrate diffusion and space charge into a single calculation that predicts the behavior of the DMA transfer function at high number concentrations. Finally, we compare our predictions with the simplified analytical model recently suggested by Alonso and Kousaka [12].

Deterministic trajectories

In the absence of diffusion and space charge effects, particles will migrate through the DMA along the deterministic trajectories governed by the equations

$$\begin{aligned} \frac{dr}{dt} &= u_r + Z_p E_r^{ap} \\ \frac{dz}{dt} &= u_z + Z_p E_z^{ap} \end{aligned} \tag{5.22}$$

where r and z denote the radial and axial coordinates, u_r and u_z, the radial and axial components of the gas flow velocity, E_r^{ap} and E_z^{ap}, the radial and axial components of the applied electric field, and Z_p, the particle electric mobility.

Introducing the fluid stream function ψ, which is defined such that

$$\begin{aligned} u_r &= \frac{1}{r}\frac{\partial \psi}{\partial y} \\ u_z &= -\frac{1}{r}\frac{\partial \psi}{\partial r} \end{aligned} \tag{5.23}$$

and the electric potential ϕ defined such that

$$\begin{aligned} E_r^{ap} &= \frac{1}{r}\frac{\partial \phi}{\partial y} \\ E_z^{ap} &= -\frac{1}{r}\frac{\partial \phi}{\partial r} \end{aligned} \tag{5.24}$$

it can be shown that Eq. 5.22 implies that particles will migrate through the DMA

along trajectories of constant particle stream function [7],

$$\Gamma = \psi + Z_p \phi \tag{5.25}$$

This problem has been solved by Knutson and Whitby [3] for the CDMA and by Zhang and Flagan [7] for the RDMA. The resulting transfer function has the shape of a truncated isosceles triangle whose centroid and exact angles depend on the flow rates and the applied field (Fig. 3.8).

Diffusion effects

Brownian diffusion leads to a spatial distribution of particles around the deterministic trajectories defined in the previous section. Two different approaches have been traditionally used to account for this phenomenon, namely, the direct numerical solution of the diffusion equation [8], and the semianalytical evaluation of the variance of the particle spatial distribution [9].

In this work we obtain a numerical solution for the diffusion problem by solving Eq. 5.22 including Gaussian spreading at every step of the way. Although not identical, this approach is equivalent to the numerical solution of the diffusion equation [8]. We assume that as the particles are advected by the gas, diffusion takes place only in the direction normal to the flow. To solve this problem a rectangular mesh of $(n+1)\times(m+1)$ points is defined in the classification region of the DMA as illustrated in Fig. 5.7. Such a mesh delimits a two-dimensional array of $n \times m$ rectangular cells which are populated by discrete size distributions $N_{i,j}(\tilde{Z})$. Thus, particles are assumed to occupy cells of finite dimensions d and h parallel and perpendicular to

the gas flow, respectively.

As particles of an arbitrary cell (i,j) are advected from column j to column $j+1$ (Fig. 5.7), Brownian motion causes them to diffuse and be spread over the cells of column $j+1$. Such a spreading can be described by a Gaussian distribution. Thus, the number concentration at cell $(i,j+1)$ for a certain normalized mobility $\tilde{Z}$ is given by

$$N_{i,j+1}(\tilde{Z}) = \sum_{k=1}^{n} \frac{N_{kj}(\tilde{Z})h}{2\sqrt{\pi \mathcal{D}(\tilde{Z})t}} \exp\left(-\frac{(x_{j+1}-x_k)^2}{4\mathcal{D}(\tilde{Z})t}\right) \tag{5.26}$$

with the time t given by

$$t = \frac{d}{v_x} \tag{5.27}$$

where d is the cell dimension in the gas flow direction and v_x, the gas velocity at column j. Notice that Eq. 5.26 makes use of coordinate x, which denotes the direction normal to the gas flow. For the CDMA $x \equiv r$ whereas in the RDMA $x \equiv z$.

By solving numerically Eq. 5.22 in the described cell array and using Eq. 5.26 to account for the diffusion at each step of the way, the diffusion broadened transfer function can be calculated.

In order to make sure that this calculation predicts the diffusion broadened transfer function accurately, we have compared it with an alternative solution based on the semianalytical model first introduced by Stolzenburg [9]. In this model, a local, orthogonal curvilinear coordinate system is defined based on the distance s along the particle streamline, Γ_i, and the distance normal to Γ_i, x. The variance of the spatial distribution of particles about their entry streamline increases with time according to

$$d\sigma_x^2 = 2\mathcal{D}dt \tag{5.28}$$

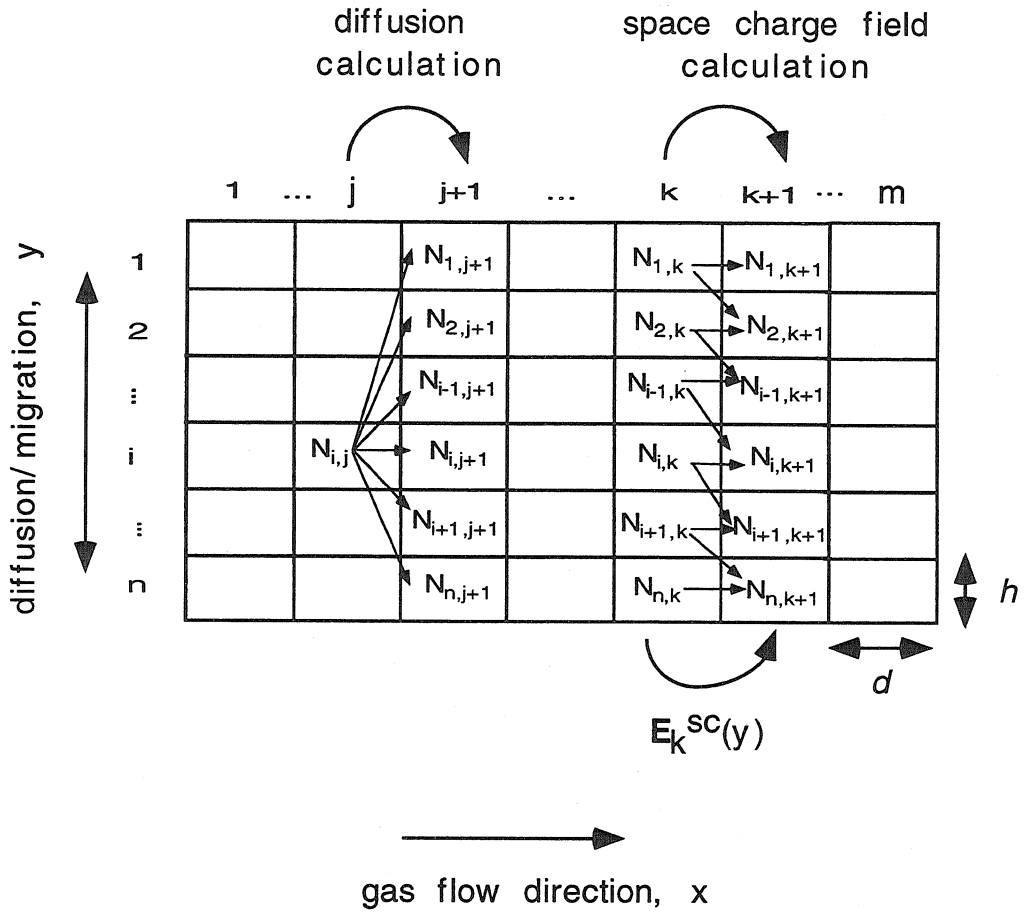

Figure 5.7: Schematic of the two-dimensional cell array defined in the classification region of the DMA to calculate diffusional broadening and space charge effects.

The variance in particle stream functions is [9]

$$d\sigma_\Gamma^2 = \left(\frac{\partial \Gamma}{\partial x}\right)^2 d\sigma_x^2 \approx 2\mathcal{D}v^2 r^2 dt \tag{5.29}$$

The particle stream function variance is determined by integrating along the particle streamline at which the particle entered the DMA, i.e.,

$$\sigma_\Gamma^2 = 2\mathcal{D}\int_{\Gamma^*} v^2 r^2 dt \tag{5.30}$$

Particles that enter the DMA at stream function Γ_i are normally distributed about Γ_i at the DMA outlet according to the variance σ_Γ^2. Using Eq. 5.25, the probability that a particle entering at fluid stream function ψ_i will exit between ψ_0 and $\psi_0 + d\psi_0$ is

$$f_{trans}(\psi_i, \psi_0)d\psi_0 = \frac{1}{\sqrt{2\pi}} \exp\left[-\frac{1}{2}\left(\frac{\psi_0 - \psi_i + Z_p\Delta\phi}{\sigma_\Gamma}\right)^2\right] d\psi_0 \tag{5.31}$$

By integrating Eq. 5.31 over all entering and exiting flows, one obtains the diffusion broadened transfer function [9]

$$\begin{aligned}\Omega_d &= \frac{\tilde{\sigma}}{\sqrt{2}\,\beta(1-\delta)}\left[\mathcal{E}\left(\frac{\tilde{Z}_p - (1+\beta)}{\sqrt{2}\tilde{\sigma}}\right) + \mathcal{E}\left(\frac{\tilde{Z}_p - (1-\beta)}{\sqrt{2}\tilde{\sigma}}\right)\right. \\ &- \left.\mathcal{E}\left(\frac{\tilde{Z}_p - (1+\beta\delta)}{\sqrt{2}\,\tilde{\sigma}}\right) - \mathcal{E}\left(\frac{\tilde{Z}_p - (1-\beta\delta)}{\sqrt{2}\,\tilde{\sigma}}\right)\right]\end{aligned} \tag{5.32}$$

where $\mathcal{E}(x)$ is defined in terms of the error function $\mathrm{erf}(x)$ as

$$\mathcal{E}(x) \equiv \int_0^x \mathrm{erf}(u)du = x\mathrm{erf}(x) + \frac{1}{\sqrt{\pi}}\exp(-x^2) \tag{5.33}$$

and

$$\beta \equiv \frac{Q_a + Q_s}{Q_e + Q_{sh}} \tag{5.34}$$

$$\delta \equiv \frac{Q_a - Q_s}{Q_a + Q_s} \tag{5.35}$$

$$\tilde{Z}_p \equiv \frac{Z_p}{Z_p^*} \tag{5.36}$$

$$\tilde{\sigma} \equiv \frac{\sigma_\Gamma}{-\Delta\psi^*} \tag{5.37}$$

In the definitions of Eqs. 5.34 through 5.37 Q_a, Q_{sh}, Q_s, and Q_e are the aerosol, the sheath, the sample, and the excess flow rates, respectively. Z_p^* is the centroid mobility and $\Delta\psi^*$ is the range of fluid stream functions crossed by the particles at the centroid of the transfer function. The dimensionless variance in the particle streamfunction, $\tilde{\sigma}$ may be further expressed as

$$\tilde{\sigma}^2 = \frac{\tilde{G}}{\mathrm{Pe}_{mig}} \tag{5.38}$$

where Pe_{mig} is the migration Peclet number (Eq. 5.1), and $\tilde{G}$ is a dimensionless geometry factor. Their expressions for the radial and cylindrical DMAs are given in Table I. A value of $\tilde{G} = 2.55$ has been estimated for the CDMA based upon a fully developed laminar flow within the analyzer column [9]. For the RDMA a value of $\tilde{G} = 3.03$ has been suggested based upon the creeping flow limit for the radial flow between parallel disks [10].

Figure 5.8 shows the predictions of our numerical calculation and the ones by Stolzenburg's model for the diffusion broadened transfer function of the RDMA. The predictions are essentially indistinguishable. We point out, however, that the numerical solution predicts a feature not present in the solution by Stolzenburg's model, namely, the assymetry of the transfer function. This assymetry arises from the dependence of the diffusion coefficient on the particle mobility. This dependence is explicitly taken into account in Eq. 5.26 while it is approximated by its value at Z_p^*

in Stolzenburg's model. This feature can also be incorporated in the semianalytical model in a rather simple way. It just requires that the integral over all entering and exiting flows at the very last step of the transfer function calculation be replaced by a numerical integration.

Aside the minor discrepancies mentioned, both models describe quite well the diffusional broadening of the transfer function and are in good agreement with experiment [8, 9, 10]. Therefore, in the self-consistent calculation of the space charge field including diffusion, we will use the numerical solution described here.

Table I. Dimensionless parameters used in determining the diffusion broadening of the transfer function of the cylindrical and radial DMAs.

Parameter	CDMA	RDMA
$\tilde{G}$	$\frac{1}{\bar{L}}\int_{\Gamma^*}\tilde{v}^2\tilde{r}^2 d\tilde{t}$	$\frac{8}{\bar{R}_2^2-\bar{R}_1^2}\int_{\Gamma^*}\tilde{v}^2\tilde{r}^2 d\tilde{t}$
$\tilde{r}$	$\frac{r}{R_2}$	$\frac{r}{b}$
$\tilde{v}$	$\frac{v}{v_E^*}=\frac{4\pi R_2 L v}{Q_{sh}+Q_e}$	$\frac{v}{v_E^*}=\frac{2\pi(R_2^2-R_1^2)v}{Q_{sh}+Q_e}$
$\tilde{t}$	$\frac{2v_E^* t}{R_2}=\frac{2(Q_E+Q_{sh})t}{4\pi R_2^2 L}$	$\frac{tb}{v_E^*}=\frac{2\pi(R_2^2-R_1^2)bt}{Q_{sh}+Q_e}$
Pe_{mig}	$\frac{v_E^*(R_2-R_1)}{\mathcal{D}}=\frac{qV}{kT}\frac{1-\tilde{R}_1}{\ln\frac{1}{\tilde{R}_1}}$	$\frac{(Q_{sh}+Q_e)b}{2\pi(R_2^2-R_1^2)\mathcal{D}}=\frac{qV}{kT}$

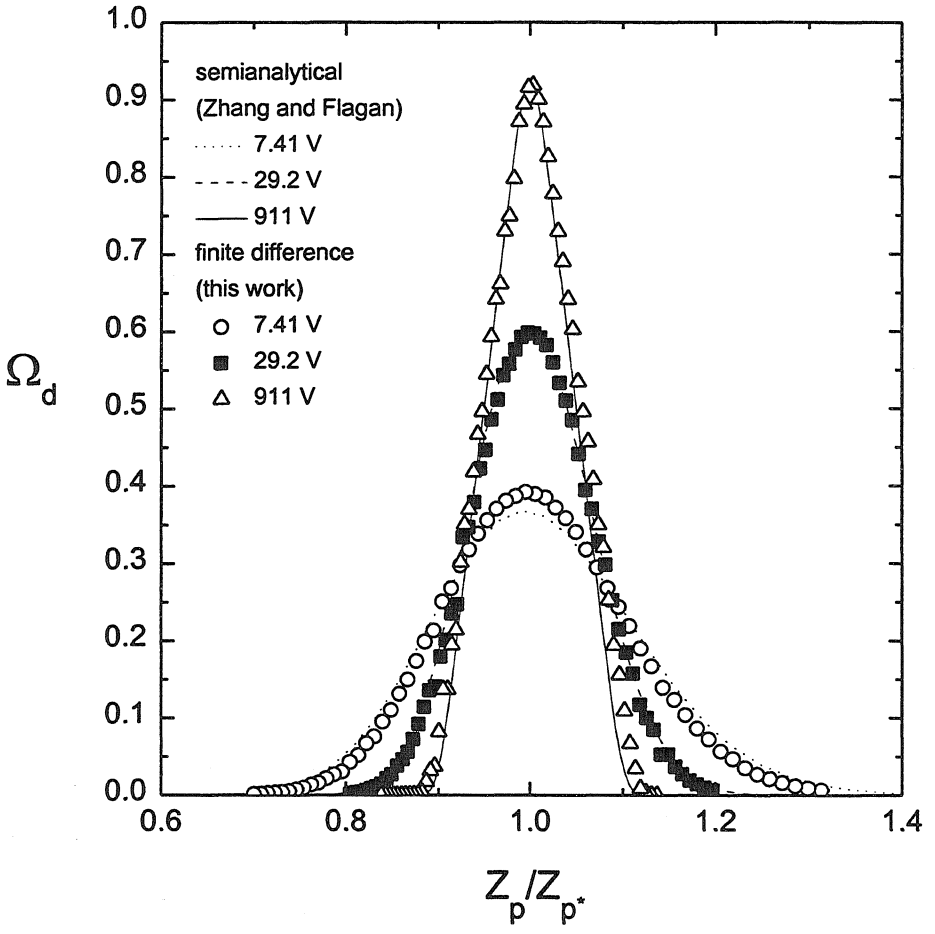

Figure 5.8: Diffusion broadened transfer function for the radial DMA with $\beta = 0.1$. Comparison between the semianalytical solution of Stolzenburg's model and the finite difference numerical solution used in this work.

Inclusion of space charge effects

The electric field generated by the charged particles inside the DMA leads to further changes in the particle trajectories. These changes can be taken into account by rewriting Eq. 5.22 as

$$\begin{aligned} \frac{dr}{dt} &= u_r + Z_p(E_r^{ap} + E_r^{sc}) \\ \frac{dz}{dt} &= u_z + Z_p(E_z^{ap} + E_z^{sc}) \end{aligned} \tag{5.39}$$

where E_r^{sc} and E_z^{sc} denote the radial and axial components of the space charge field, or the electric field generated by the charged particles themselves. In principle this field can be calculated using Poisson's equation,

$$\nabla^2\phi(r,z) = -\frac{\rho(r,z)}{\epsilon_0} \tag{5.40}$$

where

$$\mathbf{E}^{sc}(r,z) = -\nabla\phi(r,z) \tag{5.41}$$

The difficulty in using this approach is twofold. First of all $\rho(r,z)$ depends on the details of the particle trajectories which in turn depend on $\rho(r,z)$ via the space charge field. Secondly $\rho(r,z)$ is a two-dimensional function and a fairly involved calculation may be necessary to solve Eq. 5.40. The first problem can be dealt with by performing a self-consistent numerical solution of Eqs. 5.39 and 5.40. To avoid having to solve Poisson's equation in two dimensions, we approximate $\rho(r,z)$ by a one-dimensional charge density that changes only in the direction normal to the gas flow. The value assigned to this one-dimensional charge density is the value of $\rho(r,z)$ at the location where the solution of Poisson's equation is to be performed. With

this approximation we solve Poisson's equation in one dimension successively as the particles are advected through the DMA. Thus, we neglect the component of the space charge field in the gas flow direction. Variations of the space charge density up and downstream the location where Poisson's equation is being solved are also neglected by this approximation. For the CDMA this can be written as

$$E_z^{sc} = 0 \tag{5.42}$$

$$E_r^{sc} = -\frac{\partial \phi(r)}{\partial r} \tag{5.43}$$

where $\phi(r)$ is found from

$$\frac{1}{r}\frac{\partial}{\partial r}\left(r\frac{\partial \phi(r)}{\partial r}\right) = -\frac{\rho(r)}{\epsilon_0} \tag{5.44}$$

For the RDMA these equations take the form

$$E_r^{sc} = 0 \tag{5.45}$$

$$E_z^{sc} = -\frac{\partial \phi(z)}{\partial z} \tag{5.46}$$

where $\phi(z)$ is found from

$$\frac{\partial^2 \phi(z)}{\partial z^2} = -\frac{\rho(z)}{\epsilon_0} \tag{5.47}$$

Since even this simplified problem cannot be solved analytically, a finite-difference numerical method was employed. The two-dimensional cell array described in the previous section and illustrated in Fig. 5.7 is once again used here. Particles that drift by an arbitrary cell (i, k) between times t and $t + dt$ have their number concentration $N_{i,k}(\tilde{Z})$ assigned to that cell. The spatial distribution of particles at a given column k is then determined from the flow rate ratio β for $k = 1$ and by integration over all

particle mobilities for $k \neq 1$. The charge density is immediately found and used to calculate $\mathbf{E}_k^{sc}$ by integrating the one-dimensional Poisson's equation in the direction perpendicular to the gas flow. Subsequently, particles are allowed to drift along the gas flow direction to the next column $(k+1)$. In this process their deterministic trajectories are calculated by Eq. 5.39 using $\mathbf{E}_k^{sc}$. These trajectories are then corrected for diffusion broadening by Eq. 5.26 in order to calculate the new spatial distribution of particles at column $k+1$ and $\mathbf{E}_{k+1}^{sc}$. This process is repeated until the particles traverse the entire classification region. An approximation of the transfer function including diffusional broadening and space charge effects is then found from the ratio of particles that exit the DMA to the ones that entered it.

$$\Omega_{d,sc} = \frac{\frac{1}{\beta n}\sum_{i=n-\beta n}^{n} N_{i,m}(\tilde{Z})}{N_{1,1}(\tilde{Z})} \tag{5.48}$$

Calculated transfer functions

The transfer function $\Omega_{d,sc}$ of Eq. 5.48 has been calculated for different size distributions entering the DMA. For total number concentrations above 10^6 cm^{-3}, systematic shifts in the peak position are predicted as a function of aerosol concentration. Flow rates and applied voltages were also varied in order to evaluate the importance of the space charge effect under different operation conditions. Figures 5.9 and 5.10 present these calculated transfer functions for the RDMA, assuming that the aerosol entering the instrument is bipolar with Fuchs charge distribution (Fig. 3.5), and that sampled particles are positively charged.

In the discussion that follows, the expression *low flow rates* refers to simulations

performed using $Q_a = 0.3$ lpm and $Q_{sh} = 3.0$ lpm, while the expression *high flow rates* refers to $Q_a = 1.5$ lpm and $Q_{sh} = 15$ lpm. Similarly, we will refer to the size distribution with median diameter $D_{pg} = 8.62$ nm and geometric standard deviation $\sigma_g = 1.47$ as *narrower size distribution*, while the size distribution with $D_{pg} = 39.2$ nm and $\sigma_g = 1.87$ will be referred to as *broader size distribution.*

In Fig. 5.9(a) and (b), predictions are shown for low flow rates. The space charge field generated by the narrower size distribution (Fig. 5.9(a)) causes shifts towards lower mobilities. When a voltage of 2.76 V is used (size classification at 3.0 nm) the transfer function peak is predicted to shift by as much as 20% for a total number concentration of $N_e = 10^8$ cm^{-3} (Fig.5.9(a)). Figure 5.9(b) reveals that in the case of the broader size distribution, for approximately the same conditions, space charge causes shifts towards higher mobilities. This is an interesting effect, indicating how sensitive the space charge effect is to the details of the size distribution. The difference in the direction of the mobility shift can be understood in terms of the charge distribution inside the DMA, recollecting that Fuchs charge distribution has been assumed for the bipolar aerosol. In the case of the narrower size distribution, D_{pg} is also low (8.62 nm), and a large fraction of the negatively charged particles are lost to the top electrode of the RDMA, causing the remaining aerosol to have a positive net charge that enhances the field experienced by the particles undergoing significant migration ($\sim$ 3 nm diameter). The result is a mobility shift towards lower mobilities. For the broader size distribution, however, D_{pg} is rather high (32.9 nm), and few negative particles are lost causing the aerosol to conserve its negative net

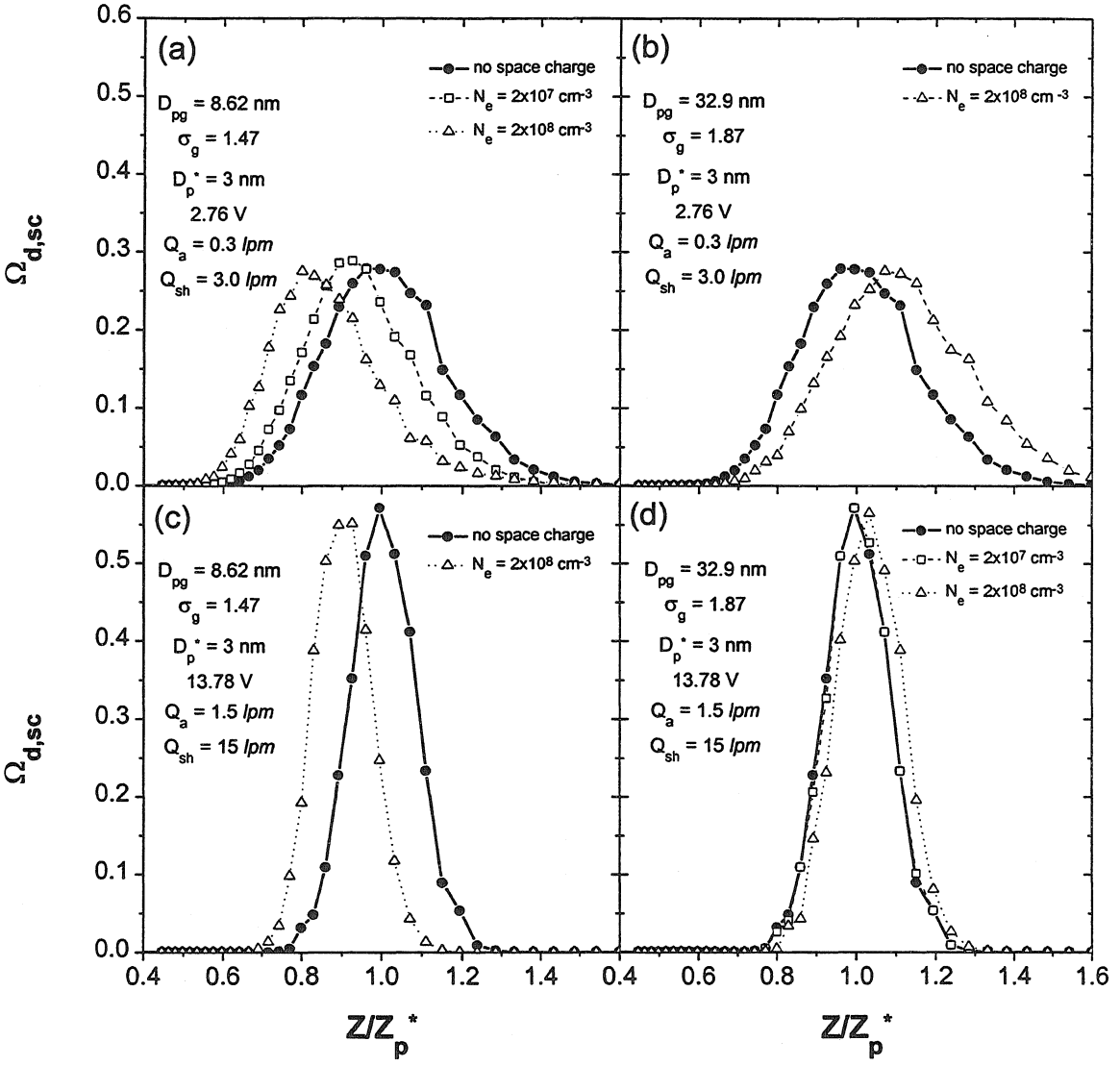

Figure 5.9: Space charge effect calculated for two different size distributions and two different voltages. Predictions for the radial DMA when classifying particles with 3.0 nm diameter.

charge predicted by Fuchs. This leads to a reduction in the field experienced by the migrating particles ($\sim$ 3 nm diameter) and the result is a shift to higher mobilities.

The same trends are predicted when high flow rates are used in the RDMA as shown in Fig. 5.9(c) and (d). The difference is that higher flow rates imply higher applied fields to classify same-sized particles. As a result, the importance of the space charge effect is diminished. Mobility shifts of about 10% are now predicted for a total number concentration of $N_e = 10^8$ cm^{-3} for the case of the narrower size distribution (Fig.5.9(a)). As known from previous calculations, diffusion broadening of the transfer function is significantly limited when higher voltages and flows are employed.

In Fig. 5.10 predictions are shown when particles of 30 nm diameter are classified with voltages of 256 V and 1280 V for low and high flow rates, respectively. As expected, the influence of space charge fields become much smaller. However, if number concentrations above 10^9 cm^{-3} are used, the generated shifts should be measurable in TDMA experiments. Small shifts like these may need to be accounted for in potential high resolution differential mobility analysis. The direction of the mobility shifts seems to follow the opposite trend of the ones noticed in Fig. 5.9. Once again thinking in terms of the charge distribution in the DMA, in Figs. 5.9(a) and (c) shifts are expected to be to higher mobility because the negatively charged particles have been lost and most of the aerosol is ahead of the centroid trajectory ($\sim$ 30 nm particles) reducing the field. The shifts in Figs. 5.9(b) and (d) are towards lower mobilities because the negatively charged particles were lost and most of the

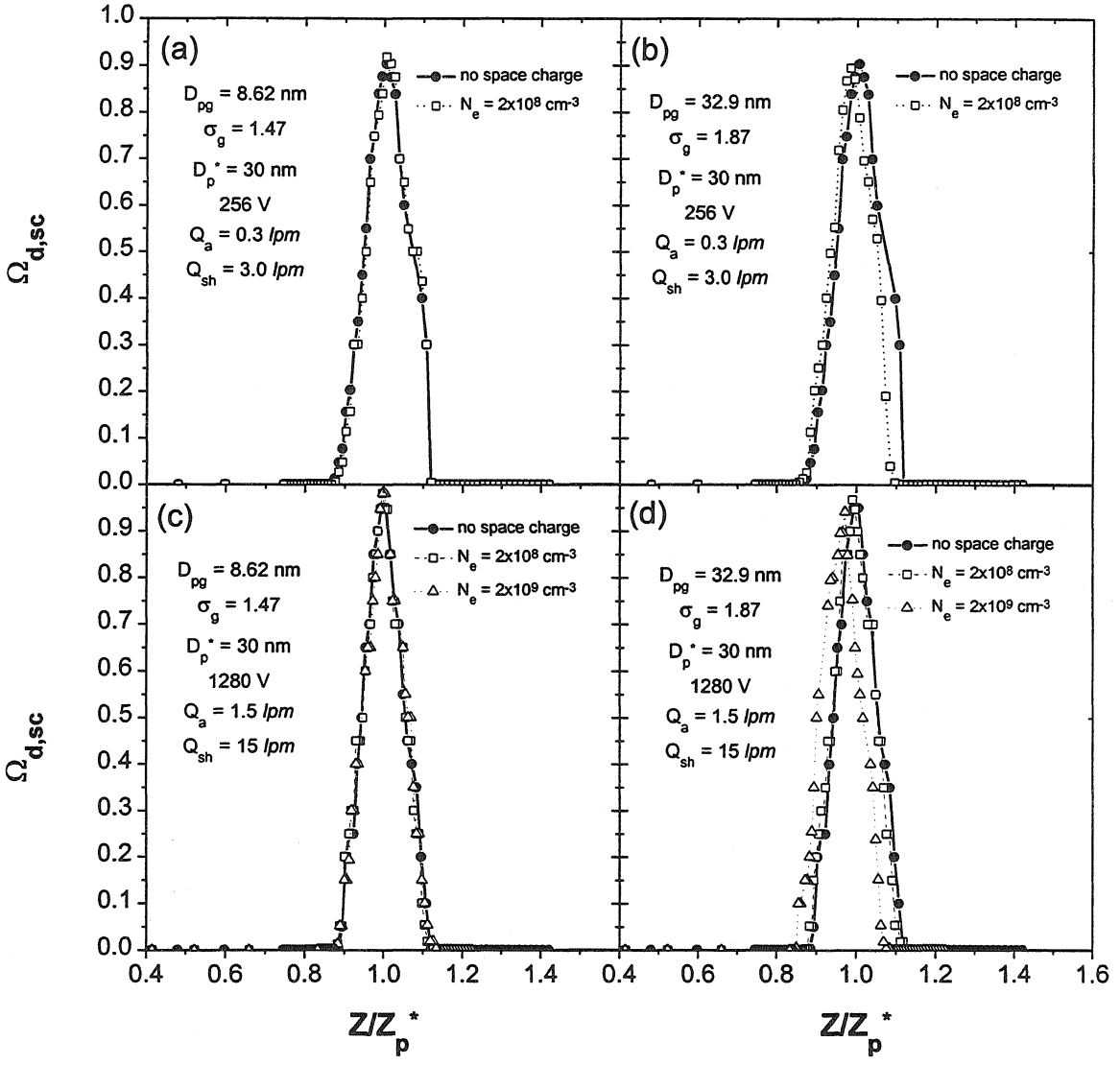

Figure 5.10: Space charge effect calculated for two different size distributions and two different voltages. Predictions for the radial DMA when classifying particles with 30 nm diameter.

aerosol is behind the centroid trajectory enhancing the field.

Figure 5.11 summarizes the results of Figs. 5.9 and 5.10, plotting the resolving power and error in peak location of the RDMA transfer function. Inspection of Fig. 5.11(a) reveals that up to a number concentration of 10^8 cm^{-3}, no reductions in the resolving power of the RDMA are introduced due to the inclusion of space charge effects. Diffusion is the limiting factor for the resolution even when space charge effects introduce changes of as much as 20% in the electric field in the DMA. On the contrary, space charge seems to cause a slight increase in the resolving power. This is probably because under their mutual repulsive field, particles undergoing classification tend to move away from each other compensating some of the diffusion broadening of the transfer function.

The error in peak location, however, is much more sensitive to the space charge effect as indicated in Fig. 5.11(b). Such distortion becomes particularly severe for operation under 20 V or so. The shift in peak location is also dependent on the details of the size distribution. Notice that for the limited set of data points presented in Fig. 8(b), shifts towards higher mobilities are predicted for a size distribution with D_{pg} = 32.9 nm and $\sigma_g = 1.87$ whereas shifts towards lower mobilites are expected when D_{pg} = 8.62 nm and $\sigma_g = 1.47$. It is important to mention that at voltages below 20 V, the direction of the mobility shifts depends strongly on the assumption that the aerosol has Fuchs charge distribution. At these low voltages large particles with negative polarity have a long residence time in the DMA before being lost to the grounded electrode, and that is taken into account by the shifts predicted in Fig. 5.11(b). When

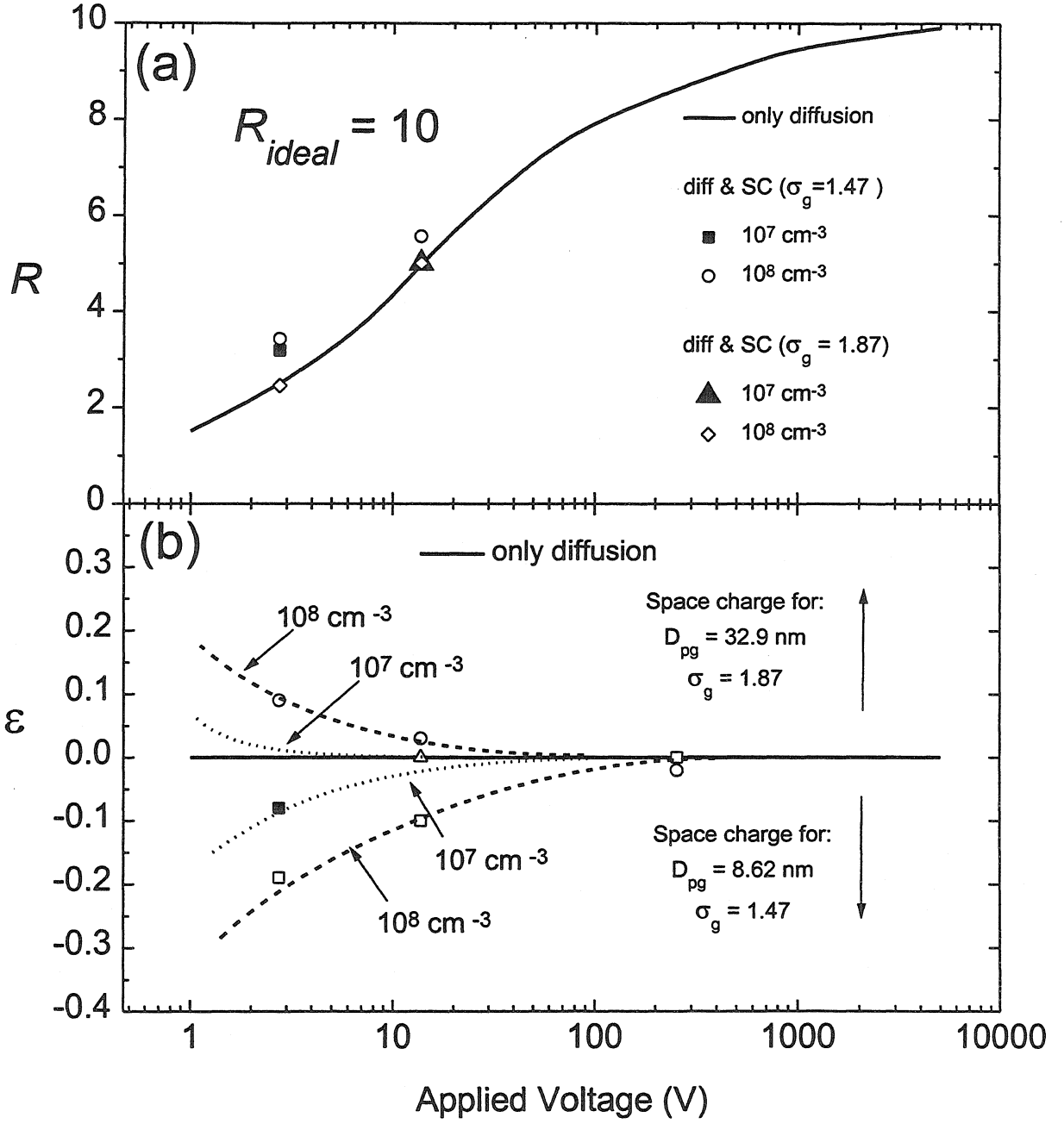

Figure 5.11: Calculated resolving power R and error in peak location $\mathcal{E}$ as a function of applied voltage for the radial differential mobility analyzer at room temperature.

high voltages are used or large particles are absent, the rule of thumb to determine whether the error in peak location is negative or positive involves a simple comparison between the size at which classification is aimed, D_p^*, and the median diameter of the size distribution, D_{pg}. If $D_p^* < D_{pg}$ occur towards lower mobilities (larger particles) due to enhanced field in the region of the centroid trajectory. When $D_p^* > D_{pg}$ shifts occur towards higher mobilities (smaller particles) due to reduced field in the region of the centroid trajectory. This general rule is also valid if a unipolar aerosol is used in the calculations.

Comparison to analytical model

Recently a simplified analytical model has been proposed by Alonso and Kousaka to account for space charge effects in the CDMA [12]. In this model an approximation for the space charge field is obtained assuming that all particles entering the instrument have the same mobility, chosen to be the geometric mean mobility of the incoming size distribution.

The charge density $\rho(r, x)$ is assumed to be constant between certain boundaries $r_a(x)$ and $r_b(x)$ and vanish elsewhere, i.e.,

$$\rho(r,x) = \begin{cases} eN(x), & r_a(x) \leq r \leq r_b(x) \\ 0, & \text{elsewhere} \end{cases} \tag{5.49}$$

where $N(x)$ gives the variation of the particle concentration due to the space charge field along the path as the aerosol traverses the DMA. Assuming that all particles have mobility Z_g, $N(x)$ takes the form

$$N(x) = \frac{N_0}{1 + \frac{N_0 e Z_g}{u\epsilon_0} x} \tag{5.50}$$

with N_0 being the total number concentration, Z_g the geometric mean mobility representing the size distribution of the entering aerosol, and u the average flow velocity.

Using Eqs. 5.49 and 5.50, the solution of Poisson's equation for the CDMA yields a total electric field in the region $r_a(x) \leq r \leq r_b(x)$ given by

$$E(r,x) = -\frac{V_0}{r\ln(r_2/r_1)} + \frac{eN(x)}{2\epsilon_0}\left(r - \frac{r^{*2}}{r}\right) \tag{5.51}$$

where r^* is the point where the space charge field vanishes and is given by

$$r^{*2}(x) = r_a^2 + \frac{\frac{r_b^2(x)-r_a^2(x)}{2} + r_b^2(x)\ln\left(\frac{r_2}{r_b(x)}\right) - r_a^2(x)\ln\left(\frac{r_2}{r_a(x)}\right)}{\ln(r_2/r_1)} \tag{5.52}$$

In these equations, V_0 is the applied voltage and r_1 and r_2 the radius of the inner and outer CDMA electrodes, respectively. In principle, the values of $r_a(x)$ and $r_b(x)$ are needed to calculate the space charge field. A further simplifying approximation can be done by assuming $r^*(x) \approx r_g(x)$, i.e., that the space charge field vanishes at the average particle trajectory, where $r_g(x)$ is given by

$$r_g(x) = \sqrt{r_{20}^2 - \frac{2VZ_g}{u\ln(r_2/r_1)}x} \tag{5.53}$$

with

$$r_{20} = \sqrt{r_2^2 - \frac{Q_a}{Q_a+Q_{sh}}\frac{r_2^2-r_1^2}{2}} \tag{5.54}$$

Figure 5.12 presents a comparison between the space charge effect in the transfer function of the Vienna CDMA, as calculated with Alonso and Kousaka's analytical model and with the self-consistent approach of our work. These calculations were performed assuming a unipolar aerosol with $D_{pg} = 3.2$ nm and $\sigma_g = 1.6$. The flow rates are $Q_a = 6$ lpm and $Q_{sh} = 38$ lpm, and the applied voltage is 3 V ($D_{pg} =$

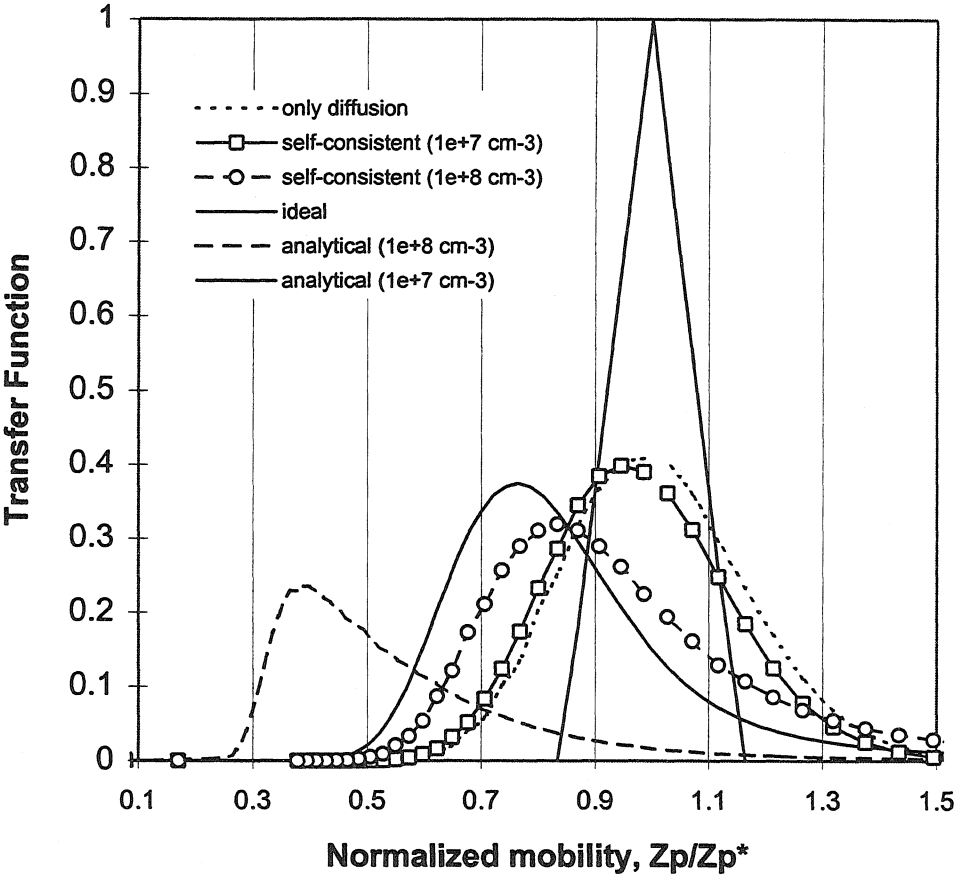

Figure 5.12: Comparison between transfer functions calculated by Alonso and Kousaka's analytical model and by the self-consistent numerical solution developed in this work. Results are for the Vienna CDMA with $Q_a = 6$ lpm, $Q_{sh} = 38$ lpm, and 3 V. The incoming size distribution has $D_{pg} = 3.2$ nm and $\sigma_g = 1.6$. The aerosol is assumed to be unipolar.

1.72 nm). The figure reveals that the analytical model predicts significantly larger shifts than the self-consistent numerical calculation. Mobility shifts of $\sim$ 25% and $\sim$ 60% are predicted by the analytical model for number concentrations of 10^7 cm^{-3} and 10^8 cm^{-3}, respectively. The numerical model predicts more modest peak shifts of $\sim$ 5% and $\sim$ 15% for the same concentrations. According to our discussion about dimensionless groups presented previously in this section, the space charge number for this case takes values of 0.012 and 0.12 for number concentrations of 10^7 cm^{-3} and 10^8 cm^{-3}, respectively. These values of the space charge number are in closer agreement with the predictions of the numerical calculation. This suggests that the analytical model may be overestimating the space charge field in the DMA. In order to verify that, we show in Fig. 5.13 the analytical and the self-consistent total electric field as calculated midway along the length of the Vienna CDMA column for a number concentration of 10^8 cm^{-3}. The figure shows that, when the approximation is made that the field vanishes at $r_g(x)$ in the analytical model ($r^*(x) \approx r_g(x)$), a discrepancy of as much as 400 V/m is observed between the analytical and self-consistent fields. This estimation of a higher field is the reason for the larger shifts predicted by the analytical model. When the value of $r^*(x)$ is calculated directly from Eq. 5.52 using $r_a(x)$ and $r_b(x)$ determined numerically, the analytical and self-consistent fields become essentially the same in the region where most of the particles are ($r_a \leq r \leq r_b$). In this case, the mobility shifts of the analytical transfer function collapse into the ones predicted by the self-consistent calculation.

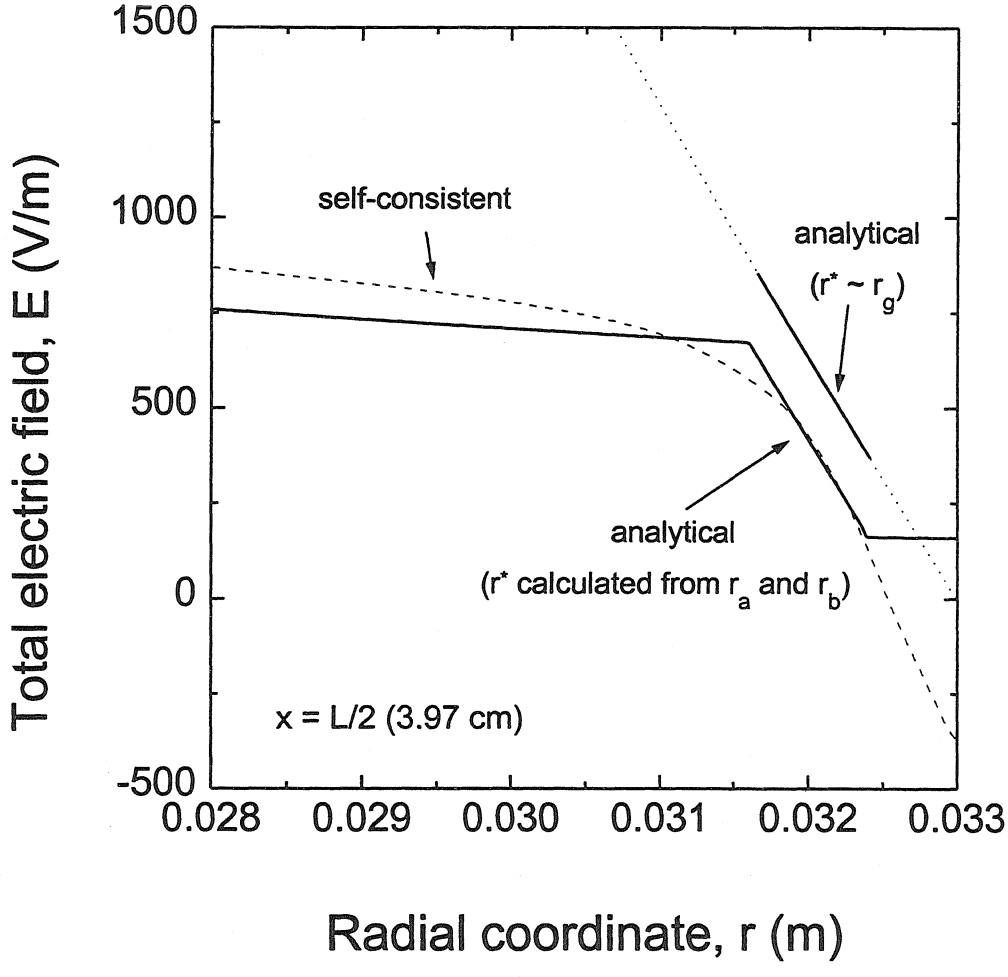

Figure 5.13: Comparison between analytical and self-consistent total field in the Vienna CDMA midway in the analyzer column ($x = L/2$). The conditions are the same of Fig. 5.12.

5.4 Differential mobility analyzer design

From the predictions of the modeling of the previous section, it becomes apparent that the critical parameter that should be optimized to limit space charge distortions and diffusion broadening of the transfer function is the applied voltage. The expressions for the migration Peclet number (Eqs. 5.3 and 5.5) and the space charge number (Eq. 5.14) indicate that for classification at a given size of interest, the maximum possible voltage should be used to minimize diffusion and space charge effects.

Commonly available DMAs are not designed to operate at high voltages in the classification of particles below 10 nm because that implies a severe limitation in their dynamic range. For the specific purpose of synthesizing semiconductor nanocrystals in the 1-10 nm range at high concentrations, however, the DMA design can be optimized to allow the best performance in the size and concentration range of interest. To increase the required applied voltage for sub-10 nm particles, one ought to shorten the classification region and increase the sheath gas flow rate. In Fig. 5.14 we present the sketch of a CDMA with short classification region (L = 1 cm) that, if operated at high flow rates ($\sim$ 25 lpm sheath gas flow), should allow excellent performance with minimum space charge distortions. This design is essentially a shortened version of the CDMA, whose original classification region is about 45 cm long. In principle the classification region could be shortened even below 1 cm, but field and flow distortions at the entrance and exit region may become a problem. The instrument sketched in Fig. 5.14 has been implemented by shortening the column of an existing CDMA. Currently, it is undergoing initial evaluations and a thorough calibration should be

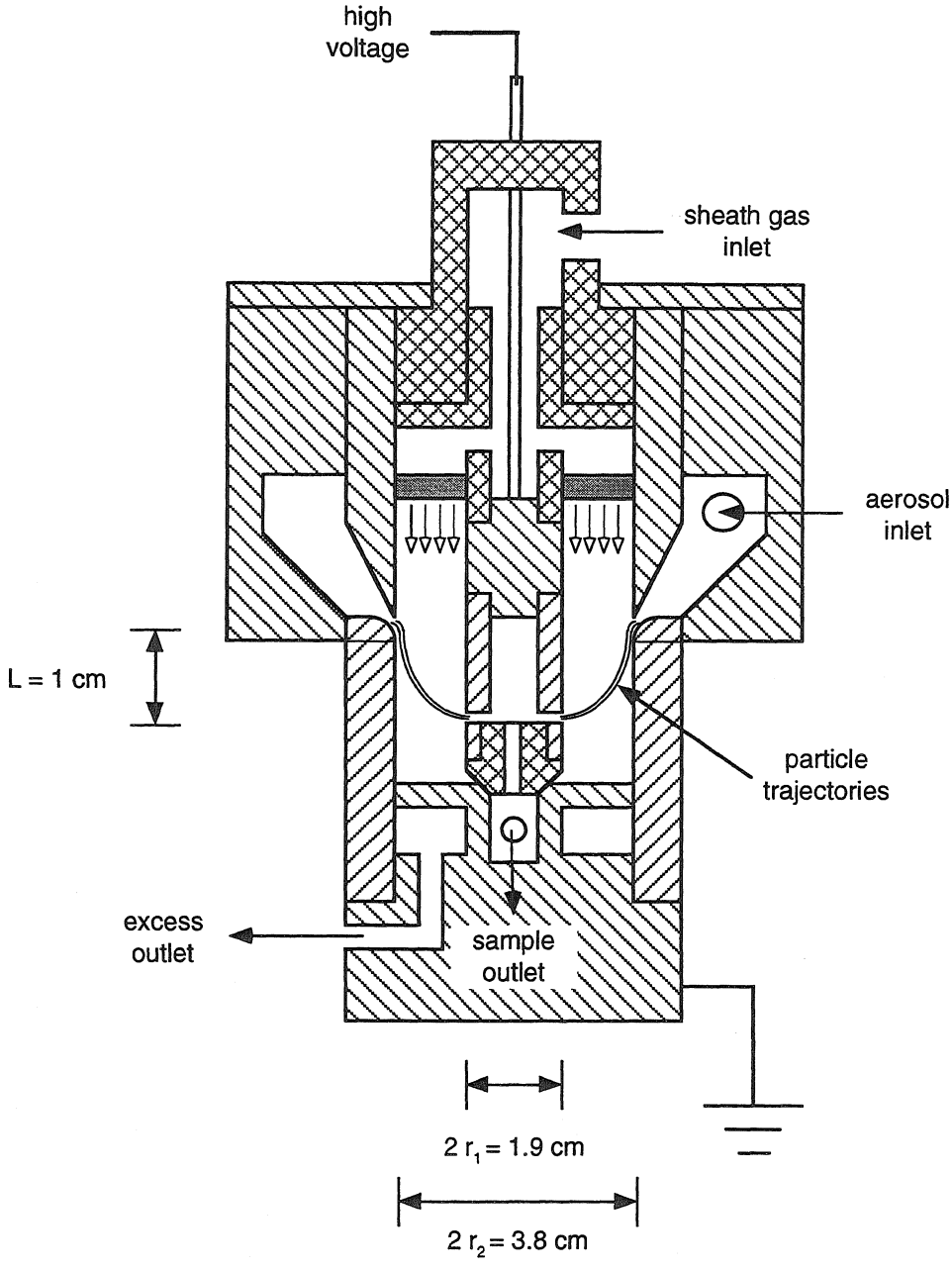

Figure 5.14: Sketch of a cylindrical differential mobility analyzer with short classification region.

performed to determine its performance in the size range of interest.

The voltage required to classify particles of a certain size with this instrument is presented in Fig. 5.15 for a sheath flow rate of 25 lpm. The same relationship for other DMA designs with typical flow rates is also presented for comparison. The short CDMA (SCDMA) of Fig. 5.14 classifies particles in the 2-10 nm size range using voltages between 100 and 1000 V, while the other instruments make use of tens of volts in the same size range.

An evaluation of the effect of space charge fields and diffusion was made for the SCDMA using the self-consistent numerical calculation of previous section. The predictions are presented in Fig. 5.16 for both a bipolar aerosol with Fuchs charge distribution (Fig. 5.16(a)) and a unipolar aerosol (Fig. 5.16(b)). In these simulations, a size distribution with $D_{pg} = 8.62$ nm and $\sigma_g = 1.47$ was used for the aerosol entering the instrument, and classification was done for 3 nm particles using a voltage of 207 V. The figure reveals that operation at these voltages allows classification of 3 nm particles with very little diffusion broadening of the transfer function, increasing the resolving power of the instrument at this size to $R = 8$ from a value of $R = 4.5$ for the RDMA with maximum flow rates. Therefore, this instrument should allow high resolution synthesis of semiconductor nanocrystals. In fact, a similar instrument recently reported in the literature has been demonstrated to be effective also for sizing large ions [2].

In terms of space charge effects, the onset for distortions is predicted to move up in number concentration by approximately two orders of magnitude if compared with

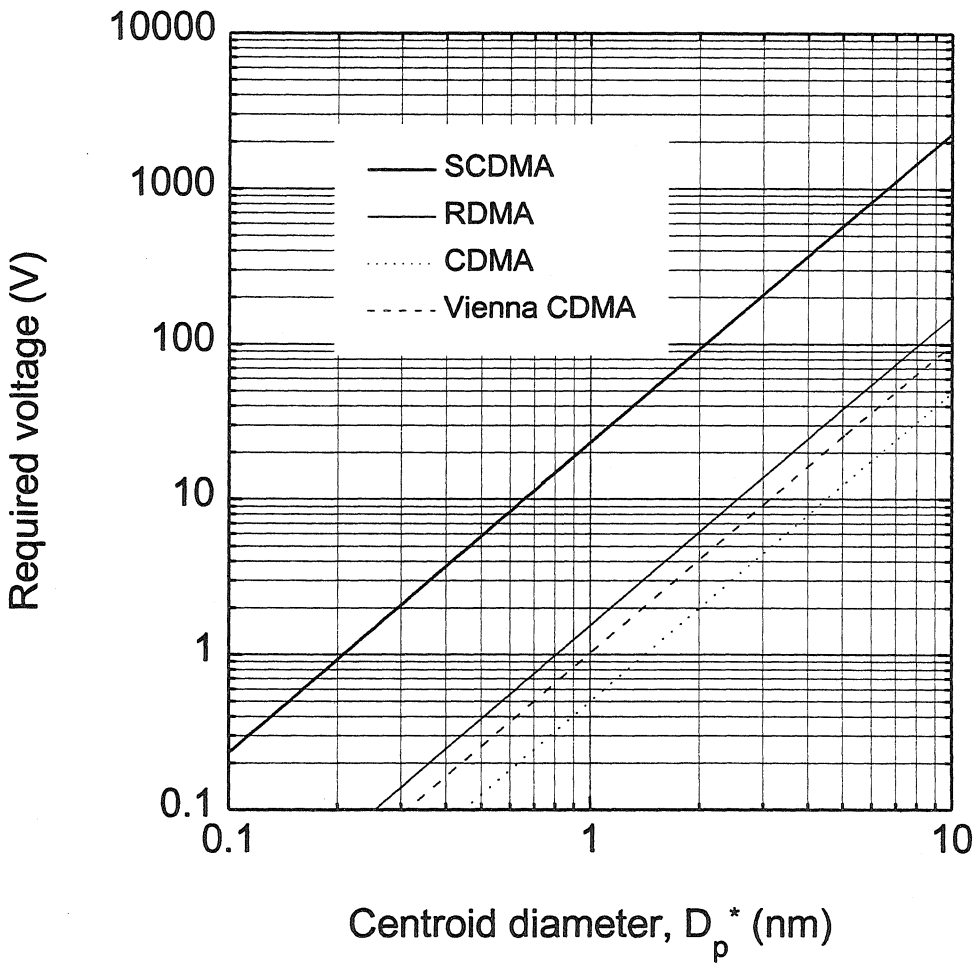

Figure 5.15: Voltage as a function of centroid diameter for the short cylindrical differential mobility analyzer and for other common analyzer designs. The sheath flow rates assumed are: 25 lpm (SCDMA), 15 lpm (RDMA), 25 lpm (CDMA), 38 lpm (Vienna CDMA).

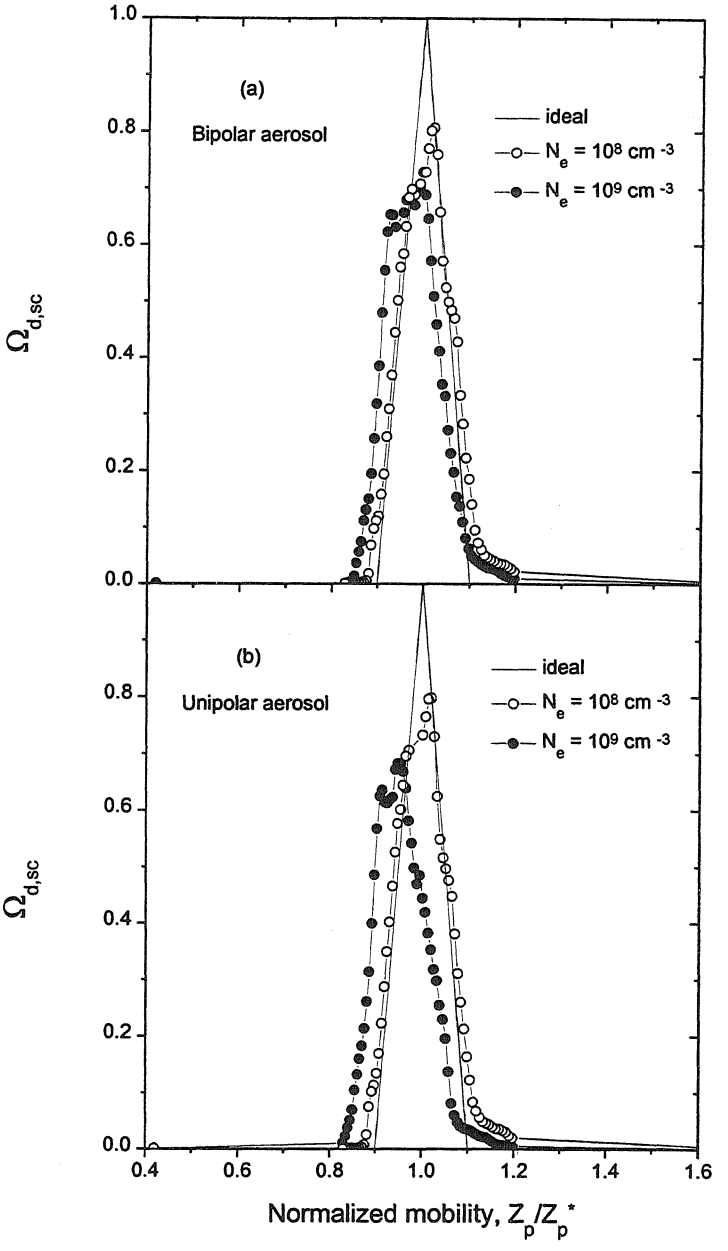

Figure 5.16: Predicted transfer functions for the short cylindrical differential mobility analyzer of Fig. 5.14.

the RDMA. No measurable mobility shifts are predicted for concentrations up to 10^8 cm^{-3}. For concentrations of 10^9 cm^{-3} small shifts of $\sim 3\%$ and $\sim 5\%$ are predicted for the bipolar and unipolar aerosols, respectively. These shifts are significantly smaller than the ones predicted for the RDMA at its optimum operation conditions. In that case, shifts of $\sim 25\%$ in the peak mobility are predicted for a bipolar aerosol with classification at 3 nm.

5.5 Summary

In this chapter we have demonstrated the importance of considering diffusion as well space charge effects in differential mobility analysis. In general, DMAs are operated at typical number concentrations well below 10^5 cm^{-3}. These concentrations are totally consistent with the study of dilute systems that seek to elucidate the dynamics of aerosol populations. Today's condensation nucleus counters have allowed single particle detection down to 3 nm and low concentrations are usually preferred as they are known to avoid space charge effects in the DMAs. For materials processing, however, the operation at higher number concentrations is unavoidable. It is often imperative the production of dense deposits containing *miligrams* of mobility classified particles, which can only be achieved in reasonable times and flow rates if number concentrations well above 10^5 cm^{-3} are utilized.

Self-consistent calculations of the particle transport in the RDMA including Brownian diffusion and space charge effects predict that the resolving power of the instrument does not suffer any reduction due to space charge up to concentrations of 10^9

cm^{-3}. However, serious errors in peak location are expected above 10^7 cm^{-3} if voltages below 10 V are used for classification. In the range of concentrations examined (up to 10^9 cm^{-3}), and using well characterized bipolar and unipolar aerosol charge states, space charge effects manifest themselves by shifts in the peak mobility of the transfer function. In all cases examined, these shifts are below $\sim$ 40%. Severe classification breakdown as described in section 5.2.2 with particles being transmitted even at zero voltage, is, therefore, not expected within this concentration range and charge states. This suggests that when classification breakdown occurs, concentrations above 10^{10} cm^{-3} of highly charged aerosols are present in the RDMA.

Given operation at room temperature, the crucial parameter for the DMA design turns out to be the applied voltage. Analyzers designed to operate at high voltages and high flow rates are the ones to achieve optimum resolving power in the nanometer size regime. The operation at high voltages also guarantees minimum space charge distortions of the mobility classification up to elevated number concentrations, providing the throughputs necessary for the processing of materials.

Bibliography

[1] R. P. Camata, H. A. Atwater, K. J. Vahala, and R. C. Flagan, "Size classification of silicon nanocrystals," *Appl. Phys. Lett.*, vol. 68, pp. 3162–3164, 1996.

[2] J. Rosell-Llompart, I. G. Loscertales, D. Bingham, and J. Fernández de la Mora, "Sizing nanoparticles and ions with a short differential mobility analyzer," *J. Aerosol Sci.*, vol. 27, pp. 695–719, 1996.

[3] E. O. Knutson and K. T. Whitby, "Aerosol classification by electric mobility: apparatus, theory, and applications," *J. Aerosol Sci.*, vol. 6, pp. 453–460, 1975.

[4] G. P. Reischl, "The relationship of input and output aerosol characteristics for an ideal differential mobility analyzer particle standard," *J. Aerosol Sci.*, vol. 22, pp. 297–312, 1991.

[5] W. Winklmayr, G. P. Reischl, A. O. Lidner, and A. Berner, "A new electromobility spectrometer for the measurement of aerosol size distributions in the size range from 1 to 1000 nm," *J. Aerosol Sci.*, vol. 22, pp. 289–296, 1991.

[6] B. Mesbah, "Le Spectrometre de Mobilite Electrique Circulaire: Theorie, Performances et Applications," Ph.D. Thesis, University of Paris, 1994.

[7] S. -H. Zhang, Y. Akutsu, L. M. Russell, R. C. Flagan, and J. H. Seinfeld, "Radial Differential Mobility Analyzer," *Aerosol Sci. Technol.*, vol. 23, pp. 357–372, 1995.

[8] Y. Kousaka, K. Okuyama, M. Adachi, and T. Mimura, "Effect of Brownian diffusion on electrical classification of ultrafine aerosol particles in Differential Mobility Analyzer," *J. Chem. Eng. Japan*, vol. 19, pp. 401–407, 1986.

[9] M. R. Stolzenburg, "An Ultrafine Aerosol Size Distribution Measuring System," Ph.D. Thesis, University of Minnesota, 1988.

[10] S. -H. Zhang and R. C. Flagan, "Resolution of the radial differential mobility analyzer," *J. Aerosol Sci.*, vol. 27, pp. 1179–1200, 1996.

[11] H. F. Tammet, *The aspiration method for the determination of atmospheric-ion spectra*, Israel Program for Scientific Translations, Jerusalem, 1970 (original work in Russian published in 1967).

[12] M. Alonso and Y. Kousaka, "Mobility shift in the Differential Mobility Analyzer due to Brownian Diffusion and space-charge effects," *J. Aerosol Sci.*, vol. 27, pp. 1201–1225, 1996.

Chapter 6

Optical properties of aerosol synthesized silicon nanocrystals

6.1 Introduction

Visible photoluminescence (PL) and electroluminescence from silicon (Si) nanocrystals have been demonstrated during the past few years [1, 2, 3, 4]. Numerous investigations of this luminescence have been carried out, motivated by the potential device applications of this new material, and in the attempt to understand the physical phenomena responsible for this behavior.

The study of the luminescence mechanisms in Si nanocrystals has been one of the motivating factors throughout this thesis work. As discussed in chapter 2, the complexity of the interfacial region of free-standing, air-exposed Si nanocrystals calls for different possible origins for the luminescence. Quantum confinement in the crystallites, defects in the oxide layer, and hydrogen related states may all contribute

to the optical properties of these structures. The large inhomogeneity in nanocrystal size and shape, present in typical samples, introduce further complications. In the work presented in previous chapters, a significant effort was made to control the nanocrystal size. This was done in the attempt to tune size-dependent optical properties, and reduce ambiguities in the interpretation of optical data. However, the optical characterization of size-classified deposits has proved more challenging than anticipated, owing to low nanocrystal concentration and instability upon air exposure. Consequently, the results presented in this chapter are partial. Nevertheless, the measurements performed show some general trends in the optical properties of size-classified and polydisperse silicon nanocrystals, that may be useful as new and more definite results become available in the future.

Although limited in its conclusions, this chapter represents the continuing effort to characterize the optical properties of Si nanocrystals synthesized and processed by aerosol techniques.

6.2 Room temperature photoluminescence setup

The optical properties of nanocrystal samples were probed by room temperature photoluminescence measurements. The experimental setup utilized for the measurements is shown schematically in Fig. 6.1. Samples are excited using the 457 nm or 488 nm spectral lines of an Ar^+ ion laser. A prism and a slit are used in the excitation beam to eliminate unwanted fluorescence lines of the laser in the red and violet spectral regions. The detection is done using either a photomultiplier tube, for serial data ac-

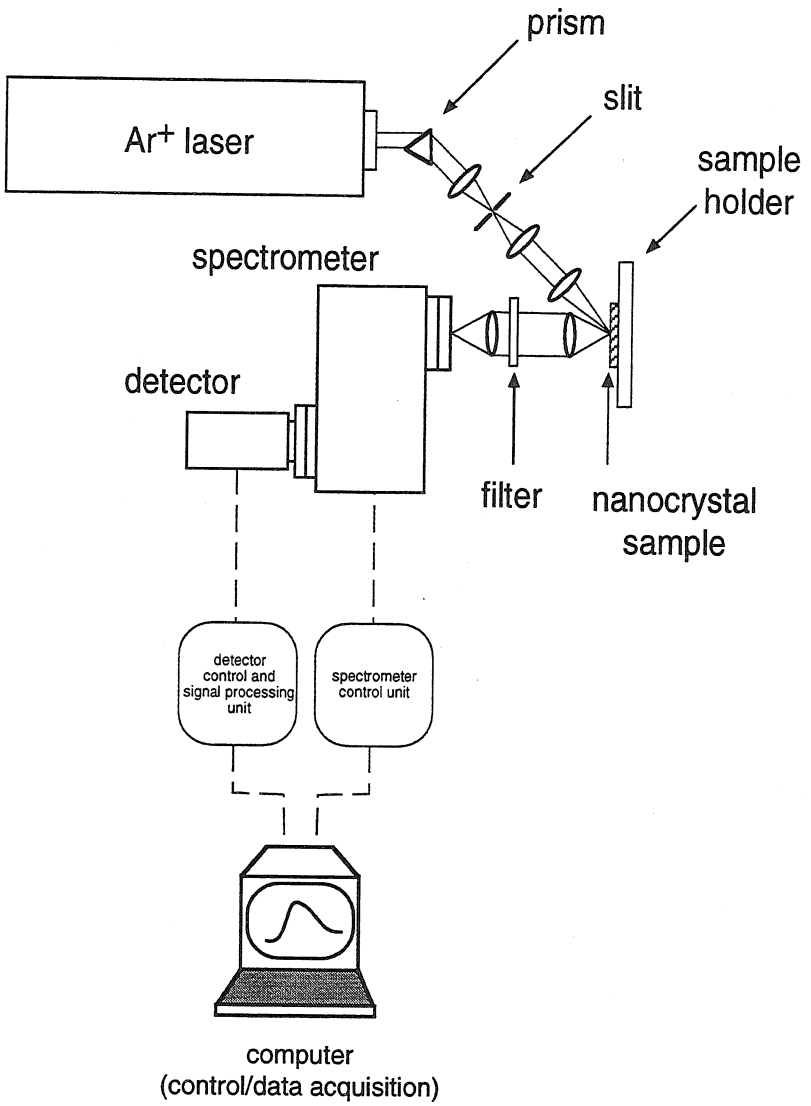

Figure 6.1: Experimental setup for room temperature photoluminescence measurements. The detector was, alternatively, a photomultiplier tube (serial data acquisition and signal processing with a lock-in amplifier) or a charged coupled device (CCD) camera (parallel data acquisition).

quisition, or a charged coupled device camera, for parallel data acquisition. When the photomultiplier tube is used, conventional signal processing is employed, i.e., optical chopper, pre-amplifier, and lock-in amplifier. With the camera, exposure times up to several minutes often help overcome low signal-to-noise problems. In both cases, the experimental data is corrected for the system response based on calibrations using a blackbody radiation source.

6.3 Polydisperse silicon nanocrystals

As described in section 4.3.2, polydisperse nanocrystal samples are characterized by large chains of agglomerated nanoparticles with the primary particle size in the 3-10 nm range. In the case of samples generated by laser ablation, a significant population of micron-sized crystallites is also present. These polydisperse samples invariably exhibit broadband room temperature PL in the 650-900 nm spectral region. An example of this PL is shown in Fig. 6.2 for a sample generated by spark ablation and collected by thermophoresis on a bulk Si substrate. In this case the PL measurement was performed in air and the excitation was done over a spot size of approximately 1 mm^2. As shown in the figure, the PL efficiency decreases as a function of increasing excitation power. As radiative recombination times in Si nanocrystals with 3 nm are calculated to be in the hundreds of microseconds range (Fig. 2.4(b)), this power saturation might be lifetime-related.

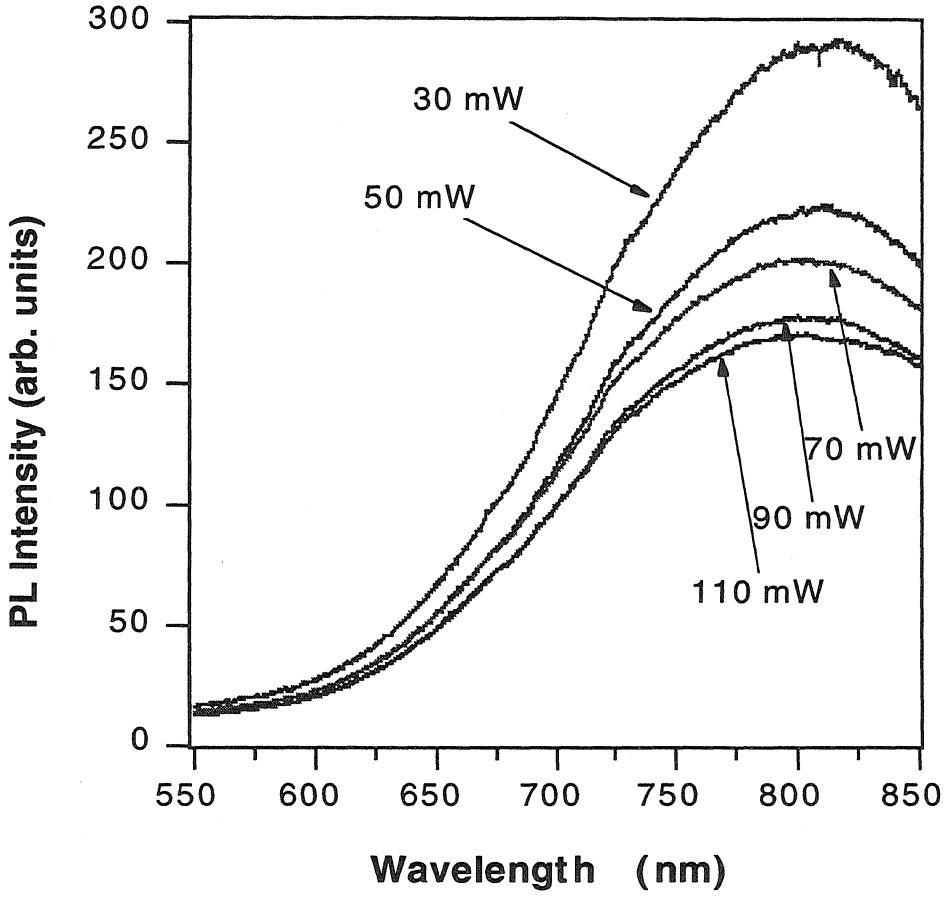

Figure 6.2: Room temperature photoluminescence as a function of excitation power from a sample of polydisperse silicon nanocrystals produced by spark ablation. Data normalized to excitation power. Excitation over a spot size of $\sim$ 1 mm^2 (The morphology of this sample is shown is Fig. 4.3).

6.3.1 Aging of air-exposed polydisperse nanocrystals

When removed from the inert gas synthesis chamber, polydisperse samples exhibit little or no luminescence. Upon air exposure, however, the luminescence efficiency increases dramatically. Figure 6.3 shows how the PL spectrum of a polydisperse sample evolves as it ages in air for an excitation power density of $\sim$ 200 mW/mm^2 at a wavelength of 457 nm.

The change in PL efficiency due to air exposure over a longer period of time may be seen in Fig. 6.4 for the same excitation conditions of Fig. 6.3. In this case measurements were made on two samples, generated simultaneously under identical conditions. One of them was continuously exposed to air after synthesis, while the other was kept in a vacuum chamber under inert gas atmosphere. Both samples were then subjected to periodic room temperature PL measurements in air. The sample kept under inert gas was, therefore, briefly exposed to air at times to undergo the PL data acquisition. Figure 6.4 shows a comparison between the PL time evolution of these two samples. For a wavelength of 780 nm, the sample exposed to air exhibits PL that increases up to $\sim$ 70 hours after the initial air exposure. The PL eventually decreases and reaches an equilibrium value that seems to be stable for years. The increase in PL intensity is slower for the sample kept under inert gas atmosphere. Up to 250 hours its intensity has not reached the maximum observed for the sample continuously exposed to air. As no intensity reduction is observed either, it is likely that the sample under inert atmosphere reproduces the result of the first sample, but with a time lag of $\sim$ 200 hours.

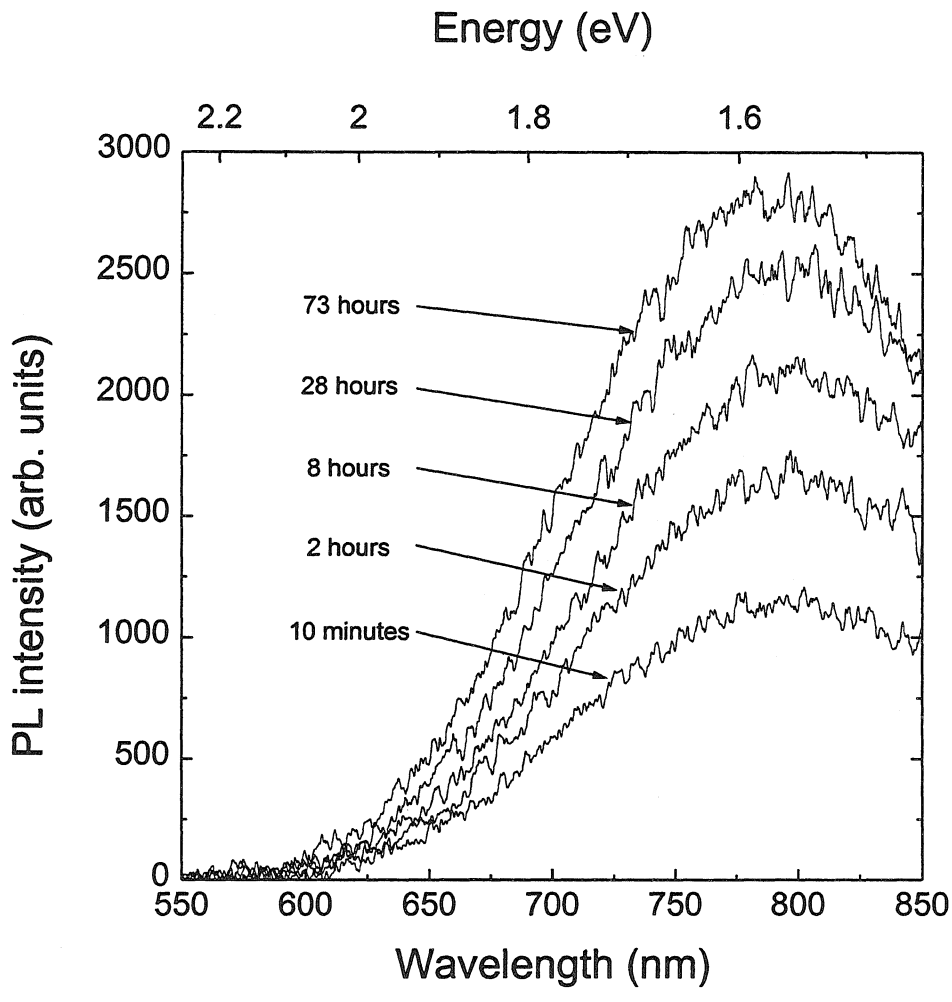

Figure 6.3: Photoluminescence from polydisperse silicon nanocrystals as a function of air exposure time, for an excitation power density of $\sim$ 200 mW/mm^2 at a wavelength of 457 nm.

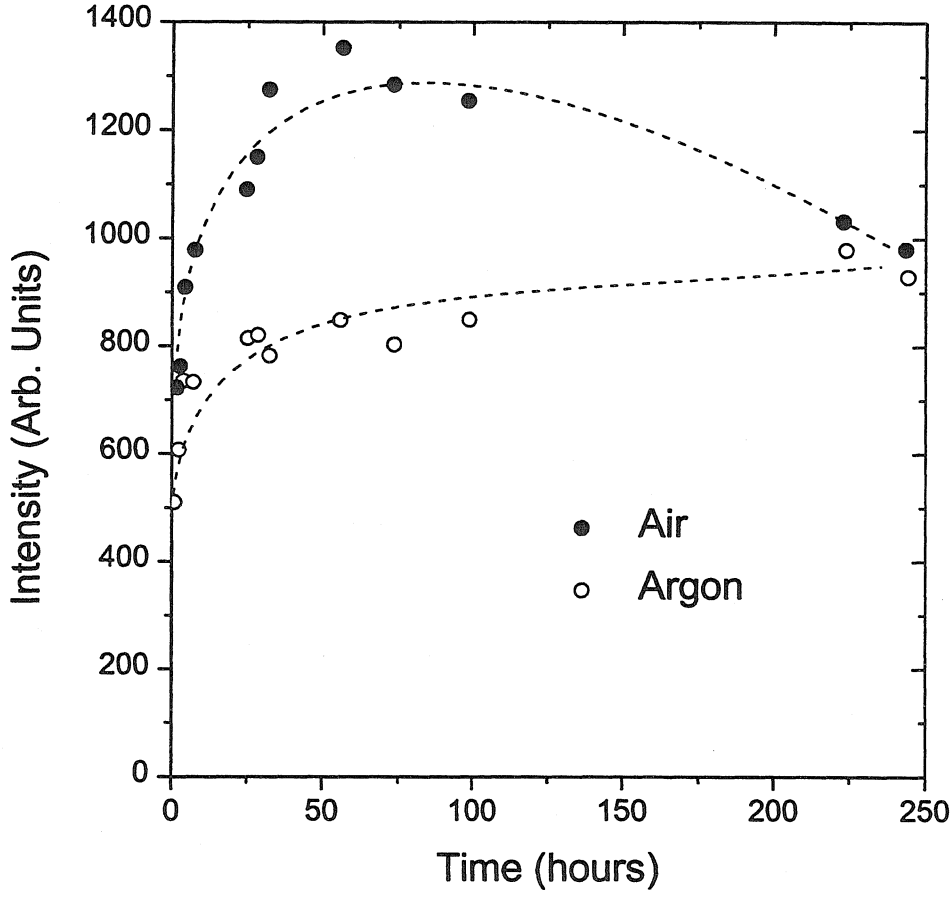

Figure 6.4: Photoluminescence from polydisperse silicon nanocrystals as a function of air exposure time observed for a wavelength of 780 nm. Comparison between a sample continuosly exposed to air and another kept under inert gas atmosphere and exposed to air only during measurement. The excitation conditions are the same as in Fig. 6.3.

The growth of a native oxide on the Si nanocrystals upon air exposure is certainly one of the phenomena that occurs at the same time that the PL intensity is observed to increase. To probe the nanocrystal oxidation, we have used Si 2p core level x-ray photoelectron spectroscopy (XPS) performed using 1487 eV Al $K\ \alpha$ radiation at a resolution of about 0.7 eV. The correlation between XPS and PL measurements on samples exposed to air for 50 minutes and 244 hours is shown in Fig. 6.5. The XPS measurements present spectral features for both oxidized and unoxidized states on the nanocrystals. Oxidized Si states have electron binding energies in the 100-103 eV range, while signals from unoxidized states are found at a binding energy of $\sim$ 99 eV. In thin, uniform thickness SiO_2 films on Si, the relative intensities of the oxidized and unoxidized features, or peaks, can be used to estimate the oxide thickness [9]. In the case of Si nanocrystals covered by an oxide layer, similar estimates are more complicated because the assumption of uniform thickness cannot be made. Furthermore, differences in surface-to-volume ratio are also expected to influence the results. Nevertheless, in this and the following sections, we will use these relative intensities to obtain a very rough estimate of the average oxide thickness in our samples. For this purpose, we will assume that the unoxidized peak is generated by photoelectrons from the nanocrystal core and the oxidized states lie in the surface oxide. This assumption, used with the established calculation procedure for thin SiO_2 films on Si [9], probably overestimates the oxide thickness due to the large surface-to-volume ratio of the nanocrystals. Therefore, the estimated thickness values are only a guide for qualitative comparisons of samples with similar morphologies, and should

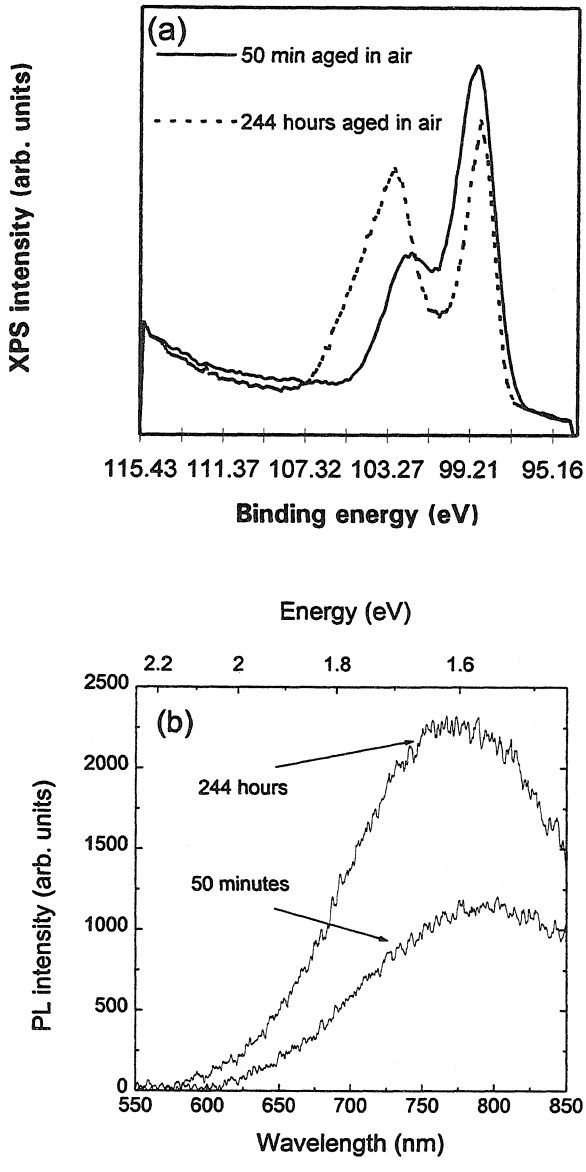

Figure 6.5: (a) X-ray photoelectron and (b) photoluminescence measurements on samples aged in air for 50 minutes and for 244 hours. Photoelectron measurements at a resolution of $\sim$ 0.7 eV and luminescence due to an excitation of $\sim$ 200 mW/mm^2 at 457 nm.

not be interpreted in an absolute sense.

Adopting an escape depth value of 2.6 nm for photoelectrons in SiO_2 [8], an oxide thickness equivalent to what would be obtained from a 1.7 nm thick continuous oxide film is estimated in the sample exposed for 50 minutes. The same estimate for the sample exposed for 244 hours gives an equivalent oxide thickness of 3.9 nm. Furthermore, the peak corresponding to the oxidized Si 2p core level shifts from an average position at $\sim$ 102 eV in the sample exposed to air for 50 minutes to $\sim$ 103 eV in the sample aged for 244 hours. This peak shift is associated with a change in the overall oxidation state of the silicon atoms on the nanocrystal surface [6]. Thus, as aging progresses, one moves from a suboxide in the 50-minute sample, towards a stoichiometric oxide in the 244-hour sample. Even for this last aging time, however, it is evident from the width of the XPS feature that low oxidation states are still present. This reveals that a fully stoichiometric oxide has not yet been achieved. At the same time that the oxide evolves in this manner, an overall increase of about a factor of 3 is observed in PL intensity (Fig. 6.5).

It is clear, therefore, that the growth of a native silicon oxide layer on the nanocrystals plays an important role in the observed PL. The PL seems to increase as the oxide thickens and moves towards the stoichiometry of SiO_2.

An increase in PL intensity is also observed upon nanocrystal re-oxidation following chemical etching of the oxide layer. A polydisperse Si nanocrystal sample made by laser ablation was treated in a 48% aqueous solution of hydrofluoric acid (HF) for 10 seconds (1000 Å/min etch rate for SiO_2). In Fig. 6.6 we show the effect of air

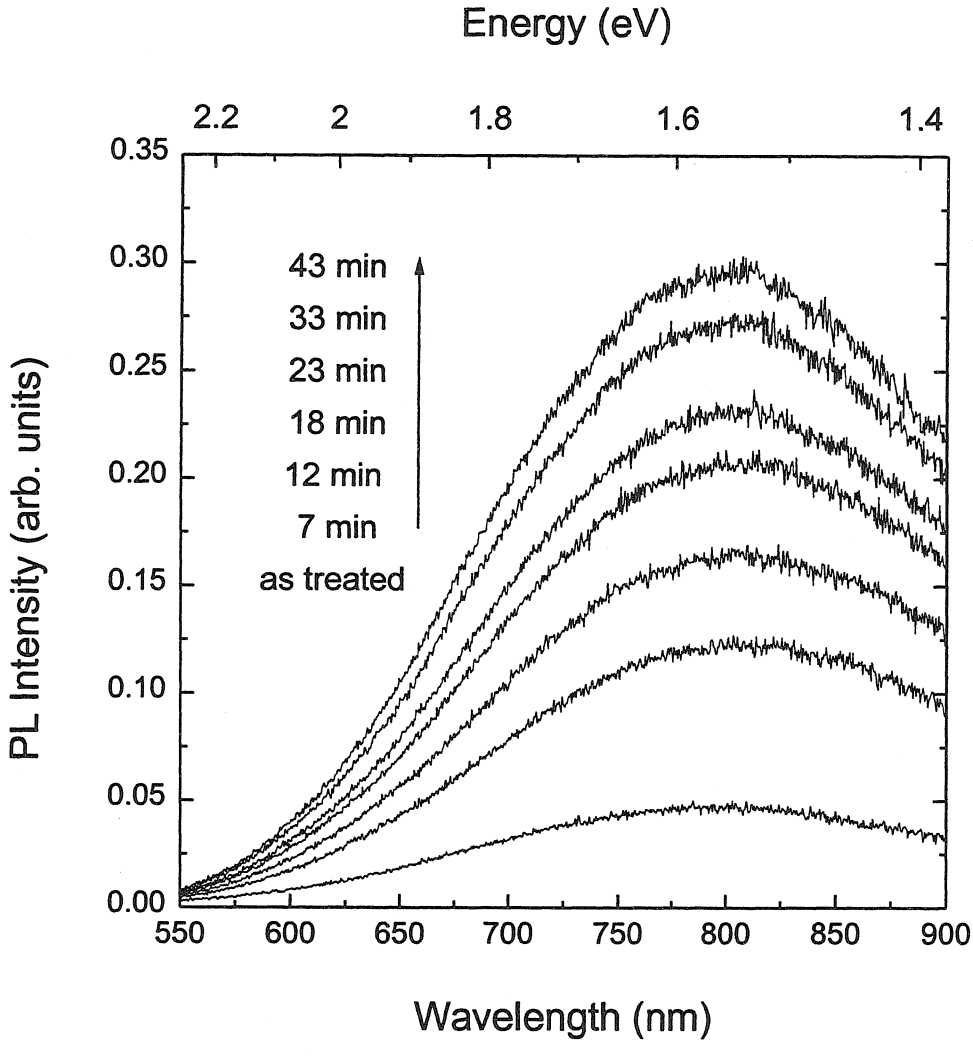

Figure 6.6: Photoluminescence recovery of polydisperse silicon nanocrystals upon air exposure under laser irradiation after HF treatment. Excitation power density of ~ 10 mW/mm^2 at 457 nm.

exposure under laser irradiation on the PL of this sample. Dipping in the HF solution causes a decrease in PL intensity of about two orders of magnitude (not shown in figure) owing, at least in part, to the loss of material to the liquid medium. Upon air exposure under laser irradiation, however, the PL intensity recovers, and a tenfold increase is observed in the first 43 min after HF treatment.

Based on these observations of the correlation between surface oxidation and increase in PL, one might speculate that the PL originates from the recombination of quantum confined excitons, which becomes more efficient due to increased confinement and improved surface passivation. However, the low temperature oxidation of Si is bound to generate large concentrations of defects that may be optically active in the analyzed spectral region [10]. Photoluminescence from such defects would also scale with oxide thickness. Furthermore, OH groups adsorbed from the atmosphere might also play a role in stabilizing oxide defects [11], or form optically active siloxene-like compounds [12]. Photoluminescence lifetime measurements on these samples would be helpful to distinguish these different possible origins for the luminescence.

6.3.2 Effect of deuteration on the photoluminescence

Hydrogenation is a useful tool in the study of passivation effects in semiconductors. In Si and Ge nanocrystals embedded in glass matrices, hydrogenation has been instrumental in distinguishing luminescence from quantum confined and defect-related states [4, 5].

Following the procedure proposed by Min et al. [5], we have performed a passivation experiment on aerosol synthesized polydisperse Si nanocrystals using deuterium

(D). Deuterium is preferable to hydrogen in these experiments as it allows more accurate concentration determination. The experiment was performed employing a Kauffman ion beam source at a beam energy of 400 eV. Using the TRIM code [7], the projected range of 400 eV D^+ ions in SiO_2 and Si is estimated to be about 10 nm, with a FWHM of 5 nm. This implantation profile, associated with the fast diffusion of these species in Si and SiO_2 at room temperature [13], should provide enough range for the D^+ ions to passivate nanocrystals throughout entire samples.

Figure 6.7 shows the effect of deuteration on a polydisperse Si nanocrystal sample made by laser ablation. A D^+ dose in the $10^{14}/cm^2$ range was used, as estimated from elastic recoil spectrometry calibrations using a 2 MeV $^4He^{++}$ beam. The overall effect of deuteration is a reduction by approximately a factor of 5 in the PL intensity. It should be pointed out, however, that a different trend is observed for the spectral region below $\sim$ 575 nm. Although PL in that range is originally much weaker than in the 700-800 nm range, an apparent increase in the PL is observed upon deuteration. Evidently, caution must be exercised when comparing PL intensities if the sample has been moved or conditions changed. In this case, although the experimental conditions were the same, the sample was transferred into a vacuum chamber where the deuteration was performed, being subsequently moved back in the PL setup. As a result, PL is probably not being sampled from exactly the same location on the sample. Therefore, one can affirm with confidence that the factor of 5 drop in the overall spectrum is real, but the slight PL increase below $\sim$ 575 nm might be an artifact (inset of Fig. 6.7).

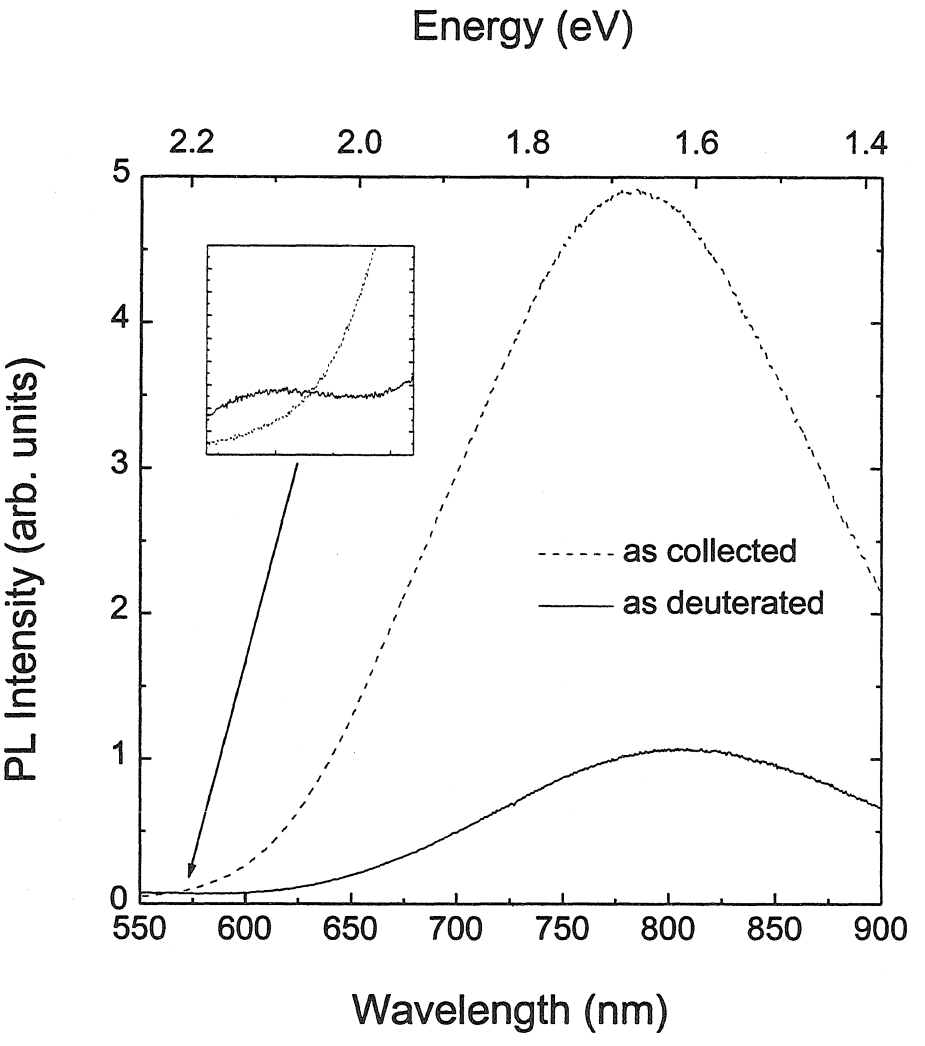

Figure 6.7: Effect of deuteration on the photoluminescence of polydisperse silicon nanocrystals by laser ablation. Excitation power density of $\sim$ 10 mW/mm^2 at 457 nm.

Upon air exposure and laser irradiation, the PL intensity of the deuterated sample undergoes further changes as shown in Fig. 6.8. In the spectral range from 600 to 900 nm the PL recovers to about 40% of its original value during the first 35 minutes. In the region below 600 nm, however, a clear drop in the PL is observed towards the intensity before deuteration. In this case there are no ambiguities in the interpretation of the PL intensities because the sample position and the experimental conditions were constant throughout the experiment. The intensity drop below 600 nm is evidence that indeed a different regime exists in that spectral range as suggested by Fig. 6.7. These measurements show evidence that more than one luminescence mechanism are at work in the nanocrystals, and that upon deuteration, the efficiency of one process is enhanced while the other is inhibited. The limited scope of the experiment, however, does not allow any definite statements regarding the origin of the PL. Once again, as quantum confinement-related emission has PL lifetimes much longer than defect-related luminescence (Fig. 2.4(b)) [4], measurements of the radiative decay rates in these samples would be very useful. They may allow us to determine whether quantum confinement in the nanocrystals or defects in the oxide layer can be ascribed to the observed PL bands.

6.4 Size-classified silicon nanocrystals

Polydisperse nanocrystal samples exhibit PL signals that are easy to detect due to their elevated nanocrystal concentration ($> 10^{14}$ cm^{-2}). In size-classified samples, however, the study of the optical properties is more challenging as the concentration

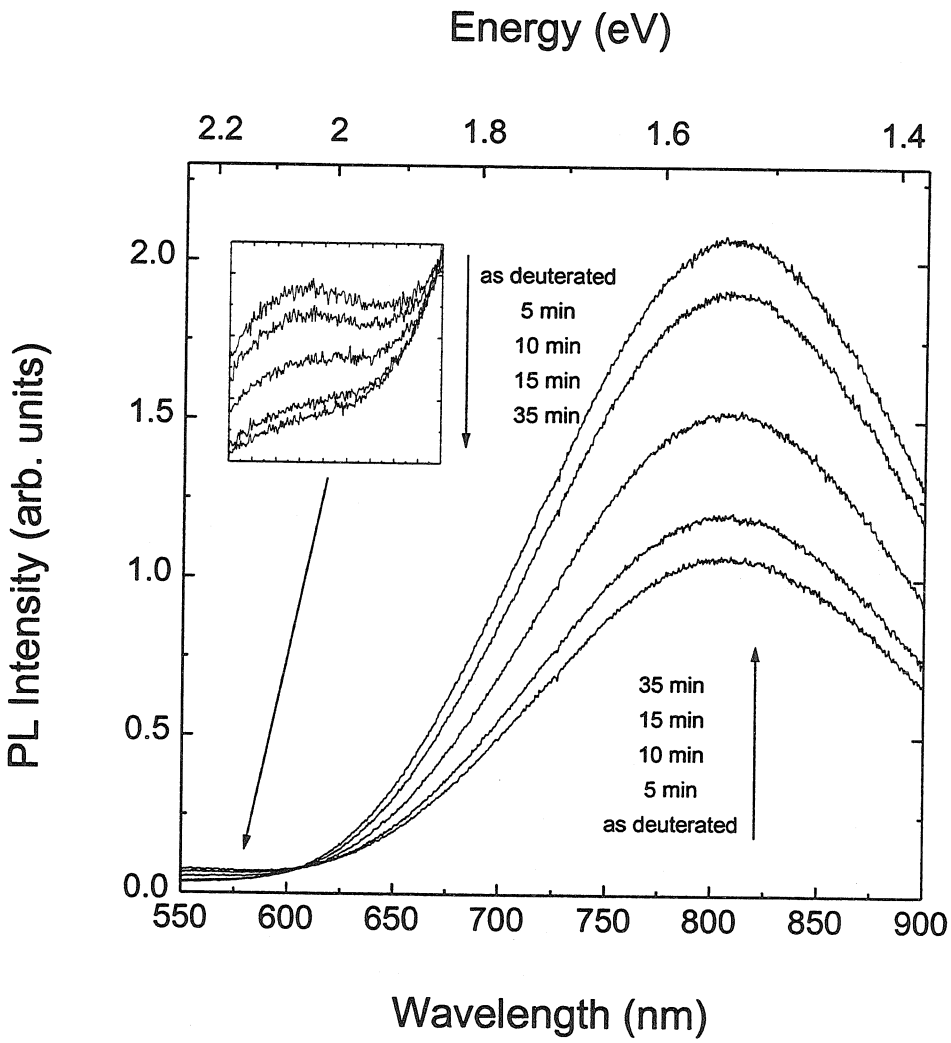

Figure 6.8: Changes in the photoluminescence of deuterated nanocrystals upon air exposure and laser irradiation. Intensity scale and excitation conditions identical to Fig. 6.7.

of the deposits is in the 10^{11} cm^{-2} range. To overcome this problem, we have operated the system of Fig. 4.1 at its maximum number concentration (1-5$\times 10^5$ cm^{-3}) for periods of time up to 18 hours. These long hours of operation allow the generation of deposits with coverages close to one monolayer of nanocrystals, enabling PL data acquisition.

The post-synthesis oxidation upon air exposure is another problem that requires careful consideration in size-classified nanocrystals. As we shall see in what follows, an *in situ* approach is necessary to properly characterize and process these particles. To meet this requirement, a system for *in situ* synthesis and characterization of size-classified nanocrystals is designed and implemented.

6.4.1 Photoluminescence of air-exposed size-classified nanocrystals

In order to perform PL measurements on size-classified Si nanocrystals, a high coverage sample, size classified for 10 nm, was generated. For that purpose, the setup of Fig. 4.1 was used with the laser ablation source. The collection was done with the electrostatic precipitator on a germanium substrate, and the obtained deposit is estimated to have a coverage of approximately one nanocrystal monolayer.

The PL from this sample was acquired in air, and the spectra obtained for an excitation power density of $\sim$ 40 mW/mm^2 at 457 nm are shown in Fig. 6.9(a). For comparison, the spectrum of a polydisperse Si nanocrystal sample is also shown. The spectrum of the size-classified sample presents two luminescence bands. One band is identified in the 500-600 nm spectral region and another in the 700-800 nm region. This behavior is different from the one observed for polydisperse nanocrystals

which have a single broad luminescence feature in the 700-900 nm range. Upon laser irradiation, the PL band in the 500-600 nm range decreases in intensity while the band in the 700-800 nm range is unaltered. Photoluminescence measurements made under the same conditions several days later show the complete disappearance of the 700-800 nm luminescence feature.

These measurements suggest that more than one mechanism is involved in the luminescence of this size-classified sample. One that is attenuated under laser irradiation but essentially stable when unperturbed, and another that is unaffected by laser irradiation but is only stable for a few days. This behavior may be consistent with radiative recombination of excitons in nanocrystals giving rise to the PL band in the 700-800 nm spectral region and defects in SiO_x generating the luminescence in the 500-600 nm range. Photo-induced oxidation might lead to a reduction in the number of defects causing the observed drop in the 500-600 nm feature upon laser irradiation. On the other hand, the complete oxidation of nanocrystals after several days might cause the depletion of the 700-800 nm band.

In an attempt to clarify the observed PL and probe the degree of oxidation of this sample, Si 2p core level XPS measurements at a resolution of $\sim$ 1 eV were performed. The results are shown in Fig. 6.9(b). The spectrum is dominated by the signal of the oxidized states. A very weak unoxidized feature also seems to be present. Based on the observed relative peak intensities and in a 2.6 nm escape depth of photoelectrons in SiO_2 [8], an estimated oxide thickness in excess of 9 nm is obtained. As the particles were size-classified for 10 nm, this seems to suggest their complete oxida-

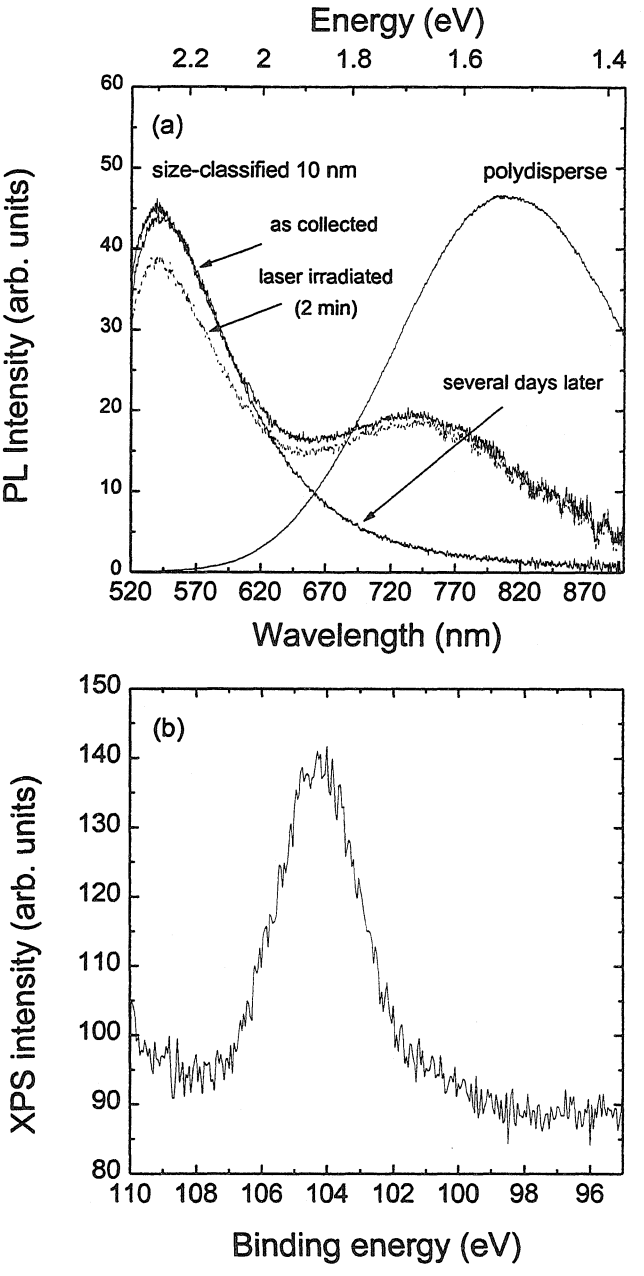

Figure 6.9: (a) Photoluminescence and (b) x-ray photoelectron measurements on air-exposed size-classified silicon nanocrystals generated by laser ablation. Size-classification was performed at 10 nm. The resolution of the photoelectron measurement was $\sim$ 1 eV.

tion. As previously discussed, however, the calculated oxide thickness may be grossly overestimated due to the large surface-to-volume ratio of the 10 nm particles. Therefore, it is difficult to determine whether the weak unoxidized feature observed in the XPS spectrum is attributable to a silicon-rich oxide, or whether a small nanocrystal core still exists embedded in the particles. Although XPS measurements are useful in probing the nanocrystal oxidation, information regarding the oxide thickness can only be retrieved while an unoxidized feature is detectable. When the unoxidized peak is absent, no definite statements can be made by XPS alone. The nanocrystal may have been completely oxidized, or electrons from a Si core may not be able to escape through the oxide. A combination of XPS measurements and carefully controlled HF etching cycles would be an alternative to decide between these possibilities.

It is clear, therefore, that measurements on air-exposed size-classified samples are difficult to interpret. The loss of thickness information on XPS, once a certain oxide thickness is reached, contributes to the problem. One might think that a partial solution for this question would be simply to limit the air exposure to short periods of time. In the next section, however, we show that even air exposures of the order of minutes lead to XPS spectra totally dominated by the oxidized Si 2p peak, causing the loss of information regarding the oxide thickness on photoelectron studies of these size-classified Si nanocrystal samples.

6.4.2 In situ photoluminescence of size-classified nanocrystals

The need for in situ studies of size-classified nanocrystals

X-ray photoelectron measurements on air-exposed size-classified Si nanocrystals demonstrate that *in situ* characterization is a requirement for the quantitative studies of these samples. This necessity is made clear by the data of Fig. 6.10. In this figure, samples size classified for 10 nm with sub-monolayer coverage were transferred from the synthesis apparatus into the ultra high vacuum (UHV) chamber of a surface analysis system with different transfer times, ranging from a minimum of $\sim$ 3 minutes up to over 1 hour. The samples were then analyzed by XPS at a resolution of $\sim$ 1 eV.

Sample A was air exposed for $\sim$ 3 minutes. Its spectrum shows a large peak corresponding to the unoxidized Si 2p core level, and a smaller feature related to oxidized states. The relative peak intensities suggest an oxide layer of $\sim$ 1 nm for this short exposure time. Sample C was air exposed for $\sim$ 9 minutes and its spectrum shows the absence of the unoxidized Si 2p peak. A third sample, specified as sample B, was transferred with an air exposure time of the same order of magnitude used for samples A and C, but unfortunately the exact time was not recorded. The shape of its XPS spectrum, however, suggests that an exposure time between 3 and 9 minutes was probably used. In the case of sample B, the feature corresponding to the oxidized states is stronger in intensity and shifted towards higher binding energies if compared to sample A, while the unoxidized signal has a lower intensity. An oxide thickness of $\sim$ 3 nm is suggested by the relative peak intensities obtained for sample B. After these measurements were performed, sample B was exposed to air for approximately

1 hour and re-analyzed by XPS. The measured spectrum shows, as expected, the disappearance of the unoxidized peak.

The absence of the unoxidized peak in samples air exposed for longer than ~ 9 minutes might indicate the complete nanocrystal oxidation, or, if a Si core is still present, emitted electrons from that region can no longer escape through the oxide layer.

The hypothesis of complete nanocrystal oxidation seems to be inconsistent with our previous results in chapter 4. In section 4.5.3, electron diffraction from samples size-classified at 10 nm and air-exposed for several days shows the presence of crystalline Si. In addition, HRTEM on similar samples suggests oxide thickness of only 1-3 nm and clearly visible crystalline cores (sections 4.3.5). Therefore, it seems that the prevalence of the oxidized Si 2p peak in XPS from size-classified samples is severely affecting our ability to estimate the oxide thickness.

In order to check that, we have removed sample C (9 minutes air exposure) and sample B (after 1 hour air exposure) from the UHV chamber and dipped them into a 1% HF solution for 20 minutes. Subsequently, they were returned to UHV and XPS measurements were once again performed. Spectra acquired after HF treatment show the recovery of the unoxidized Si peak in sample C but not in sample B, which is consistent with their difference in air-exposure time. This result indicates that XPS is a good probe for nanocrystal oxidation, but our rough estimates of oxide thickness based on thin film assumptions are indeed grossly overestimated.

These measurements demonstrate that, if accurate quantitative information on

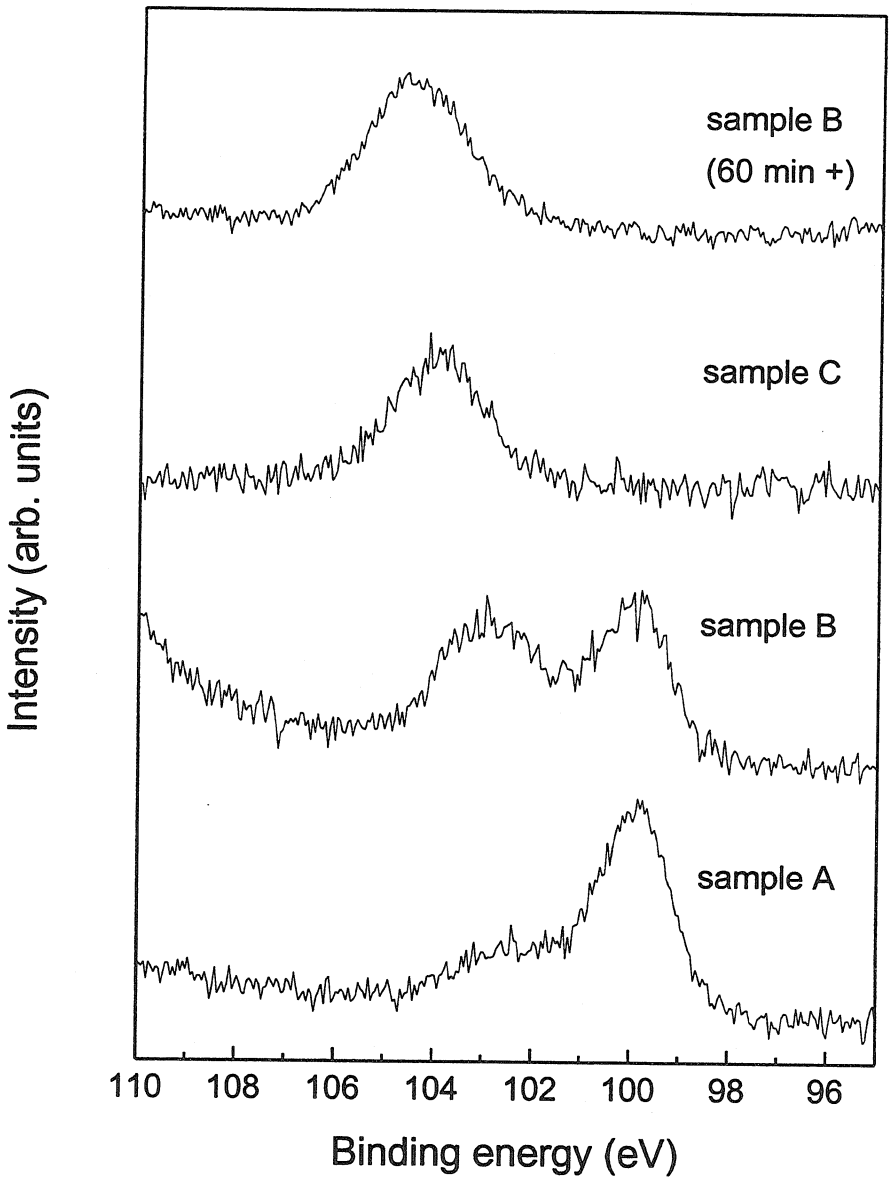

Figure 6.10: X-ray photoelectron spectroscopy measurements as a function of air-exposure time on samples size classified for 10 nm at a resolution of $\sim$ 1 eV. Air-exposure times are 3 and 9 minutes for samples A and C, respectively. Exposure time for sample B is not known exactly. See text for details.

nanocrystal oxidation is to be obtained from XPS, a systematic study has to be performed to take into account the changes in the relative intensity of the Si 2p peaks as a function of nanocrystal size.

The fact that the XPS spectrum evolution for size-classified Si nanocrystals happens on a much shorter time scale than for polydisperse samples is an interesting observation. We have shown in previous sections that XPS spectra from polydisperse nanocrystals have a clear unoxidized peak, even after air exposure for 244 hours (Fig. 6.5) and annealing in air at 400°C for 15 minutes (Fig. 4.4). This is probably an indication that in polydisperse samples the XPS signal is dominated by large particles with small surface-to-volume ratio. By looking at size-classified samples, only nanocrystals with large surface-to-volume ratio are probed, causing an enhancement of the oxidized XPS feature (surface-related) with respect to the unoxidized one (volume-related). Due to the approximately uniform surface-to-volume ratio present in size-classified samples, they may provide an interesting opportunity for XPS studies of Si nanoparticle oxidation, if the data dependence on the surface-to-volume ratio can be taken into account quantitatively.

From the point of view of the optical characterization of size-classified Si nanocrystals, Fig. 6.10 has a basic message: If XPS measurements are expected to help in the characterization of these particles, *in situ* strategies must be used to limit and control nanocrystal oxidation. In what follows, we present a scheme to achieve this purpose.

In situ experimental setup

The need for *in situ* characterization led us to design and implement a system that couples the synthesis apparatus of Fig. 4.1 with a UHV facility for surface analysis and PL measurements. Here we describe this system and present preliminary *in situ* results on size-classified samples. In Fig. 6.11 a schematic of the experimental setup is shown. The nanocrystals, size-classified using the classification experiment described in chapter 4 (Fig. 4.1), are introduced directly into the modified load-lock chamber of the surface analysis system. A new design of the electrostatic precipitator allows particle deposition directly on a substrate placed in the load-lock chamber. Generated samples can then be anaerobically transferred into the UHV chamber of the surface analysis system, or undergo high temperature oxidation in a furnace. In addition, *in situ* PL measurements can be made using an Ar^+ ion laser for excitation and an optical multichannel analyzer for light collection.

Preliminary *in situ* results

Preliminary *in situ* results on a sample size-classified for 10 nm have been obtained using the setup of Fig. 6.11.

In this initial experiment, a sample that has undergone air exposure for a short time was used. This sample was originally generated using the setup of Fig. 4.1 with the thermal evaporation source, and then transferred into the UHV chamber of the surface analysis system with air exposure of $\sim$ 3 minutes due to the transfer. The Si 2p core level XPS spectrum of this sample has a strong signal for the unoxidized Si peak,

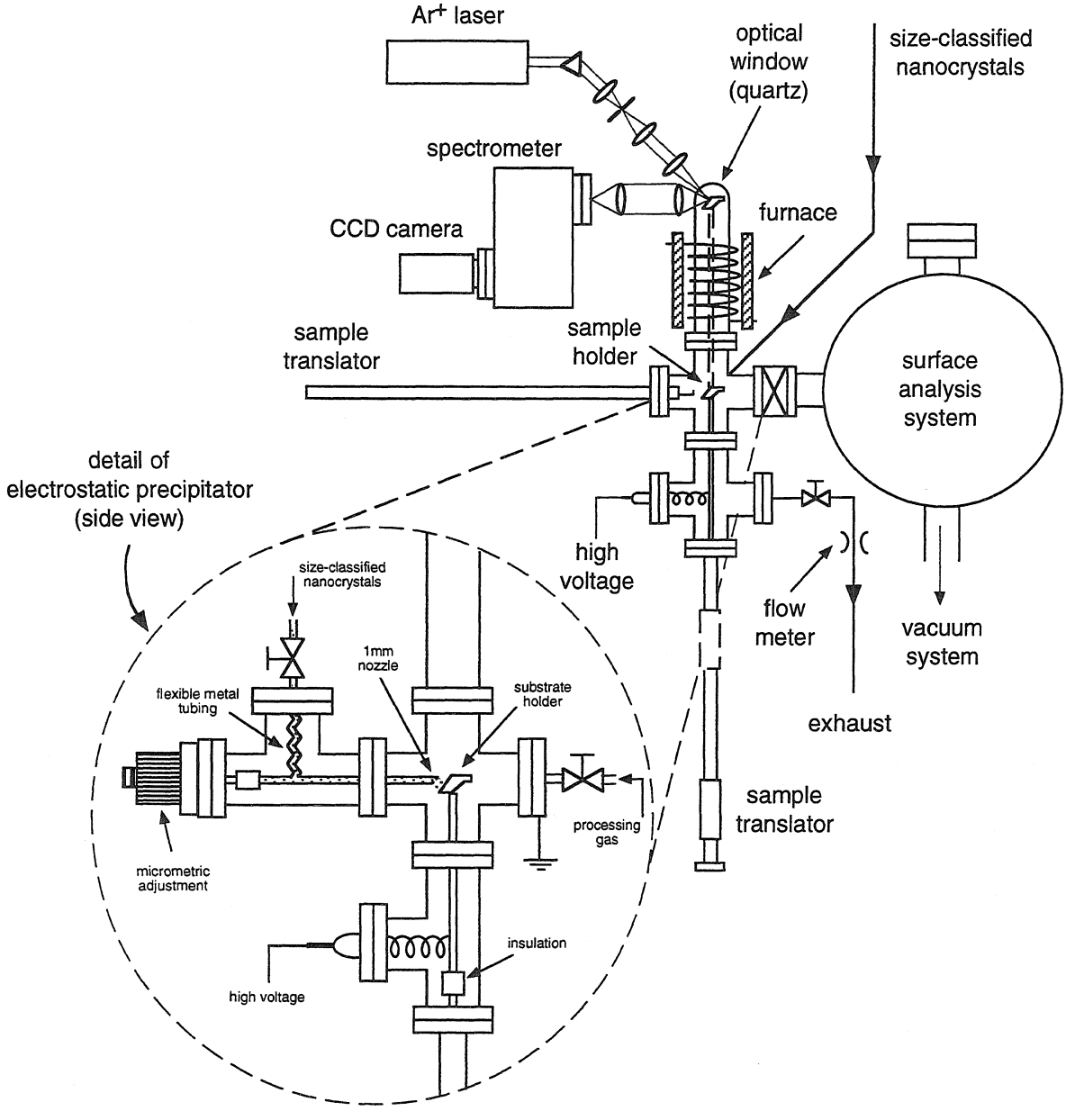

Figure 6.11: Schematic of the experimental setup for *in situ* characterization and processing of silicon nanocrystals.

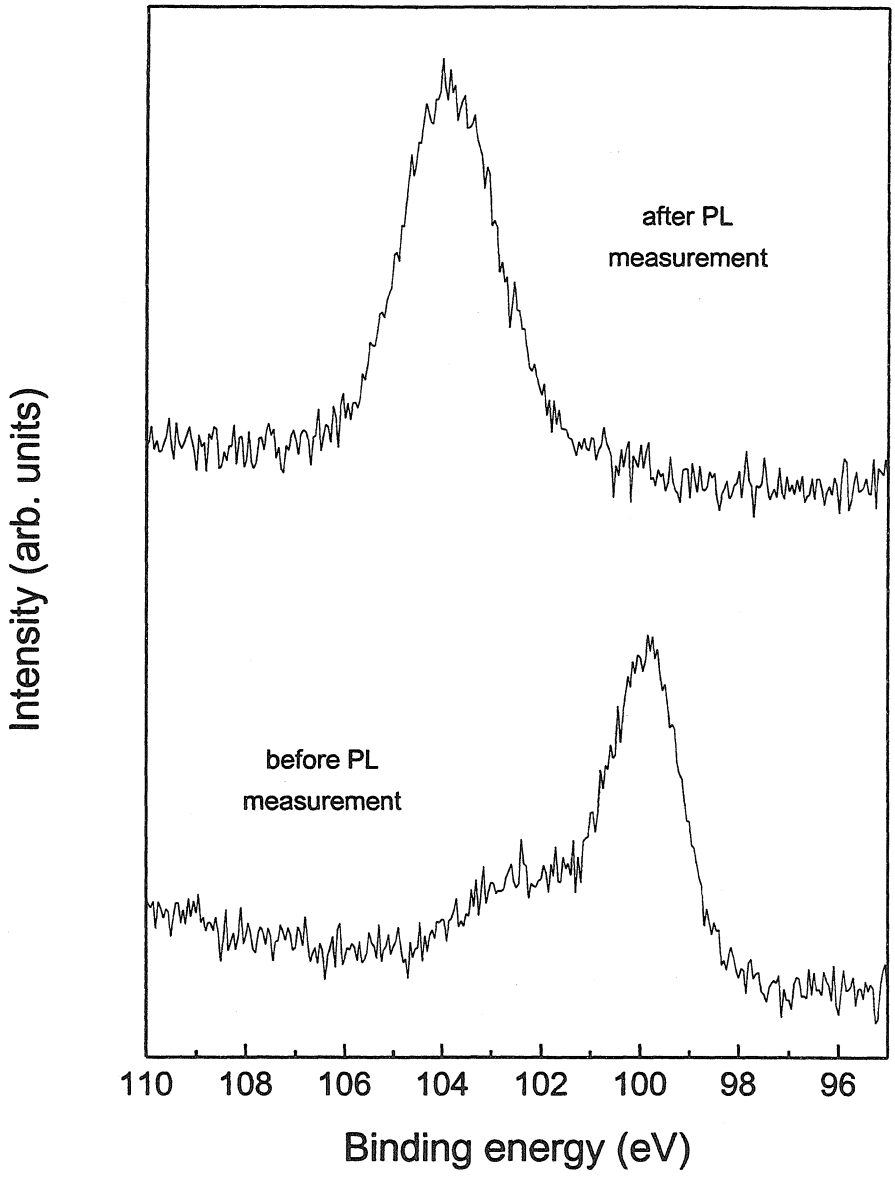

Figure 6.12: X-ray photoelectron spectra from a sample size-classified for 10 nm.

with a small feature corresponding to suboxide states, as shown in Fig. 6.12. After XPS analysis was performed, it was transferred to the load-lock chamber in order to undergo PL data acquisition. The sample remained in the load-lock chamber for two days under a pressure of 10^{-5} Torr. Due to the low intensity of the PL, an excitation power density of $\sim$ 70 mW/mm^2 was used for spectrum acquisition. As a result of the load-lock conditions, upon reinsertion in the UHV chamber the sample presents XPS spectrum totally dominated by oxidized states for Si, with no signal for the unoxidized peak. Two treatment cycles in 1% HF solution for 15 minutes did not cause the recovery of the unoxidized XPS peak. The corresponding PL measurements are presented in Fig. 6.13. A single luminescence band is observed in the 500-600 nm range. This band is not stable under the laser irradiation conditions used. It shows a tenfold reduction during the first 30 minutes of irradiation and it does not recover.

This behavior is essentially identical to the one observed in air-exposed samples in the same spectral region. It is, however, different from the PL of polydisperse nanocrystals, except, perhaps, for the weak band observed to increase upon deuteration of those samples. Although our XPS measurements after repeated HF treatments were not able to detect a Si core, an oxidized feature was still clearly observable, indicating that a crystallite might still be present. However, the PL instability under laser irradiation in vacuum does not seem consistent with emission from quantum-confined states. Once again, as suggested for the sample continuously exposed to air (Fig. 6.9), defect states are likely candidates for the origin of this PL band in the 500-600 nm spectral region. A less exciting possibility that cannot be ruled out at

this point is that this PL may be simply related to hydrocarbon contamination during the synthesis or the brief air exposure. If that is the case, heat treatments at modest temperatures in vacuum should eliminate this luminescence.

This first attempt to perform *in situ* measurements indicates that further improvements in the experimental setup are necessary. Lower load-lock pressure and significantly shorter stays in that chamber should be used in order to prevent nanocrystal oxidation if XPS is to be used to probe the oxide thickness. Temperature treatments are also required to rule out the possibility of hydrocarbon contamination.

Although this first experiment did not achieve the original goal, its output is useful. It demonstrates that PL and XPS measurements can be combined in an *in situ* configuration to probe the optical properties of size-classified Si nanocrystals. A PL band is detected in these samples oxidized at room temperature that seems to be defect- or contamination-related, given its instability under laser irradiation in vacuum. As the load-lock vacuum conditions are improved, systematic studies in this *in situ* system should lead to identification of the luminescence mechanisms in these samples.

6.5 Discussion

In this chapter we have described our efforts to carry out the optical characterization of aerosol synthesized Si nanocrystals.

Although limited in scope, PL experiments in both polydisperse and size-classified samples reveal some general features of their optical behavior. First of all, the ob-

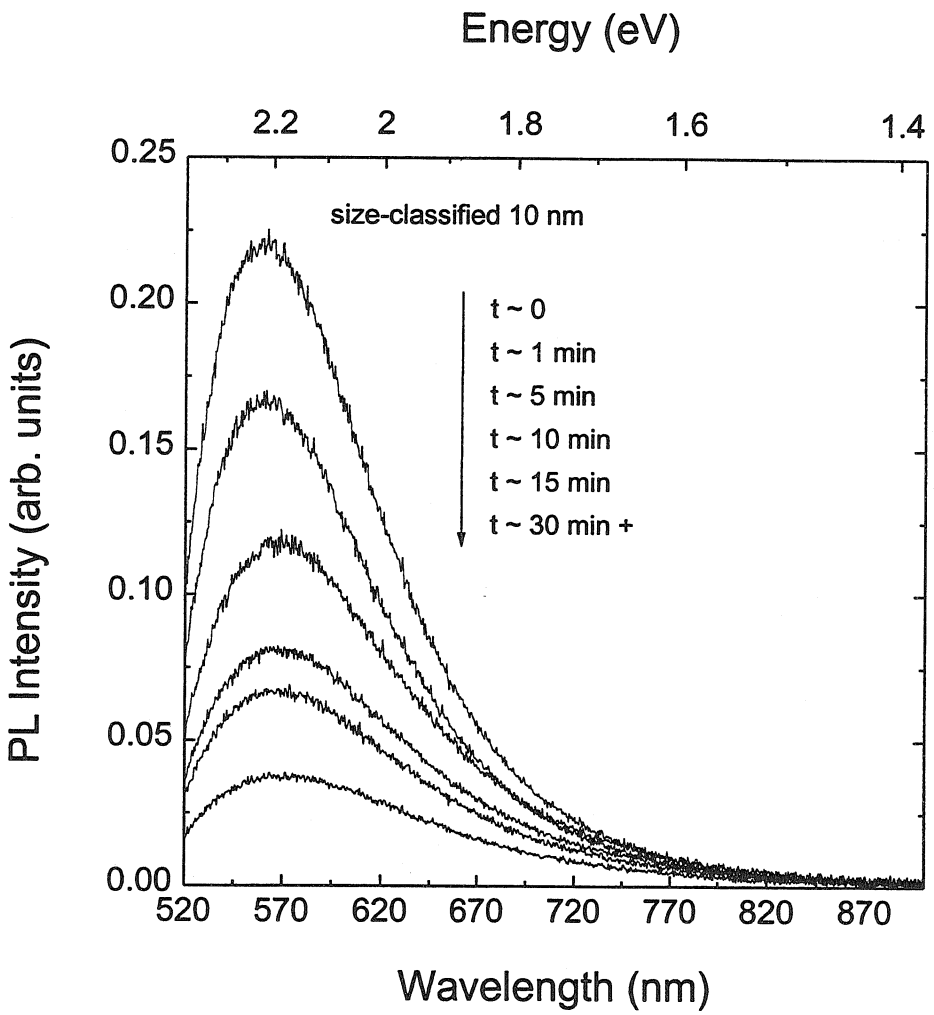

Figure 6.13: *In situ* photoluminescence of a sample size classified for 10 nm. Excitation power density of 70 mW/mm^2 at 488 nm.

served luminescence seems to have distinct characteristics in two different spectral regions, i.e., one in the 500-600 nm range, and another in the 700-900 nm range. This suggests that at least two different PL mechanisms are at work in this material.

In polydisperse samples, PL measurements as a function of air exposure, combined with HF treatment, reveal that the nanocrystal oxidation plays a key role in the PL efficiency of the 700-900 nm band. This observation might be consistent with emission from quantum confined states, enhanced by surface passivation. However, intrinsic defects optically active in this spectral range may also be present in the room temperature native oxides. One way to decide between these two possibilities would be to perform PL lifetime measurements on these samples.

Passivation experiments show opposite trends on the PL intensity in the 500-600 nm range and in the 700-900 nm range of polydisperse samples. This strengthens the case for the presence of two different emission mechanisms. In size-classified samples, measurements suggest that the 700-900 nm band may be quantum confinement-related, while the 500-600 nm band seems to be defect- or contamination-related due to its instability upon laser irradiation.

Although we are not able to draw any definite conclusions on the Si nanocrystal luminescence mechanism, we have demonstrated that spark ablation, laser ablation, and thermal evaporation coupled with aerosol processing are suitable techniques for the production of polydisperse and size-classified visible luminescent silicon nanocrystals. One of the major advantages of the synthesis techniques used is the control of the nanocrystal size. This advantage remains as a promising feature in the studies

of size-dependent optical properties of Si nanocrystals. Its full potential will only be realized, however, when the oxidation and cleanliness of the nanocrystal surface can be limited and controlled. This should be achievable upon further improvements in the implemented *in situ* system for nanocrystal synthesis and characterization.

Bibliography

[1] L. T. Canham, "Silicon quantum wire array fabrication by electrochemical and chemical dissolution of wafers," *Appl. Phys. Lett.*, vol. 57, pp. 1046–1048, 1990.

[2] W. A. Saunders, P. C. Sercel, R. B. Lee, H. A. Atwater, K. J. Vahala, R. C. Flagan, and E. J. Escorcia-Aparcio, "Synthesis of luminescent silicon clusters by spark ablation," *Appl. Phys. Lett.*, vol. 63, pp. 1549–1551, 1993.

[3] W. L. Wilson, P. F. Szajowski, and L. E. Brus, "Quantum confinement in size-selected, surface-oxidized silicon nanocrystals," *Science*, vol. 262, pp. 1242–1244, 1993.

[4] K. S. Min, K. V. Shcheglov, C. M. Yang, H. A. Atwater, M. L. Brongersma, and A. Polman, "Defected-related versus excitonic light emission from ion beam synthesized Si nanocrystals in SiO_2," *Appl. Phys. Lett.*, vol. 69, pp. 2033–2035, 1996.

[5] K. S. Min, K. V. Shcheglov, C. M. Yang, H. A. Atwater, M. L. Brongersma, and A. Polman, "The role of quantum-confined excitons vs defects in the visible luminescence of SiO_2 films containing Ge nanocrystals," *Appl. Phys. Lett.*, vol. 68, pp. 2511–2513, 1996.

[6] S. Hayashi, S. Tanimoto, and K. Yamamoto, "Analysis of surface oxides of gas-evaporated Si small particles with infrared spectroscopy, high-resolution electron microscopy, and x-ray photoemission spectroscopy," *J. Appl. Phys.*, vol. 68, pp. 5300–5308 (1990).

[7] J. F. Ziegler, J. P. Biersack, and U. Littmark, *The stopping and range of ions in solids*, Pergamon, New York, 1985.

[8] F. J. Himpsel, F. R. McFeely, A. Taleb-Ibrahimi, J. A. Yarmoff, and G. Hollinger, "Microscopic structure of the SiO_2/Si interface," *Phys. Rev. B*, vol. 38, pp. 6084–6096, 1988.

[9] D. Briggs and M. P. Seah, *Practical surface analysis*, vol. 1, Wiley, Chichester, Second editon, 1990, pp. 244–248.

[10] L. Skuja, "Time resolved low-temperature luminescence of nonbridging oxygen hole-centers in silica glasses," *Solid State Commun.* vol. 84, pp. 613–616, 1992.

[11] S. Munekuni, T. Yamanaka, Y. Shimogaichi, R. Tohmon, Y. Ohki, K. Nagasawa, and Y. Hama, "Various types of nonbridging oxygen hole centers in high-purity silica glass," *J. Appl. Phys.* vol. 68, pp. 1212–1217, 1990.

[12] M. S. Brandt, H. D. Fuchs, M. Stutzmann, J. Weber, and M. Cardona, "The origin of visible luminescence from porous silicon - a new interpretation," *Solid State Commun.* vol. 81, pp. 307–312, 1992.

[13] D. L. Griscom, "Diffusion of radiolytic molecular-hydrogen as a mechanism for the post-irradiation buildup of interface states in SiO_2-on-Si structures," *J. Appl. Phys.*, vol. 58, pp. 2524–2533, 1985.

Chapter 7

Conclusions and prospects

Semiconductor nanocrystals present the potential for meeting some of the future demands of semiconductor technologies. Their size-dependent electronic and optical properties, in particular, open the possibility for engineering device characteristics by controlling the nanocrystal size. From the fundamental point of view, these materials are also interesting as they provide the opportunity for observation of new physical phenomena in the nano-scale regime.

In this work, we have concentrated our efforts in the synthesis and characterization of silicon (Si) nanocrystals, motivated by their potential applications in Si-based light-emitting and single electron devices. Aerosol methods were used to generate, process, and measure these particles.

Synthesis of size-classified, unagglomerated deposits of Si nanocrystals in the 2-10 nm size range was demonstrated with size control between 15% and 20%. This was achieved by processing an ultrafine Si aerosol through a radial differential mobility analyzer (RDMA), followed by collection in an electrostatic precipitator or hyper-

sonic impactor. The system used for processing showed maximum concentrations of classified aerosol in the 1-5$\times 10^5$ cm^{-3} range, leading to deposits of about 10^{11} nanocrystals/cm^2. The ability to perform size-classification down to 1 nm with the RDMA was also verified, although no deposits were generated at this extreme size. The size-classified deposits were characterized by transmission electron microscopy, and comparison with the RDMA diffusion broadened transfer function shows agreement within the experimental error.

One of the motivations in the synthesis of size-classified Si nanocrystals was the study of their predicted size-dependent optical properties due to quantum confinement. However, size-classified samples have proved challenging for optical measurements because of low nanocrystal concentration and instability upon air exposure. Nevertheless, partial optical characterization experiments on polydisperse and size-classified nanocrystal samples were performed. The results suggest that at least two distinct mechanisms are at work in the light emission from aerosol synthesized Si nanocrystals. Although evidence for defect-related emission has been observed, conclusive results require measurements in a controlled environment, where the nanocrystal oxidation can be limited and manipulated. To achieve this goal, a new system for *in situ* nanocrystal synthesis and characterization was implemented and continuing work in this context should allow the clarification of the light emission mechanisms in this material.

In the attempt to overcome the problem of low deposit concentrations of nanocrystals processed by the RDMA, we have operated this instrument with highly charged

aerosols and number concentrations well above 10^5 cm^{-3}. However, operation under these high charge conditions was found to distort the size-classification due to space charge effects. In extreme cases, nanocrystals were transmitted through the instrument even with no applied voltage, indicating the complete disruption of the classification. In order to study this phenomenon and determine limits for the operation of differential mobility analyzers (DMAs) in general, we have developed self-consistent numerical calculations of the particle transport in the DMA taking into account, simultaneously, Brownian diffusion and space charge fields. Our results indicate that the DMA design can be optimized for classification in the size regime of interest for semiconductor nanocrystal processing. A short cylindrical DMA design with maximized voltage and flow rates was suggested to enable high throughput, high resolution classification in the 0.5-10 nm size range.

The conception of a high throughput, high resolution size-classification system involves issues beyond the DMA design itself. Several additional questions have to be considered at different levels of the synthesis process. First of all, the nanocrystal source has to be appropriate. In our investigations, it has become clear that the long term stability of the aerosol source is crucial, as fluctuations in number concentration compromise size classification over extended periods of time. Although the spark ablation and laser ablation techniques have demonstrated useful aspects, thermal evaporation provides a simple and highly stable method for production of high concentration nanocrystal aerosols. The use of laser ablation is also attractive from the viewpoint of flexibility in the choice of source material. If laser ablation is to

be used in high concentration nanocrystal synthesis, however, systematic parametric studies should be carried out to minimize the generation of micron-sized particulates.

In our system, the combination of a thermal evaporation source, a ^{85}Kr neutralizer, and a RDMA, leads to maximum number concentrations in the 1-5$\times 10^5$ cm^{-3} range for nanocrystals classified at 10 nm. The limiting factors in attaining higher number concentrations are the $\sim$ 10-second residence time of the system and the low charging efficiency of the bipolar charger (order of a percent). Therefore, two approaches exist to increase the number concentration: reduce the residence time to limit coagulation, or improve the charging efficiency to increase the number of particles available for classification.

Shortening of the residence time is a challenging but interesting possibility. It requires the redesign of the entire system into a compact unit, including the nanocrystal source, the charger, the DMA, and the collection device. Improvements by more than a factor of 3 or so in the number concentration may require careful engineering, but the concept is worth exploring as a long term alternative.

Increases in the charging efficiency offer a simpler, more immediate option to attain higher number concentrations. This can probably be achieved using an aerosol charger with better performance in the sub-10 nm regime. The charging efficiency of regular unipolar corona discharge chargers with DC bias is estimated to be as high as 20-40% between 2 and 10 nm. However, the loss of charged particle is dramatic, with virtually all particles in that size range being lost due to the charger electric field. The use of an AC grid voltage, instead of the standard DC bias, has been shown to

decrease particle losses in the instrument. In this way, overall transmission of singly charged 5 nm particles of 5% efficiency has been demonstrated [1].

Another approach involves a hybrid charger. It employs a radioactive alpha particle source and a DC field to generate a unipolar ion distribution [2]. With this instrument, charging efficiencies of 50% at 10 nm have been reported. Particle loss of only $\sim$ 20% in the same size range indicate that overall transmission of singly charged 10 nm particles as high as 40% can be achieved.

The use of these high-efficiency chargers may increase the throughput of the current classification system by as much as one order of magnitude. However, the use of a highly charged aerosol in the RDMA may cause space charge effects to become severe, in which case, the short cylindrical DMA design optimized for classification in the sub-10 nm range is recommended.

Another issue that should be addressed in our synthesis method relates to the nanocrystal shape. Particles below 10 nm made by spark ablation and thermal evaporation present shapes that approach sphericity. However, nanocrystals in the 10 nm range have the appearance of small agglomerates. Nanocrystals generated by laser ablation present the largest deviations from spherical shape, probably due to faster cooling rates. These size inhomogeneities may currently be the limiting factor in achieving narrow optical properties for these structures. To overcome this problem, another processing step should be introduced in the experiment, i.e., a sintering furnace. Temperature treatments in the range of 800-1100°C for a few seconds should provide enough surface diffusion to completely sinter unoxidized 10 nm

Si agglomerates [3]. A parametric study may be performed to determine optimized sintering temperatures and times in the size of interest. If sintering is done before size-classification, improved size control is also expected due to the presence of particles of more uniform shape in the DMA. However, it should be pointed out that the impact of thermophoretic losses in the total number concentration is a question that will have to be considered carefully.

A topic that also requires further attention is the passivation of electronic surface states in the nanocrystals. Poor passivation may be severely hindering the optical characterization of size-classified samples. One approach to deal with this problem is the growth of a high quality oxide. This involves high temperature oxidation of the nanocrystal surface, where the reaction is limited by the availability of oxygen, which can be done in the implemented *in situ* system. Processing the nanocrystals in this manner should also provide an alternative way to control the size of the crystalline core, and allow tuning of the emission wavelength, if quantum confined-related luminescence is achieved.

Ultimately, the stabilization of the nanocrystal deposit in a matrix will probably be necessary if these particles are to be applied in a device. Once a high quality passivation layer has grown on the nanocrystals, a matrix of inferior quality may be tolerated. Polymer matrices or an oxide grown by chemical vapor deposition are interesting alternatives.

Aerosol techniques are powerful tools to manipulate the size and shape of semiconductor nanostructures. The study presented in this thesis demonstrated some of the

advantages and challenges of nanocrystal synthesis using these methods. However, their full potential as synthesis and processing methods for semiconductor nanocrystals is far from having been reached. Many opportunities exist for improvements, and, at least from the viewpoint of fundamental investigations, the aerosol approach holds the promise for unveiling new facets of the behavior of these new materials.

Bibliography

[1] P. Büscher and A. Schmidt-Ott, "A new concept for a unipolar diffusion charger," *J. Aerosol Sci.*, vol. 21, Suppl. 1, pp. S567–S570, 1990.

[2] M. Adachi, F. J. Romay, and D. Y. H. Pui, "High-efficiency unipolar aerosol charger using a radioactive alpha source," *J. Aerosol Sci.*, vol. 23, pp. 123–137, 1992.

[3] M. M. Lunden, "Sintering of aerosol agglomerates," Ph.D. Thesis, California Institute of Technology, Pasadena, California, 1995.

Appendix A

Program for simulating the space charge effect in the differential mobility analyzer

A.1 Radial differential mobility analyzer version

The source code for a program to simulate the space charge effect in the RDMA is presented in this section. The program is written in Turbo Pascal for Windows 3.1. It was typically run in a Pentium 100 MHz computer.

The data entry for the program is done in two different stages. Initially, information pertaining the size distribution entering the DMA must be given in the section specified as DATA ENTRY-RDMA-1.

The size distribution (SD) is divided in three sections: a low resolution region in the small-size side delimited by Dmin and Dpmin (npl points), a high resolution

region delimited by Dpmin and Dpmax (nphr points), and a low resolution region in the large-size side delimited by Dpmax and Dmax (npr points). Dmin and Dmax were typically 0.5 and 100 nm, respectively. The values for Dpmin and Dpmax have to be adjusted in the region where high resolution of the transfer function behavior becomes necessary. The specific input values required at this point are as follows (typical default values are shown in parenthesis):

Dmin = minimum diameter of the size distribution (SD) (nm) (0.5);

npl = number of points in the small size, low resolution part of the SD (5-10);

Dpmin = minimum diameter of the high resolution region of the SD (nm) (1.5);

Dpmax = maximum diameter of the high resolution region of the SD (nm) (4.5);

nphr = number of points in high resolution part of the SD (60);

Dmax = maximum diameter of the size distribution (SD) (nm) (100);

npr = number of points in the large size, low resolution part of the SD (10-15);

sg = geometric standard deviation of SD (1.87);

dpg = mean diameter of SD (nm) (32.9);

Ne = total number concentration of incoming positive particles (cm^{-3}) (10^8);

dps = D_p^* , centroid diameter of intended classification (nm) (3);

ccorr = factor to alter Fuchs charge distribution if desired (0).

Upon compilation of the code, additional information regarding the DMA operation conditions is requested. The aerosol flow rate, the sheath flow rate, the number of

radial (NRS) and vertical (NVS) steps for generation of the mesh, and the number of points per vertical step for the electric field calculation must be provided. An option to include or not space charge effects and diffusion can be made at this point. Excellent resolution of simulated transfer functions were obtained for NRS = 20 and NVS = 1000 as compared with the semianalytical results of Zhang and Flagan's (chapter 5). These number of points, however, require simulation times in excess of a day for a single transfer function. Therefore, in reality, satisfactory but less than perfect numerical resolution was obtained for NRS = 10 and NVS = 200.

The program also allows simulations for two DMAs in series (TDMA arrangement). Upon finishing the calculation for the first DMA, the option is given to automatically introduce the resulting SD in a second identical instrument and the transport is again calculated. If simulations of a TDMA experiment are to be performed, additional information regarding the voltage scanning on the second DMA must be provided. This is done in the section specified as DATA ENTRY-RDMA-2. Here, two factors are introduced to delimit the scanning of centroid mobilities in the second DMA, specified as follows (typical default values are shown in parenthesis):

fmmin = minimum for normalized mobility (Z_p/Z_p^*) on DMA-2 (0.6);

fmmax = maximum for normalized mobility (Z_p/Z_p^*) on DMA-2 (1.4);

nms2s = number of points between fmmin and fmmax (20).

The data output of the program provides the transfer function after the simulation

is completed for the first DMA. The results are saved in a file named TF.DAT as a function of particle diameter and normalized mobility. If the calculation is chosen to proceed into a second DMA, an additional file named N2N1.DAT is created upon completion. This file gives the predicted ratio n_2/n_1 of particles that exited the second DMA (n_2) to the particles that exited the first DMA (n_1), as a function of normalized mobility of the second instrument (particle loss between the instruments is neglected).

A listing of the source code follows.

```
(*****************************************************************************)
(*                    RDMA - Space charge simulation - Renato P. Camata - 1997                    *)
(*****************************************************************************)

program RDMAsim; {$N+}

Uses unp,unm,unptr,unmtr,WinCrt; {Pascal units at the end of listing}

const
 e:real=1.6e-19; {Coulombs}
 pi:real=3.141592654;
 a:real=1.257;
 b:real=0.40;
 g:real=1.10;
    {a,b,g=alfa, beta, gama in the expression for the slip        }
    {     correction factor Cc=1+Kn(a+bexp(-g/Kn))               }
 l:real=6.51e-8;  {m}              {value for air, T=298 K, 1 atm}
 u:real=1.8e-5;   {kg m-1 s-1}   {value for air, T=298 K, 1 atm}
 eps:real=8.8e-12;{F/m}           {value for vacuum            }
 kT:real=4.16e-21; {SI}           {value for T=298 K           }
    {l=lambda, mean free path of the gas                       }
    {u=mu, gas viscosity                                       }
    {kT=Boltzmann constant * Temperature (T~300 K )            }

(************************RDMA parameters*******************************)
 r1:real=0.24e-2;
 r2:real=5.04e-2;
 deltar:real=4.77e-2;
 s:real=1e-2;
    {r1=RDMA outlet diameter Rout (m)                          }
    {r2=RDMA inlet diameter Rin (m)                            }
    {deltar=r2-r1 (m)                                          }
    {s=spacing between electrodes (m)                          }

type
 vsmall = array[1..80] of real;
 vsmallDP = array[0..81] of real;
 vlarge = array[0..200] of double;
 cube = array[1..80] of array[1..200]of single;
 vtrans = array[1..80] of array[1..200] of single;

var

(******************VARIABLES RELATED TO GRAPHIC FEATURES**************)
 I:integer;

(******************VARIABLES RELATED TO THE HANDLING OF FILES*********)
 arq:text;
 arq2:text;
 name,nome:string[20];

(************VARIABLES RELATED TO THE SIZE DISTRIBUTIONS**************)
 idp,nbins:integer;
 dp:vsmallDP;
```

```
 n,nf,nm0,np0:vsmall;

 km0,km1,km2,km3,kp0,kp1,kp2,kp3:real;
    {idp=index for the bins of the size distributions            }
    {nbins=total number of bins of the size distributions        }
    {dp[idp]=mobility diameter (nm)                              }
    {n[idp]=initial number concentration (cm-3) (before neutralizer) }
    {nf[idp]=final number concentration (cm-3) (corr. for charging)  }
    {kmi=coefficients of the gaussian fit for Fuchs charge dist.     }
    {    for q=-1e                                               }
    {kpi=coefficients of the gaussian fit for Fuchs charge dist.     }
    {    for q=+1e                                               }
    {nm0[idp]=initial negative number concentration (cm-3):particles }
    {    from initial size distribution which acquire charge q=-1e   }
    {np0[idp]=initial positive number concentration (cm-3):particles }
    {    from initial size distribution which acquire charge q=+1e   }
    {nm[idp,iz,p]=evolving negative number concentration (cm-3)      }
    {np[idp,iz,p]=evolving positive number concentration (cm-3)      }

(*VARIABLES RELATED TO THE ELECTRIC FIELD/TRAJECTORIES CALCULATION****)
 nrs,nrsdb2,nvs,nssl,nts,ir,irr,iz,it,iv,jz,lz,kz,idtr,npvs,npvsdv2:integer;
 dr,r,dtr,dz,v,dt,z0,z1,zz,h,Et0,Et1,Vmin,Vmax:real;
 Et,ro:vlarge;
 ve,veant:array[1..201] of real;
 dif,conv,w:real;
 iter:integer;
 sig:real;
    {nrs=number of radial steps for calculation                  }
    {nrs=number of vertical steps for calculation                }
    {nrsdb2=nrs/2                                                }
    {nts=number of time steps for z(t) calculation               }
    {r=radial position of the vertical slab (origin at RDMA center)(m)}
    {rnext=radial position of the next vertical slab (m)         }
    {dr=radial step thickness (m)                                }
    {dz=vertical step thickness (m)                              }
    {dtr=time it takes the aerosol to traverse dr (radial motion)    }
    {dt=time slab for the integration in z (vertical motion)         }
    {npvs=number of points per vertical step (for E(z) integration)  }
    {npvsdv2=npvs/2                                              }
    {h=dz/npvs                                                   }
    {v=radial velocity of the aerosol (m/s)                      }
    {ir,irr=index for radial change                              }
    {iz,jz,lz,kz=indexes for vertical change                     }
    {it=index for time change                                    }
    {idtr=index for dtr: idtr=Round(dtr)                         }
    {Et[iz]=total electric field: Et = (Vap/s) + Esc             }
    {z0,z1=position of a particle that is migrating across the DMA   }
    {zz=position of a particle once diffusion is taken into account  }
    {Et0,Et1=electric field at the points in the vertical step       }
    {ro[iz]=charge density                                       }
    {sig=standard deviation for the diffusional broadening       }

(*********VARIABLES RELATED TO THE RDMA OPERATION**********************)
 qa,qs,vap:real;
```

```
    {qa=aerosol flow rate (LPM immediatly converted to m3/s)       }
    {qs=sheath flow rate (LPM immediatly converted to m3/s)       }
    {vap=voltage applied to the RDMA electrodes (V)             }

(****************VARIABLES RELATED TO THE AEROSOL*********************)
 Kn,Cc:real;
 Zp,D:vsmall;
    {Kn=Knudsen number; Kn=2l/Dp                              }
    {Cc=Slip correction factor                              }
    {Zp[idp]=Electrical mobility (here Zp is calculated for a single }
    {       elementary charge, using only its absolute value in the }
    {       expression for Zp - the charge sign is not included)   }
    {D[idp]=Brownian diffusivity                              }

(********VARIABLES RELATED TO THE DIFF. EQUATIONS SOLUTION************)
 k1,k2,k3,k4:real;
    {k1,k2,k3,k4=coefficients in Runge-Kutta's formula          }

(************************AUXILIARY VARIABLES**************************)
 ch,sc,df,BABA:char;
 somat,nn,nmom,SUM,SOM,AUXR,SOMA,incre,arg,NMTI,NPTI,NMT,NPT:real;
 ntrans:vlarge;
 imax,jzmax,jzmin,itempo,p,pp,AUX:integer;

(********VARIABLES RELATED TO THE INITIAL SIZE DISTRIBUTION************)
 DlogDp,DlogDpl,DlogDpr,Dmin,Dpmin,Dpmax,Dmax,sg,dpg,Ne,area,alfac,ccorr:real;
 npl,npr,nphr:integer;
 tf:vsmall;
    {Ne=total number concentration of singly charged positive particles}
    {  determined from experiment                             }
    {  to be used to generate initial size dist. that entered DMA    }

(************VARIABLES FOR THE TDMA EXPERIMENT************************)
 dps,ms1,fmmin,fmmax,ms2min,ms2max,ms2inc,n1:real;
 RDMA,nms2s:integer;
 n2,mob:array[0..30] of real;
    {dps=size classified from RDMA-1 = Dp* (nm)                 }
    {ms1=mobility corresponding to dps (SI)                   }
    {fmmin,fmmax=multiplicative factors that define mobility range for }
    {       RDMA-2                                          }
    {nms2s=number of Zp*,2 steps                              }
    {ms2min,ms2max,ms2inc=min,max, and inc to Zp*,2              }
    {RDMA=(1)RDMA-1, (2)RDMA-2                                }
    {mob[iv]=Zp*,2 for each step in the RDMA-2 scan             }
    {n1=N1 in Zhang and Flagan's papar on diffusional broadening     }
    {n2[iv]=N2 in Zhang and Flagan's papar on diffusional broadening  }

begin
New(np);
New(nm);
New(nptrans);
New(nmtrans);

(************************GRAPHIC INTRODUCTION**********************)
```

```
 ClrScr;
 Write(Char(201));
 for I := 1 to 78 do
  Write(Char(205));
 Write(Char(187));
 Write(Char(186));
 GotoXY(80,2);
 Write(Char(186));
 Write(Char(200));
 for I := 1 to 78 do
  Write(Char(205));
 Write(Char(188));
 Writeln;
  GotoXY(4,2);
 Write('                    RDMAsim ');
 GotoXY(46,2);
 writeln;
 writeln;
 writeln;
 writeln('       This program calculates the size distribution at the RDMA');
 writeln('            sampling outlet taking into account:');
 writeln;
 writeln('            * MIGRATION DUE TO THE APPLIED FIELD');
 writeln('            * BROWNIAN DIFFUSION');
 writeln('            * SPACE CHARGE EFFECTS');
 writeln('            * PARTICLE LOSS TO THE TOP ELECTRODE');
 writeln;

 (*************************************************************************)
(*********************DATA ENTRY*****************************************)
(***********SIZE DISTRIBUTION & APPLIED VOLTAGE**************************)
(*****************  RDMA-1 ********************************************)
 Dmin:=1;
 npl:=5;
 Dpmin:=1.5;
 Dpmax:=4.5;
 nphr:=60;
 Dmax:=100;
 npr:=15;
 sg:=1.87;
 dpg:=32.9;
 Ne:=2.13e+8;
 dps:=3;
 ccorr:=0;  {correction for charging}

(*************************************************************************)
 Kn:=(2*l)/(dps*1e-9);
 Cc:=1+(Kn*(a+(b*Exp(-(g/Kn)))));
 ms1:=(e*Cc)/(3*pi*u*dps*1e-9);

 { REMEMBER: nbins:=npl+nphr+npr-1   }

(*************************************************************************)
(*****************  RDMA-2 ********************************************)
```

```
 fmmin:=0.6;  {minimum for Zp*,2/Zp*,1}
 fmmax:=1.4;  {maximum for Zp*,2/Zp*,1}
 nms2s:=20;   {number of points in between}

(*************************************************************************)
 ms2min:=fmmin*ms1;
 ms2max:=fmmax*ms1;
 ms2inc:=(ms2max-ms2min)/nms2s;
 (*************************************************************************)

RDMA:=1;
FOR IV:=0 TO (NMS2S+1) DO
BEGIN
 for idp:=1 to nbins do
  nf[idp]:=0;
IF RDMA=1 THEN    {Begins preparation for RDMA-1}
BEGIN
 nbins:=npl+nphr+npr-1;
  Dlogdpl:=Ln(Dpmin/Dmin)/(npl-1);
 for idp:=1 to (npl-1) do
  Dp[idp]:=Exp(Ln(Dmin)+((idp-1)*Dlogdpl));
 Dlogdp:=Ln(Dpmax/Dpmin)/(nphr);
 for idp:=npl to (npl+nphr-1) do
  Dp[idp]:=Exp(Ln(Dpmin)+((idp-(npl-1)-1)*Dlogdp));
 Dlogdpr:=Ln(Dmax/Dpmax)/(npr-1);
 for idp:=(npl+nphr) to nbins do
  Dp[idp]:=Exp(Ln(Dpmax)+((idp-(npl+nphr-1)-1)*Dlogdpr));
 Dp[nbins+1]:=(2*Dp[nbins])-Dp[nbins-1];
 Dp[0]:=(2*Dp[1])-Dp[2];
 if Dp[0]<0 then Dp[0]:=0;
 for idp:=1 to nbins do
  np0[idp]:=(Ne/(Sqrt(2*pi)*Ln(sg)))*Exp(-((Sqr(Ln(dp[idp])-Ln(dpg)))/(2*Sqr(Ln(sg)))));

(*APPLYING FUCHS CHARGE DISTRIBUTIONS TO THE INITIAL SIZE DISTRIBUTION*)
(*Gaussian fits to the results in A. Wiedensohler, J. Aerosol Sci. 19**)
(*pp.387 (1988)*********************************************************)
{ We start with np0[idp], because that is the one we have access experimentally. Then, we calculate n[idp] and }
{ nm0[idp] using Fuchs charge distribution.}                    }
 kp0:=0.206553;
 kp1:=-0.263344;
 kp2:=-25.9357;
 kp3:=52.64;
 for idp:=1 to nbins do
  n[idp]:=np0[idp]/(kp0+(kp1*Exp( -Sqr (((dp[idp]-kp2)/kp3))  )));
 km0:=0.272151;
 km1:=-0.319269;
 km2:=-19.1046;
 km3:=47.8427;
 for idp:=1 to nbins do
  nm0[idp]:=ccorr*(km0+(km1*Exp(-Sqr(((dp[idp]-km2)/km3)))))*n[idp];

(****************DETERMINATION OF THE ALFA CONSTANT*********************)
(*              alfac=Ne/(Area under nm0[idp])                 *)
 area:=0;
```

```
 for idp:=1 to nbins do
  area:=area+( np0[idp] * (0.5*(dp[idp+1]-dp[idp-1])) );
 alfac:=Ne/area;

(*DISPLAYS SIZE DISTRIBUTION AND EFFECT OF FUCHS CHARGE DIST.**)
 clrscr;
 writeln;
 writeln('                    INITIAL MONODISPERSE AEROSOLS');
 writeln;
  writeln('          Dp (nm)        N(cm-3)       N[-1](cm-3)     N[+1](cm-3)');
 writeln;
  for idp:=1 to nbins do
  begin
   write('          ',Dp[idp]:3:2,'          ',n[idp]:7:0,'          ');
   writeln(nm0[idp]:5:0,'          ',np0[idp]:5:0);
   ch:=readkey;
  end;
 writeln;
  writeln('               IF THIS IS CORRECT PRESS ANY KEY TO CONTINUE');
 ch:=readkey;
(*********************READING IMPORTANT VARIABLES************************)
 repeat
  begin
   clrscr;
   writeln;
   writeln;
   write('                  INPUT AEROSOL FLOW RATE (LPM) = ');
   read(qa);
   qa:=(qa*0.001)/60;
   writeln;
   write('                   INPUT SHEATH FLOW RATE (LPM) = ');
   read(qs);
   qs:=(qs*0.001)/60;
   writeln;
   writeln;
   write('       INPUT NUMBER OF RADIAL STEPS (EVEN:10-1000) = ');
   read(nrs);
   writeln;
   write('         INPUT NUMBER OF VERTICAL STEPS (10-1000) = ');
   read(nvs);
   writeln;
   write('              INPUT TIME RESOLUTION FOR z(t) (s) = ');
   read(dt);
   writeln;
   writeln('  INPUT NUMBER OF POINTS PER VERTICAL STEP FOR E(z)');
   write('                              (EVEN:2-10) = ');
   read(npvs);
   npvsdv2:=Round(npvs/2);
   writeln;
   write('              INCLUDE SPACE CHARGE EFFECTS ? (Y/N) ');
   sc:=readkey;
   writeln;
   writeln;
   write('                      INCLUDE DIFFUSION ? (Y/N) ');
```

```
  df:=readkey;
  writeln;
  writeln;
  write('            DO YOU WANT TO CHANGE ANYTHING ? (Y/N) ');
  ch:=readkey;
  writeln;
 end;
until (ch='n') or (ch='N');
for idp:=1 to nbins do
 begin
  tf[idp]:=0;
  nf[idp]:=0;
 end;

(******CALCULATING ELECTRICAL MOBILITY AND BROWNIAN DIFFUSIVITY*********)
for idp:=1 to nbins do
 begin
  Kn:=(2*l)/(dp[idp]*1e-9);
  Cc:=1+(Kn*(a+(b*Exp(-(g/Kn)))));
  Zp[idp]:=(e*Cc)/(3*pi*u*dp[idp]*1e-9);
  D[idp]:=(kT*Cc)/(3*pi*u*dp[idp]*1e-9);
 end;
Vap:=-(qs*s)/(pi*ms1*(Sqr(r2)-Sqr(r1)));
Vmin:=(qs*s)/(pi*ms2min*(Sqr(r2)-Sqr(r1)));
Vmax:=(Vmin*ms2min)/ms2max;
END             {Ends preparation for RDMA-1}
ELSE
BEGIN           {Begins preparation for RDMA-2}
for idp:=1 to nbins do
 begin
  np0[idp]:=tf[idp];
  nm0[idp]:=0;       {assuming that only positive particles made it}
 end;             {to the RDMA-2                    }
mob[iv]:=ms2min+((iv-1)*ms2inc);
vap:=-(Vmin*ms2min)/mob[iv];
SC:='N';
END;            {Ends preparation for RDMA-2}

dr:=deltar/nrs;
dz:=s/nvs;
h:=dz/npvs;
nssl:=Round((qa/qs)*nvs);
for idp:=1 to nbins do
 begin
  for kz:=1 to nssl do
   begin
    np^[idp,kz]:=np0[idp];
    nm^[idp,kz]:=nm0[idp];
   end;
  for jz:=(nssl+1) to nvs do
   begin
    np^[idp,jz]:=0;
    nm^[idp,jz]:=0;
   end;
```

```
 end;
for iz:=0 to nvs do
 Et[iz]:=-Vap/s;

p:=1;
pp:=2;

for ir:=1 to nrs do
 begin
  writeln('RDMA-',RDMA,' ',iv,'/',(nms2s+1),' RADIAL POSITION IR = ',ir,' Vap = ',vap:3:2);

 r:=deltar-((ir-0.5)*dr);
 v:=(qs)/(2*pi*r*s);
 dtr:=dr/v;
 nts:=Round(dtr/dt);
 for idp:=1 to nbins do
  begin
   for jz:=1 to nvs do
    begin
     nptrans^[idp,jz]:=0;
     nmtrans^[idp,jz]:=0;
    end;
  end;

 for iz:=1 to nvs do
  begin
   for idp:=1 to nbins do
    begin

     np^[idp,iz]:=((1e+6)*np^[idp,iz])*dz;
                    {numb.conc changed from cm-3 to m-2 }

     z0:=(iz-0.5)*dz;
     for it:=1 to nts do
      begin
       jz:=Round((z0/dz)+0.5);

       if jz>nvs then
        begin
         itempo:=it;
         it:=nts;
         z1:=10.5e-3;
        end
       else
        begin
         k1:=dt*Zp[idp]*Et[jz];
         jz:=Round(((z0+(0.5*k1))/dz)+0.5);
        end;

       if jz>nvs then
        begin
         itempo:=it;
         it:=nts;
         z1:=10.5e-3;
```

```
 end
 else
 begin
  k2:=dt*Zp[idp]*Et[jz];
  jz:=Round(((z0+(0.5*k2))/dz)+0.5);
 end;

 if jz>nvs then
 begin
  itempo:=it;
  it:=nts;
  z1:=10.5e-3;
 end
 else
 begin
  k3:=dt*Zp[idp]*Et[jz];
  jz:=Round(((z0+k3)/dz)+0.5);
 end;

 if jz>nvs then
 begin
  itempo:=it;
  it:=nts;
  z1:=10.5e-3;
 end
 else
 begin
  k4:=dt*Zp[idp]*Et[jz];
  z1:=z0+((k1+(2*k2)+(2*k3)+k4)/6);
  z0:=z1;
 end;

 if z1>s then
 begin
  itempo:=it;
  it:=nts;
  z1:=10.5E-3;
 end;
end;

jz:=Round(((z1/dz)+0.5));
z1:=(jz-0.5)*dz;

if jz>nvs then
 z1:=z1+Zp[idp]*Et[nvs]*(nts-itempo)*dt;

if (df='n') or (df='N')
 then
 begin
  if jz<(nvs+1) then
   nptrans^[idp,jz]:=nptrans^[idp,jz]+(np^[idp,iz]/dz);
 end
 else
 begin
```

```
sig:=Sqrt(2*D[idp]*dtr);
jzmax:=Round((((z1+(5*sig))/dz)+0.5));
jzmin:=Round((((z1-(5*sig))/dz)+0.5));
somat:=0;
for kz:=jzmin to 0 do
 begin
  zz:=(kz-0.5)*dz;
  arg:=(-Sqr(zz-z1))/(4*D[idp]*dtr);
  if arg>(-100)
   then
    begin
     nmom:=((np^[idp,iz]/(2*Sqrt(pi*D[idp]*dtr)))*Exp(arg));
     somat:=somat+(nmom*dz);
    end;
 end;

for kz:=1 to nvs do
 ntrans[kz]:=0;

for kz:=1 to nvs do
 begin
  zz:=(kz-0.5)*dz;
  arg:=(-Sqr(zz-z1))/(4*D[idp]*dtr);
  if arg>(-100)
   then
    begin
     ntrans[kz]:=((np^[idp,iz]/(2*Sqrt(pi*D[idp]*dtr)))*Exp(arg));
     somat:=somat+(ntrans[kz]*dz);
    end;
 end;

for kz:=(nvs+1) to jzmax do
 begin
  zz:=(kz-0.5)*dz;
  arg:=(-Sqr(zz-z1))/(4*D[idp]*dtr);
  if arg>(-100)
   then
    begin
     nmom:=((np^[idp,iz]/(2*Sqrt(pi*D[idp]*dtr)))*Exp(arg));
     somat:=somat+(nmom*dz);
    end;
 end;

if somat<(1e-10)
 then
  nn:=0
 else
  nn:=np^[idp,iz]/somat;
for kz:=1 to nvs do
 nptrans^[idp,kz]:=nptrans^[idp,kz]+(nn*ntrans[kz]);
{numb.conc. calculated in m-3}
{using Eq. (1) in Glenn E. Spangler, Anal. Chem. 64, 1312 (1992)}
{nn=normalization constant for gaussian}
```

```
    end;
  end;
 end;

for iz:=1 to nvs do
 begin
  for idp:=1 to nbins do
   begin
    nm^[idp,iz]:=((1e+6)*nm^[idp,iz])*dz;
                    {numb.conc changed from cm-3 to m-2   }
    z0:=(iz-0.5)*dz;
    for it:=1 to nts do
     begin
      jz:=Round((z0/dz)+0.5);
      if jz<1 then
       begin
        itempo:=it;
        z1:=-1e-4;
        it:=nts;
       end
      else
       begin
        k1:=-dt*Zp[idp]*Et[jz];
        jz:=Round(((z0+(0.5*k1))/dz)+0.5);
       end;

      if jz<1 then
       begin
        itempo:=it;
        z1:=-1e-4;
        it:=nts;
       end
      else
       begin
        k2:=-dt*Zp[idp]*Et[jz];
        jz:=Round(((z0+(0.5*k2))/dz)+0.5);
       end;

      if jz<1 then
       begin
        itempo:=it;
        z1:=-1e-4;
        it:=nts;
       end
      else
       begin
        k3:=-dt*Zp[idp]*Et[jz];
        jz:=Round(((z0+k3)/dz)+0.5);
       end;

      if jz<1 then
       begin
        itempo:=it;
        z1:=-1e-4;
```

```
   it:=nts;
  end
 else
  begin
   k4:=-dt*Zp[idp]*Et[jz];
   z1:=z0+((k1+(2*k2)+(2*k3)+k4)/6);
   z0:=z1;
  end;

 if z1<0 then
  begin
   itempo:=it;
   z1:=-1e-4;
   it:=nts;
  end;
 end;
jz:=Round(((z1/dz)+0.5));
z1:=(jz-0.5)*dz;
if jz<1 then
 z1:=z1-Zp[idp]*Et[1]*(nts-itempo)*dt;

if (df='n') or (df='N')
 then
  begin
   if jz>0 then
    nmtrans^[idp,jz]:=nmtrans^[idp,jz]+(nm^[idp,iz]/dz);
  end
 else
  begin
   sig:=Sqrt(2*D[idp]*dtr);

   jzmax:=Round((((z1+(5*sig))/dz)+0.5));
   jzmin:=Round((((z1-(5*sig))/dz)+0.5));
   somat:=0;
   for kz:=jzmin to 0 do
    begin
     zz:=(kz-0.5)*dz;
     arg:=(-Sqr(zz-z1))/(4*D[idp]*dtr);
     if arg>(-100)
      then
       begin
        nmom:=((nm^[idp,iz]/(2*Sqrt(pi*D[idp]*dtr)))*Exp(arg));
        somat:=somat+(nmom*dz);
       end;
    end;

   for kz:=1 to nvs do
    ntrans[kz]:=0;

   for kz:=1 to nvs do
    begin
     zz:=(kz-0.5)*dz;
     arg:=(-Sqr(zz-z1))/(4*D[idp]*dtr);
     if arg>(-100)
```

```
        then
         begin
          ntrans[kz]:=((nm^[idp,iz]/(2*Sqrt(pi*D[idp]*dtr)))*Exp(arg));
          somat:=somat+(ntrans[kz]*dz);
         end;
       end;
      for kz:=(nvs+1) to jzmax do
       begin
        zz:=(kz-0.5)*dz;
        arg:=(-Sqr(zz-z1))/(4*D[idp]*dtr);
        if arg>(-100)
         then
          begin
           nmom:=((nm^[idp,iz]/(2*Sqrt(pi*D[idp]*dtr)))*Exp(arg));
           somat:=somat+(nmom*dz);
          end;
       end;

      if somat<(1e-10)
       then
        nn:=0
       else
        nn:=nm^[idp,iz]/somat;

      for kz:=1 to nvs do
       nmtrans^[idp,kz]:=nmtrans^[idp,kz]+(nn*ntrans[kz]);

     {numb.conc. calculated in m-3 }
     {using Eq. (1) in Glenn E. Spangler, Anal. Chem. 64, 1312 (1992)}
     {nn=normalization constant for gaussian}

     end;
   end;
 end;

for iz:=1 to nvs do  {changes numb.conc. back to cm-3}
 begin
  for idp:=1 to nbins do
   begin
    nptrans^[idp,iz]:=(nptrans^[idp,iz])/(1e+6);
    nmtrans^[idp,iz]:=(nmtrans^[idp,iz])/(1e+6);
   end;
 end;


ro[0]:=0;
for iz:=1 to nvs do
 begin
  ro[iz]:=0;
  for idp:=1 to nbins do
   ro[iz]:=ro[iz]+( 0.5*(dp[idp+1]-dp[idp-1]) * (1e+6*(nptrans^[idp,iz]-nmtrans^[idp,iz])) );
  ro[iz]:=(alfac*e)*ro[iz];
 end;
 if (sc = 'y') or (sc = 'Y')
```

```
 then
  begin
   ve[1]:=0;
   ve[nvs+1]:=vap;
   for kz:=2 to nvs do
    ve[kz]:=0;
   dif:=0;
   conv:=0.00000001;
   w:=1.5;
   iter:=1;
   repeat
    begin
     {writeln('Iteration # ',iter,' dif ',dif:5:9,' ve[90] ',ve[90]:5:7);}
     for kz:=2 to nvs do
      begin
       veant[kz]:=ve[kz];
       ve[kz]:= (  (w/2)*(ve[kz+1]+ve[kz-1] + ( (ro[kz-1]/eps)*(dz*dz) )) ) + ((1-w)*ve[kz]);
      end;
     dif:=0;
     for kz:=2 to nvs do
      begin
       if Abs(ve[kz]-veant[kz]) > dif then
        dif:=Abs(ve[kz]-veant[kz]);
      end;

     iter:=iter+1;
    end;
   until (dif<conv);

   for kz:=1 to nvs do
    Et[kz]:=-((ve[kz+1]-ve[kz])/dz);
  end;

 nome:='efield.dat';
assign(arq,nome);
rewrite(arq);
writeln(arq,nvs);
for kz:=1 to nvs do
 writeln(arq,((kz-0.5)*dz):0:5,' ',Et[kz]:5:5);
close(arq);

nome:='potential.dat';
assign(arq,nome);
rewrite(arq);
writeln(arq,nvs);
for kz:=1 to nvs do
 writeln(arq,((kz-0.5)*dz):0:5,' ',ve[kz]:5:5);
close(arq);

writeln('Efield calculated');
ch:=readkey;    }

if p=1
 then
```

```
  begin
   p:=2;
   pp:=1;
  end
 else
  begin
   p:=1;
   pp:=2;
  end;

 for idp:=1 to nbins do
  begin
   for kz:=1 to nvs do
    begin
     np^[idp,kz]:=nptrans^[idp,kz];
     nm^[idp,kz]:=nmtrans^[idp,kz];
    end;
  end;
end;

for idp:=1 to nbins do
begin
 for kz:=(nvs-nssl) to nvs do
  nf[idp]:=nf[idp]+((np^[idp,kz])/nssl);   {/(kp0+(kp1*Exp(-Sqr(((dp[idp]-kp2)/kp3))))));}
end;

{These expressions for nf[idp] using np[idp,nvs,p] and nm[idp,nvs,p] }
{are valid only for nrs even                                        }

IF RDMA=1
 THEN                {For the TDMA program TF isn't the transfer}
                     {function anymore, but the size distribution}
 BEGIN
  RDMA:=2;
  sc:='n';         {that exited the RDMA-1 and entered RDMA-2}
  for idp:=1 to nbins do
   tf[idp]:=nf[idp];
  n1:=0;
  for idp:=1 to nbins do
   n1:=n1+( 0.5*(dp[idp+1]-dp[idp-1]) * nf[idp] );
  n1:=alfac*n1;

  nome:='tf.dat';
  assign(arq,nome);
  rewrite(arq);
  writeln(arq,nbins);
  for idp:=1 to nbins do
   writeln(arq,dp[idp]:3:2,' ',Zp[idp]/ms1:3:5,' ',tf[idp]/np0[idp]:1:5);
  close(arq);

  WRITELN('DONE WITH RDMA-1 - PRESS <RETURN> TO CONTINUE');
  CH:=READKEY;

 END
```

```
 ELSE

  BEGIN
   n2[iv]:=0;
   for idp:=1 to nbins do
    n2[iv]:=n2[iv]+( 0.5*(dp[idp+1]-dp[idp-1]) * nf[idp] );
   n2[iv]:=alfac*n2[iv];
   n2[iv]:=n2[iv]/n1;      {n2[iv] now is n2/n1}
  END;

  {In the last expression we use nf/n instead of np/np0 to leave open the possibility of strong space charge effects}
  {   that would give rise to the sampling of negative particles along with positive ones.            }

 nome:='n2_n1.dat';
 assign(arq,nome);
 rewrite(arq);
 writeln(arq,nbins);
 for i:=1 to iv do
  writeln(arq,(mob[i]/ms1):1:5,' ',n2[i]:1:5);
 close(arq);

END;    {ends iv loop for RDMA-2}

dispose(nm);
dispose(np);
dispose(nmtrans);
dispose(nptrans);
nm:=nil;
np:=nil;
nptrans:=nil;
nmtrans:=nil;

end.

(*****************************************************************************)
(*                                Required Pascal units                      *)
(*****************************************************************************)

unit unm;
interface
uses ubas;
type
 cube = array[1..80] of array[1..200] of single;
var
 nm:^cube;
implementation
end.

unit unmtr;
interface
uses ubas;
type
 cube = array[1..80] of array[1..200] of single;
```

```
var
 nmtrans:^cube;
implementation
end.

unit unp;
interface
uses ubas;
type
 cube = array[1..80] of array[1..200] of single;
var
 np:^cube;
implementation
end.

unit unptr;
interface
uses ubas;
type
 cube = array[1..80] of array[1..200] of single;
var
 nptrans:^cube;
implementation
end.
```

A.2 Cylindrical differential mobility analyzer version

A version of the space charge simulation was also developed for the CDMA. Although the structure and data entry of the code is identical to the RDMA version, sufficient modifications were made on the program to require a new listing. This listing can be found in the pages that follow.

```
(*****************************************************************************)
(*                    CDMA – Space charge simulation – Renato P. Camata – 1997                    *)
(*****************************************************************************)

program CDMAsim; {$N+}

{This program was adapted from RDMAsim for the CDMA}

Uses unp,unm,unptr,unmtr,WinCrt;

const
 e:real=1.6e-19; {Coulombs}
 pi:real=3.141592654;
 a:real=1.257;
 b:real=0.40;
 g:real=1.10;
    {a,b,g=alfa, beta, gama in the expression for the slip        }
    {     correction factor Cc=1+Kn(a+bexp(-g/Kn))              }
 l:real=6.51e-8;  {m}          {value for air, T=298 K, 1 atm}
 u:real=1.8e-5;   {kg m-1 s-1}  {value for air, T=298 K, 1 atm}
 eps:real=8.8e-12;{F/m}        {value for vacuum          }
 kT:real=4.16e-21; {SI}        {value for T=298 K          }
    {l=lambda, mean free path of the gas                    }
    {u=mu, gas viscosity                                }
    {kT=Boltzmann constant * Temperature (T~300 K )              }

(************************CDMA parameters*******************************)
 {r1:real=0.24e-2;}
 {r2:real=5.04e-2;}
 deltar:real=1e-2;
 deltarv:real=1e-2;
 s:real=9.8171e-3;
 rr1:real=9.4488e-3;
 rr2:real=19.2659e-3;
 z1fora:real=9.8671e-3;
    {r1=CDMA outlet diameter position (m)  NECESSARY ?          }
    {r2=CDMA inlet diameter position (m)   NECESSARY ?          }
    {rr1=CDMA inner radius (m)                          }
    {rr2=CDMA outer radius (m)                          }
    {deltarv=the real deltar, used to calculate Vap given dp*    }
    {deltar=r2-r1=L of the CDMA  (m) deltar necessary to match TF with analytical }
    {s=rr2-rr1=spacing between electrodes (m)                    }

type
 vsmall = array[1..80] of real;
 vsmallDP = array[0..81] of real;
 vlarge = array[0..200] of double;
 cube = array[1..80] of array[1..200]of single;
 vtrans = array[1..80] of array[1..200] of single;

var

(******************VARIABLES RELATED TO GRAPHIC FEATURES**************)
 I:integer;

(******************VARIABLES RELATED TO THE HANDLING OF FILES*********)
```

```
 arq:text;
 arq2:text;
 name,nome:string[20];

(************VARIABLES RELATED TO THE SIZE DISTRIBUTIONS**************)
 idp,nbins:integer;
 dp:vsmallDP;
 n,nf,nm0,np0:vsmall;
 km0,km1,km2,km3,kp0,kp1,kp2,kp3:real;
    {idp=index for the bins of the size distributions            }
    {nbins=total number of bins of the size distributions        }
    {dp[idp]=mobility diameter (nm)                              }
    {n[idp]=initial number concentration (cm-3) (before neutralizer) }
    {nf[idp]=final number concentration (cm-3) (corr. for charging)  }
    {kmi=coefficients of the gaussian fit for Fuchs charge dist.     }
    {   for q=-1e                                                }
    {kpi=coefficients of the gaussian fit for Fuchs charge dist.     }
    {   for q=+1e                                                }
    {nm0[idp]=initial negative number concentration (cm-3):particles }
    {   from initial size distribution which acquire charge q=-1e    }
    {np0[idp]=initial positive number concentration (cm-3):particles }
    {   from initial size distribution which acquire charge q=+1e    }
    {nm[idp,iz,p]=evolving negative number concentration (cm-3)      }
    {np[idp,iz,p]=evolving positive number concentration (cm-3)      }


(*VARIABLES RELATED TO THE ELECTRIC FIELD/TRAJECTORIES CALCULATION****)
 nrs,nrsdb2,nvs,nssl,nts,ir,irr,iz,it,iv,jz,lz,kz,idtr,npvs,npvsdv2:integer;
 dr,r,dtr,dz,v,dt,z0,z1,zz,h,Et0,Et1,Vmin,Vmax:real;
 Et,ro:vlarge;
 ve,veant:array[1..201] of real;
 dif,conv,w:real;
 iter:integer;
 sig:real;
    {nrs=number of radial steps for calculation                  }
    {nrs=number of vertical steps for calculation                }
    {nrsdb2=nrs/2                                                }
    {nts=number of time steps for z(t) calculation               }
    {r=radial position of the vertical slab (origin at RDMA center)(m)}
    {rnext=radial position of the next vertical slab (m)         }
    {dr=radial step thickness (m)                                }
    {dz=vertical step thickness (m)                              }
    {dtr=time it takes the aerosol to traverse dr (radial motion)    }
    {dt=time slab for the integration in z (vertical motion)         }
    {npvs=number of points per vertical step (for E(z) integration)  }
    {npvsdv2=npvs/2                                              }
    {h=dz/npvs                                                   }
    {v=radial velocity of the aerosol (m/s)                      }
    {ir,irr=index for radial change                              }
    {iz,jz,lz,kz=indexes for vertical change                     }
    {it=index for time change                                    }
    {idtr=index for dtr: idtr=Round(dtr)                         }
    {Et[iz]=total electric field: Et = (Vap/s) + Esc             }
    {z0,z1=position of a particle that is migrating across the DMA   }
    {zz=position of a particle once diffusion is taken into account  }
    {Et0,Et1=electric field at the points in the vertical step       }
```

```
    {ro[iz]=charge density                              }
    {sig=standard deviation for the diffusional broadening        }

(*********VARIABLES RELATED TO THE RDMA OPERATION**********************)
 qa,qs,vap:real;
    {qa=aerosol flow rate (LPM immediatly converted to m3/s)       }
    {qs=sheath flow rate (LPM immediatly converted to m3/s)        }
    {vap=voltage applied to the RDMA electrodes (V)              }

(****************VARIABLES RELATED TO THE AEROSOL*********************)
 Kn,Cc:real;
 Zp,D:vsmall;
    {Kn=Knudsen number; Kn=2l/Dp                          }
    {Cc=Slip correction factor                          }
    {Zp[idp]=Electrical mobility (here Zp is calculated for a single }
    {       elementary charge, using only its absolute value in the }
    {       expression for Zp - the charge sign is not included)   }
    {D[idp]=Brownian diffusivity                          }

(********VARIABLES RELATED TO THE DIFF. EQUATIONS SOLUTION************)
 k1,k2,k3,k4:real;
    {k1,k2,k3,k4=coefficients in Runge-Kutta's formula           }

(************************AUXILIARY VARIABLES*****************************)
 ch,sc,df,BABA:char;
 somat,nn,nmom,SUM,SOM,AUXR,SOMA,incre,arg,NMTI,NPTI,NMT,NPT,zzz:real;
 ntrans:vlarge;
 imax,jzmax,jzmin,itempo,p,pp,AUX:integer;

(*******VARIABLES RELATED TO THE INITIAL SIZE DISTRIBUTION************)
 DlogDp,DlogDpl,DlogDpr,Dmin,Dpmin,Dpmax,Dmax,sg,dpg,Ne,area,alfac,ccorr:real;
 npl,npr,nphr:integer;
 tf:vsmall;

    {Ne=total number concentration of singly charged positive particles}
    {  determined from experiment                          }
    {  to be used to generate initial size dist. that entered DMA     }

(************VARIABLES FOR THE TDMA EXPERIMENT************************)
 dps,ms1,fmmin,fmmax,ms2min,ms2max,ms2inc,n1:real;
 RDMA,nms2s:integer;
 n2,mob:array[0..30] of real;

    {dps=size classified from RDMA-1 = Dp* (nm)                }
    {ms1=mobility corresponding to dps (SI)                  }
    {fmmin,fmmax=multiplicative factors that define mobility range for }
    {         RDMA-2                                  }
    {nms2s=number of Zp*,2 steps                          }
    {ms2min,ms2max,ms2inc=min,max, and inc to Zp*,2              }
    {RDMA=(1)RDMA-1, (2)RDMA-2                            }
    {mob[iv]=Zp*,2 for each step in the RDMA-2 scan              }
    {n1=N1 in Zhang and Flagan's paper on diffusional broadening      }
    {n2[iv]=N2 in Zhang and Flagan's paper on diffusional broadening   }

begin
New(np);
```

```
New(nm);
New(nptrans);
New(nmtrans);

(************************GRAPHIC INTRODUCTION**********************)
 ClrScr;
 Write(Char(201));
 for I := 1 to 78 do
  Write(Char(205));
 Write(Char(187));
 Write(Char(186));
 GotoXY(80,2);
 Write(Char(186));
 Write(Char(200));
 for I := 1 to 78 do
  Write(Char(205));
 Write(Char(188));
 Writeln;

 GotoXY(4,2);
 Write('                    CDMAsim ');
 GotoXY(46,2);

 writeln;
 writeln;
 writeln;

 writeln('       This program calculates the size distribution at the CDMA');
 writeln('            sampling outlet taking into account:');
 writeln;
 writeln('             * MIGRATION DUE TO THE APPLIED FIELD');
 writeln('             * BROWNIAN DIFFUSION');
 writeln('             * SPACE CHARGE EFFECTS');
 writeln('             * PARTICLE LOSS TO THE TOP ELECTRODE');
 writeln;

(*************************************************************************)
(*********************DATA ENTRY*****************************************)
(***********SIZE DISTRIBUTION & APPLIED VOLTAGE**************************)
(*****************  RDMA-1 ***********************************************)

 Dmin:=0.5;
 npl:=10;

 Dpmin:=2.8;
 Dpmax:=3.4;
 nphr:=60;

 Dmax:=100;
 npr:=10;

 sg:=1.47;
 dpg:=8.62;
 Ne:=1e+10;
 dps:=3.0;
```

```
 ccorr:=0;  {correction for charging}
(*************************************************************************)
 Kn:=(2*l)/(dps*1e-9);
 Cc:=1+(Kn*(a+(b*Exp(-(g/Kn)))));
 ms1:=(e*Cc)/(3*pi*u*dps*1e-9);
 {WRITELN('Zp = ',ms1);
 ch:=readkey;        }

 { REMEMBER: nbins:=npl+nphr+npr-1   }

(*************************************************************************)
(****************** RDMA-2 ***********************************************)
 fmmin:=0.6;  {minimum for Zp*,2/Zp*,1}
 fmmax:=1.4;  {maximum for Zp*,2/Zp*,1}
 nms2s:=20;   {number of points in between}

(*************************************************************************)
 ms2min:=fmmin*ms1;
 ms2max:=fmmax*ms1;
 ms2inc:=(ms2max-ms2min)/nms2s;

(*************************************************************************)
(*************************************************************************)

RDMA:=1;
FOR IV:=0 TO (NMS2S+1) DO
BEGIN
 for idp:=1 to nbins do
  nf[idp]:=0;

IF RDMA=1 THEN    {Begins preparation for RDMA-1}
BEGIN
 nbins:=npl+nphr+npr-1;

 Dlogdpl:=Ln(Dpmin/Dmin)/(npl-1);
 for idp:=1 to (npl-1) do
  Dp[idp]:=Exp(Ln(Dmin)+((idp-1)*Dlogdpl));

 Dlogdp:=Ln(Dpmax/Dpmin)/(nphr);
 for idp:=npl to (npl+nphr-1) do
  Dp[idp]:=Exp(Ln(Dpmin)+((idp-(npl-1)-1)*Dlogdp));

 Dlogdpr:=Ln(Dmax/Dpmax)/(npr-1);
 for idp:=(npl+nphr) to nbins do
  Dp[idp]:=Exp(Ln(Dpmax)+((idp-(npl+nphr-1)-1)*Dlogdpr));

 Dp[nbins+1]:=(2*Dp[nbins])-Dp[nbins-1];
 Dp[0]:=(2*Dp[1])-Dp[2];
 if Dp[0]<0 then Dp[0]:=0;

 for idp:=1 to nbins do
  np0[idp]:=(Ne/(Sqrt(2*pi)*Ln(sg)))*Exp(-((Sqr(Ln(dp[idp])-Ln(dpg)))/(2*Sqr(Ln(sg)))));

(*APPLYING FUCHS CHARGE DISTRIBUTIONS TO THE INITIAL SIZE DISTRIBUTION*)
(*Gaussian fits to the results in A. Wiedensohler, J. Aerosol Sci. 19**)
(*pp.387 (1988)*********************************************************)
```

```
{we start with np0[idp], because that is }
{ the one we have access experimentally. Then, we calculate n[idp] and }
{ nm0[idp] using Fuchs charge distribution.                    }

kp0:=0.206553;
kp1:=-0.263344;
kp2:=-25.9357;
kp3:=52.64;

for idp:=1 to nbins do
 n[idp]:=np0[idp]/(kp0+(kp1*Exp( -Sqr (((dp[idp]-kp2)/kp3))  )));

km0:=0.272151;
km1:=-0.319269;
km2:=-19.1046;
km3:=47.8427;

for idp:=1 to nbins do
 nm0[idp]:=ccorr*(km0+(km1*Exp(-Sqr(((dp[idp]-km2)/km3)))))*n[idp];


(*****************DETERMINATION OF THE ALFA CONSTANT*********************)
(*              alfac=Ne/(Area under nm0[idp])                *)
area:=0;
for idp:=1 to nbins do
 area:=area+( np0[idp] * (0.5*(dp[idp+1]-dp[idp-1])) );
alfac:=Ne/area;

(*DISPLAYS MONODISPERSE AEROSOLS AND EFFECT OF FUCHS CHARGE DIST.**)

clrscr;
writeln;
writeln('                  INITIAL MONODISPERSE AEROSOLS');
writeln;
writeln('        Dp (nm)       N(cm-3)      N[-1](cm-3)    N[+1](cm-3)');
writeln;

for idp:=1 to nbins do
 begin
  write('        ',Dp[idp]:3:2,'          ',n[idp]:7:0,'         ');
  writeln(nm0[idp]:5:0,'          ',np0[idp]:5:0);
  ch:=readkey;
 end;
writeln;

writeln('              IF THIS IS CORRECT PRESS ANY KEY TO CONTINUE');
ch:=readkey;

(*********************READING IMPORTANT VARIABLES************************)

repeat
 begin
  clrscr;
  writeln;

  writeln;
```

```
  write('                INPUT AEROSOL FLOW RATE (LPM) = ');
  read(qa);
  qa:=(qa*0.001)/60;
  writeln;
  write('                INPUT SHEATH FLOW RATE (LPM) = ');
  read(qs);
  qs:=(qs*0.001)/60;
  writeln;
  writeln;
  write('   INPUT NUMBER OF VERTICAL STEPS IN CDMA COLUMN (EVEN:10-1000) = ');
  read(nrs);
  writeln;
  write('        INPUT NUMBER OF RADIAL STEPS IN CDMA (10-1000) = ');
  read(nvs);
  writeln;
  write('             INPUT TIME RESOLUTION FOR z(t) (s) = ');
  read(dt);
  writeln;
  writeln('  INPUT NUMBER OF POINTS PER RADIAL STEP FOR E(r)');
  write('                              (EVEN:2-10) = ');
  read(npvs);
  npvsdv2:=Round(npvs/2);
  writeln;
  write('             INCLUDE SPACE CHARGE EFFECTS ? (Y/N) ');
  sc:=readkey;
  writeln;
  writeln;
  write('                    INCLUDE DIFFUSION ? (Y/N) ');
  df:=readkey;

  writeln;
  writeln;
  write('             DO YOU WANT TO CHANGE ANYTHING ? (Y/N) ');
  ch:=readkey;
  writeln;
 end;
until (ch='n') or (ch='N');

for idp:=1 to nbins do
 begin
  tf[idp]:=0;
  nf[idp]:=0;
 end;

(******CALCULATING ELECTRICAL MOBILITY AND BROWNIAN DIFFUSIVITY*********)
for idp:=1 to nbins do
 begin
  Kn:=(2*l)/(dp[idp]*1e-9);
  Cc:=1+(Kn*(a+(b*Exp(-(g/Kn)))));
  Zp[idp]:=(e*Cc)/(3*pi*u*dp[idp]*1e-9);
  D[idp]:=(kT*Cc)/(3*pi*u*dp[idp]*1e-9);
 end;

Vap:=-(qs*Ln(rr2/rr1))/(2*pi*deltarv*ms1);
Vmin:=(qs*Ln(rr2/rr1))/(2*pi*deltarv*ms2min);
Vmax:=(Vmin*ms2min)/ms2max;
```

```
END             {Ends preparation for RDMA-1}
ELSE
BEGIN           {Begins preparation for RDMA-2}

 for idp:=1 to nbins do
  begin
   np0[idp]:=tf[idp];
   nm0[idp]:=0;       {assuming that only positive particles made it}
  end;              {to the RDMA-2                          }

 mob[iv]:=ms2min+((iv-1)*ms2inc);
 vap:=-(Vmin*ms2min)/mob[iv];
 SC:='N';

END;            {Ends preparation for RDMA-2}

 dr:=deltar/nrs;
 dz:=s/nvs;
 h:=dz/npvs;

 nssl:=Round((qa/qs)*nvs);

 for idp:=1 to nbins do
  begin
   for kz:=1 to nssl do
    begin
     np^[idp,kz]:=np0[idp];
     nm^[idp,kz]:=nm0[idp];
    end;
  end;

 for idp:=1 to nbins do
  begin
   for jz:=(nssl+1) to nvs do
    begin
     np^[idp,jz]:=0;
     nm^[idp,jz]:=0;
    end;
  end;

 for iz:=0 to nvs+1 do
  begin
   zzz:=(iz-0.5)*dz;
   zzz:=-zzz+rr2;
   if zzz>rr2 then zzz:=rr2;
   if zzz<rr1 then zzz:=rr1;
   Et[iz]:=-Vap/(zzz*Ln(rr2/rr1));
  end;

 p:=1;
 pp:=2;

 for ir:=1 to nrs do
  begin
```

```
writeln('RDMA-',RDMA,' ',iv,'/',(nms2s+1),' RADIAL POSITION IR = ',ir,' Vap = ',vap:3:2);


r:=deltar-((ir-0.5)*dr);
v:=(qs+qa)/(pi*(Sqr(rr2)-Sqr(rr1)));
dtr:=dr/v;
nts:=Round(dtr/dt);
for idp:=1 to nbins do
 begin
  for jz:=1 to nvs do
   begin
    nptrans^[idp,jz]:=0;
    nmtrans^[idp,jz]:=0;
   end;
 end;

for iz:=1 to nvs do
 begin
  for idp:=1 to nbins do
   begin

    np^[idp,iz]:=((1e+6)*np^[idp,iz])*dz;
                    {numb.conc changed from cm-3 to m-2 }

    z0:=(iz-0.5)*dz;
    for it:=1 to nts do
     begin
      jz:=Round((z0/dz)+0.5);

      if jz<1 then
       begin
        itempo:=it;
        it:=nts;
        z1:=-1e-4;
       end
      else
       begin
        if jz>nvs then
         begin
          itempo:=it;
          it:=nts;
          z1:=z1fora;
         end
        else
         begin
          k1:=dt*Zp[idp]*Et[jz];
          jz:=Round(((z0+(0.5*k1))/dz)+0.5);
         end;
       end;

      if jz<1 then
       begin
        itempo:=it;
        it:=nts;
        z1:=-1e-4;
       end
```

```
else
 begin
  if jz>nvs then
   begin
    itempo:=it;
    it:=nts;
    z1:=z1fora;
   end
  else
   begin
    k2:=dt*Zp[idp]*Et[jz];
    jz:=Round(((z0+(0.5*k2))/dz)+0.5);
   end;
 end;

if jz<1 then
 begin
  itempo:=it;
  it:=nts;
  z1:=-1e-4;
 end
else
 begin
  if jz>nvs then
   begin
    itempo:=it;
    it:=nts;
    z1:=z1fora;
   end
  else
   begin
    k3:=dt*Zp[idp]*Et[jz];
    jz:=Round(((z0+k3)/dz)+0.5);
   end;
 end;

if jz<1 then
 begin
  itempo:=it;
  it:=nts;
  z1:=-1e-4;
 end
else
 begin
  if jz>nvs then
   begin
    itempo:=it;
    it:=nts;
    z1:=z1fora;
   end
  else
   begin
    k4:=dt*Zp[idp]*Et[jz];
    z1:=z0+((k1+(2*k2)+(2*k3)+k4)/6);
    z0:=z1;
   end;
```

```
  end;

 if jz<1 then
  begin
   itempo:=it;
   it:=nts;
   z1:=-1e-4;
  end
 else
  begin
   if z1>s then
    begin
     itempo:=it;
     it:=nts;
     z1:=z1fora;
    end;
  end;


end;

jz:=Round(((z1/dz)+0.5));
z1:=(jz-0.5)*dz;

if jz>nvs then
 z1:=z1+Zp[idp]*Et[nvs]*(nts-itempo)*dt;

if jz<1 then
 z1:=z1+Zp[idp]*Et[1]*(nts-itempo)*dt;

if (df='n') or (df='N')
 then
  begin
   if jz<(nvs+1) then
    nptrans^[idp,jz]:=nptrans^[idp,jz]+(np^[idp,iz]/dz);
  end
 else
  begin

   sig:=Sqrt(2*D[idp]*dtr);

   jzmax:=Round((((z1+(5*sig))/dz)+0.5));
   jzmin:=Round((((z1-(5*sig))/dz)+0.5));

   somat:=0;

   for kz:=jzmin to 0 do
    begin
     zz:=(kz-0.5)*dz;
     arg:=(-Sqr(zz-z1))/(4*D[idp]*dtr);
     if arg>(-100)
      then
       begin
        nmom:=((np^[idp,iz]/(2*Sqrt(pi*D[idp]*dtr)))*Exp(arg));
        somat:=somat+(nmom*dz);
       end;
```

```
      end;

     for kz:=1 to nvs do
      ntrans[kz]:=0;

     for kz:=1 to nvs do
      begin
       zz:=(kz-0.5)*dz;
       arg:=(-Sqr(zz-z1))/(4*D[idp]*dtr);
       if arg>(-100)
        then
         begin
          ntrans[kz]:=((np^[idp,iz]/(2*Sqrt(pi*D[idp]*dtr)))*Exp(arg));
          somat:=somat+(ntrans[kz]*dz);
         end;
      end;

     for kz:=(nvs+1) to jzmax do
      begin
       zz:=(kz-0.5)*dz;
       arg:=(-Sqr(zz-z1))/(4*D[idp]*dtr);
       if arg>(-100)
        then
         begin
          nmom:=((np^[idp,iz]/(2*Sqrt(pi*D[idp]*dtr)))*Exp(arg));
          somat:=somat+(nmom*dz);
         end;
      end;

     if somat<(1e-10)
      then
       nn:=0
      else
       nn:=np^[idp,iz]/somat;


     for kz:=1 to nvs do
      nptrans^[idp,kz]:=nptrans^[idp,kz]+(nn*ntrans[kz]);

     {numb.conc. calculated in m-3}
     {using Eq. (1) in Glenn E. Spangler, Anal. Chem. 64, 1312 (1992)}
     {nn=normalization constant for gaussian}

    end;

  end;

 end;

for iz:=1 to nvs do
 begin
  for idp:=1 to nbins do
   begin

    nm^[idp,iz]:=((1e+6)*nm^[idp,iz])*dz;
                  {numb.conc changed from cm-3 to m-2   }
```

```
z0:=(iz-0.5)*dz;
for it:=1 to nts do
 begin
  jz:=Round((z0/dz)+0.5);

  if jz<1 then
   begin
    itempo:=it;
    z1:=-1e-4;
    it:=nts;
   end
  else
   begin
    k1:=-dt*Zp[idp]*Et[jz];
    jz:=Round(((z0+(0.5*k1))/dz)+0.5);
   end;

  if jz<1 then
   begin
    itempo:=it;
    z1:=-1e-4;
    it:=nts;
   end
  else
   begin
    k2:=-dt*Zp[idp]*Et[jz];
    jz:=Round(((z0+(0.5*k2))/dz)+0.5);
   end;

  if jz<1 then
   begin
    itempo:=it;
    z1:=-1e-4;
    it:=nts;
   end
  else
   begin
    k3:=-dt*Zp[idp]*Et[jz];
    jz:=Round(((z0+k3)/dz)+0.5);
   end;

  if jz<1 then
   begin
    itempo:=it;
    z1:=-1e-4;
    it:=nts;
   end
  else
   begin
    k4:=-dt*Zp[idp]*Et[jz];
    z1:=z0+((k1+(2*k2)+(2*k3)+k4)/6);
    z0:=z1;
   end;

  if z1<0 then
   begin
```

```
   itempo:=it;
   z1:=-1e-4;
   it:=nts;
  end;
 end;

jz:=Round(((z1/dz)+0.5));
z1:=(jz-0.5)*dz;

if jz<1 then
 z1:=z1-Zp[idp]*Et[1]*(nts-itempo)*dt;

if (df='n') or (df='N')
 then
  begin
   if jz>0 then
    nmtrans^[idp,jz]:=nmtrans^[idp,jz]+(nm^[idp,iz]/dz);
  end
 else
  begin
   sig:=Sqrt(2*D[idp]*dtr);

   jzmax:=Round((((z1+(5*sig))/dz)+0.5));
   jzmin:=Round((((z1-(5*sig))/dz)+0.5));

   somat:=0;

   for kz:=jzmin to 0 do
    begin
     zz:=(kz-0.5)*dz;
     arg:=(-Sqr(zz-z1))/(4*D[idp]*dtr);
     if arg>(-100)
      then
       begin
        nmom:=((nm^[idp,iz]/(2*Sqrt(pi*D[idp]*dtr)))*Exp(arg));
        somat:=somat+(nmom*dz);
       end;
    end;

   for kz:=1 to nvs do
    ntrans[kz]:=0;

   for kz:=1 to nvs do
    begin
     zz:=(kz-0.5)*dz;
     arg:=(-Sqr(zz-z1))/(4*D[idp]*dtr);
     if arg>(-100)
      then
       begin
        ntrans[kz]:=((nm^[idp,iz]/(2*Sqrt(pi*D[idp]*dtr)))*Exp(arg));
        somat:=somat+(ntrans[kz]*dz);
       end;
    end;

   for kz:=(nvs+1) to jzmax do
    begin
```

```
        zz:=(kz-0.5)*dz;
        arg:=(-Sqr(zz-z1))/(4*D[idp]*dtr);
        if arg>(-100)
         then
          begin
           nmom:=((nm^[idp,iz]/(2*Sqrt(pi*D[idp]*dtr)))*Exp(arg));
           somat:=somat+(nmom*dz);
          end;
       end;

      if somat<(1e-10)
       then
        nn:=0
       else
        nn:=nm^[idp,iz]/somat;

      for kz:=1 to nvs do
       nmtrans^[idp,kz]:=nmtrans^[idp,kz]+(nn*ntrans[kz]);

     {numb.conc. calculated in m-3 }
     {using Eq. (1) in Glenn E. Spangler, Anal. Chem. 64, 1312 (1992)}
     {nn=normalization constant for gaussian}

    end;


  end;
 end;

for iz:=1 to nvs do  {changes numb.conc. back to cm-3}
 begin
  for idp:=1 to nbins do
   begin
    nptrans^[idp,iz]:=(nptrans^[idp,iz])/(1e+6);
    nmtrans^[idp,iz]:=(nmtrans^[idp,iz])/(1e+6);
   end;
 end;

NPT:=0;
ro[0]:=0;
for iz:=1 to nvs do
 begin
  NPT:=0;
  ro[iz]:=0;
  for idp:=1 to nbins do
   begin
    ro[iz]:=ro[iz]+( 0.5*(dp[idp+1]-dp[idp-1]) * (1e+6*(nptrans^[idp,iz]-nmtrans^[idp,iz])) );
    NPT:=NPT+ (0.5*(DP[IDP+1]-DP[IDP-1]))*NPTRANS^[IDP,IZ];
   end;
  NPT:=NPT*ALFAC;
  ro[iz]:=(alfac*e)*ro[iz];

if (sc = 'y') or (sc = 'Y')
 then
  begin
   ve[1]:=0;
```

```
  ve[nvs+1]:=vap;
  for kz:=2 to nvs do
   ve[kz]:=0;
  dif:=0;
  conv:=0.00000001;
  w:=1.5;
  iter:=1;

  repeat
   begin
    {writeln('Iteration # ',iter,' dif ',dif:5:9,' ve[90] ',ve[90]:5:7);}
    for kz:=2 to nvs do
     begin
      zzz:=(kz-1-0.5)*dz;
      zzz:=-zzz+rr2;
      veant[kz]:=ve[kz];
      ve[kz]:=w*((((zzz-dz)*ve[kz+1])+(zzz*ve[kz-1])+((zzz*dz*dz*ro[kz-1])/eps))/((2*zzz)-dz)) + ((1-w)*ve[kz]);
     end;
    dif:=0;
    for kz:=2 to nvs do
     begin
      if Abs(ve[kz]-veant[kz]) > dif then
       dif:=Abs(ve[kz]-veant[kz]);
     end;

    iter:=iter+1;
   end;
  until (dif<conv);

  for kz:=1 to nvs do
   Et[kz]:=-((ve[kz+1]-ve[kz])/dz);

 end;

nome:='efield.dat';
assign(arq,nome);
rewrite(arq);
writeln(arq,nvs);
for kz:=1 to nvs do
 writeln(arq,((kz-0.5)*dz):0:5,' ',Et[kz]:5:5);
close(arq);
writeln('Efield calculated');
ch:=readkey;                                    }

if p=1
 then
  begin
   p:=2;
   pp:=1;
  end
 else
  begin
   p:=1;
   pp:=2;
  end;
```

```
 for idp:=1 to nbins do
  begin
   for kz:=1 to nvs do
    begin
     np^[idp,kz]:=nptrans^[idp,kz];
     nm^[idp,kz]:=nmtrans^[idp,kz];
    end;
  end;


 end;

for idp:=1 to nbins do
 begin
  for kz:=(nvs-nssl) to nvs do
   nf[idp]:=nf[idp]+((np^[idp,kz])/nssl);   {/(kp0+(kp1*Exp(-Sqr(((dp[idp]-kp2)/kp3))))));}
 end;

 {These expressions for nf[idp] using np[idp,nvs,p] and nm[idp,nvs,p] }
 {are valid only for nrs even                                        }


IF RDMA=1
 THEN                {For the TDMA program TF isn't the transfer}
                    {function anymore, but the size distribution}
 BEGIN
  RDMA:=2;
  sc:='n';         {that exited the RDMA-1 and entered RDMA-2}
  for idp:=1 to nbins do
   tf[idp]:=nf[idp];
  n1:=0;
  for idp:=1 to nbins do
   n1:=n1+( 0.5*(dp[idp+1]-dp[idp-1]) * nf[idp] );
  n1:=alfac*n1;

  nome:='tf.dat';
  assign(arq,nome);
  rewrite(arq);
  writeln(arq,nbins);
  for idp:=1 to nbins do
   writeln(arq,dp[idp]:3:2,' ',Zp[idp]/ms1:3:5,' ',tf[idp]/np0[idp]:1:5);
  close(arq);

  WRITELN('DONE WITH RDMA-1 - PRESS <RETURN> TO CONTINUE');
  CH:=READKEY;

 END

 ELSE

 BEGIN

  n2[iv]:=0;
  for idp:=1 to nbins do
   n2[iv]:=n2[iv]+( 0.5*(dp[idp+1]-dp[idp-1]) * nf[idp] );
  n2[iv]:=alfac*n2[iv];
```

```
  n2[iv]:=n2[iv]/n1;      {n2[iv] now is n2/n1}

  END;

  {In the last expression we use nf/n instead of np/np0 to leave open the }
  {possibility of strong space charge effects that would give rise to the }
  {sampling of negative particles along with positive ones.              }

 nome:='n2_n1.dat';
 assign(arq,nome);
 rewrite(arq);
 writeln(arq,nbins);
 for i:=1 to iv do
  writeln(arq,(mob[i]/ms1):1:5,' ',n2[i]:1:5);
 close(arq);

END;    {ends iv loop for RDMA-2}

dispose(nm);
dispose(np);
dispose(nmtrans);
dispose(nptrans);
nm:=nil;
np:=nil;
nptrans:=nil;
nmtrans:=nil;

end.
```